

**The stratigraphic evolution of exhumed submarine lobes in
unstable and complex basin margins**

**A thesis submitted to the University of Manchester for the degree of
Doctor of Philosophy in the Faculty of Science and Engineering**

2022

Ander Martinez-Doñate

Department of Earth and Environmental Sciences

This page was intentionally left blank

TABLE OF CONTENTS

List of figures	8
List of tables	18
Abstract	19
Declaration	20
Author contributions	20
Copyright Statement.....	23
Acknowledgements	24
1. Deep-water systems	25
1.1. INTRODUCTION	25
1.2. SEDIMENT GRAVITY FLOWS.....	29
1.2.1. Turbulent flows	29
1.2.2. Laminar flows	33
1.2.3. Transitional flows.....	35
1.3. SEDIMENT GRAVITY FLOW DEPOSITS	37
1.3.1. Low-density turbidites.....	37
1.3.2. High-density turbidites	38
1.3.3. Debrisites	41
1.3.4. Transitional flow deposits	42
1.4. SUBMARINE LANDSLIDES	44
1.4.1. Submarine landslide deposits	47
1.5. INTERACTION BETWEEN SEDIMENT GRAVITY FLOWS AND SEAFLOOR TOPOGRAPHY	48
1.5.1. Termination styles	53
1.6. GEOMORPHIC ELEMENTS OF DEEP-WATER SYSTEMS.....	56
1.6.1. Canyons.....	57
1.6.2. Channels	59

1.6.3. Channel-lobe transition zones (CLTZs).....	65
1.6.4. Submarine lobes	66
2. Rationale	74
2.1: HOW DO SUBMARINE LANDSLIDE DEPOSITS IMPACT YOUNGER DEPOSITIONAL SYSTEMS?	74
2.2 ARE ALL INTRASLOPE LOBES MADE EQUAL?	76
2.3 HOW ARE CREVASSE LOBES FORMED AND PRESERVED IN STRUCTURALLY CONFINED AND TECTONICALLY ACTIVE INTRASLOPE SETTINGS?.....	80
3. Substrate entrainment, depositional relief, and sediment capture: impact of a submarine landslide on flow process and sediment supply	82
3.1 ABSTRACT.....	82
3.2 INTRODUCTION	83
3.3 GEOLOGICAL SETTING.....	85
3.3.1. Study area: Chacay Melehue Graben	86
3.4 METHODOLOGY	90
3.5 RESULTS: SUBDIVISION AND CHARACTERISATION OF SEDIMENTARY UNITS 1-4.....	90
3.5.1. Unit 1.....	91
3.5.2. Unit 2.....	92
3.5.3. Unit 3.....	99
3.5.4. Unit 4.....	105
3.6 DEPOSITIONAL ARCHITECTURE OF THE DEBRITE AND OVERLYING UNITS	110
3.6.1. Large scale architecture: debrite relief	110
3.6.2. Small-scale architecture: foundered sandstones.....	113
Type 1	113
Type 2	115
Type 3	116
3.7 DISCUSSION	117
3.7.1. Basal shear zone and impact on the substrate	117

3.7.2. Dynamic debrite topography and impact on overlying strata	119
3.7.3. Origin and role of the mass-wasting process as a trigger for turbidite system development	122
3.8 CONCLUSIONS	124
4. Stratigraphic change in flow transformation processes recorded in early post-rift deep-marine lobe complexes in an intraslope setting	126
4.1. ABSTRACT.....	126
4.2. INTRODUCTION	127
4.3. GEOLOGICAL SETTING.....	129
4Study area: Chachil Graben.....	131
4.4. DATA AND METHODS.....	133
4.5. BED TYPES	134
4.5.1. Type A beds	136
4.5.2. Type B beds.....	137
4.5.3. Type C beds.....	140
4.5.4. Type D beds	142
4.5.5. Type E beds	144
4.5.6. Type F beds	147
4.5.7. Type G beds	149
4.5.8. Type H beds	149
4.6. PETROGRAPHY	150
4.6.1. Compositional trends.....	151
4.7. LOBE SUB-ENVIRONMENTS.....	153
4.7.1. Lobe axis	154
4.7.2. Lobe off-axis	155
4.7.3. Lobe fringe	156
4.8. INTRASLOPE LOBE COMPLEX ARCHITECTURE AND BED TYPE DISTRIBUTION.....	157
4.8.1. Lower Lobe Complex.....	160

4.8.2. Upper Lobe Complex	160
4.9. DISCUSSION	161
4.9.1. Controls on bed types and flow transformation	161
4.9.2. Sediment routing pathways and mud availability	162
4.9.3. Impact of topography on the pinch-out pattern	165
4.9.4. The steepness of the confining slope and comparison with other systems .	166
4.9.5. Controls on stratigraphic architecture	167
4.10. CONCLUSIONS	169
5. The impact of slope instabilities on submarine channels and development of crevasse lobes in tectonically active settings: an exhumed example from the Eocene Aínsa Basin (Spain)	170
5.1. ABSTRACT.....	170
5.2. INTRODUCTION	171
5.2.1. Study Area: San Vicente (Aínsa Basin)	173
5.3. GEOLOGICAL SETTING.....	175
5.4. DATA AND METHODS.....	176
5.5. FACIES ASSOCIATIONS.....	177
5.5.1. FA1: Overbank deposits.....	177
5.5.2. FA2: Terrace deposits	187
5.5.3. FA3: Channel-fill deposits	189
5.5.4. FA4: Crevasse scour-fill deposits	190
5.5.5. FA5: Crevasse lobe deposits	191
5.6. DEPOSITIONAL ARCHITECTURE	192
5.6.1. Channel belt.....	192
5.6.2. Overbank	193
5.7. DISCUSSION	198
5.7.1. Channel wall collapse and crevasse complex development.....	198
5.7.2. The impact of submarine landslides on channelised flows and terraces.....	202

5.7.3. Avulsion mechanism(s) in the Banastón II channel system.....	204
5.8. CONCLUSIONS	205
6. Synthesis and conclusions.....	206
6.1 HOW DO SUBMARINE LANDSLIDE DEPOSITS IMPACT YOUNGER DEPOSITIONAL SYSTEMS?	206
6.2 ARE ALL INTRASLOPE LOBES MADE EQUAL?	209
6.2.1. Why are the investigated intraslope lobes in the Neuquén Basin largely built by transitional flow deposits?.....	211
6.3. INFLUENCE OF SUBTLE SEAFLOOR TOPOGRAPHY ON SEDIMENT GRAVITY FLOW BEHAVIOUR.....	213
6.3.1. Event-bed scale	214
6.3.2. Stratal packages.....	214
6.4. RECOMMENDATIONS FOR FUTURE WORK	216
6.5. CONCLUSIONS	221
7. References	222
8. Appendix	260
Table 1 – Mineralogy table of detrital grains of the analysed samples: Lithoclast group is subdivided into volcanic (Lv), metamorphic (Lm), and sedimentary (Ls) lithoclasts.....	260
Table 2 –Grain size table. The modal grain size, mean and median grain size (mm) and sorting (F & W) of each sample are shown.	261

List of figures

Figure 1.1. Stylised map of the deep-sea fans (in yellow) and river drainages (in green). A, Amazon; AT, Astoria–Tufts fans; B, Bengal; BT, Bounty; C, Congo; CB, California borderland fans; I, Indus; M, Monterey; MS, Mississippi; S, Surveyor; V, Var; VC, Veracruz (Hessler and Fildani, 2019).....	25
Figure 1.2. Cartoon illustrating the source-to-sink system. Note the development of a deep-sea fan where the shelf is narrowest (Hessler and Fildani, 2019).	26
Figure 1.3. Flume tank experiment showing a scour at the base of a slope. The view height is about 0.4 m (cm-scale at the bottom). The progressively negative slope eventually forced the flow through the jump (Postma et al., 2009).....	28
Figure 1.4. Sketch of hydraulic jumps and their behaviour in different environments, including (a) open channel flow; (b) cyclic steps; (c) stratified subaqueous flow (Dorrell et al., 2016).....	28
Figure 1.5. Schematic plots of characteristic density/concentration profiles (dashed lines) and downstream velocity profiles (solid lines). (a) A two-layer model type concentration profile, dividing the flow into a constant density lower region (the current) and an upper region of fluid detrained from the head (Britter and Simpson, 1978; Simpson and Britter, 1979; Middleton, 1993). (b) Low-concentration, weakly depositional flow showing a smooth profile (e.g. Garcia, 1994; Altinakar et al., 1996) (c) High concentration and erosional flow showing a stepped concentration profile (García, 1993). (d) Distribution of sediment grain sizes observed in turbidity currents (e.g. Garcia, 1994). Note the difference between coarse material, concentrated at the lower part of the flow, whereas the finer fraction is homogeneously distributed throughout the vertical profile of the flow (Kneller and Buckee, 2000).....	30
Figure 1.6. Definition sketches for sediment gravity flow showing: (a) flow steadiness (waxing/waning) and unsteadiness (Kneller and Branney, 1995) and (b) flow uniformity (accumulative/depletive) and non-uniformity, where u is flow velocity, t is time, and x is space (Kneller, 1995).....	32
Figure 1.7. Structure of turbidity current in (A) laboratory experiments (surge-like) and (B) in the Congo Canyon (sustained flow) (Azpiroz-Zabala et al., 2017).	33
Figure 1.8. Classification of subaqueous sediment gravity flows according to sediment support mechanism and their deposits (Middleton and Hampton, 1973).....	34
Figure 1.9. Phase diagram and schematic models (Baas et al., 2009) for different kaolinite concentrations. Arrows show two trajectories producing a hybrid event bed (Sumner et al., 2009).....	36
Figure 1.10. Summary of subaqueous turbulent flows' transport mechanism and respective deposits (Talling et al., 2012).....	39
Figure 1.11. Summary of subaqueous laminar flows' transport, depositional phases, and respective deposits (Talling et al., 2012).....	41
Figure 1.12. Schematic diagram of a single hybrid flow and related the facies heterogeneity model along down-dip (Fonnesu et al., 2015).	43
Figure 1.13. Different interpretations for the depositional processes of an idealised hybrid event bed and its divisions (HEB)(Baas et al., 2011).....	44

Figure 1.14. Schematic diagram of an idealised submarine landslide deposit and various kinematic indicators. (1) Headwall scarp. (2) Extensional ridges and blocks. (3) Lateral margins. (4) Basal shear surface ramps and flats. (5) Basal shear surface grooves. (6) Basal shear surface striations. (7) Remnant blocks. (8) Translated blocks. (9) Outrunner blocks. (10) Folds. (11) Longitudinal shears/first-order flow fabric. (12) Second order flow fabric. (13) Pressure ridges. (14) Fold and thrust systems (Bull et al., 2009)..... 45

Figure 1.15. (A) Seismic reflection dataset showing the geomorphological impact at the base of an MTC, including the erosional edge on the west, megascours in the centre of the image, and secondary scours on the east side (Moscardelli et al., 2006). 45

Figure 1.16. (A) Cartoon illustrating the bulking of a submarine landslide and the entrainment of the substrate during its passage. (B) Cartoon illustrating the basal shear surface and related features such as ramps and flats, lineations, scours with megaclasts, and deformation zones (Hodgson et al., 2019). 46

Figure 1.17. Geologic map of part of Cumbria (NW England) showing palaeocurrent vector means of turbidites within Windermere Group. Note the divergence between ripples (formed from deflected dilute (parts of) flows, while sole structures (formed from denser flows) run parallel to the SW-NE topography (Kneller et al., 1991). 49

Figure 1.18. Elevation maps of four experimental runs in a flume tank with variable topography show erosion in blue and deposition in yellow, orange and red. (A) Unconfined; (B) laterally confined; (C) obliquely confined; and (D) frontally confined (Soutter et al., 2021). 51

Figure 1.19. Schematic diagram illustrating the interaction between sediment gravity flows of different magnitudes relative to the relief of the underlying submarine landslide deposits. Note the difference in the resultant deposits depending on the bypass or flow ponding (Kneller et al., 2016). 52

Figure 1.20. Schematic diagrams illustrating different bathymetric configurations and responses of the sedimentary systems. (A) In a silled sub-basin, when sand-transporting flows are small in volume relative to the scale of the accommodation. (B) In a silled sub-basin, when sand-transporting flows are large in volume relative to the accommodation. Note the spilling to the next sub-basin downslope. (C) In a connected tortuous corridor, when sand-transporting flows are small in volume relative to the potential flow path. (D) In a connected tortuous corridor, when sand-transporting flows are large in volume relative to the potential flow path (Smith, 2004b). 53

Figure 1.21. Schematic diagrams illustrating termination styles close to topographic heights and basin margin. (A) Simple onlap, (B) draping onlap and (C) bed thickening show terminations within relatively sand-prone stratigraphic, whereas (D) advancing pinch-out, (E) convergent pinch-out and (F) convergent thickening show heterolithic pinch-out successions (Bakke et al., 2013, after McCaffrey and Kneller, 2001; Gardiner, 2006; Patacci, 2010). 54

Figure 1.22. A photograph (top) and sketch (bottom) of the outcrop at Chalufy (France) displaying a range of lateral termination styles of the deep-water Grès d'Annot Formation onto the Marnes Bleues Formation (Bakke et al., 2013). 55

Figure 1.23. Schematic cross-section illustrating the facies evolutions of a lateral onlap in the Grès d'Annot (France) towards the basin margins. Note that the variable style of

the termination depends on high- and low-density turbidites and hybrid event beds (Soutter et al., 2019).	56
Figure 1.24. Map of the Late Quaternary Axial Congo Fan showing submarine canyon, channels and lobes (Picot et al., 2016).	56
Figure 1.25. (a) Map of the architecture and sedimentary processes of the Ogooue Fan. (b, c, d) Longitudinal profiles along the northern, central, and southern parts of the Ogooue Fan. Note the correlation between the differences in slope gradient and sedimentary processes (Mignard et al., 2019).	58
Figure 1.26. Compilations of features and cartoons illustrating differences between submarine canyons formed in active and passive margins (Harris and Whiteway, 2011).	58
Figure 1.27. Bathymetric map of the Congo Canyon (Azpiroz-Zabala et al., 2017).	59
Figure 1.28. Cartoons highlight the difference between (A) instantaneous confinement and (B) progressive confinement in submarine channels (Hodgson et al., 2016).	60
Figure 1.29. Two-dimensional schematic cross-sections and a map view of channelform sedimentary bodies common in slope strata emphasise a broad range of scales. (A) multiple channel elements and submarine landslide deposits form several channel complexes contained inside the channel belt of a channel complex set. (B–D) Examples of individual channel elements are generally less than 300 m wide and 30 m thick. (E). Two-dimensional cross-sections show the facies and architecture of a channel element. (F) Planform view of channel complex set (Hubbard et al., 2014).	62
Figure 1.30. (A) Schematic diagram showing channel-levee morphology and nomenclature for levee subenvironments. (B) Nomenclature of internal levees (Kane and Hodgson, 2011). (C) Channel-levee cross-section comprising depositional terraces (Hansen et al., 2015).	63
Figure 1.31. (A) Bathymetric map of the seafloor showing submarine channels morphology. (B and C) Cross-sections show the active channel and the depositional terraces. The location of seismic lines is indicated in (A). The dashed lines indicate the channel-belt base (Hansen et al., 2017a).	64
Figure 1.32. Schematic representation of (A) a channel-lobe transition zone (Hodgson et al., 2022). (B) Gravity flow is confined within a channel, and (C) flow-relaxation after lateral spreading and thinning lowers the maximum velocity towards the substrate, causing erosion (Pohl et al., 2019).	66
Figure 1.33. Intraslope lobe development on out-of-grade areas in a steeped slope. Bathymetric map (10 m contour interval) and seismic amplitude (colour) of the seafloor on the western Niger Delta continental slope. Note the development of the intraslope lobe on the flat in the north while the channel in the south does not develop any intraslope lobe due to constant gradient (Jobe et al., 2017).	67
Figure 1.34. Perched and ponded intraslope lobes on the Brazos-trinity basin, Gulf of Mexico (Prather et al., 2017).	68
Figure 1.35. The hierarchical scheme of Prélat et al. (2009) recognises four scales of elements: bed, lobe element, lobe and lobe complex.	69
Figure 1.36. Progradational-aggradational-retrogradational stacking patterns of lobes. (A) and (B) Cross sections showing the architecture of the deposits after 5 runs within a	

flume-tank experiment. Mean discharge of each run is different: Run 1 (20 m³/hr), Run 2 (30 m³/hr), Run 3 (40 m³/hr), Run 4 (30 m³/hr), Run 5 (20 m³/hr). Note the progradational stacking pattern while the discharge increases in contrast to the retrogradational stacking pattern developed when the discharge decreases. (C) Modified interpretation from the correlation in Kane et al. (2017) suggests that the uppermost thin-bedded interval represents the back-stepping of Fan 3 (Ferguson et al., 2020). (D) Similar interpretation and stacking patterns of Fan 3 (Hodgson et al., 2006). 70

Figure 1.37. Seismic profiles illustrate the architecture of the latest Pleistocene lobe complex of the northern margin of East Corsica in a pseudo-three-dimensional view. Note the compensational stacking pattern of lobes in yellow, green and purple (Gervais et al., 2006). 71

Figure 1.38. A schematic diagram on a plan view of a terminal lobe illustrates lobe sub-environments' distribution and facies associations (see logs). Schematic diagram showing some dominant flow processes in lobe (B) distal and (C) lateral fringes (Spychala et al., 2017b). 73

Figure 2.1. Diagram illustrating the main research question and the common objectives that link the different chapters. 74

Figure 2.2. Schematic diagram illustrating styles of accommodation associated with MTDs (Kneller et al., 2016). 76

Figure 2.3. Schematic diagrams of an intraslope submarine fan (left) and base-of-slope submarine fan (right) highlight their differing geomorphological characteristics and facies distributions. Due to the bypass of muddy sediment and erosion at the distal parts of the intraslope step, intraslope submarine lobe deposits show more sand-rich facies architecture (left) than predicted by traditional base-of-slope lobe facies models (right) (Jobe et al., 2017). 78

Figure 2.4. Block diagram showing the key recognition criteria for intraslope lobes according to Sychala et al. (2015). Compensational stacking patterns with a strong aggradational component; onlap terminations onto mud-prone slope combined with sandstone injectites; highly amalgamated deposits in lobe complex axis; lobe-off axis are dominated by climbing-ripple lamination; bidirectional ripple laminations dominate lobe fringes. Incision by their feeder channels as a result of the progradation and slope readjustment (B) Simplified logs of facies associations of intraslope lobes (Spychala et al., 2015). 79

Figure 2.5. Seismic amplitude map of the Upper Puchkirchen interval. Note the high-amplitude of the W–E–trending channel belt with crevasse splay or overbank lobes on the outer bend of the main channel (top right) and small tributary channel (centre). Palaeoflow's direction was towards E. (B) A schematic diagram of the depositional system highlights the channel system's main elements in the Puchkirchen and basal Hall formations. The Channel belt is 3–5 km wide (De Ruig and Hubbard, 2006). 81

Figure 3.1. (A) Location map of the Neuquén Basin and the study area Chacay Melehue (red star). (B) Location map of the study area. (C) Map of the Chacay Melehue area with the formations (modified from Llambías et al. 2007) and the locations of the logs. See the studied units and their distribution. 88

Figure 3.2. (A) General stratigraphic column of Chacay Melehue Graben (modified after Gulisano and Gutiérrez Pleimling (1995), Llambías et al. (2007) and Leanza et al. (2013)). (B) Stratigraphic column of Los Molles Formation and the Tábanos Formation in the Chacay Melehue Graben (modified after Gulisano and Gutiérrez Pleimling (1995)). (C) Schematic log of the study interval. (D) Panoramic view from UAV photograph (car on the road for scale) showing the deep-water Los Molles Formation overlain by evaporitic deposits of the Tábanos Formation. The study interval and the two datums used to constrain the base and top of the correlation panel are shown. See the location of logs CML-19, -20 and -21 in Figure 3.1C. 89

Figure 3.3. Correlation panels show the spatial relationship between stratigraphic units in the Bathonian succession of the Los Molles Formation and the different depositional architectures constrained by flattening on the top and basal datums. (A) Correlation panel including Units 1 to 4 with the Tuff marker as a datum (Datum B) showing stepped slope. (B) Correlation panel with the basal Burro marker bed (Datum A) as a datum showing the complex ramp-flat geometry and the basal-shear zone elements (brown coloured zone) at the base of Unit 2 and the correlation within Unit 4A based on two continuous sandstone marker beds. Note the heterogeneous distribution of Unit 3 and the pinching of Unit 4B in the central sector. 94

Figure 3.4. Representative sedimentary facies photos. (A) Unit 1: Planar-laminated mudstone (F1) with a few thin- to medium-bedded intercalated siltstone beds (F2) (Burro marker bed; Datum A) and sandstone beds (F5). (B) Unit 1: Basal shear-zone characterised by imbricated thrusts with drag folding. Geologist for scale. (C) Unit 4A: Heterolithic deposits consisting of the alternation between siltstones (F2) to (very) fine-grained sandstones (F3). (D) Unit 4A: Gravelly thin bed (F4) locally eroded into fine-grained sandstones (F3). (E) Unit 4A: Medium-bedded sandstones with cross-bedding (F6). (F) Unit 2: 140 m long conglomerate megaclast, bearing oyster and belemnite fragments and sitting above Unit 1. See a fragment of an oyster in the inset (G). (H) Unit 2, 3 and 4A: Foundered sandstones onlapping the matrix-rich debrite (F14) with deformed heterolithic megaclasts draped by the thin-bedded deposits of Unit 4A. (I) Unit 4A: Gravelly and (J) Tuff-marker bed within 4A. See the correlation in Figure 3.3 and Figure 3.9 (red and white dashed lines). (K) Unit 4B: Amalgamated medium- (F6) to thick-bedded (F11) sandstones. (L) Unit 4B: Medium-bedded banded sandstone (F7) overlain by massive matrix-poor sandstones (F5). Note the vergent flame structures within the amalgamation surface. (M) Unit 4B: Thin- (F9) and medium-bedded (F10) hybrid event beds with a linked debrite consisting of matrix-rich sandy division with elongated mudstone clasts. 95

Figure 3.5. (A) Panorama of the exposure showing the upper division of Unit 2 overlaid by Unit 3 foundered sandstone. (B) Sketched exposure of A. Note the matrix-supported texture and the chaotic distribution of clasts. (C) and (D) the same exposure of (A) from a different perspective. Note the unconformable base and conformable flat top interface of Unit 3 sandstones. 102

Figure 3.6. Foundered sandstones (Unit 3) diagram. (A) Illustrative correlation of sandstone foundering (Unit 3) into debrite (Unit 2). Note the difference between the conformable bed tops of matrix-poor and traction-dominated sandstones (right-hand

stereonet) and the mudstone clast- and matrix-rich sandstone texture near the unconformable bed bases (left-hand stereonet), which shows the architecture of these sandstone bodies. (B) Thick-bedded banded sandstones with bedding-parallel sill injection (F8). See mudstone clasts (type B) in the inset (C). (D) Convolute-laminae with NE vergence. (E) Sandstones showing rotation and growth strata. (F) Lower division comprising thick-bedded structureless argillaceous (F13) sandstone division with a patchy and random distribution of mudstone clasts overlain by upper division comprising thick-bedded banded sandstones (F8). (G) Thick-bedded structureless sandstone with an undulating irregular base comprising decimetre-scale mudstone clasts (type A) (F12).

..... 103
 Description: Unit 4 (10-27.3 m thick) has a sharp and concordant contact with the underlying Unit 2 and Unit 3 (Figure 3.2C). It comprises two sub-units: a lower heterolithic interval (Unit 4A) and an upper sandstone-prone interval (Unit 4B; Figure 3.2C and Figure 3.3). Unit 4A is a thin- to medium-bedded (0.01-0.5 m; Figure 3.4H) heterolithic succession (F1, F2, F3 and F5) with a maximum thickness of 22 m, thinning to 8 m in the central sector above where Unit 2 is thickest (Figure 3.3 and Figure 3.9). Most thin beds (0.01-0.1 m thick) are fine- to medium-grained normally graded sandstones, matrix-poor, moderately well-sorted, and structureless with common planar-parallel lamination and/or starved-ripple lamination near bed tops (F3). Palaeocurrent measurement shows a consistent flow trend towards the NE (Figure 3.9). Unit 4A also comprises coarse- to granular normal-graded sandstones, relatively low matrix content with common grain-size breaks (0.07-0.2 m thick), erosive bases and sharp-planar tops (F4; Figure 3.4D) and two medium-bedded matrix-supported conglomerates with sandstone clasts (F14; 0.25 and 0.35 m thick, respectively) that pinch out towards the central sector (Figure 3.9). One of these thin gravelly beds, which lacks any lateral thinning or fining trend (Figure 3.4I), was traced across the exposure (gravelly marker bed; dashed red line in Figure 3.9). In addition, a 0.15 m thick tuff layer (Figure 3.4J) was also used for correlation purposes (tuff marker bed; dashed white line in Figure 3.9). The medium-bedded sandstones (0.1–0.5 m thick) are structureless, ungraded, with planar-parallel and convolute lamination at bed tops, except one that shows cross-bedding (F6; Figure 3.4E). These sandstones have sharp bed bases and tops and lack mudstone clasts. In the eastern sector, Unit 4A is dominated by thin- to medium-bedded heterolithic succession that lacks any gravelly (F5) or matrix-supported conglomerate beds (F14) (Figure 3.7 and Figure 3.9)..... 105

Figure 3.8. Facies associations of Units 1, 3 and 4. See Table 3.1, Figure 3.4 and Figure 3.6 for more detail. See Figure 3.9 for the lateral variability of each facies association.

..... 110
 Figure 3.9. The correlation panel focuses on the strata (Unit 3 and 4) overlying the debrite (Unit 2). Note the colour bar next to each log representing the facies associations (see Figure 3.8). Unit 3 is only present in western and eastern sectors whilst absent in the debrite high (CML-12). The lower part of Unit 4A thins and onlaps the debrite, while the upper one shows a larger lateral extent. Note the gravelly and tuff marker beds (red and white dashed lines, respectively). Unit 4A alternates between fine-grained lobe fringes and coarser healing lobe fringes in the western sector. Coarse-grained healing fringes

pinch out, developing fine-grained lobe fringes in the eastern sector. Unit 4B consists of amalgamated thick-bedded sandstone of lobe axis, thinning into medium-bedded dominate lobe off-axis environment in the western sector. The sand-rich lobe thins and fines towards the east, pinching out in the central sector and interfingering with the lobe fringe deposits of Unit 4A. Note that the pinch-out terminations are developed where the debrite relief is highest. The rose diagram shows the details of ripples (green), vergent convolute lamination (orange), asymmetric flame structures (yellow) and cross-bedding (red). Mean vectors of each type are shown, all suggesting a NE trend, except in Unit 4B, where the ripples suggest an E-directed palaeoflow indicating deflection processes. The perimeter of the rose diagrams corresponds to 100% of the value..... 112

Figure 3.10. Illustrative diagram of foundered sandstone architecture and a model for their development. 115

Figure 3.11. Down-dip oriented schematic diagram illustrating the relief created by the debrite and the impact on younger sand-rich units. Foundered sandstones fill the small-scale rugosity, leaving the kilometre-scale accommodation underfilled. The submarine gravity flows are deflected by long-lived subtle debrite-related relief (right block). Partial healing and drapping of the debrite with the progradation of the lobe, which is gently impacted by the long-lived inherited relief. Note the white dashed line representing the correlation shown in Figure 3.3 and Figure 3.9..... 122

Figure 3.12. Schematic diagram illustrating the role of the mass failure recorded in the Chacay Melehue depocenter as the trigger for downslope remobilisation of sand from shallow-marine settings. 124

Figure 4.1. (A) Location map of the Neuquén Basin and the Chachil Graben. (B) Map of the Chachil Graben (Privat et al., 2021). (C) Detailed map of the Chachil Graben showing Los Molles Formation with the location of measured sections, adapted from Privat et al. (2021). See Figure 4.2 for A-A'-A'' cross-section. 130

Figure 4.2. Schematic correlation shows the architecture of Lower and Upper Lobe Complexes and the debrites (modified from Privat et al., 2021). The onset of the early-post rift stage is recorded by the drowning and deepening of a carbonate system and the subsequent development of a deep-water lobe system. The palaeoflow direction is towards NE (from left to right) (see rose diagrams in Figure 4.13). Note that the debrites pinch out in a more proximal position than the lobe complexes, which show a progressive basinward advancement of their pinch-out from the base to the top (more detail in Figure 4.13)..... 131

Figure 4.3. Bed type descriptions, depositional process interpretations and the generalised relationship between flow rheology and termination style (modified from Bakke et al., 2013). 135

Figure 4.4. Summary diagrams illustrating Type A beds, (A) outcrop photo of the sampled bed, (B) detailed log (1:2 scale) of the sample bed, (C) grain size (200 measurements per sample), (D) sorting and (E) mineralogy (400 measurements per sample). Representative thin section (F; CH-25 and G; CH-26) scans, photomosaic and photomicrographs (PPL and XPL). Note black squares indicating the location of the photomosaic and red squares in the photomosaic indicating the position of the photomicrographs. The arrows in the top right show the top of the samples. 136

Figure 4.5. Summary diagrams illustrating Type B beds, (A) outcrop photo of the sampled bed, (B) detailed log (1:2 scale) of the sample bed, (C) grain size (200 measurements per sample), (D) sorting and (E) mineralogy (400 measurements per sample). Representative thin section (F; CH-7 and G; CH-E) scans, photomosaic and photomicrographs (PPL and XPL). Note black squares indicating the location of the photomosaic and red squares in the photomosaic indicating the position of the photomicrographs. The arrows in the top right show the top of the samples. 138

Figure 4.6. Summary diagrams illustrating Type C beds, (A) outcrop photo of the sampled bed, (B) detailed log (1:2 scale) of the sample bed, (C) grain size (200 measurements per sample), (D) sorting and (E) mineralogy (400 measurements per sample). Representative thin section (F; CH-20 and G; CH-21) scans, photomosaic and photomicrographs (PPL and XPL). Note black squares indicating the location of the photomosaic and red squares in the photomosaic indicating the position of the photomicrographs. The arrows in the top right show the top of the samples. 141

Figure 4.7. Summary diagrams illustrating Type D beds, (A) outcrop photo of the sampled bed, (B) detailed log (1:2 scale) of the sample beds (red line represents the amalgamation surface between them), (C) grain size (200 measurements per sample), (D) sorting and (E) mineralogy (400 measurements per sample). Representative thin section (F; CH-4 and G; CH-5) scans, photomosaic and photomicrographs (PPL and XPL). Note black squares indicating the location of the photomosaic and red squares in the photomosaic indicating the position of the photomicrographs. The arrows in the top right show the top of the samples. 143

Figure 4.8. Summary diagrams illustrating Type E beds, (A) outcrop photo of the sampled bed, (B) detailed log (1:2 scale) of the sample bed, (C) grain size (200 measurements per sample), (D) sorting and (E) mineralogy (400 measurements per sample). Representative thin section (F; CH-29 and G; CH-30) scans, photomosaic and photomicrographs (PPL and XPL). Note black squares indicating the location of the photomosaic and red squares in the photomosaic indicating the position of the photomicrographs. The arrows in the top right show the top of the samples. 145

Figure 4.9. Summary diagrams illustrating Type F beds, (A) outcrop photo of the sampled bed, (B) detailed log (1:2 scale) of the sample bed, (C) grain size (200 measurements per sample), (D) sorting and (E) mineralogy (400 measurements per sample). Representative thin section (F; CH-B and G; CH-18) scans, photomosaic and photomicrographs (PPL and XPL). Note black squares indicating the location of the photomosaic and red squares in the photomosaic indicating the position of the photomicrographs. The arrows in the top right show the top of the samples. 148

Figure 4.10. Graph showing matrix content as a function of the mean grain size of each sample (n= 40) according to the bed type. The dashed line at the 15% matrix represents the threshold for matrix-poor and matrix-rich intervals (Pettijohn et al., 1972). Note that the high-density turbidites (Type B beds) are the coarsest and less argillaceous, in contrast to most TFDs (Type C, D, E, and F beds) and low-density turbidites (Type A bed)... 151

Figure 4.11. Ternary diagrams of the 40 analysed samples. (A) QmFLt (Dickinson et al., 1983) show a mixed and arc provenance. (B) Lv-Lm-Ls (Ingersoll and Suczek, 1979) show a volcanic arc source of the samples due to the dominance of volcanic lithoclasts

(Lv) over sedimentary (Ls) and metamorphic (Lm) lithoclasts. (C) Qp-Lv-Lsm diagram (Dickinson, 1985) showing volcanic arc source.....	152
Figure 4.12. Bed type association representing lobe sub-environments: lobe axis, lobe off-axis and lobe fringe of Lower and Upper Lobe Complexes.....	153
Figure 4.13. Detailed correlation panel showing the different lobe sub-environments, both lobe complexes' overall architecture and pinch-out positions. Rose diagrams show palaeocurrents for each lobe complex and log. Tool marks show higher divergence than ripples lamination as denser flows/divisions are more sensitive to intrabasinal topography than dilute flows/divisions.....	158
Figure 4.14. (A) Graphs showing sandstone-mudstone proportion (left), bed type proportion (centre) and bed type occurrence (right) from both Lower and Upper Lobe Complexes in proximal (Log 1-4), medial (Log 5-6), and distal (Logs 7-8) parts (see Figure 4.1C for location). (B) Summary diagram of different flow evolution showing deposit variability from proximal to pinch-out areas. Denser flows tend to decelerate more abruptly and produce strong deposit variability, unlike dilute flows, which can maintain their efficiency for longer distances. The greater the incorporation of cohesive mud, the shorter the distance over which flows transform into low-efficiency cohesive flows, resulting in rapid flow collapse.	159
Figure 4.15. Schematic diagrams show (A) the response of parental sediment gravity flows interacting with the early post-rift seafloor relief (B) and a submarine lobe from Lower and Upper Lobe Complexes. The Lower Lobe Complex pinch-out is more proximal than the Upper Lobe Complex due to the flattening of the inherited early post-rift topography over time. Denser flows or parts of flows are restricted to the topographic lows, while the more dilute ones can travel further into the compaction hinge, depositing low-density turbidites. Note the positions of the logs marked by black squares.....	164
Figure 5.1. (A) Structural map of the Pyrenees (after Muñoz et al., 2013) and location of the Aínsa Basin (See black square). (B) Geologic map of the Banastón system and the main structures (after Bayliss and Pickering, 2015). Note the black square indicating the location of the study area. (C) Geologic map of the study area near the San Vicente town (after Pickering and Bayliss, 2009; Bayliss and Pickering, 2015) and the sedimentary logs collected in this study.	174
Figure 5.2. Outcrop photographs of Lf1-Lf4b lithofacies.	178
Figure 5.3. Outcrop photographs of Lf5 and Lf6 lithofacies.	181
Figure 5.4. Outcrop photographs of Lf7a-Lf7d lithofacies.	183
Figure 5.5. Representative sedimentary log, sandstone proportion and photograph of the stratal packages representing facies associations (A) FA1: Overbank deposits, (B) FA2: Terrace deposits, (C) FA3: Channel-fill deposits, (D) FA4: Crevasse scour-fill deposits and (E) FA5: Crevasse lobes deposit.....	187
Figure 5.6. A) Logs and (B) Histograms showing the lithology, mean sandstone proportion, submarine landslide content and facies associations of the 111 m thick study interval. The section is mudstone-dominated, especially on the upper half where the overbank facies association overlies channel-fill and terrace deposits. Note the variation of submarine landslide deposits along the section.....	195

Figure 5.7. (A) General stratigraphic column of the investigated interval (111 m thick) of the Banastón II member and the different facies associations. Note that it is made of different sedimentary logs. (B) Interpreted UAV photographs with the different facies associations and sedimentary logs. Note the San Vicente town in the right top corner. 196

Figure 5.8. Correlation panel of the Banastón II member near the San Vicente town. See Figure 5.1C and Figure 5.7B for the location of the sedimentary logs. Note the rose diagrams of the palaeocurrents on crevasse lobes, overbank and channel belts (Channel-fill and terrace deposits). 197

Figure 5.9. Interpreted UAV photographs of the multiple submarine landslides found within the overbank (FA1) and the crevasse scour-fills (FA4) and crevasse lobes deposits (FA5). 199

Figure 5.10. (A) Interpreted UAV photograph showing a basal slide overlain by the crevasse complex. (B) Location of the sedimentary logs of the crevasse complex. (C) Correlation panel of a crevasse complex showing the juxtaposition of crevasse lobes over the basal crevasse scour-fill deposits. (D) Model illustrating the crevasse lobe juxtaposed over a slump and laterally onlapping the slide scar. 200

Figure 5.11. (A) Evolutionary model illustrating the crevasse lobe deposition on the active margin due to submarine landslide emplacement, deflecting channelised flows towards the slide scar and (B) how the continuous transversely-sourced submarine landsliding is a potential mechanism of avulsion of the Banastón II member. 203

Figure 6.1. Down-dip oriented block diagram illustrating the relief created by the debrite and the impact on younger sand-rich units. The left block shows how foundered sandstones fill the small-scale rugosity, leaving the kilometre-scale accommodation underfilled. The middle block shows potential mechanisms that could have rejuvenated the debrite relief. The right block shows how the accumulation of thin beds draped the debrite, followed by the progradation of the intraslope lobe, which is gently impacted by the long-lived inherited relief. Modified from Martínez-Doñate et al. (2021). 208

The studies in Chacay Melehue (Chapter 3) and Chachil Graben (Chapter 4) enabled the characterisation of exhumed early post-rift intraslope lobes. The intraslope lobe of the Chacay Melehue Graben is 5.7 m thick and at least 4.3 km long. These intraslope lobes comprise a lobe axis dominated by argillaceous high-density turbidites with banded tops evolving down-dip into medium-bedded transitional flow deposit-dominated lobe off-axis and thin-bedded lobe fringe sub-environments. The intraslope lobes in Chachil Graben are 4.5 to 7 m thick and ~ 3 km long. Their dimensions are comparable to those reported in Sychala et al. (2015) and Brooks et al. (2018c) in the Karoo Basin but largely differ from the turbidite-dominated sub-environments: lobe axis is built by structureless thick-bedded turbidites, lobe off-axis by structured medium-bedded turbidites comprising wavy and climbing-ripple laminations and fringes show are built by thin sandstones beds characterised by bidirectional ripple lamination (Figure 6.2). The sandy nature of intraslope lobes is attributed to the preferential trapping of the coarser fraction of the sediment gravity flows while the more dilute fine-grained top of the turbidity currents bypasses (e.g. Sychala et al., 2015). Similar sedimentary facies were documented in the crevasse lobes of the Ainsa Basin (Chapter 5). However, the Early Jurassic intraslope

frontal lobes of the Los Molles Formation are predominately built by deposits from transitional flows across all sub-environments (Figure 6.3), which inhibited effective grain size segregation and resulted in flow collapse as a result of flow deceleration, and, therefore very different pinch-out architectures. 209

Figure 6.4. Block diagram illustrating turbidite-dominated (yellow coloured) crevasse lobes (Chapter 5 and Morris et al., 2014a); frontal intraslope lobes (Spychala et al., 2015) developed in simple stepped slope profiles and/or fed by a channel-levee system (see Jobe et al., 2017); TFD-dominated intraslope lobes (green coloured) developed over a submarine landslide (Chapter 3) and in structurally complex stepped slopes where distributary systems are poorly developed (Chapter 4). 212

Figure 6.5. (A) The general stratigraphic column of the studied interval in the Chacay Melehue Graben (Chapter 3) is overlain by a 'chaotic sandy unit' showing a range of mud-rich features. (B) Discordant mudstone injection onto sandstone and (C) inset on the mudstone injection. (D) Discordant 14 m long mudstone injection. Note its discordant nature on the stereonet, which shows regional bedding gently dipping towards SE while the contacts of the mudstone injectite (measured every 50 cm on both sides from base top) and the long axis of some clast within it show a sub-vertical trend. (E) Inset on the contact between the mudstone injectite and the host sandstones. 217

List of tables

Table 3.1. Descriptions of the facies recognised in the Los Molles stratigraphy of the Chacay Melehue area, including lithologies, thicknesses, and interpretations of their depositional processes. 99

Table 5.1. Description, process interpretation and photographs of the lithofacies investigated in the studied interval. 185

Abstract

Submarine fans are the largest sediment accumulations on Earth and form valuable archives for paleoclimatic and paleogeographic reconstructions. Sand-rich lobes are a major fan component, recording erosion and transport of clastic sediments from terrestrial highs to deep-marine lows. Submarine lobe evolution and architecture are inherently linked to complex interactions between sediment gravity flow processes and the evolving physiography of continental slopes, which induces complex facies transitions and pinch-out styles. In the subsurface, predictions of the pinch-out character at bed- to lobe-scale are limited by the resolution of seismic reflection data and sparse borehole coverage. To bridge the resolution gap, this thesis presents three field-based studies of exceptionally well-exposed examples of intraslope lobes associated with submarine landslide deposits (frontal lobes from the Neuquén Basin, Argentina, and crevasse lobe Aínsa Basin, Spain) and develops new models for submarine lobes developed above inherited tectonic and depositional relief and compares the impact of variable degree of confinement in each system.

The main outcomes and novelty of this thesis are 1) the relief along the upper surfaces of submarine landslides can be hierarchical and highly dynamic, which influences the behaviour of gravity flows in more complex ways than simple passive healing of topography; 2) seafloor relief can be rejuvenated progressively due to compaction-driven deformation, or more abruptly due to catastrophic mass failures, which is recorded by the architecture and stacking patterns of lobes; and 3) intraslope lobes can be dominated by transitional flow deposits where immature routing pathways and clay-rich and poorly-consolidated substrates are present, such as in post-rift settings. Therefore, this thesis highlights the inherent complexity of sedimentary processes along unstable slopes, which demonstrably impacted the nature of the investigated lobes.

Declaration

University of Manchester PhD candidate declaration

Candidate name: Ander Martinez-Doñate

Faculty: Science and Engineering

School: Department of Earth and Environmental Sciences

Thesis Title: The stratigraphic evolution of exhumed submarine lobes in unstable and complex basin margins

I, Ander Martinez-Doñate, declare that this thesis has been entirely written by myself and that the work, other than that identified below, has not been submitted for any other degree or professional qualification. I also confirm that the work is my own, and the work that formed part of jointly-authored publications is included. The contribution of the authors is explicitly indicated below.

Author contributions

Chapter 3: Substrate entrainment, depositional relief, and sediment capture: impact of a submarine landslide on flow process and sediment supply.

Status: Published in *Frontiers in Earth Science*. Research Issue: Source or Sink? Erosional and Depositional Signatures of Tectonic Activity in Deep-Sea Sedimentary Systems, Volume 9, 2021. DOI: 10.3389/feart.2021.757617.

Author contributions:

- Martinez-Doñate, A: Main author. Responsible for the data acquisition, processing and characterisation. Wrote the manuscript.
- Privat, A. M-L. J.: Data acquisition, in-depth discussion and manuscript review.
- Hodgson, D. M.: Data acquisition, in-depth discussion and manuscript review.
- Jackson, C. A-L.: Data acquisition, and manuscript review.
- Kane, I. A.: In-depth discussion and manuscript review.
- Spychala, Y. T.: Data acquisition, and manuscript review.
- Duller, R. A.: Data acquisition, and manuscript review.
- Stevenson, C.: Data acquisition, and manuscript review.
- Keavney, E.: Data acquisition (field assistance).
- Schwarz, E.: manuscript review.
- Flint, S.S.: manuscript review.

Chapter 4: Stratigraphic change in flow transformation processes recorded in early post-rift deep-marine lobe complexes in an intraslope setting.

Status: Submitted to Sedimentology.

Author contributions:

- Martinez-Doñate, A: Main author. Responsible for the data acquisition, processing and characterisation. Wrote the manuscript.
- Kane, I. A.: In-depth discussion and manuscript review.
- Hodgson, D.M.: In-depth discussion and manuscript review.
- Privat, A. M-L. J: preliminary data acquisition, in-depth discussion and manuscript review.

- Jackson, C.A-L.: manuscript review.
- Schwarz, E.: manuscript review.
- Flint, S.S.: manuscript review.

Chapter 5: The impact of slope instabilities on submarine channels and development of crevasse lobes in tectonically active settings: an exhumed example from the Eocene Aínsa basin (Spain).

Status: In preparation.

Author contributions:

- Martínez-Doñate, A.: Main author. Responsible for the data acquisition, processing and characterisation. Wrote the manuscript.
- Soutter, E. L.: Field assistance, in-depth discussion and manuscript review.
- Kane, I.A.: Field assistance, in-depth discussion and manuscript review
- Poyatos-Moré, M.: in-depth discussion and manuscript review.
- Hodgson, D.M.: manuscript review.
- Flint, S.S.: manuscript review.

Copyright Statement

- i. The author of this thesis (including any appendices and/or schedules to this thesis) owns certain copyright or related rights in it (the "Copyright") and they have given the University of Manchester certain rights to use such Copyright, including for administrative purposes.

- ii. Copies of this thesis, either in full or in extracts and whether in hard or electronic copy, may be made only in accordance with the Copyright, Designs and Patents Act 1988 (as amended) and regulations issued under it or, where appropriate, in accordance with licensing agreements which the University has from time to time. This page must form part of any such copies made.

- iii. The ownership of certain Copyright, patents, designs, trademarks and other intellectual property (the "Intellectual Property") and any reproductions of copyright works in the thesis, for example graphs and tables ("Reproductions"), which may be described in this thesis, may not be owned by the author and may be owned by third parties. Such Intellectual Property and Reproductions cannot and must not be made available for use without the prior written permission of the owner(s) of the relevant Intellectual Property and/or Reproductions.

- iv. Further information on the conditions under which disclosure, publication and commercialisation of this thesis, the Copyright and any Intellectual Property and/or Reproductions described in it may take place is available in the University I.P. Policy (see <http://documents.manchester.ac.uk/DocuInfo.aspx?DocID=24420>), in any relevant Thesis restriction declarations deposited in the University Library, the University Library's regulations (see <http://www.library.manchester.ac.uk/about/regulations/>) and in the University's policy on Presentation of Theses.

Acknowledgements

I would like to thank my supervisors, Ian Kane, David Hodgson, Chris Jackson, Steve Flint and Ernesto Schwarz, for making me part of the LOBE3 project and their support throughout the last four years. I would like to thank Ian as the good friend he is today for all the great moments and laughs we shared together. For many more years, Ian. I'd also like to further thank Dave, whose endless patience, dedication and capacity to make me feel he'll always be there made me strong in the toughest moments. Dave, massive thank you. And to Chris, for making the effort to come to Patagonia to show me the wild Neuquén Basin and for always supporting me during these 4 years. And Steve for being amazing and supporting the Strat Group and me. And to Ernesto, for the IAS fieldtrip, the discussions, help with the samples and for the asados in your house in La Plata.

I want to thank my colleagues and good friends from uni Euan, Ashley, Max, Kevin, Dan, Zoe, Arka, Ross, Arne, Rhys, Aurelia, Miquel, Orrin, Rodrigo, Manu, Jorge, Tim, Damjan, and my favourite rock band from Manchester, Chemtrails. A special thank you to my good friend Ed Keavney, the former master's student who made an effort to come to Argentina to field-assist me in the windy Andes and share a few miles in our old grey Chevrolet. I would also like to thank all my Basque Country and Manchester friends; without them, I could have probably finished this book sooner, but this experience would have been empty. Also, a special thank you to Zuri for all the love and great moments we shared in the past.

To my parents, Bego and Txema, sister Leire and the rest of the family members, without their unconditional support and love wouldn't be typing this right now. I dedicate this work to them, with a special mention to my granddad Aitite Esteban, who taught me the beauty of nature and triggered the curiosity that brought me here.

Also, thanks to the LOBE 3 consortium project supported by sponsorship from Aker BP, BHP, BP, Equinor, HESS, NEPTUNE, Petrobras, PetroChina, Total, Vår Energi and Woodside. And lastly, to all the local farmers of different regions of Patagonia for their hospitality and permission to carry out field studies on their land.

**'Caught in a landslide,
no escape from topography.'
Adapted from Mercury et al. (1975)**

1. Deep-water systems

In this chapter, I will review some of the main processes and products of deep-marine sedimentary environments to provide context for the following chapters.

1.1. Introduction

The deep oceans host the largest sediment accumulations on Earth (Figure 1.1; Shanmugam and Moiola, 1988; Curray et al., 2002; Talling et al., 2015) and are also the least understood of all sedimentary environments (Nichols, 2009). The term 'deep-water' refers to bathyal environments below the storm wave base, where the direct effect of waves and tides are absent (Figure 1.2). Sediment is transported from shallow- to deep-water areas due to gravity and the density difference between the ambient water and the mixture of fluid and solid particles (Middleton and Hampton, 1973; Kneller and Buckee, 2000).



Figure 1.1. Stylised map of the deep-sea fans (in yellow) and river drainages (in green). A, Amazon; AT, Astoria–Tufts fans; B, Bengal; BT, Bounty; C, Congo; CB, California borderland fans; I, Indus; M, Monterey; MS, Mississippi; S, Surveyor; V, Var; VC, Veracruz (Hessler and Fildani, 2019).

Deep-water sedimentary systems have received attention over the last few decades because they can store large reserves of oil and gas (Stow, 1985; Marchand et al., 2002). Despite this interest or because of, the nomenclature and classification of gravity flows and their related deposits have been controversial (Hiscott, 1995; Sohn, 1995; Shanmugam, 1996). Several contributions aimed to clarify the subaqueous gravity flow by reviewing the current flow process knowledge and classifying them based on flow rheology (Dott, 1963), morphodynamics (Kneller, 1995; Kneller and Branney, 1995; Kneller and Buckee, 2000), particle support and deposition mechanism (Middleton and Hampton, 1973; Lowe, 1982; Mulder and Alexander, 2001) and their deposits (Lowe, 1982; Talling et al., 2012).

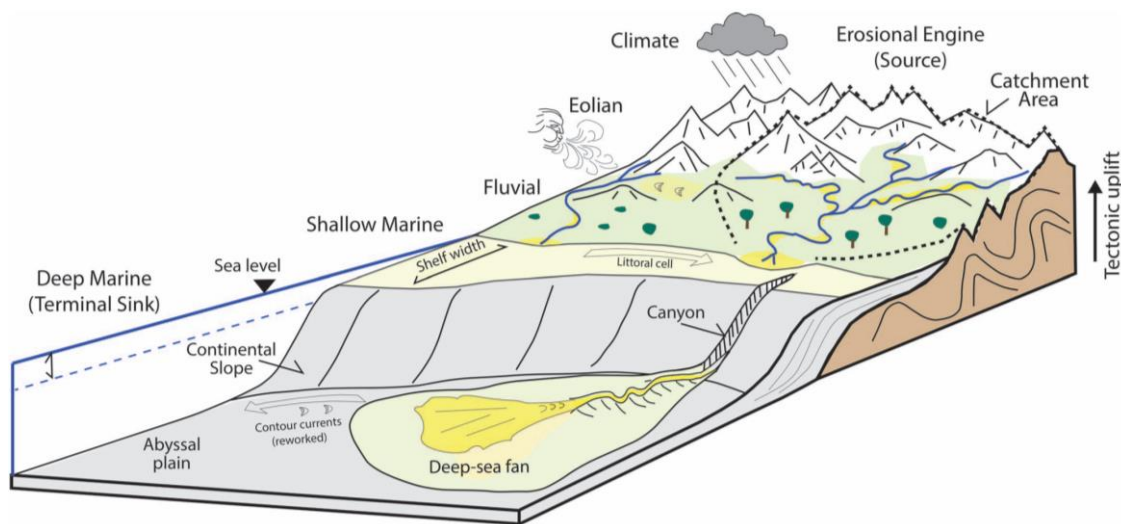


Figure 1.2. Cartoon illustrating the source-to-sink system. Note the development of a deep-sea fan where the shelf is narrowest (Hessler and Fildani, 2019).

In outcrop and core studies, deposit-based classification is used due to the limited availability of key parameters for the characterisation of sediment gravity flows, such as flow state, concentration, grain size, support mechanism and flow velocity. This information is only available in laboratory experiments (e.g. Al Ja'Aidi et al., 2004; Baas, 2004; Sumner et al., 2008; Sequeiros et al., 2009; Baas et al., 2011; Ferguson et al., 2020),

in numerical modelling studies (Felix, 2001; Cartigny et al., 2011) and active monitoring of modern systems (Azpiroz-Zabala et al., 2017; Paull et al., 2018; Heijnen et al., 2022; Pope et al., 2022). Parameters such as density, velocity, flow height, grain size and grain type govern the flow processes and impact the deposition of the transported sediments. The interplay between those variables is commonly evaluated by non-dimensional parameters such as Reynolds (Re) and densimetric Froude (Fr_d) numbers. Reynolds number refers to the ratio between inertial and viscous forces,

$$Re = \frac{(\rho_c \bar{U} d)}{\mu_s} = \frac{(\bar{U}d)}{\nu'}$$

where ρ_c is the mean current density, \bar{U} refers to depth-averaged current velocity, d is the flow thickness, μ_s is the apparent viscosity of the clay-free dispersion and ν' is the kinematic viscosity (Kneller and Buckee, 2000). Flows with $Re > 1500-2000$ are associated with turbulent states, while lower values are associated with a laminar state (Simpson, 1999). Therefore, flow turbulence increases with density, velocity and thickness, while viscosity reduces it.

Another determining parameter in flow dynamics is the flow criticality, quantified by the densimetric Froude number (Fr_d). Froude number is the ratio of inertial and gravitational forces,

$$Fr_d = \frac{\bar{U}}{\sqrt{\frac{\rho_c - \rho}{\rho} g d}}$$

where \bar{U} is depth-averaged current velocity, ρ_c is the mean current density, ρ is the ambient fluid density, g acceleration due to gravity, and d is flow thickness. Flows with a Froude number higher than 1 are termed supercritical, whereas those with values lower

than 1 are subcritical (Figure 1.3). In contrast to subcritical flows, supercritical flows are characterised by higher flow velocities than wave propagation speed. The transition from supercritical to subcritical is characterised by the development of a bore termed hydraulic jump ($Fr_d = 1$) (Figure 1.3; García, 1993; Postma et al., 2009). Hydraulic jumps are commonly developed due to flow deceleration (reduction in slope gradient or intrabasinal relief) (Figure 1.3 and Figure 1.4; e.g. Dorrell et al., 2016) and can be stationary over a certain period or migrate upstream (Edwards, 1993; Kneller and Buckee, 2000).

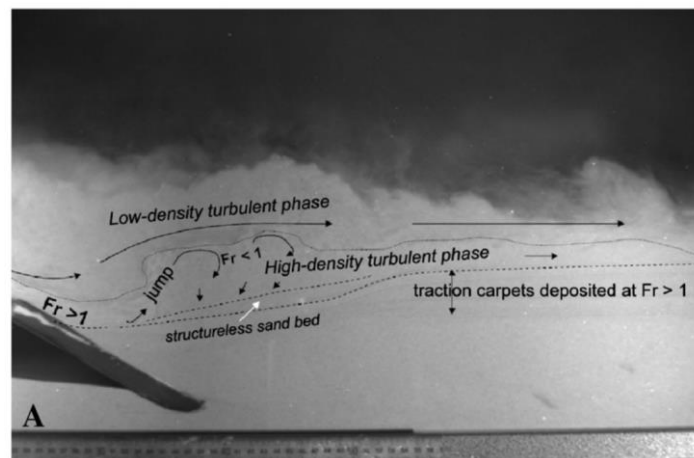


Figure 1.3. Flume tank experiment showing a scour at the base of a slope. The view height is about 0.4 m (cm-scale at the bottom). The progressively negative slope eventually forced the flow through the jump (Postma et al., 2009).

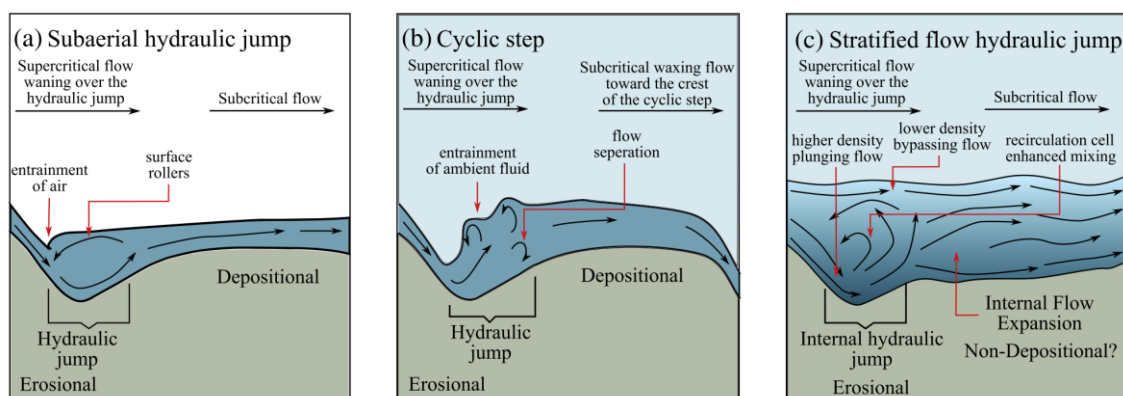


Figure 1.4. Sketch of hydraulic jumps and their behaviour in different environments, including (a) open channel flow; (b) cyclic steps; (c) stratified subaqueous flow (Dorrell et al., 2016).

1.2. Sediment gravity flows

1.2.1. Turbulent flows

The gravity-driven subaqueous mixtures of sediment and fluids where the sediment is maintained in suspension due to the flow turbulence are named turbidity currents (Lowe, 1982). When the sediment concentration is low, the sediments can be entirely supported by fluid turbulence; whilst in flows with higher concentrations, dispersive pressures from grain-to-grain interactions near the base represent an additional particle support mechanism (Bagnold, 1962; Lowe, 1982). Based on the different concentrations and subsequent flow behaviour, turbidity currents are commonly subdivided into low- and high-density turbidity currents (Lowe, 1982). The geometry of the density profile is highly dependent on the flow's sediment concentration (Figure 1.5a). Low-density turbidity currents show a logarithmic curve that decreases its value from base to top (Figure 1.5b; e.g. Altinakar et al., 1996). On the other hand, high-density turbidity currents show a stepped density profile of the coarser particles indicative of flow stratification (Figure 1.5c), while fines (clay and silt) are homogeneous from base to top in both types of turbidity current (Figure 1.5d; Garcia, 1994; Kneller and Buckee, 2000).

However, in nature, turbidity currents comprise a continuum of sediment concentrations and establishing the concentration/density threshold between sediment gravity flows is not straightforward because monitoring them in modern systems is difficult (Azpiroz-Zabala et al., 2017; Paull et al., 2018; Heijnen et al., 2022; Pope et al., 2022), and experiments based on physical modelling suggested different values. In Kuenen (1966), the distinction between low- and high-density flows was set at a density value of 1.1g/cm^3 . Middleton and Hampton (1973) show that low-density turbidity currents have a density value between 1.03 g/cm^3 and 1.2 g/cm^3 , whereas high-density flows have a

density range of 1.5-2.4 g/cm³. Bagnold (1962) proposed that in sediment concentrations below 9% (concentration of solids by volume), the grains are fully supported by fluid turbulence, whereas in higher concentrations, grain-to-grain interactions become more frequent (Lowe, 1982).

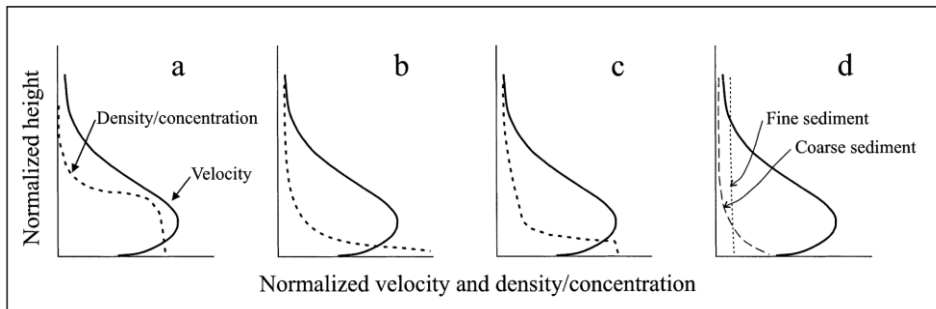


Figure 1.5. Schematic plots of characteristic density/concentration profiles (dashed lines) and downstream velocity profiles (solid lines). (a) A two-layer model type concentration profile, dividing the flow into a constant density lower region (the current) and an upper region of fluid detrained from the head (Britter and Simpson, 1978; Simpson and Britter, 1979; Middleton, 1993). (b) Low-concentration, weakly depositional flow showing a smooth profile (e.g. Garcia, 1994; Altinakar et al., 1996) (c) High concentration and erosional flow showing a stepped concentration profile (García, 1993). (d) Distribution of sediment grain sizes observed in turbidity currents (e.g. Garcia, 1994). Note the difference between coarse material, concentrated at the lower part of the flow, whereas the finer fraction is homogeneously distributed throughout the vertical profile of the flow (Kneller and Buckee, 2000).

The anatomy of turbidity currents is commonly subdivided longitudinally into three different regions: head, body and tail (Middleton, 1993). The head is the frontal and most unsteady part of the turbidity current, which comprises the highest velocities (Middleton, 1966a; Simpson and Britter, 1979; Kneller et al., 1997). The head is followed by the body and the tail, where the flow is more steady, less concentrated and velocity decreases (Kneller and Buckee, 2000; Pope et al., 2022). The head comprises a lower and denser region juxtaposed by the upper more dilute region (Middleton, 1993), also known as wall and jet regions (Altinakar et al., 1996). While the basal shear induces erosion and

entrainment of substrate material (Peakall et al., 2020; Baas et al., 2021), the upper shear is linked to ambient water entrainment (Simpson, 1969; Allen, 1971). The boundary between these two regions is defined by the maximum velocity of the flow, which increases upwards from the base in the wall region (positive velocity gradient) and decreases in the jet region (negative velocity gradient) (Altinakar et al., 1996). The geometry of the head depends on the vertical velocity profile. The maximum shear stress is developed at the base of the wall region and the top jet region, whereas it is lowest near the velocity maximum ('nose of the flow'; Kneller et al., 1999). The drag forces developed at the basal and upper boundaries control the height of the velocity maximum (Middleton, 1966b; Kneller et al., 1997), which is commonly located near the base at 0.2-0.3 of the flow thickness (Altinakar et al., 1996; Kneller et al., 1999). However, the velocity maximum can be modified depending on the substrate configuration. Rougher substrates will increase the basal friction elevating the nose and entraining more ambient water at the base (Kneller et al., 1999), while abrupt reduction of seafloor gradients can promote the lowering of the velocity maximum, enhancing the erosion and substrate entrainment (Pohl et al., 2019). Physical modelling (*sensu* Sequeiros et al., 2009, 2018) and modern systems (Azpiroz-Zabala et al., 2017; Paull et al., 2018; Pope et al., 2022) have recognised 'self-accelerating' flow cells at the head of turbidity currents due to substrate entrainment, creating a positive feedback mechanism.

Turbidity currents show velocity variation through time (Figure 1.6a; Kneller and Branney, 1995) and space (Figure 1.6b; Kneller, 1995), producing different vertical and lateral variations in their deposits. Temporal fluctuations in flow velocity are related to unsteady flows, where the acceleration phase is referred to as 'waxing' and the deceleration phase as 'waning' (Figure 1.6a; Kneller and Branney, 1995). In contrast, a

flow that does not show significant temporal fluctuations in velocity is referred to as a steady flow (Figure 1.6a; Kneller and Branney, 1995). A flow showing spatial velocity fluctuations is referred to as 'non-uniform', characterised by acceleration 'accumulative' phase and deceleration 'depletive' phase (Figure 1.6b; Kneller, 1995). Flows that show constant velocities in space are uniform (Figure 1.6b; Kneller, 1995).

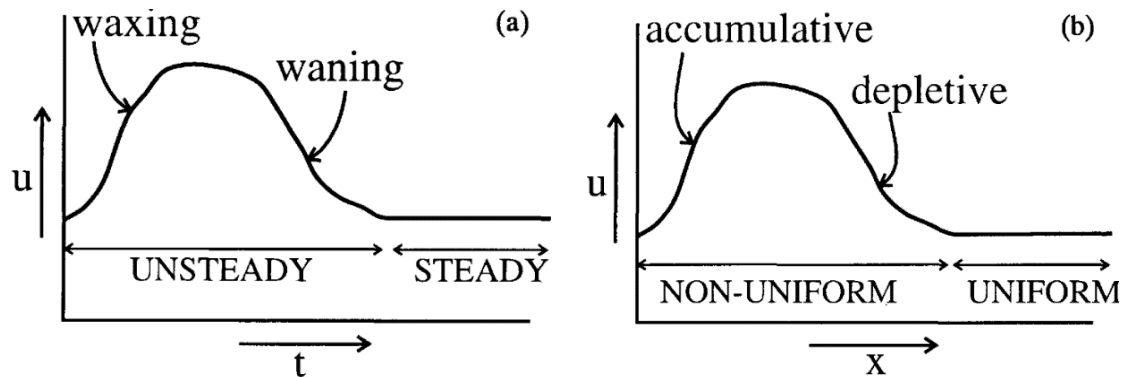
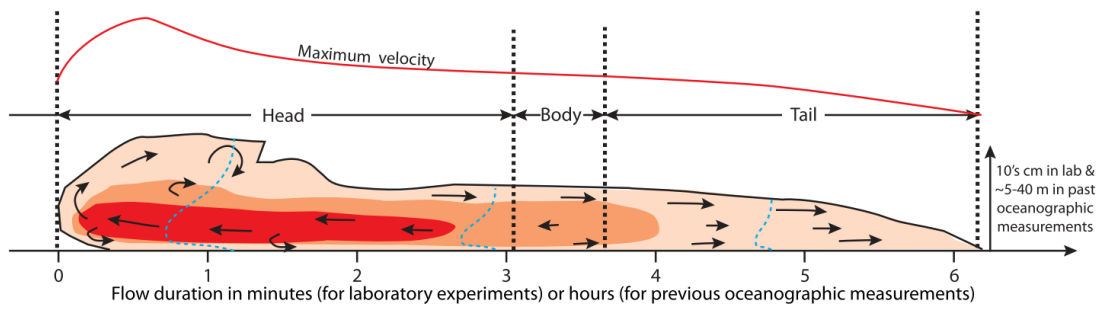


Figure 1.6. Definition sketches for sediment gravity flow showing: (a) flow steadiness (waxing/waning) and unsteadiness (Kneller and Branney, 1995) and (b) flow uniformity (accumulative/depletive) and non-uniformity, where u is flow velocity, t is time, and x is space (Kneller, 1995).

Although turbidity currents are unsteady in nature, several studies in modern systems have documented that flow velocity can remain constant over hours (Piper et al., 1988) to several days (Azpiroz-Zabala et al., 2017). Unsteady and relatively short-lived turbidity currents (seconds to minutes) are known as surges (Figure 1.7A). In contrast, long-lived gravity flows (hours to days) are termed quasi-steady or sustained flows, (Figure 1.7B; Hughes-Clarke et al., 1990; Kneller, 1995; Kneller and Branney, 1995).

A Previous surge model based on observations and experiments



B Turbidity current structure in the Congo Canyon

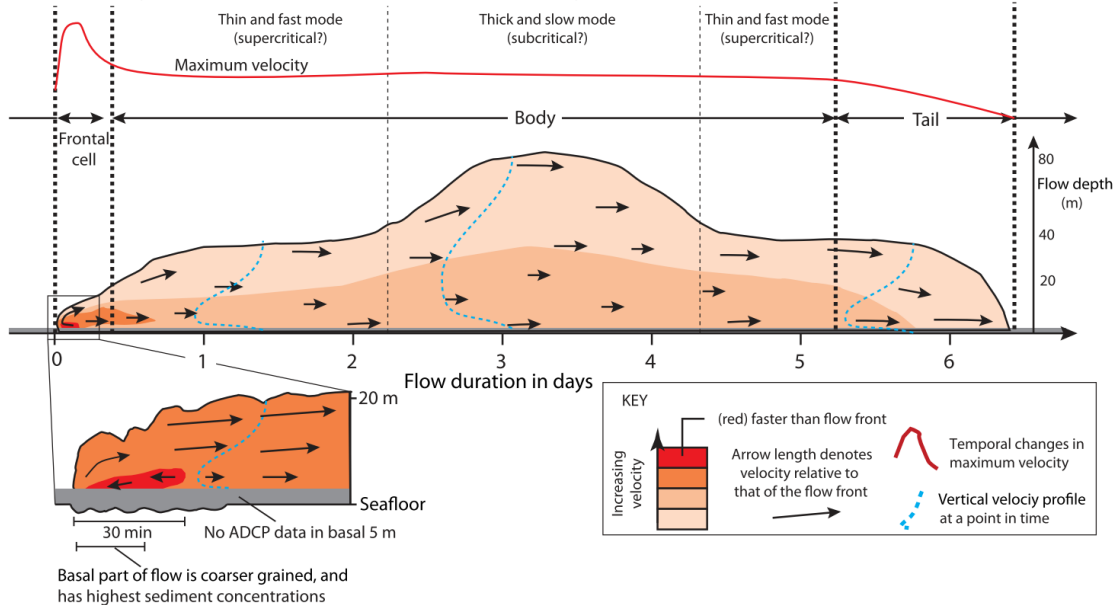


Figure 1.7. Structure of turbidity current in (A) laboratory experiments (surge-like) and (B) in the Congo Canyon (sustained flow) (Azpiroz-Zabala et al., 2017).

1.2.2. Laminar flows

Gravity-driven laminar mixtures of sediment where sediments are transported by matrix strength, excess pore pressure and grain-to-grain interactions (Iverson, 1997; Mulder and Alexander, 2001) are known as debris flows (Figure 1.8; Middleton and Hampton, 1973; Nardin et al., 1979). When the yield strength of the debris flow and friction with the substrate is greater than the shear stress (driving stress; Hampton, 1975), the flow freezes, depositing its sediment en masse (Nardin et al., 1979; Talling et al., 2012) with the deposit lacking grain size segregation (Mulder and Alexander, 2001).

Debris flows can be subdivided according to their mud content due to the impact of the clay proportion on flow behaviour (Hampton, 1975; Baas and Best, 2002; Felix and Peakall, 2006; Baas et al., 2009; Iverson et al., 2010). Increasing clay-concentration promotes the development of flocs due to the electrostatic forces of clay minerals (Van der Waals forces; Winterwerp and Van Kesteren, 2004) and induces 'gelling' of the gravity flow, suppressing turbulence of the parental flow (Felix & Peakall, 2002; Baas et al., 2009 and references therein)(Baas et al., 2009). The type of clay is also a determining parameter due to the different cohesive properties of variable clay minerals (Marr et al., 2001; Baas et al., 2016; Baker et al., 2017). In contrast, increasing shear stresses along the basal and upper interface of debris flows can promote the disaggregation of the bonds formed between the clay minerals resulting in turbulence generation and water entrainment (Marr et al., 2001; Fallgatter et al., 2017).

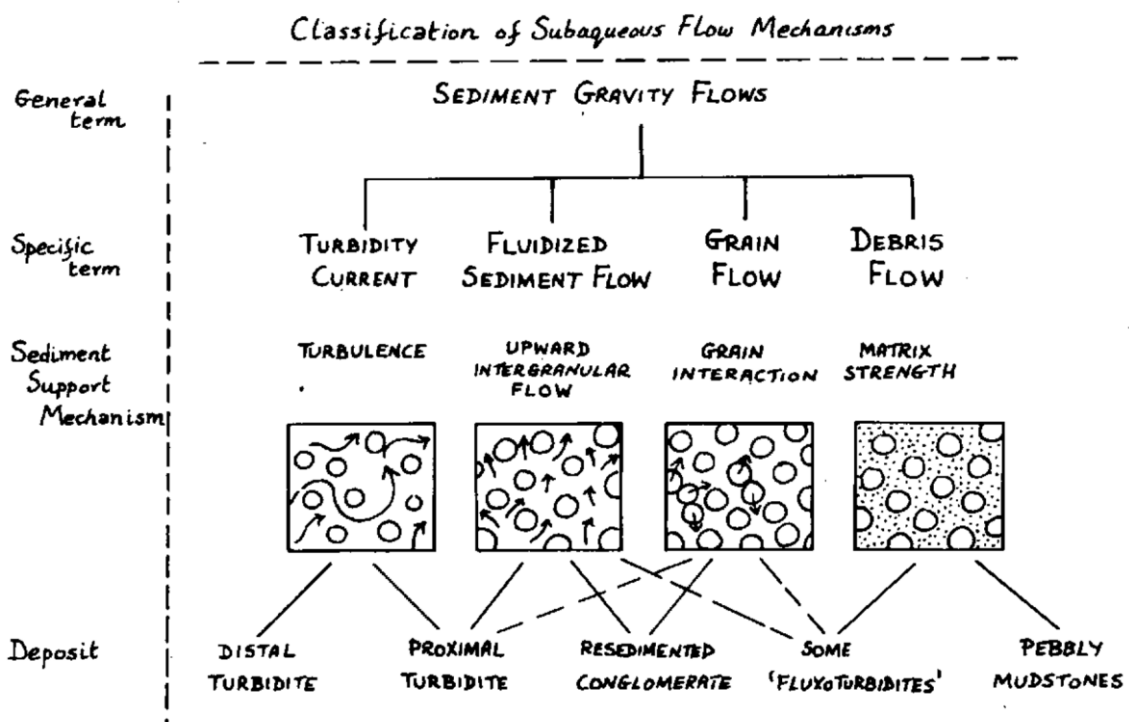


Figure 1.8. Classification of subaqueous sediment gravity flows according to sediment support mechanism and their deposits (Middleton and Hampton, 1973).

However, not all laminar flows deposited en masse are related to cohesive debris flows, as proposed by Mulder and Alexander (2001). They refer to 'hyperconcentrated density flows': mud-poor laminar flows where the concentrations are elevated enough that the particle support mechanism is driven by excess pore pressure and grain-to-grain interactions rather than turbulence or matrix strength. The pore pressure rapidly dissipates upwards due to the low clay amount (Talling et al., 2012). This dissipation results in low flow efficiency and flows depositing the sediments en masse via frictional freezing rather than cohesive freezing of mud-rich debris flows (Mulder and Alexander, 2001).

1.2.3. Transitional flows

In nature, there is a continuum spectrum in subaqueous sediment gravity flows, and their state is not fully turbulent or laminar (Baas and Best, 2002). These flows are termed transitional flows (Haughton et al., 2003; Baas et al., 2009; Kane and Pontén, 2012). This thesis refers as transitional to the flows with intermediate in properties (between turbulent or laminar) rather than representing a transition from laminar to turbulent and viceversa. Each flow transformation is produced by distinctive mechanisms responsible for rheological changes. Transformation of debris flows into transitional flows, or turbidity currents are likely to occur by entrainment of fluid and/or flow acceleration (Marr et al., 2001; Talling et al., 2002). In contrast, the transformation of turbidity currents into transitional flows is likely to occur due to increasing clay concentration, reduction in flow velocity or both (Kane et al., 2017).

Given the wide spectrum of flow behaviours that can be developed from fully turbulent to fully laminar, Baas et al. (2009) subdivided transitional flows according to the flow

stability phase (Figure 1.9): turbulence-enhanced transitional flows (TETFs), lower transitional plug flows (LTPFs), upper transitional plug flows (UTPFs) and quasi-laminar plug flows (QLPFs). Turbulence-enhanced transitional flows (TETFs) show turbulence along their entire vertical profile, being more intense at the base due to the greater shear stresses (Figure 1.9; Baas et al., 2009, 2011). Lower (LTPFs) and upper transitional plug flows (UTPFs) are characterised by a strong flow stratification and two-phase flow behaviour. In lower transitional plug flows (LTPFs), the intensity of the turbulence at the base is similar to TETFs, although it is rapidly dissipated, developing a laminar upper division (Figure 1.9; Baas et al., 2009, 2011). Upper transitional plug flows (UTPF) show lower turbulence intensity than in TETFs and LTPFs as a result of increasing cohesive forces (viscosity and yield strength), promoting thicker upper laminar division, which is propagated downwards (Figure 1.9; Baas et al., 2009, 2011). With even higher clay concentrations, the flow suppresses its turbulence forming a gel across most of the flow, with thin and weakened turbulence just over the base. These flows are named quasi-laminar plug flows (QLPFs) (Figure 1.9; Baas et al., 2009, 2011).

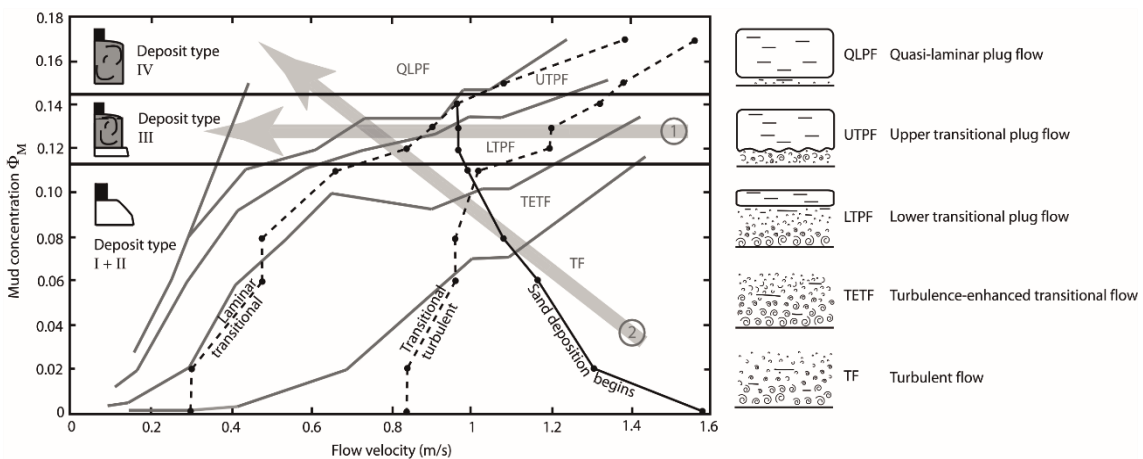


Figure 1.9. Phase diagram and schematic models (Baas et al., 2009) for different kaolinite concentrations. Arrows show two trajectories producing a hybrid event bed (Sumner et al., 2009).

1.3. Sediment gravity flow deposits

Deposit-based classification is used in outcrop and core studies given the limited availability of primary parameters such as flow state, density, support mechanism, concentration, grain size, and flow velocity. Deposits are often classified according to their texture, thickness, grain size (and their variations), sorting, matrix content and sedimentary structures. Based on outcrop and core description, deposits formed in deep-water environments under gravity-driven flows are broadly subdivided into low-density turbidites, high-density turbidites, debrites and transitional flow deposits.

1.3.1. Low-density turbidites

Low-density turbidity currents are sediment gravity flows of low concentration (< 9% sediment; Bagnold, 1962) where the sediments are maintained uniquely in suspension by fluid turbulence through the entire vertical profile (Figure 1.10; Lowe, 1982; Mulder and Alexander, 2001; Baas et al., 2009; Talling et al., 2012). When the low-density turbidity currents decelerate (wane), the sediments are deposited according to their settling velocities under slow aggradation rates, producing incremental layer-by-layer deposition (Figure 1.10; Sumner et al., 2008). Sediments with higher settling velocities (coarsest/densest sediment) are deposited first, while the finer fractions bypass down-dip (Stevenson et al., 2015). This grain size segregation and differential deposition are recorded by fining of the low-density turbidites from proximal to distal areas (Lowe, 1982).

Low-density turbidites can show heterogeneous structuration (Figure 1.10), often subdivided into divisions, known as the Bouma sequence (Bouma, 1962). From the base

to the top, these divisions are planar-laminated sandstone (T_B), ripple cross- and convolute-laminated sandstone (T_C), planar-laminated (T_D) and structureless mudstone (T_E). The juxtaposition of these divisions records the waning of turbidity currents by upwards decreasing grain size, better sorting and tractional bedforms associated with low velocities (Southard and Boguchwal, 1990; Sumner et al., 2008). However, planar laminated (T_B) divisions are also formed in high-density turbidites, and their deposition is linked to high-aggradation rates under high concentration flows (Lowe, 1982). Talling et al. (2012) propose that the boundary between low- and high-density turbidites lie on the planar laminated interval (T_B) (Figure 1.10). Ripple cross-laminated sand (T_C) is formed from fully turbulent and low-density turbidity currents with low aggradation rates (Allen, 1982a; Southard, 1991; Jobe et al., 2012). T_C division shows a range of different ripples indicating variable sedimentation rates. Starved ripples indicate very low-aggradation rates and reworking from fine-grained turbidity currents (Talling et al., 2007) while climbing ripples indicate higher sediment fallout rates (Jobe et al., 2012). Locally ripples in T_C divisions can be replaced by convolute lamination, which indicates high aggradation rates and dewatering (Tinterri et al., 2016 and references therein). T_D and T_E overlie T_C division and record low sedimentation rates from dilute flows (Allen, 1982a; Talling et al., 2012). However, division can also be repeated indicating velocity fluctuation and/or interaction with topography (Pickering & Hiscott, 1989; Jobe et al., 2012)

1.3.2. High-density turbidites

High-density turbidity currents are characterised by two-phase flow behaviour (Kuenen, 1951), and their deposits are named high-density turbidites (Figure 1.10; Lowe, 1982). The basal layer is denser (Azpiroz-Zabala et al., 2017; Pope et al., 2022), and the grain

support mechanism results predominantly from grain-to-grain interactions, in contrast to the overlying more dilute division, in which the grains are mainly supported by fluid turbulence (Figure 1.10; Lowe, 1982). High-density turbidites are formed by incremental layer-by-layer deposition (Kneller and Branney, 1995) but with higher aggradation rates than low-density turbidites (Sumner et al., 2008). The formation of tractional structures such as ripples, dunes or planar laminations can be inhibited at high vertical fallout rates (Sumner et al., 2008), inducing the deposition of massive sandstones (Lowe, 1982, 1988; Kneller and Branney, 1995; Baas, 2004; Talling et al., 2012).

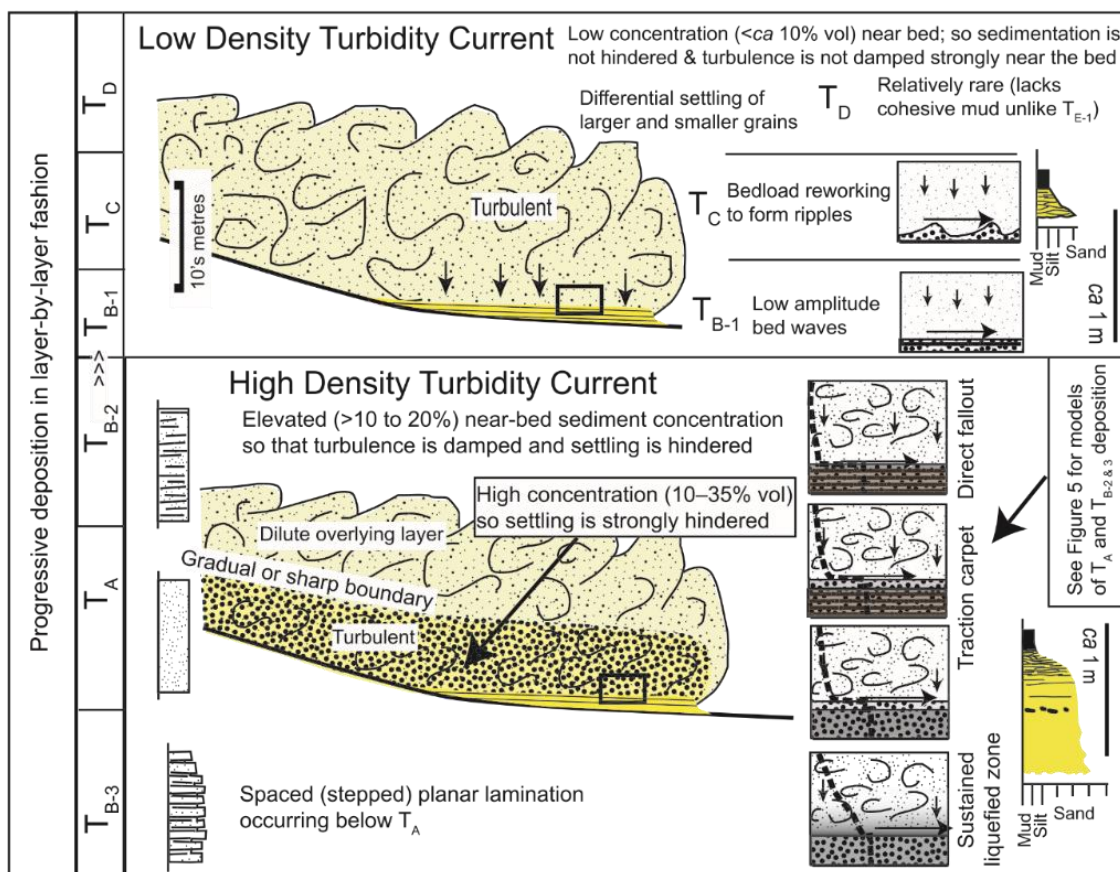


Figure 1.10. Summary of subaqueous turbulent flows' transport mechanism and respective deposits (Talling et al., 2012).

Several mechanisms and gravity flows can result in the formation of massive clean sandstone T_A which has been a challenge to reconcile for geologists. Kneller and Branney (1995) proposed that massive sandstone can be formed due to sand aggradation due to

hindered settling at the flow boundary beneath a sustained (quasi-)steady and concentrated gravity flow. This mechanism implies massive sands evolving down-dip into planar laminated deposits. In contrast, Shanmugam and Muiola (1995) and Shanmugam (1996) propose that massive sandstones should be interpreted as "sandy debris flow" due to the abrupt down-dip pinch-out of sandstone deposited from flows with a laminar state. Talling et al. (2012) reinterpreted the 'sandy debrites' of Shanmugam and Muiola (1995) and Shanmugam (1996) and attributed their formation to sustained high-density turbidites due to the 'subtle but distinct grading'. Mulder and Alexander (2001) differentiate cohesionless debris flows from high-density turbidity currents by classifying them as hyperconcentrated and concentrated gravity flows. These authors agree that hyperconcentrated flows comprise a laminar state and that deposition occurs en masse without any grain size segregation. On the other hand, sediments in concentrated flows are transported by a combination of grain-to-grain interactions and flow turbulence, resulting in an incremental layer-by-layer deposition. The main difference between these two flow processes is their driving mechanism: debris flows (or hyperconcentrated flows) are driven by their own weight in a downslope sense, whereas the near-bed laminar layer of high-density turbidity currents (or concentrated flows) is driven by the overriding more dilute division (Mulder and Alexander, 2001; Talling et al., 2012). Talling et al. (2012) differentiated the planar-laminated interval into T_{B-1} , T_{B-2} and T_{B-3} (Figure 1.10). T_{B-1} overlies T_A and is associated with low-amplitude bedload waves formed in low-density turbidity currents (Best and Bridge, 1992), while T_{B-2} and T_{B-3} are linked to rapid deposition of the coarser fraction that is effectively sheared laterally by the overriding flow (Sumner et al., 2008).

1.3.3. Debrisites

Debris flows are flows with a laminar state where the particles are not segregated according to their size and are deposited en masse (Figure 1.11; Mulder and Alexander, 2001; Talling et al., 2012); therefore, the initial thickness of debris flow deposits (debrisites) is closely related to flow thickness (Iverson, 1997).

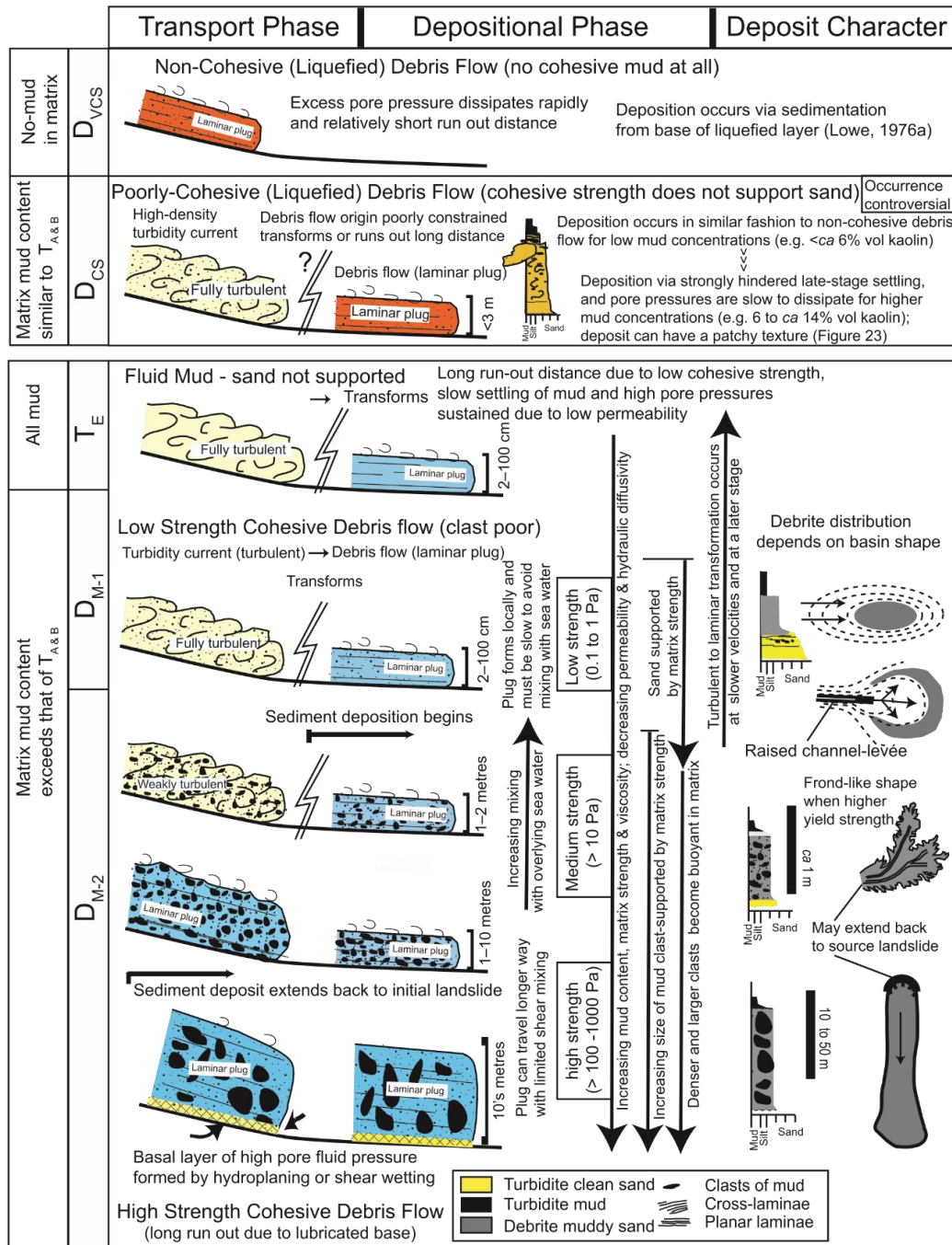


Figure 1.11. Summary of subaqueous laminar flows' transport, depositional phases, and respective deposits (Talling et al., 2012).

Debris flows can be grouped according to the cohesive mud content in their matrix (Figure 1.11) due to the impact that the cohesive clay has on permeability and, therefore, dissipation-time for the excess pore pressure, viscosity, yield strength and competence (Iverson et al., 2010). Despite the continuum of matrix content that debrites comprise, a bimodal content in cohesive mud was reported in Amy et al. (2006), where a boundary of 20% volume in cohesive mud ($< 30 \mu\text{m}$) was established. However, that threshold will vary according to clay mineralogy and the respective cohesive strength (Baker et al., 2017). Talling et al. (2012) divide cohesive debris flows into high- to moderate cohesive debrites (D_{M-2}) and low-strength ones (D_{M-1}) based on their maximum grain size (Figure 1.11). Low-strength cohesive debrites are decimetre- to metre-scale deposits, and the maximum grain size is sand to granules (Hampton, 1975; Talling et al., 2012; Talling, 2013). The high- to -moderate cohesive debrites can be up to several tens of metres thick, and the maximum clast size they comprise ranges from granules to clasts tens of metres long (named megaclast if $>4.1 \text{ m}$; Blair and McPherson, 1999) due to elevated yield strength (Figure 1.11).

1.3.4. Transitional flow deposits

The spectrum of subaqueous sediment gravity flows between fully turbulent or laminar flows have been termed 'slurry flows' (Lowe & Guy, 2000) or transitional flows (Haughton et al., 2003), and their deposits are termed transitional flow deposits (Kane & Pontén, 2012). Transitional flows are interpreted to result from initial turbulent flows that increased their near-bed clay concentration as a result of flow deceleration and/or entrainment of cohesive clay from the underlying substrate and flow bulking (Haughton et al., 2009), promoting the formation of a plug flow lacking turbulence (Baas and Best,

2002; Barker et al., 2008; Baas et al., 2009; Kane and Pontén, 2012). The progressive entrainment of cohesive clay causes turbulence suppression and induces transitional flow behaviour along down dip, which is reflected in the texture of the deposits (Figure 1.12; Kane and Pontén, 2012; Fonnesu et al., 2015; Porten et al., 2016; Kane et al., 2017).

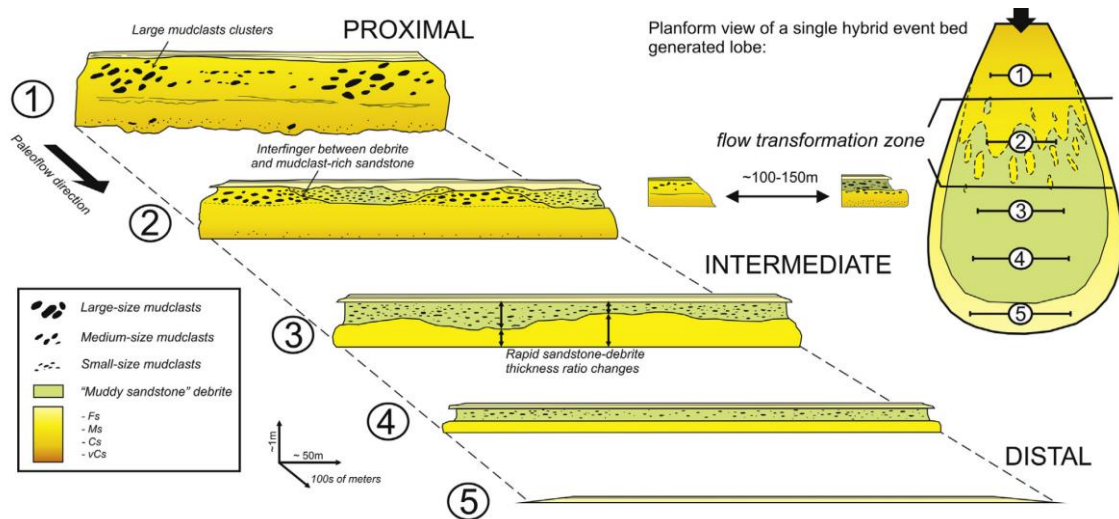


Figure 1.12. Schematic diagram of a single hybrid flow and related the facies heterogeneity model along down-dip (Fonnesu et al., 2015).

Transitional flow deposits recording the onset of transitional flow transformation commonly lack structuration and are characterised by ungraded to crudely graded profiles, similar to high-density turbidites, although with high mudstone clast and matrix contents (Figure 1.12; Lowe and Guy, 2000; Kane et al., 2017). As the transitional flows increase their concentration and viscosity along the down-dip, they develop a two-phase flow behaviour with a strong rheological heterogeneity (Figure 1.9; Baas et al., 2009; Kane et al., 2017). Such heterogeneity is reflected in the deposits named hybrid event beds (Figure 1.13; Haughton et al., 2003, 2009; Davis et al., 2009; Hodgson, 2009; Kane et al., 2017; Southern et al., 2017; Spychala et al., 2017a) and they can be classified as proximal or distal based on their texture and structuration (Figure 1.12). One of the earliest models characterising hybrid event beds was developed by Haughton et al. (2003,

2009) by subdividing them into different divisions (Figure 1.13). According to Haughton et al. (2003, 2009), an ideal hybrid bed comprises a basal structureless sandstone (H1; turbidite), a banded division (H2; transitional flow deposits), a poorly sorted mudstone clast- and matrix-rich sandstone (H3; debrite), thin-bedded structured sandstone (H4; turbidite) and a thin-bedded mudstone cap (H5; hemipelagite). Recent studies on hybrid event beds highlight that turbiditic divisions (H1 and H4) are more closely associated with transitional flow deposits (Figure 1.13) than turbidites *sensu stricto* (Baas et al., 2011; Baker and Baas, 2020; Hussain et al., 2020).

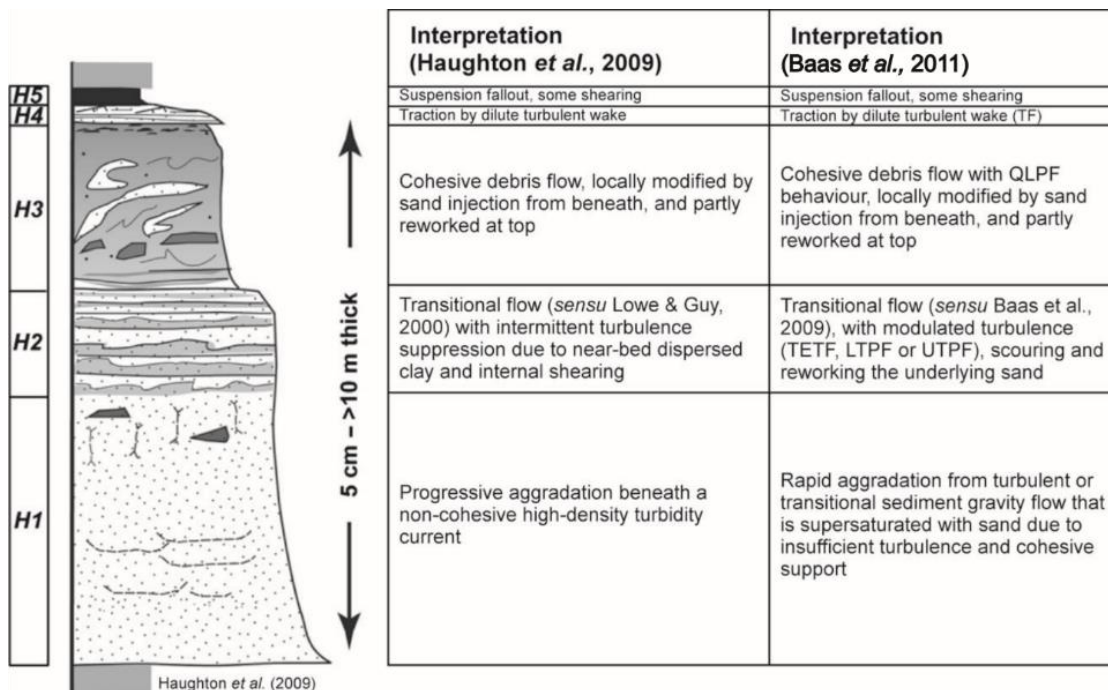


Figure 1.13. Different interpretations for the depositional processes of an idealised hybrid event bed and its divisions (HEB)(Baas et al., 2011).

1.4. Submarine landslides

Submarine landslides are coherent sedimentary bodies translated from high to lower gradient slopes due to gravity (Figure 1.14; Hampton et al., 1996; Coleman and Prior, 1998; Moscardelli and Wood, 2008; Kneller et al., 2016). The onset of downslope remobilisation, known as mass wasting, is the consequence of shear stresses exceeding

the shear strength of the sediments (driving shear stress vs resisting stress *sensu* Hampton et al., 1996). Tectonic steepening, seismicity, volcanic activity, storms and changes in the hydrostatic pressure increase the shear stresses on the material accumulated on slopes (Field and Hall, 1982; Bugge et al., 1987; Goldfinger et al., 2000; Bungum et al., 2005; Lee, 2009; Dalla Valle et al., 2015), while unconsolidated sediments and intervals of high pore pressures reduce the shear strength (Piper et al., 1997).

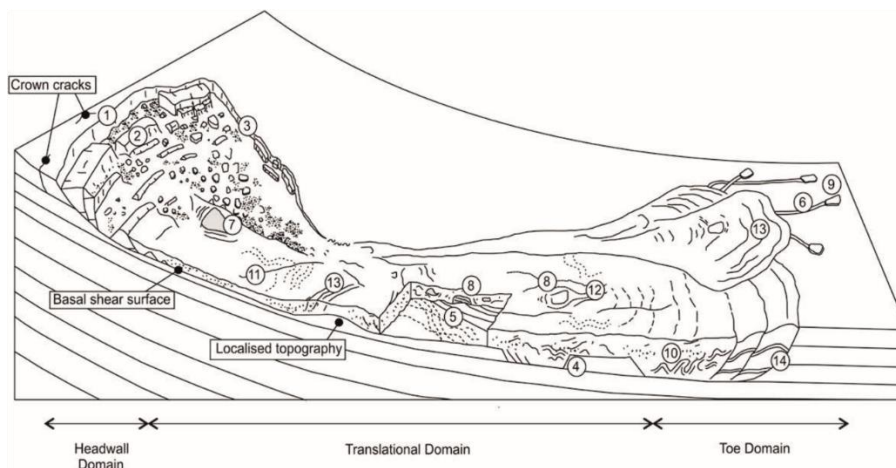


Figure 1.14. Schematic diagram of an idealised submarine landslide deposit and various kinematic indicators. (1) Headwall scarp. (2) Extensional ridges and blocks. (3) Lateral margins. (4) Basal shear surface ramps and flats. (5) Basal shear surface grooves. (6) Basal shear surface striations. (7) Remnant blocks. (8) Translated blocks. (9) Outrunner blocks. (10) Folds. (11) Longitudinal shears/first-order flow fabric. (12) Second order flow fabric. (13) Pressure ridges. (14) Fold and thrust systems (Bull et al., 2009).

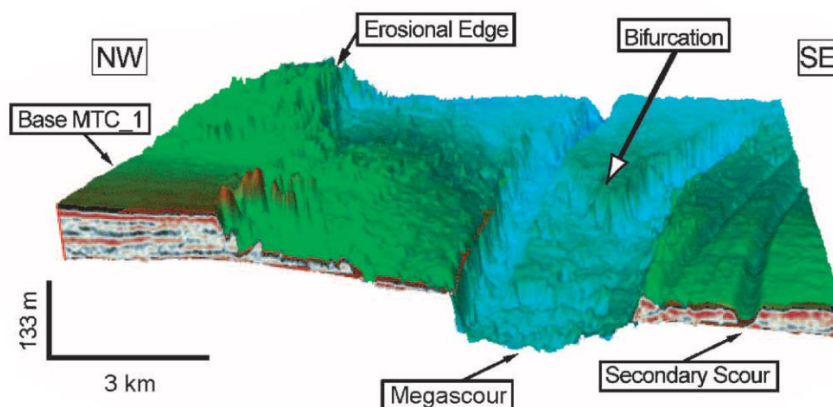


Figure 1.15. (A) Seismic reflection dataset showing the geomorphological impact at the base of an MTC, including the erosional edge on the west, megascours in the centre of the image, and secondary scours on the east side (Moscardelli et al., 2006).

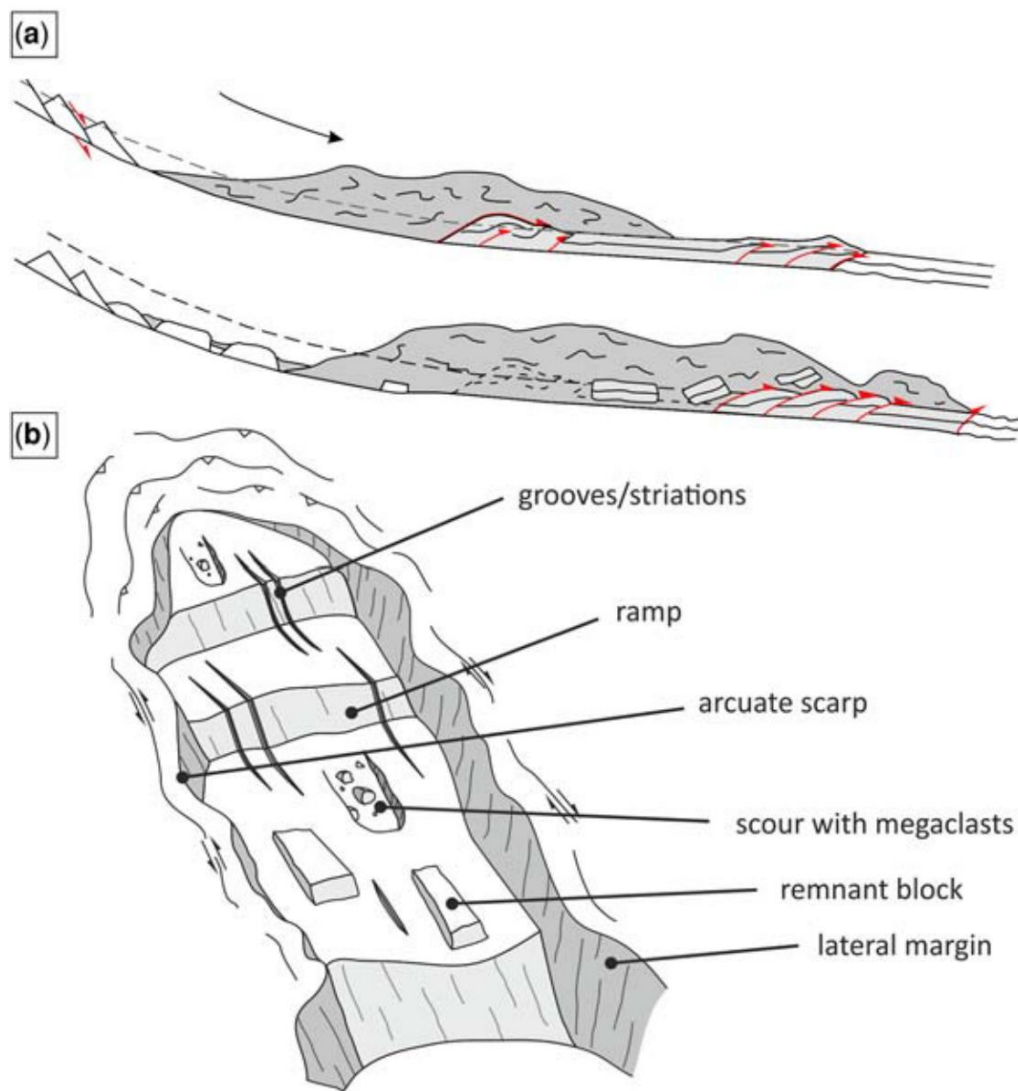


Figure 1.16. (A) Cartoon illustrating the bulking of a submarine landslide and the entrainment of the substrate during its passage. (B) Cartoon illustrating the basal shear surface and related features such as ramps and flats, lineations, scours with megaclasts, and deformation zones (Hodgson et al., 2019).

As submarine landslides travel across the seafloor, they exert shear stress and overpressure on the underlying substrate (Figure 1.14, Figure 1.15 and Figure 1.16; Bull et al., 2009; Hodgson et al., 2019; Payros and Pujalte, 2019), leading to complex styles of interactions (Sobiesiak et al., 2018). The impact of submarine landslides on the underlying substrates (Figure 1.15) has been the focus of several studies based on

subsurface (McGilvery and Cook, 2003; Moscardelli et al., 2006; Moscardelli and Wood, 2008; Bull et al., 2009; Posamentier and Martinsen, 2011; Soutter et al., 2018) and in outcrop (Lucente and Pini, 2003; Dykstra et al., 2011; Ogata et al., 2012; Dakin et al., 2013; Sobiesiak et al., 2018; Payros and Pujalte, 2019). The stress applied to the substrate during the passage of a submarine landslide can be accommodated by discrete planes (basal shear-surface) or stratigraphic intervals (basal shear-zone) (Alves and Lourenço, 2010; Butler and McCaffrey, 2010; Watt et al., 2012; Dakin et al., 2013). The deformation is commonly recorded by the development of compressional structures developed along the basal shear zone and by the entrainment of substrate material (Figure 1.14 and Figure 1.16; Moscardelli et al., 2006; Alves and Cartwright, 2009; Sawyer et al., 2009; Dakin et al., 2013; Ogata et al., 2014; Ortiz-Karpf et al., 2015; Sobiesiak et al., 2016, 2017; Hodgson et al., 2019; Valdez et al., 2019). The transport of megaclasts along their base can gouge the substrate, producing kilometres-long linear features named grooves or megascours (Figure 1.15 and Figure 1.16; Moscardelli and Wood, 2008).

1.4.1. Submarine landslide deposits

Submarine landslide deposits represent an important record in deep-water stratigraphic successions (e.g. Pickering and Corregidor, 2005; Posamentier and Martinsen, 2011), being up to 90% in their thickness (Garziglia et al., 2008). Mass Transport Deposit (Nardin et al., 1979) and Mass Transport Complex (several MTDs; Weimer et al., 2007) are commonly used terms to refer to submarine landslide deposits in seismic reflection datasets where their internal character is not resolvable. However, in outcrop-based studies, the degree of internal deformation of submarine landslide deposits is often used as a proxy for their classification. A coherent mass of sediments translated downslope over a basal glide plane with limited internal deformation (limited rotation of bedding) is referred to as a slide (Dott, 1963). The overlying sedimentary mass remains undeformed

if the shear stresses are limited to the basal glide plane. When the internal deformation is higher, and the internal bedding is folded, the deposits are named slumps (Nardin et al., 1979; Shanmugam, 2006). The vergence of the fold is commonly used as a criterion to infer the direction of the remobilisation and palaeoslope orientation (Farrell and Eaton, 1987; Bradley and Hanson, 1998). Normal faulting is common due to extensional stresses developed near the evacuation area, while low-angle thrust faults are developed in their lower compressional domains (Lewis, 1971; Martinez et al., 2005). Despite the variable deformation degree, slides and slumps are characterised by preserving the original bedding and sedimentary structures. On the other hand, debris flows are incoherent masses where the shear stress is distributed throughout the entire vertical profiles (Carter, 1975; Nardin et al., 1979). As a result, the debrites show fully dismembered texture, and the original bedding is not preserved (e.g. Pickering and Corregidor, 2005). Cohesive debris flows are characterised by the transport of oversized clast, commonly named megaclasts (> 4.1m diameter; Blair and McPherson, 1999), floating into a fine-grained matrix (Labaume et al., 1987; McGilvery and Cook, 2003; Lee et al., 2004; Jackson, 2011; Sobiesiak et al., 2016; Fallgatter et al., 2017; Nwoko et al., 2020a).

1.5. Interaction between sediment gravity flows and seafloor topography

In the absence of seafloor relief, sediment gravity flows spread radially, producing elongated fan-shaped deposits. However, seafloor relief is common in deep-water settings and can be formed by a wide variety of geological processes such as tectonism (Sinclair and Tomasso, 2002; Joseph and Lomas, 2004), salt diapirism (Hodgson et al., 1992; Prather et al., 1998, 2017; Oluboyo et al., 2014), mud diapirism (Jobe et al., 2017) and submarine landslide deposits (Fairweather, 2014; Ortiz-Karpf et al., 2015; Kneller et al., 2016).

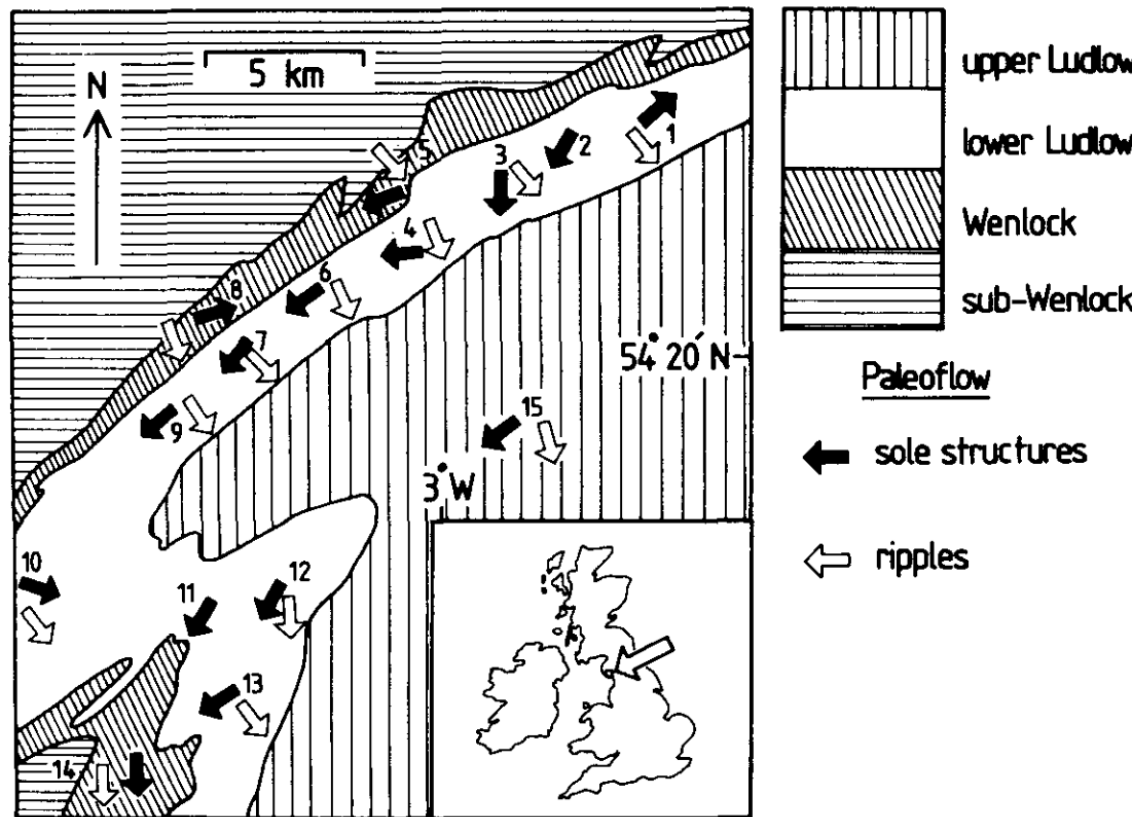


Figure 1.17. Geologic map of part of Cumbria (NW England) showing palaeocurrent vector means of turbidites within Windermere Group. Note the divergence between ripples (formed from deflected dilute (parts of) flows, while sole structures (formed from denser flows) run parallel to the SW-NE topography (Kneller et al., 1991).

Bathymetric confinement is produced when sediment gravity flows interact with basin margins or irregular topography, which affects flow velocity and flow direction of turbidity currents and, therefore, resultant deposit characteristics (Kneller, 1995; Kneller & Branney, 1995; Al Ja'Aidi et al., 2004). Sediment gravity flows systems entering a depression surrounded by enclosing topography are known as confined and contained system (Southern et al., 2015) or ponded system (Winker, 1996; Prather et al., 2017). However, not all sediment gravity flows show a similar response when interacting with topography. The interaction will depend on the flow properties (flow rheology, velocity, thickness, stratification and volume) and the nature of the topography (orientation, height, gradient and lateral extent) (Kneller and Branney, 1995; Al Ja'Aidi et al., 2004). The style

of interaction will determine the distribution, texture and architecture of the deposits within the basin (Kneller and McCaffrey, 2003; Smith, 2004b; Patacci et al., 2014; Southern et al., 2015; Soutter et al., 2019). Denser flows are more sensitive to topography than dilute flows/divisions (Figure 1.17; Kneller & Buckee, 2000; Al Ja' Aidi et al., 2004; Brunt et al., 2004; Lamb et al., 2006): low-density turbidity currents can surmount certain topography, while high-density turbidity currents and debris flows will be more restricted to topographic lows (Bakke et al., 2013). The divisions within a stratified gravity flow will respond differently according to their flow properties (flow decoupling), where dilute division will surmount the topography and dense division run parallel to its strike (Figure 1.17; Kneller et al., 1991).

The steepness and the orientation of confining topography (Figure 1.18) with respect to incoming sediment gravity flow is an additional control (Kneller et al., 1991; Kneller and Branney, 1995; Soutter et al., 2021). Lateral confinement (Figure 1.18) has been reported to enhance flow velocity and efficiency due to the channelisation produced by the confining element (Sinclair, 1994; Amy et al., 2004; Soutter et al., 2021). Due to the presence of lateral confinement and gentler or flatter margin, the resultant deposits might develop certain asymmetry (Figure 1.18; Amy et al., 2004; Soutter et al., 2021). Oblique confinement (Figure 1.18) is responsible for flow deflection (Kneller et al., 1991; Edwards et al., 1994) and partitioning of deposits (Soutter et al., 2019). Frontal confinement (Figure 1.18) is responsible for trapping sand up-dip the obstacle (Sinclair and Tomasso, 2002) due to abrupt flow deceleration and subsequent loss in flow capacity (Hiscott, 1994a). However, this is highly dependent on the magnitudes of the incoming sediment gravity flows and the topography (Sinclair and Tomasso, 2002). When the topography is similar to or larger than the flow thickness, and there is a lack of

connectivity between the topographic lows, the flow will be strongly decelerated, trapping up-dip the coarsest transported sediments (Figure 1.19; Sinclair and Tomasso, 2002; Kneller et al., 2016). In this setting, the distal parts will be mudstone-dominated or, at least, comprising thinner and finer-grained sandstones (Figure 1.19; Sylvester et al., 2015). When flow thickness exceeds the topographic height, the sediment gravity flows can largely bypass depositing the coarser fraction in the topographic lows (Figure 1.19). Furthermore, the topographic lows can be connected via tortuous corridors (Figure 1.20; *sensu* Smith, 2004), where the sediment gravity flows will not be fully ponded, and the strata overlying the topographic lows will be sandstone-dominated (depending on the source material). Therefore, the filling style in basins characterised by seafloor topography depends on the complex interplay between the bathymetric configuration and the nature of the sediment gravity flows (Figure 1.18, Figure 1.19 and Figure 1.20).

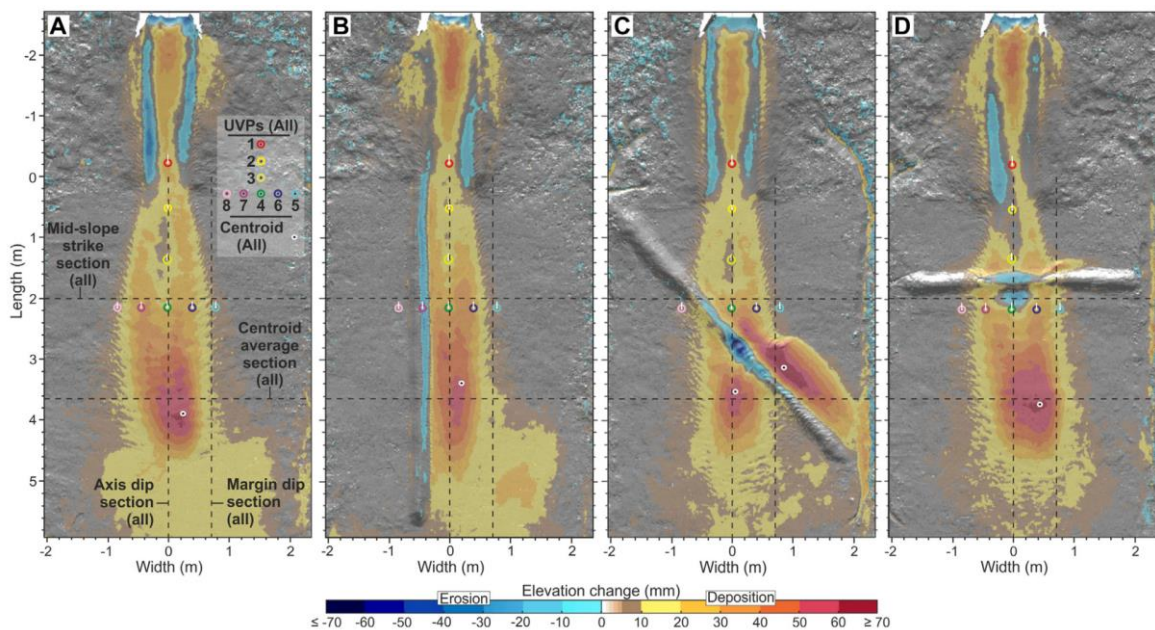


Figure 1.18. Elevation maps of four experimental runs in a flume tank with variable topography show erosion in blue and deposition in yellow, orange and red. (A) Unconfined; (B) laterally confined; (C) obliquely confined; and (D) frontally confined (Soutter et al., 2021).

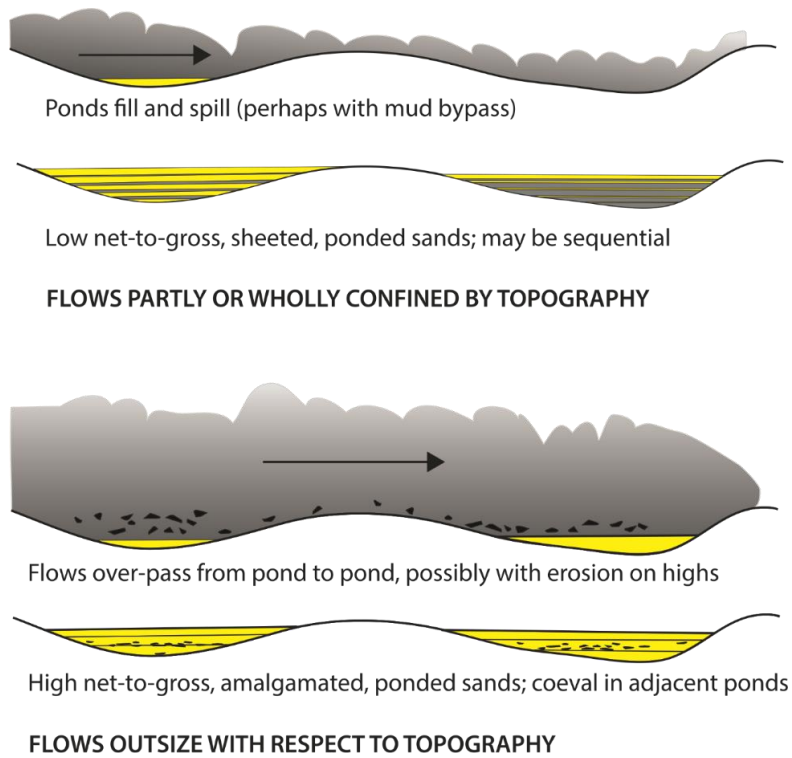


Figure 1.19. Schematic diagram illustrating the interaction between sediment gravity flows of different magnitudes relative to the relief of the underlying submarine landslide deposits. Note the difference in the resultant deposits depending on the bypass or flow ponding (Kneller et al., 2016).

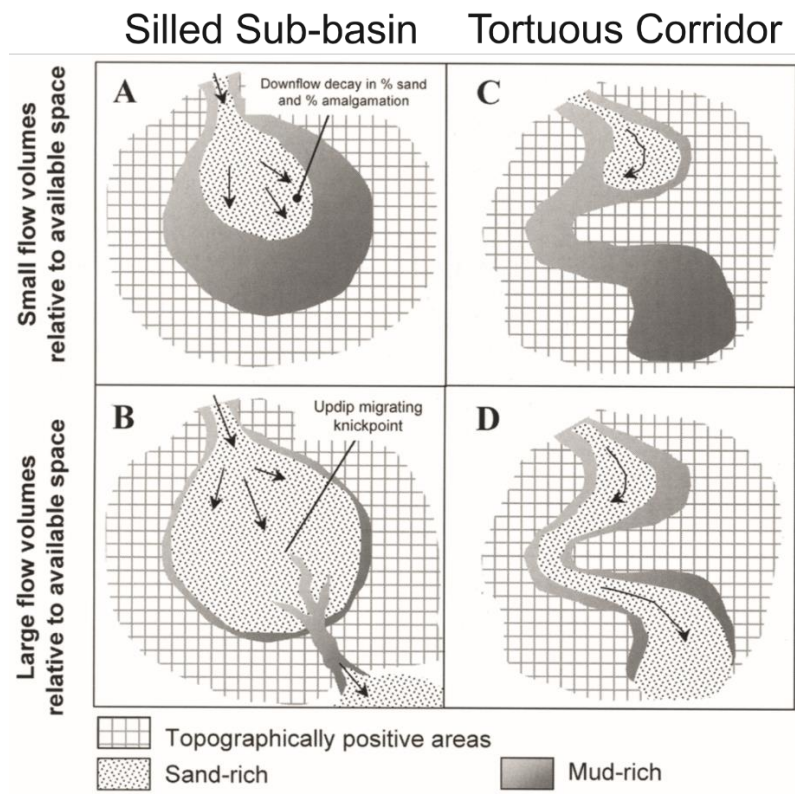


Figure 1.20. Schematic diagrams illustrating different bathymetric configurations and responses of the sedimentary systems. (A) In a silled sub-basin, when sand-transporting flows are small in volume relative to the scale of the accommodation. (B) In a silled sub-basin, when sand-transporting flows are large in volume relative to the accommodation. Note the spilling to the next sub-basin downslope. (C) In a connected tortuous corridor, when sand-transporting flows are small in volume relative to the potential flow path. (D) In a connected tortuous corridor, when sand-transporting flows are large in volume relative to the potential flow path (Smith, 2004b).

1.5.1. Termination styles

Deposition from sediment gravity flows displays characteristic facies, architectures and depositional patterns resulting from interactions with seafloor topography. The influence of topography can be interpreted from direct observation in sedimentary structures and divergence in palaeocurrents (Figure 1.17; Kneller and Branney, 1995; McCaffrey and Kneller, 2001; Tinterri et al., 2016) in facies transitions (Smith, 2004b; Spychala et al., 2017b; Soutter et al., 2019) and in angular unconformities produced by termination against topography (McCaffrey and Kneller, 2001; Smith and Joseph, 2004; Gardiner, 2006; Bakke et al., 2013). Several studies have focused on the different deep-water termination styles (Figure 1.21) as they are targets for exploration and production due to the stratigraphic trapping potential, but also for the sedimentological insights into palaeotopography (Figure 1.22 and Figure 1.23; Hurst et al., 1999; Kneller et al., 1999; Sinclair, 2000; McCaffrey and Kneller, 2001; Smith and Joseph, 2004; Gardiner, 2006; Bakke et al., 2013; Soutter et al., 2019).

Abrupt terminations are observed in thick-bedded sandstones with high amalgamation ratios and are linked to dense sediment gravity flows that undergo rapid flow deceleration and high sedimentation rates (Gardiner, 2006). Three end-member termination styles have been observed in high-density turbidites: 1) tabular deposits; 2) thinning and draping

the slope, or 3) localised thickening near the margin (Figure 1.21, Figure 1.22 and Figure 1.23; Prather et al., 2000; Sinclair, 2000; McCaffrey and Kneller, 2001; Smith and Joseph, 2004; Gardiner, 2006; Bakke et al., 2013). The localised thickening could be developed by helicoidal secondary flow cells, which are intensified by confining surfaces (McCaffrey and Kneller, 2001). However, high-density turbidity currents can be strongly stratified (Lowe, 1982; Talling et al., 2012), producing different responses within a single flow (flow decoupling *sensu* Kneller and McCaffrey, 1999). The concentrated basal division will be more restricted to topographic lows, whereas the upper, more dilute division is less affected by topography (Figure 1.17 and Figure 1.19; Kneller and McCaffrey, 1999; Sinclair and Tomasso, 2002; Amy et al., 2004; Bakke et al., 2013)

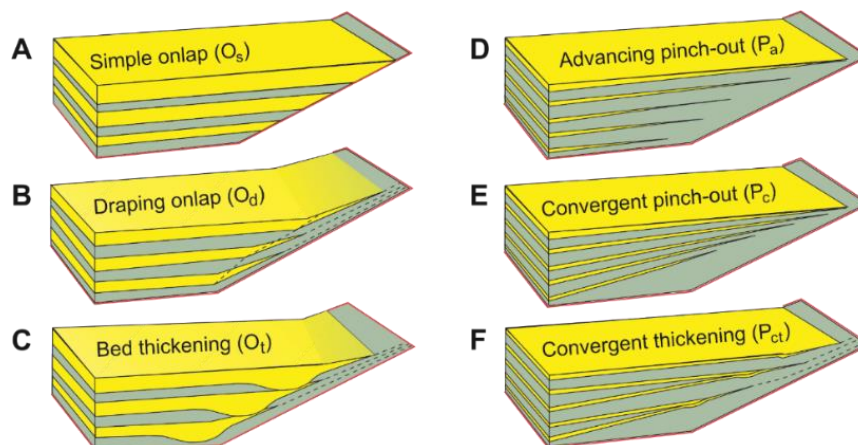


Figure 1.21. Schematic diagrams illustrating termination styles close to topographic heights and basin margin. (A) Simple onlap, (B) draping onlap and (C) bed thickening show terminations within relatively sand-prone stratigraphic, whereas (D) advancing pinch-out, (E) convergent pinch-out and (F) convergent thickening show heterolithic pinch-out successions (Bakke et al., 2013, after McCaffrey and Kneller, 2001; Gardiner, 2006; Patacci, 2010).

Some beds do not terminate against a diachronous and unconformable surface; instead, beds tend to thin gradually, lack erosional features and high-amalgamation ratios, and deposit a thin-bedded mud-prone drape on the onlap surface so that the onlap slope continually aggrades (Figure 1.21, Figure 1.22 and Figure 1.23; Haughton, 1994; Hurst

et al., 1999; Smith, 2004b; Smith and Joseph, 2004; Gardiner, 2006). Deposits displaying these terminations are commonly observed in heterolithic stratal package styles. The three end-member styles are 1) advancing pinch-out, 2) converging-pinch-out, and 3) convergent thickening (Figure 1.21; Smith, 2004b; Gardiner, 2006; Bakke et al., 2013; Spychala et al., 2017c). They are interpreted as being formed from mixed low- to high-density turbidity currents in gentler slopes (fraction of a degree) and low-density turbidity currents in steep slopes (several degrees) as dilute flows are less influenced by the bathymetric configuration of the basin (Al Ja'Aidi et al., 2004). Their ability to surmount and drape topography lies in their flow properties (Kneller & McCaffrey, 1999), such as high flow efficiency (Mutti, 1977) and lack of internal stratification. Persistent aggradational stacking may indicate flow confinement (Smith, 2004b; Spychala et al., 2017c), hindering autogenic compensation produced by the depositional relief of underlying deposits. In this scenario, the upwards thickening and coarsening patterns may not be related to depositional system progradation (Bakke et al., 2013).

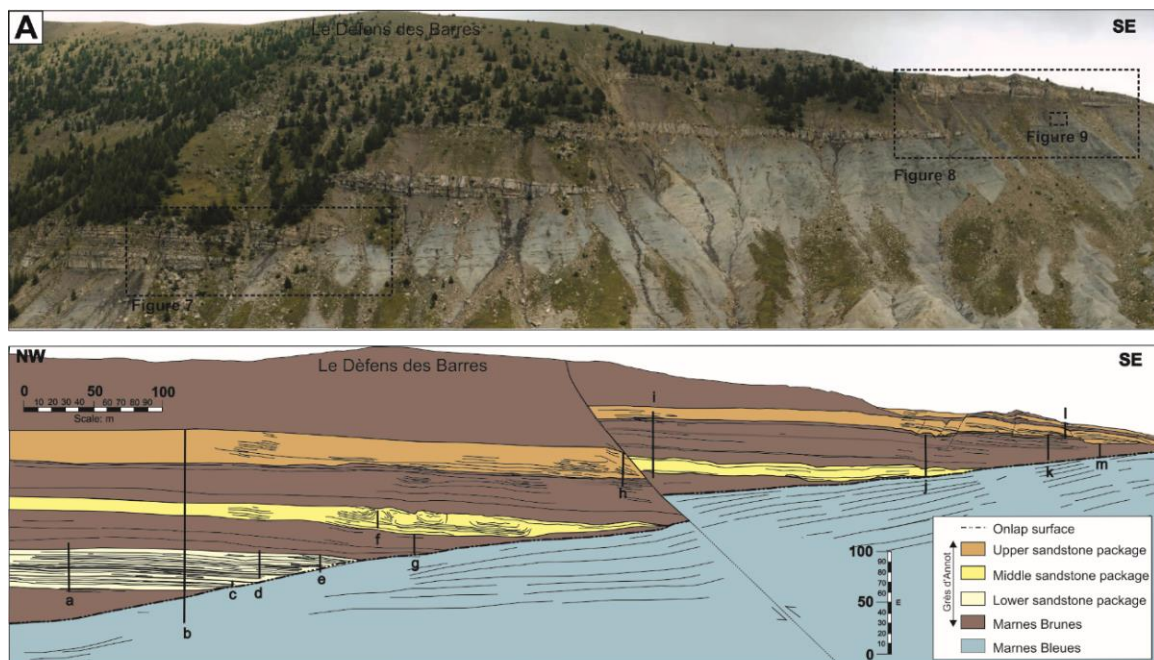


Figure 1.22. A photograph (top) and sketch (bottom) of the outcrop at Chalufy (France) displaying a range of lateral termination styles of the deep-water Grès d'Annot Formation onto the Marnes Bleues Formation (Bakke et al., 2013).

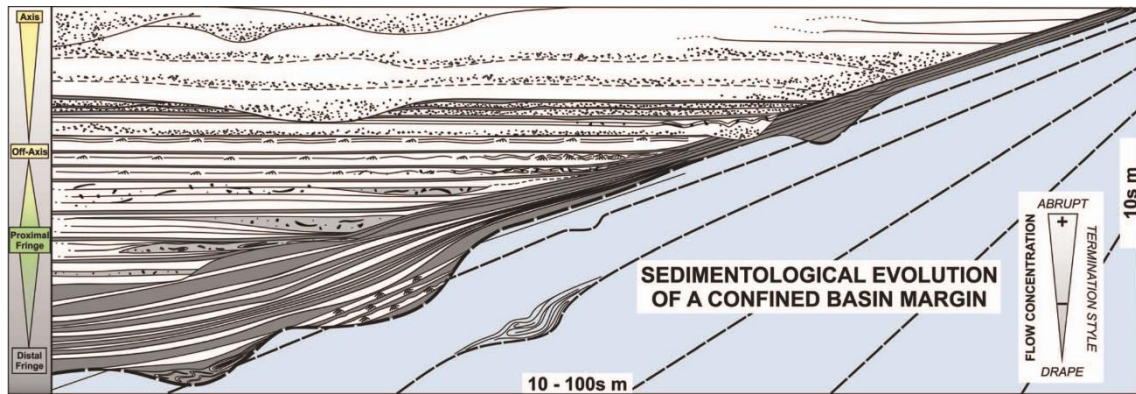


Figure 1.23. Schematic cross-section illustrating the facies evolutions of a lateral onlap in the Grès d'Annot (France) towards the basin margins. Note that the variable style of the termination depends on high- and low-density turbidites and hybrid event beds (Soutter et al., 2019).

1.6. Geomorphic elements of deep-water systems

Deep water depositional systems are commonly subdivided into geomorphic elements from shallower to deeper downslope areas (Figure 1.24 and Figure 1.25). These geomorphic elements are submarine canyons, channels, channel-lobe transition zones and lobes and have been recognised globally in modern and ancient systems. The size, architecture and transition of geomorphic elements vary depending on the frequency, nature and magnitudes of sediment gravity flows and the basin configuration (Figure 1.25).

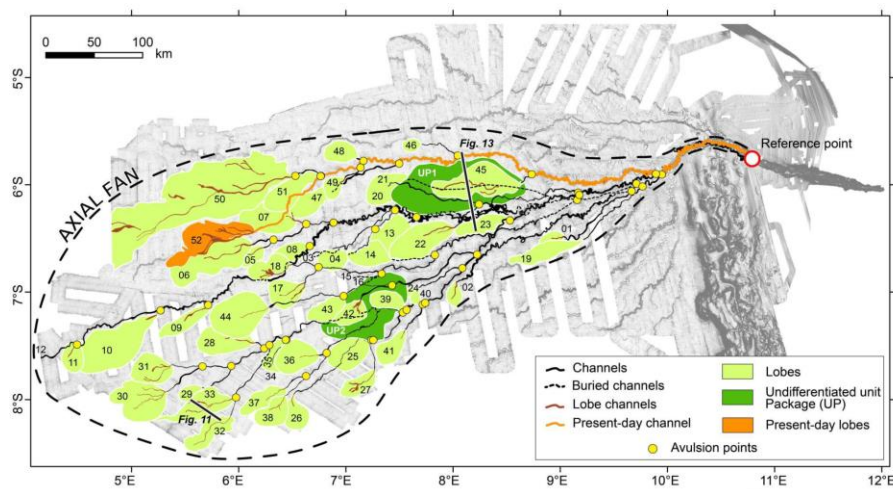


Figure 1.24. Map of the Late Quaternary Axial Congo Fan showing submarine canyon, channels and lobes (Picot et al., 2016).

1.6.1. Canyons

Submarine canyons represent the most proximal geomorphic element of the deep-water depositional system. They are a few kilometres deep, tens of kilometres wide and hundreds of kilometres long negative relief linear features in continental margins incised into the shelf or upper slope settings that act as steep conduits ($\sim 2\text{-}5^\circ$; De Pippo et al., 1999; Harris and Whiteway, 2011) for sediment delivery (Heezen et al., 1964; Nittrouer and Wright, 1994; Bertoni and Cartwright, 2005; Covault et al., 2011; Harris and Whiteway, 2011).

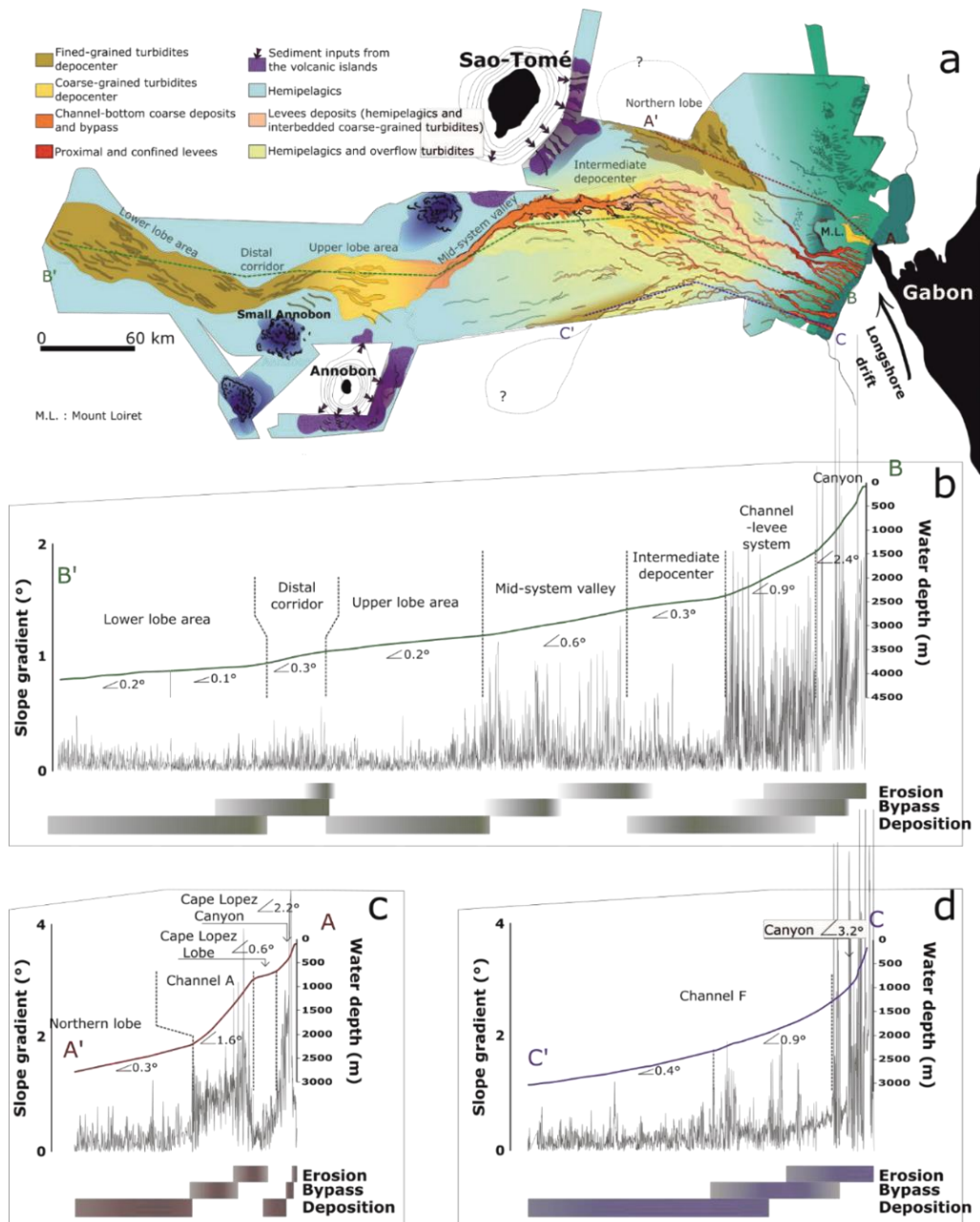


Figure 1.25. (a) Map of the architecture and sedimentary processes of the Ogooue Fan. (b, c, d) Longitudinal profiles along the northern, central, and southern parts of the Ogooue Fan. Note the correlation between the differences in slope gradient and sedimentary processes (Mignard et al., 2019).

Canyons formed in active margins are more abundant, shorter and steeper than canyons developed in passive margins (Figure 1.26; Sømme et al., 2009; Harris and Whiteway, 2011). Three major causes dictate the genesis of submarine canyons: 1) retrogressive slope failure (mass wasting events), 2) prolonged erosion from sediment gravity flows, and 3) subaerial erosion during low sea levels (Farre et al., 1983; Pratson et al., 1994; Pratson and Coakley, 1996; Fagherazzi, 2004; Piper and Normark, 2009).

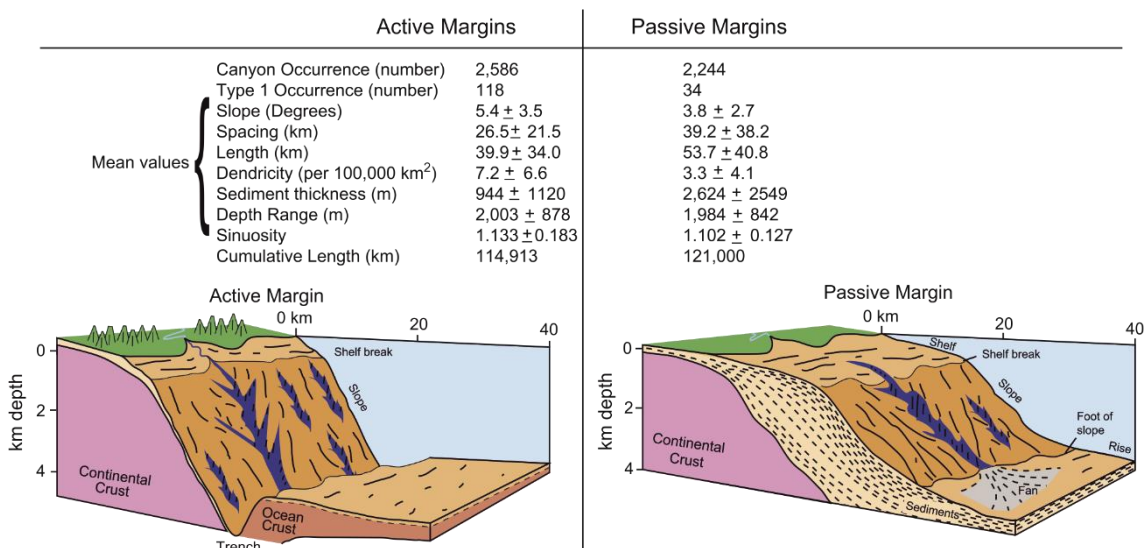


Figure 1.26. Compilations of features and cartoons illustrating differences between submarine canyons formed in active and passive margins (Harris and Whiteway, 2011).

Most sediment gravity flows do not maintain their efficiency for long, dissipating before arriving at downslope geomorphic elements (Howell and Normark, 1982; Paull et al., 2005; Talling et al., 2015). The amount of sediment that exits the canyons and is delivered to deeper-water areas depends on factors such as if canyons are shelf incised or not (shelf incising or blind *sensu* Harris and Whiteway, 2011), the magnitude of the flows travelling across the canyon walls (Jobe et al., 2018) and the bathymetric connection to a major

fluvial system (Bourget et al., 2010; Harris and Whiteway, 2011). However, recent monitoring of turbidity currents in a canyon detached from land and related fluvial systems has revealed that sediment transport across the shelf might also play a key role in the downslope remobilisation of sediments (Heijnen et al., 2022). Canyon fills commonly shows coarse-grained sandstones and conglomerates indicative of bypassing flows and fine-grained deposits derived from mass wasting of the canyon walls (Millington and Clark, 1995; Paull et al., 2005; Anderson et al., 2006). Monitoring of sediment gravity flows within submarine canyons during the last decade has expanded our limited knowledge of their morphodynamics (Figure 1.27; Azpiroz-Zabala et al., 2017; Symons et al., 2017; Paull et al., 2018; Pope et al., 2022) and recurrence (Paull et al., 2014; Hughes Clarke, 2016; Heijnen et al., 2022; Pope et al., 2022).

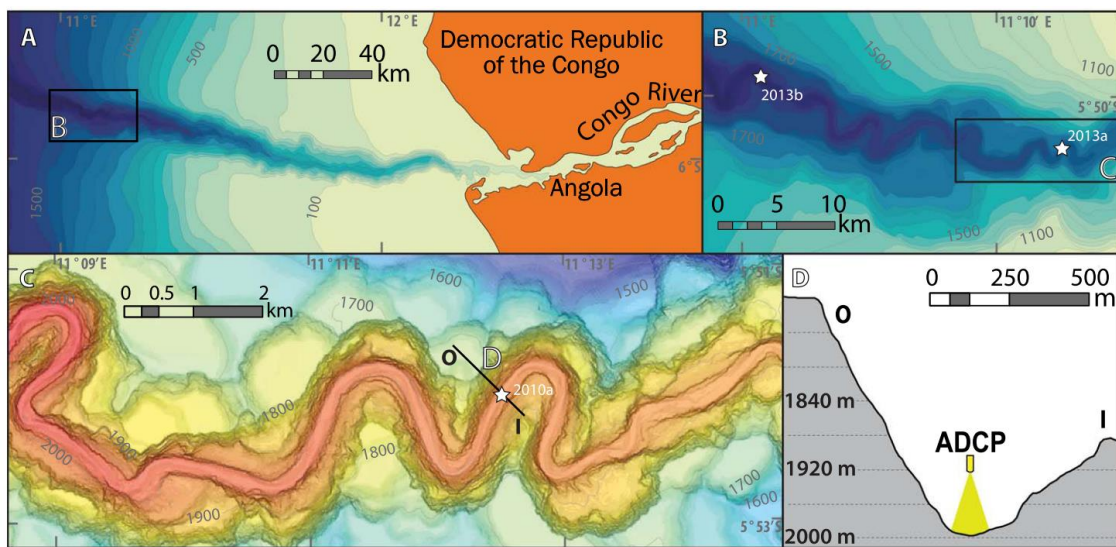


Figure 1.27. Bathymetric map of the Congo Canyon (Azpiroz-Zabala et al., 2017).

1.6.2. Channels

Submarine channels are negative relief geomorphic elements developed down-dip from submarine canyons (Figure 1.25 and Figure 1.27) and act as long-term conduits for the downdip transport of particulate matter (Normark, 1978; Piper and Normark, 1983; Beaubouef and Friedmann, 2000; Peakall et al., 2000; Mayall and Stewart, 2000; Kneller,

2003; Gee and Gawthorpe, 2006; Kane et al., 2007; McHargue et al., 2011; Kane and Hodgson, 2011; Hubbard et al., 2014; Kane and Clare, 2019; McArthur et al., 2019; Kneller et al., 2020). The onset of submarine channels is characterised by a period of erosion in the slope, which is the product of successive erosive turbidity currents (Figure 1.28; Sylvester et al., 2011; Hodgson et al., 2016) or single events (e.g. Elliott, 2000; Dakin et al., 2013).

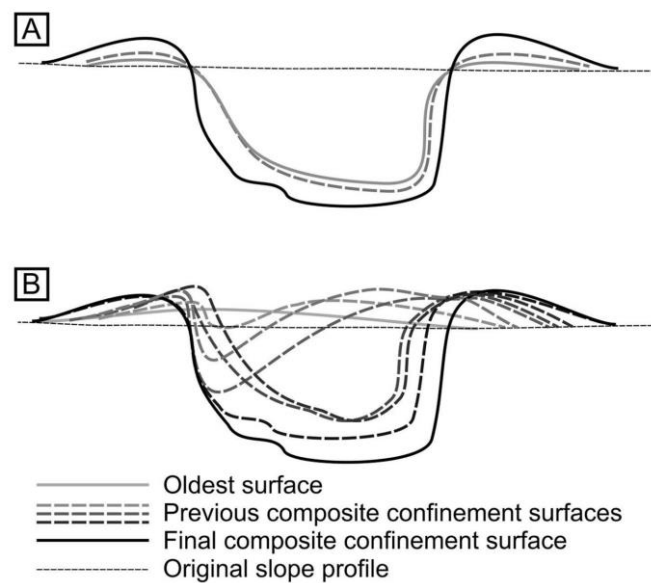


Figure 1.28. Cartoons highlight the difference between (A) instantaneous confinement and (B) progressive confinement in submarine channels (Hodgson et al., 2016).

Channels are characterised by the interplay between simultaneous erosion across different scales (Buffington, 1952; Menard, 1955; Normark, 1970; Millington and Clark, 1995; Skene et al., 2002; Kane and Hodgson, 2011; McHargue et al., 2011; Sylvester et al., 2011; Hubbard et al., 2014; Vendettuoli et al., 2019). Therefore, a hierarchical framework is commonly used based on the bounding surfaces of stratal packages of variable thickness and geometries (Figure 1.29; Sprague et al., 2005; Di Celma et al., 2011; McHargue et al., 2011; Macauley and Hubbard, 2013). The fundamental building block of a submarine channel is a 'channel element' (McHargue et al., 2011; Macauley and Hubbard, 2013) or 'storey' (Sprague et al., 2005) following the hierarchical classification

of fluvial systems (Friend et al., 1979). These primary architectural blocks can be tens to a few hundred meters wide and a few tens of meters thick (Figure 1.29; e.g. Hubbard et al., 2014). Channel elements are subdivided into sub-environments of deposition: channel axis, channel off-axis and channel margin (Figure 1.29; e.g. Hubbard et al., 2014). The channel axis can comprise a wide range of deposits such as matrix-supported conglomerates (debrites), clast-supported conglomerates and mudstone clast horizons (lag deposits), thin- and thick-bedded sandstones (high- and low-density turbidites) (Mayall et al., 2006; Bell et al., 2018). In contrast, the channel margin is dominated by thin-bedded siltstones and sandstones (low-density turbidites) (Hubbard et al., 2014). The channel off-axis is a mixture between both end members, dominated by thin- to thick-bedded sandstones. This wide range of deposits indicates the dynamic flows and environments that produce channel elements. Correlating event beds from channel axis to margin is not straightforward due to scouring and the general dynamic nature of this environment (e.g. Hubbard et al., 2020). Channel elements are bounded by flanking stratal packages (Hübscher et al., 1997; Deptuck et al., 2003; Hansen et al., 2015) named internal levees if they have a wing-style architecture (Figure 1.30; *sensu* Kane and Hodgson, 2011) or depositional terraces if they comprise sheet-like geometries (Figure 1.31; Hansen et al., 2015, 2017a, 2017b). The stacking of several genetically related channel elements forms a channel complex, and two or more genetically related channel complexes form a channel-complex set (Abreu et al., 2003; Samuel et al., 2003; Sprague et al., 2005; McHargue et al., 2011; Macauley and Hubbard, 2013). A channel-complex set is comprised of a channel belt, where the channel complexes are contained, bound by wedge-shaped flanking stratal packages which thin laterally away from the channel belt (Piper et al., 1999; Posamentier, 2003), named external levees (Figure 1.30; *sensu* Kane and Hodgson, 2011) or by a master erosional surface (e.g. Kneller et al., 2020).

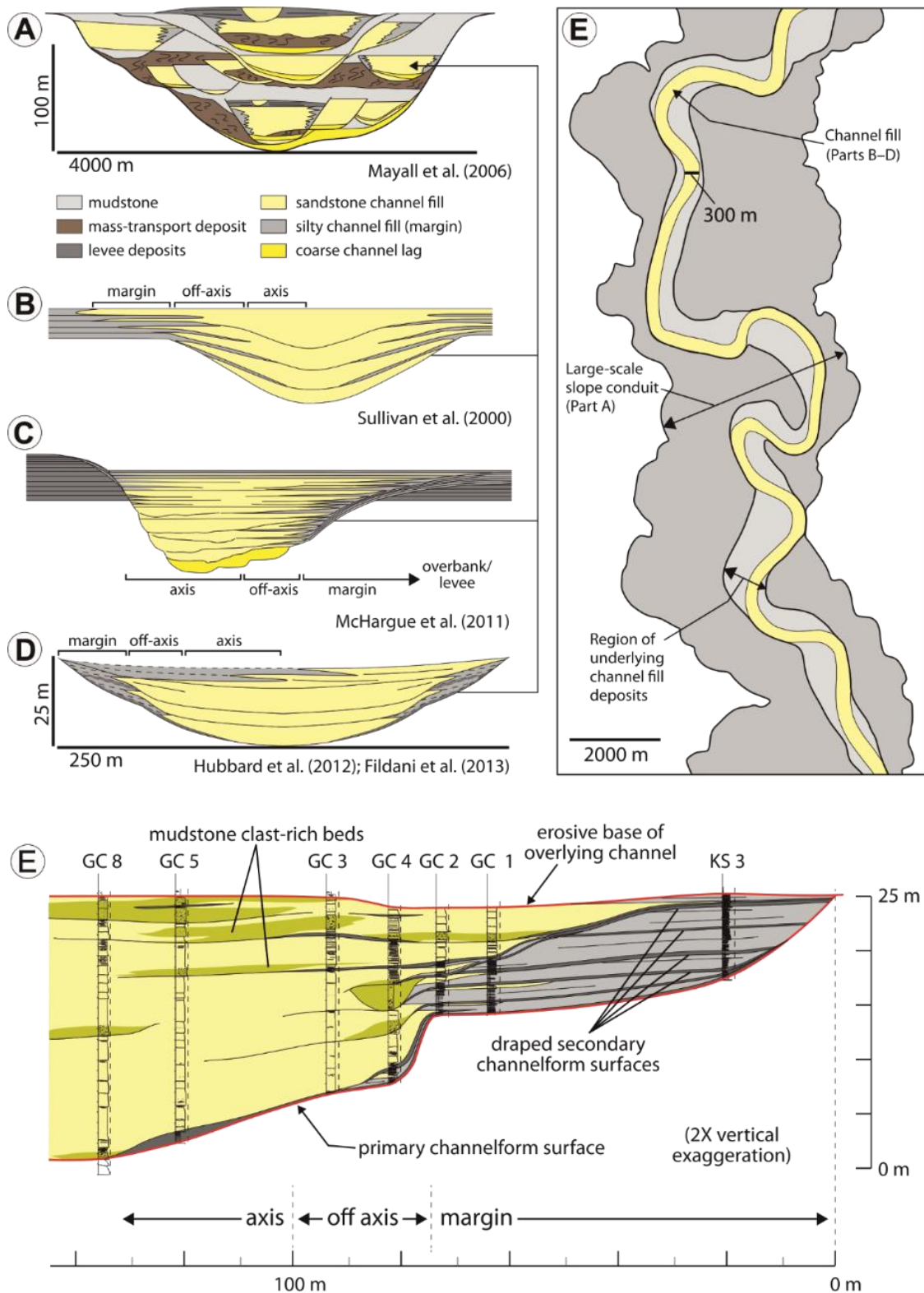


Figure 1.29. Two-dimensional schematic cross-sections and a map view of channelform sedimentary bodies common in slope strata emphasise a broad range of scales. (A) multiple channel elements and submarine landslide deposits form several channel complexes contained inside the channel belt of a channel complex set. (B–D) Examples of individual channel elements are generally less than 300 m wide and 30 m thick. (E). Two-dimensional cross-sections show the facies and architecture of a channel element. (F) Planform view of channel complex set (Hubbard et al., 2014).

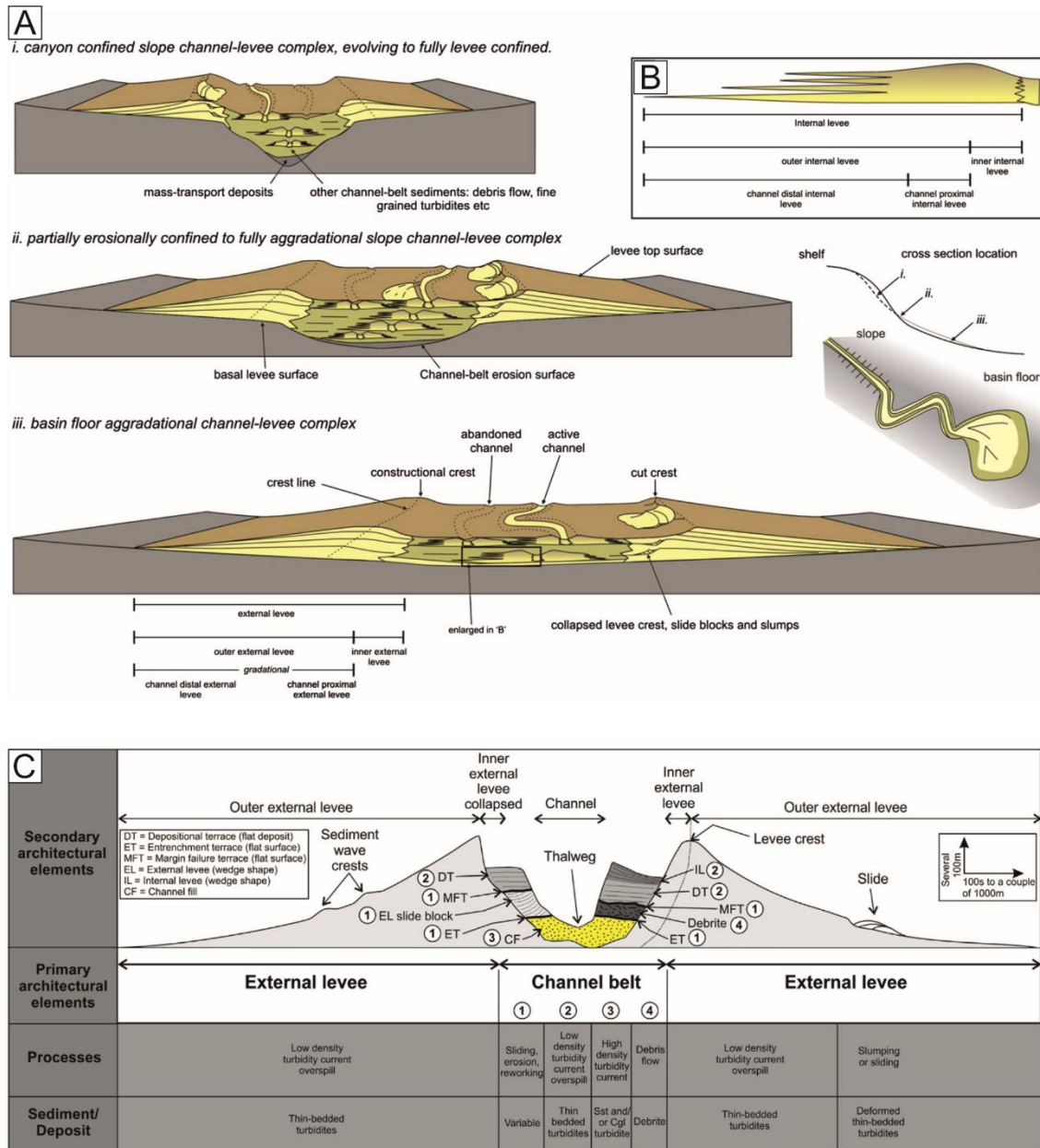


Figure 1.30. (A) Schematic diagram showing channel-levee morphology and nomenclature for levee subenvironments. (B) Nomenclature of internal levees (Kane and Hodgson, 2011). (C) Channel-levee cross-section comprising depositional terraces (Hansen et al., 2015).

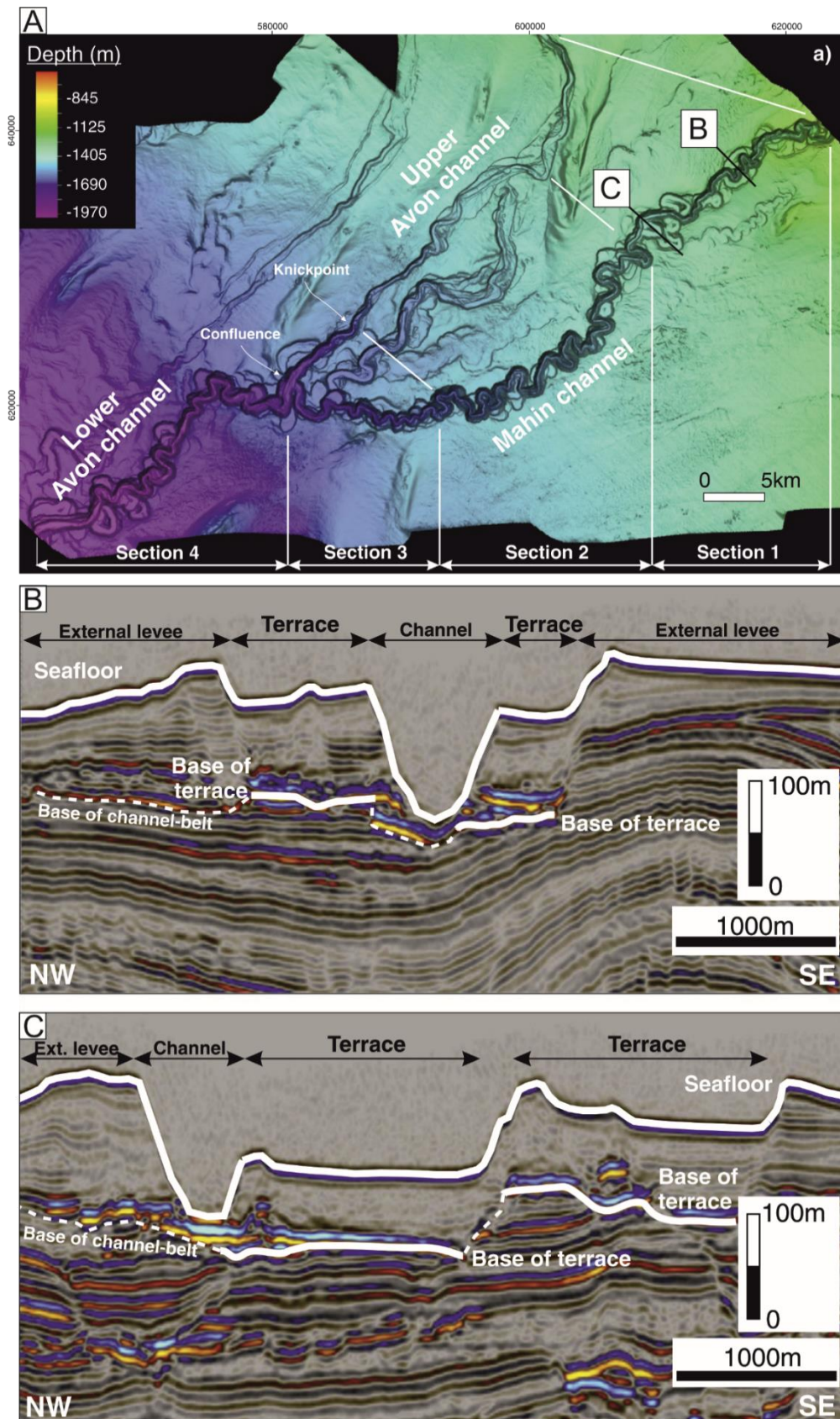


Figure 1.31. (A) Bathymetric map of the seafloor showing submarine channels morphology. (B and C) Cross-sections show the active channel and the depositional terraces. The location of seismic lines is indicated in (A). The dashed lines indicate the channel-belt base (Hansen et al., 2017a).

1.6.3. Channel-lobe transition zones (CLTZs)

Channel-lobe transition zones (CLTZs) represent intermediate geomorphic elements bridging well-developed channels and lobes (Mutti and Normark, 1987). The development of channel-lobe transition zones coincides with two morphological transitions: a reduction in seafloor gradient (slope break) and a loss of lateral confinement associated with the channel mouth (Figure 1.32A; Mutti and Normark, 1987; Wynn et al., 2002). At channel mouths, sediment gravity flows undergo expansion and deceleration, producing areas dominated by a complex interplay between erosion, bypass and deposition (Figure 1.32A; Wynn et al., 2002; Ito, 2008; Macdonald et al., 2011; Hofstra et al., 2015; Maier et al., 2018, 2020). Erosion in channel-lobe transition zones has been largely attributed to the reduction of slope gradient and subsequent hydraulic jump generation (Garcia and Parker, 1989). However, recent flow modelling suggests that expansion and lowering of maximum velocity at channel mouth settings (Figure 1.32B) could also be a primary mechanism (flow relaxation *sensu* Pohl et al., 2019).

Deposition in channel-lobe transition zones is characterised by 10s to 100s m long sediment waves and 10s metres deep and 100s metres long scour-fills (Figure 1.32A; Wynn et al., 2002; Fildani and Normark, 2004; Tudor, 2014; Hofstra et al., 2015; Pemberton et al., 2016; Maier et al., 2018; Droz et al., 2020; Hodgson et al., 2022). Channel-lobe transition zones have been recognised in the subsurface (Morris et al., 1998; Wynn et al., 2002; Droz et al., 2020) and in outcrop-based studies (Van der Merwe et al., 2014; Hofstra et al., 2015; Henstra et al., 2016; Brooks et al., 2018b, 2022; Navarro and Arnott, 2020; Mansor and Amir Hassan, 2021). However, channel-lobe transition zones are characterised by a low preservation potential due to cannibalisation and prograding submarine channels (e.g. Pemberton et al., 2016).

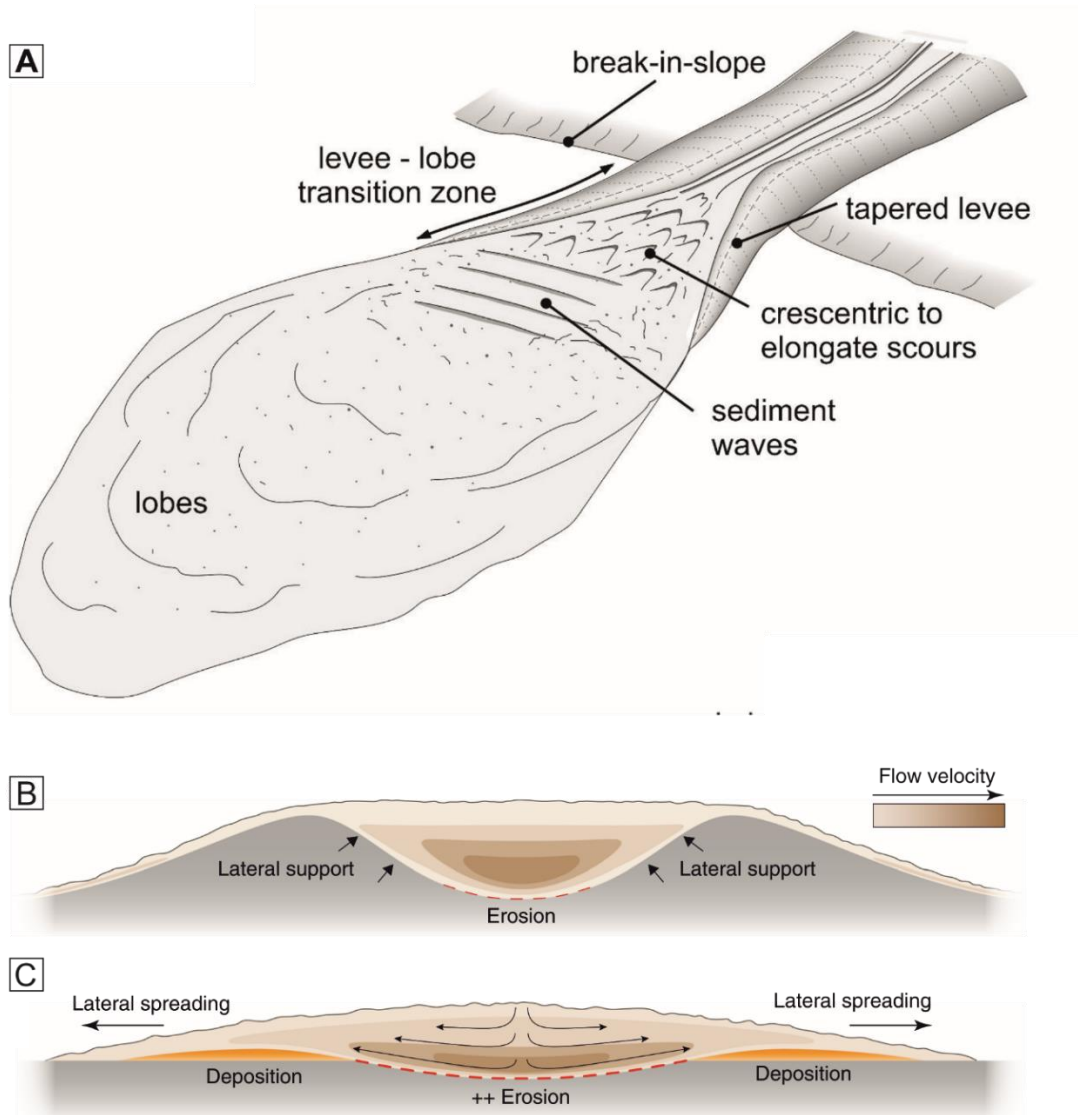


Figure 1.32. Schematic representation of (A) a channel-lobe transition zone (Hodgson et al., 2022). (B) Gravity flow is confined within a channel, and (C) flow-relaxation after lateral spreading and thinning lowers the maximum velocity towards the substrate, causing erosion (Pohl et al., 2019).

1.6.4. Submarine lobes

Submarine lobes represent a major component of submarine fans (Figure 1.24). They are built from the deposition of radially-spreading and decelerating sediment gravity flows that previously bypassed submarine canyons, channels and channel-lobe transition zones (Normark, 1978; Posamentier and Walker, 2006). Advances in the resolution of sonar (e.g. Twichell et al., 1995; Machado et al., 2004) and seismic-reflection dataset (e.g. Gervais et al., 2006) provided valuable information about the depositional finger-like

architectures within lobes rather than the previously thought sheet-like geometry ('sheets sands' *sensu* Shanmugam and Moinola, 1988).

Commonly submarine lobes are classified depending on their position with respect to the slope. Terminal lobes are deposited beyond the slope break on the basin floor (Shanmugam and Moinola, 1991; Jegou et al., 2008; Sømme et al., 2009; Prélat et al., 2010), while transient intraslope lobes are developed on relatively flat areas (Figure 1.25, Figure 1.33 and Figure 1.34) within irregular slopes product of mud and salt diapirism, faulting, submarine landsliding or differential compaction (Adeogba et al., 2005; Deptuck et al., 2008; Oluboyo et al., 2014; Spsychala et al., 2015; Jobe et al., 2017; Dodd et al., 2019; Mignard et al., 2019; Privat et al., 2021). Overall, terminal lobes are commonly an order of magnitude larger than intraslope lobes (Shanmugam and Moinola, 1988; Sømme et al., 2009; Prélat et al., 2010; Spsychala et al., 2015).

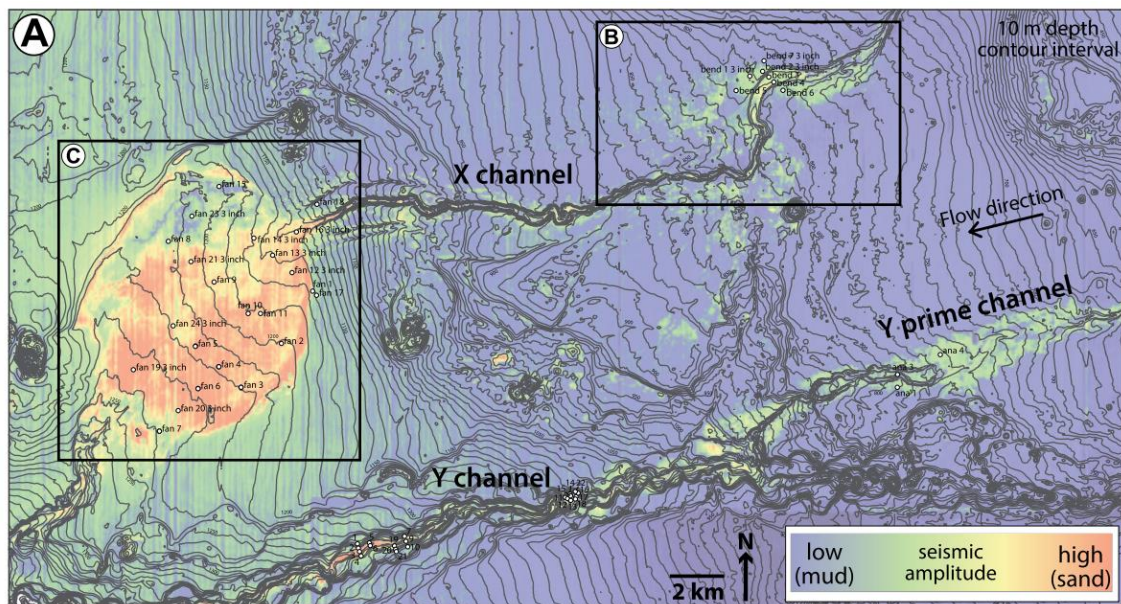


Figure 1.33. Intraslope lobe development on out-of-grade areas in a steeped slope. Bathymetric map (10 m contour interval) and seismic amplitude (colour) of the seafloor on the western Niger Delta continental slope. Note the development of the intraslope lobe on the flat in the north while the channel in the south does not develop any intraslope lobe due to constant gradient (Jobe et al., 2017).

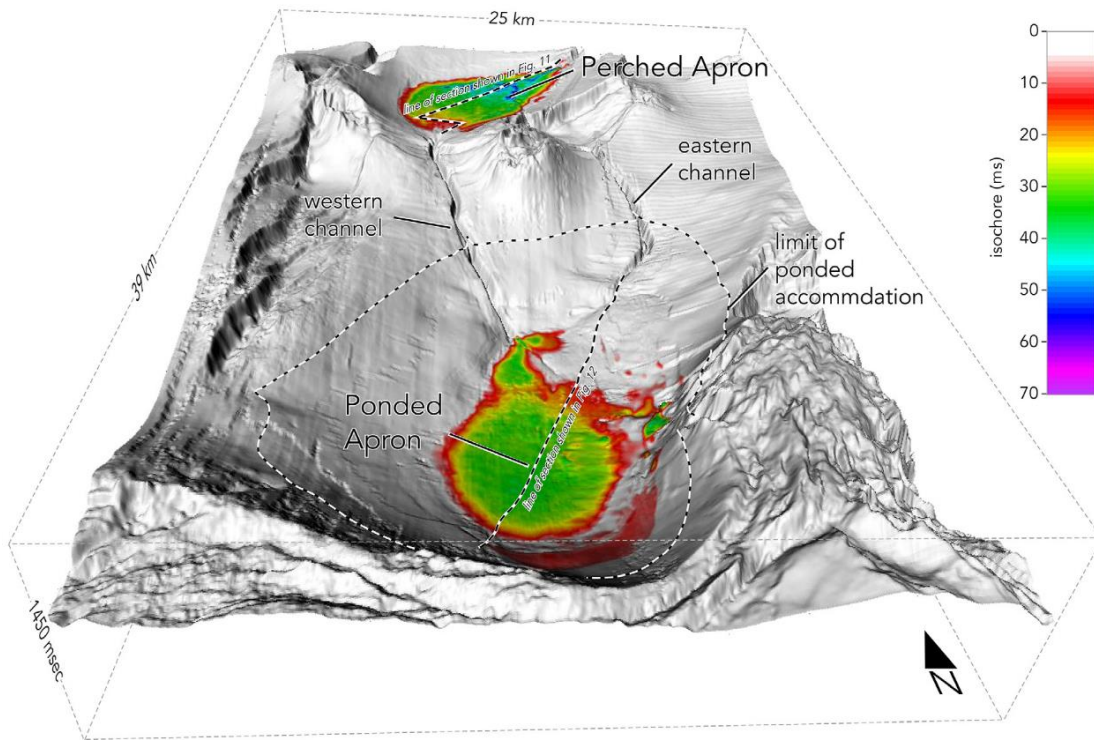


Figure 1.34. Perched and ponded intraslope lobes on the Brazos-trinity basin, Gulf of Mexico (Prather et al., 2017).

Similarly to submarine channels, a hierarchical framework refers to submarine lobes (Gervais et al., 2006; Pr elat et al., 2009; Mulder and Etienne, 2010; Sweet et al., 2020). Following the hierarchical scheme and nomenclature (Figure 1.35) of the field-based study of Pr elat et al. (2009), the fundamental building block is the event bed. Stacked event beds bounded by < 0.02 m silty intervals called 'interlobe elements' form lobe elements (2 m thick), whereas two or more genetically related lobe elements form a lobe (5-10 m thick, 30 km long), bound by < 2 m thick siltstone-prone unit called 'interlobes'. Genetically related lobes stack to form a lobe complex (10's m thick, 10's km long), bound at their base and top by < 0.5 m thick claystone named 'interlobe complex'. Recent sedimentological work on the claystones of the interlobe complexes has shown that they can represent event beds of the distal or lateral equivalents of lobes deposited elsewhere (Boulesteix et al., 2020).

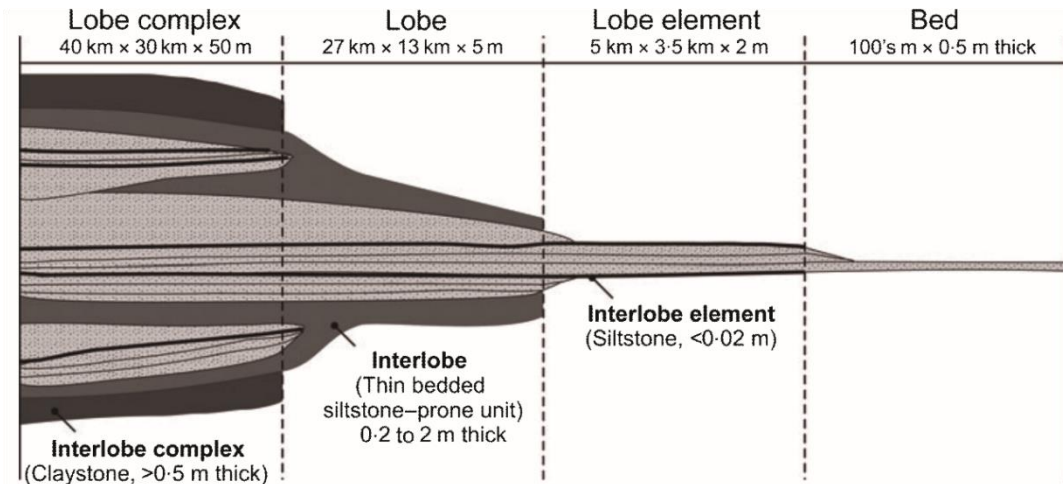


Figure 1.35. The hierarchical scheme of Prélat et al. (2009) recognises four scales of elements: bed, lobe element, lobe and lobe complex.

The study of the stacking patterns of lobes provides information about the bathymetrical configuration of the receiving basin (Figure 1.36). In unconfined settings such as flat basin floors, lobes show a compensational stacking pattern, depositing lobes where the depositional relief of the previous lobe is thinnest and the accommodation space largest (Figure 1.37; Mutti and Sonnino, 1981; Gervais et al., 2006; Prélat et al., 2009). In confined settings, the compensation of lobes is hindered by the limited available accommodation, and they typically show an aggradational stacking pattern (Marini et al., 2015), and sheets can be developed instead of lobes (Liu et al., 2018; Tóké & Patacci, 2018). Additionally, when a simultaneous juxtaposition and advancement or back-stepping of a lobe over an older one is developed, the term longitudinal stacking pattern is used (Figure 1.36; progradational or retrogradational, respectively). Progradational stacking is linked to increased sediment supply, tectonic tilting and/or smoothing of the seafloor relief (Grundvåg et al., 2014 and references therein), while retrogradational is commonly related to a reduction in sediment supply (Figure 1.36; Ferguson et al., 2020 and references therein). Furthermore, in nature, the stacking of lobes can show an intermediate behaviour between the end-member stacking patterns mentioned above

(semi-confined lobes; Marini et al., 2015; Dodd et al., 2019) or a dynamic behaviour during the lobe complex formation (Figure 1.36; progradational-aggradational-retrogradational stacking pattern; Hodgson et al., 2006).

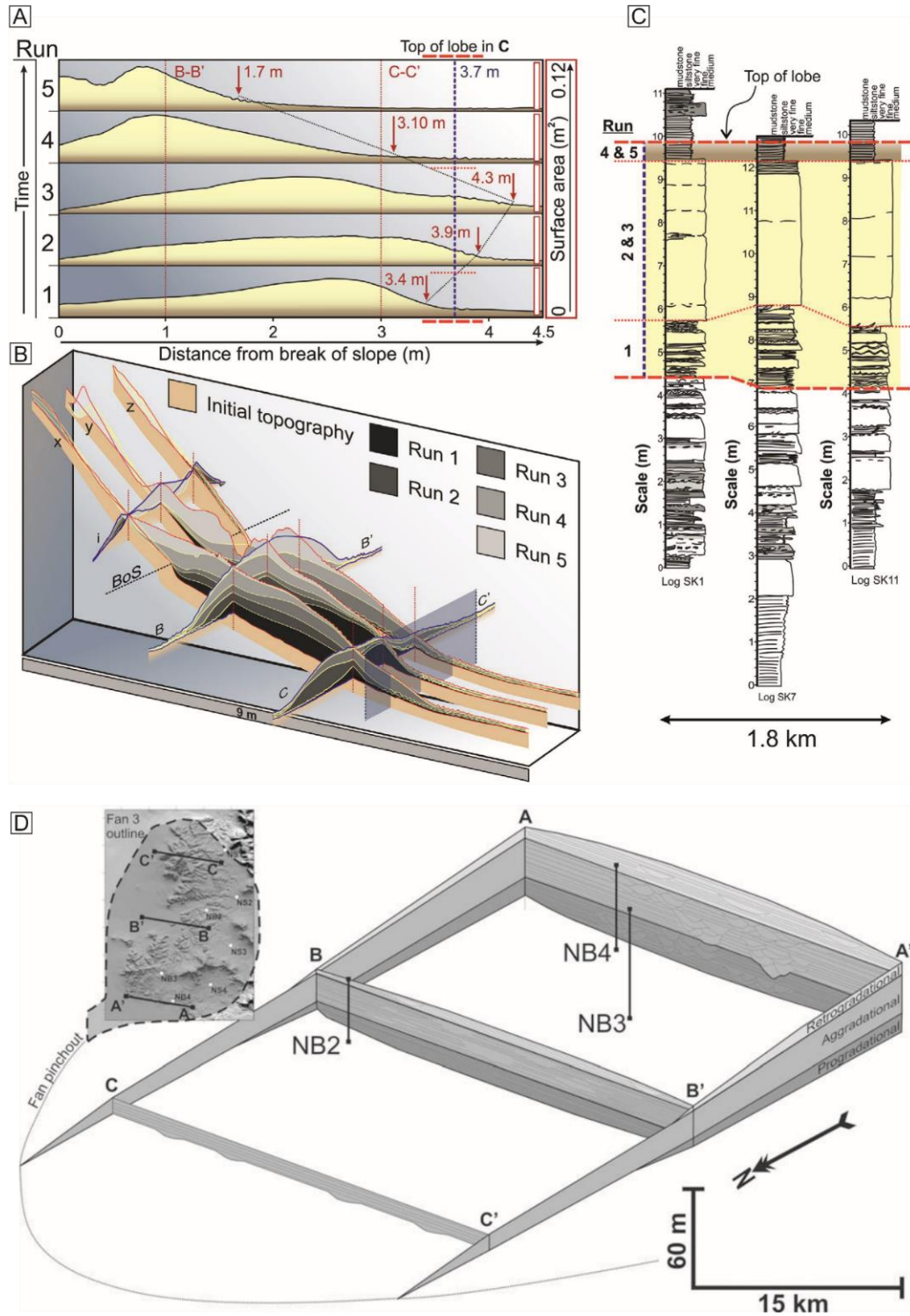


Figure 1.36. Progradational-aggradational-retrogradational stacking patterns of lobes. (A) and (B) Cross sections showing the architecture of the deposits after 5 runs within a flume-tank experiment. Mean discharge of each run is different: Run 1 (20 m³/hr), Run 2

(30 m³/hr), Run 3 (40 m³/hr), Run 4 (30 m³/hr), Run 5 (20 m³/hr). Note the progradational stacking pattern while the discharge increases in contrast to the retrogradational stacking pattern developed when the discharge decreases. (C) Modified interpretation from the correlation in Kane et al. (2017) suggests that the uppermost thin-bedded interval represents the back-stepping of Fan 3 (Ferguson et al., 2020). (D) Similar interpretation and stacking patterns of Fan 3 (Hodgson et al., 2006).

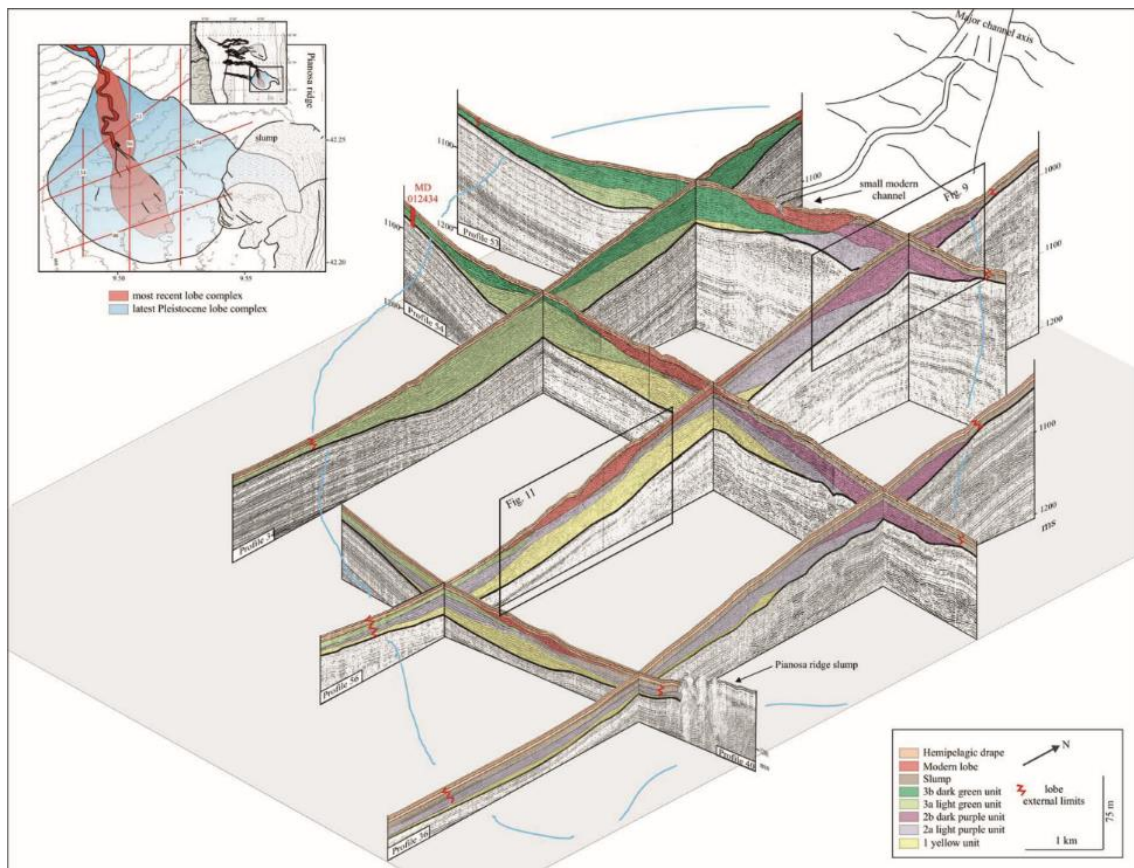


Figure 1.37. Seismic profiles illustrate the architecture of the latest Pleistocene lobe complex of the northern margin of East Corsica in a pseudo-three-dimensional view. Note the compensational stacking pattern of lobes in yellow, green and purple (Gervais et al., 2006).

Outcrop-based studies have enabled the characterisation of facies and facies association and relate them to lobe sub-environments such as lobe axis, lobe off-axis and lobe fringe (Figure 1.38; Pr elat et al., 2009; Grundv ag et al., 2014; Terlaky et al., 2016; Kane et al., 2017; Spychala et al., 2017b; Hansen et al., 2019). The lobe axis represents the most axial and proximal parts of the lobe (Figure 1.38). This environment often features the thickest

stratal packages, commonly dominated by thick-bedded, structureless and amalgamated sandstones (high-density turbidites). High-density turbidity currents escaping channel confinement spread radially and decelerate progressively. These energetic and turbulent flows commonly scour the substrate and entrain a substantial amount of substrate (Kane et al., 2017 and reference therein). Therefore, lobe axis high-density turbidites commonly show erosive bases and mudstone clasts distributed along amalgamation surfaces or throughout their vertical profile (Prélat et al., 2009; Grundvåg et al., 2014; Dodd et al., 2019). The lobe axis transitions into the lobe off-axis (Figure 1.38). A range of structured thin- to thick-bedded sandstones of variable matrix content indicate the development of internal stratification and rheologies within the flows (or parts of) bypassing the lobe axis. Entrainment of clay from erosive high-density turbidity currents in up-dip areas and mudstone clasts disaggregation promote the formation of oversaturated and cohesive flows (transitional flows; Haughton et al., 2009; Kane and Pontén, 2012; Kane et al., 2017) that could not transport their sediment load to distal parts of the lobe, promoting capacity-driven deposition (Hiscott, 1994). In contrast, low-density turbidites indicate deposition under relatively low- to moderate aggradation rates and tractional reworking (e.g. Jobe et al., 2012), revealing more stable flow conditions than denser flows (Al Ja'Aidi et al., 2004). Lobe off-axis transitions into lobe fringe, representing the most distal lobe sub-environment (Figure 1.38). Lobe fringe comprises thin-bedded heterolithic packages with a rare bed amalgamation product of the deposition of flows (or parts of) that bypasses the lobe axis and off-axis. This lobe sub-environment is often subdivided into lateral or frontal lobe fringes. Lateral fringes are dominated by thin-bedded structured sandstones (low-density turbidites) as a result of the lateral spreading and deceleration of low-density turbidity currents (Spychala et al., 2017b and references therein). In contrast, frontal lobe fringes comprise a prevalence of argillaceous sandstones (hybrid event beds)

over low-density turbidites (Figure 1.38; Kane et al., 2017; Southern et al., 2017; Spychala et al., 2017b).

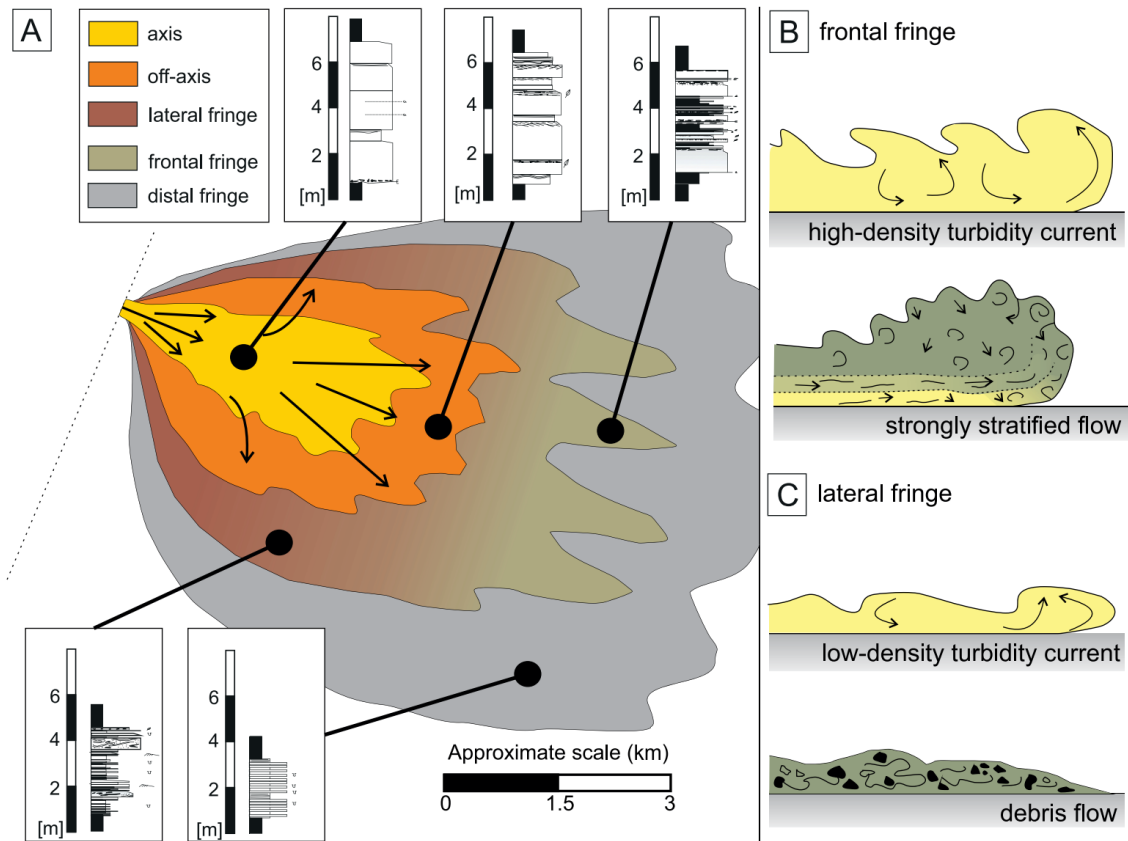


Figure 1.38. A schematic diagram on a plan view of a terminal lobe illustrates lobe sub-environments' distribution and facies associations (see logs). Schematic diagram showing some dominant flow processes in lobe (B) distal and (C) lateral fringes (Spychala et al., 2017b).

This review has highlighted the natural variability of deep-marine sedimentary systems and some key research that has been fundamental to our understanding of these systems. This wealth of previous research shows the evolution of our understanding through time, recently driven by major new insights into modern deep-marine systems and provides the necessary context for the following chapters.

2. Rationale

In this chapter, I will highlight the main research question that motivated this research and each of the chapters (see colored squares in Figure 2.1). Furthermore, the three data chapters (Chapters 3-5) are linked to each other by a series of common objectives (see bullet points in Figure 2.1)

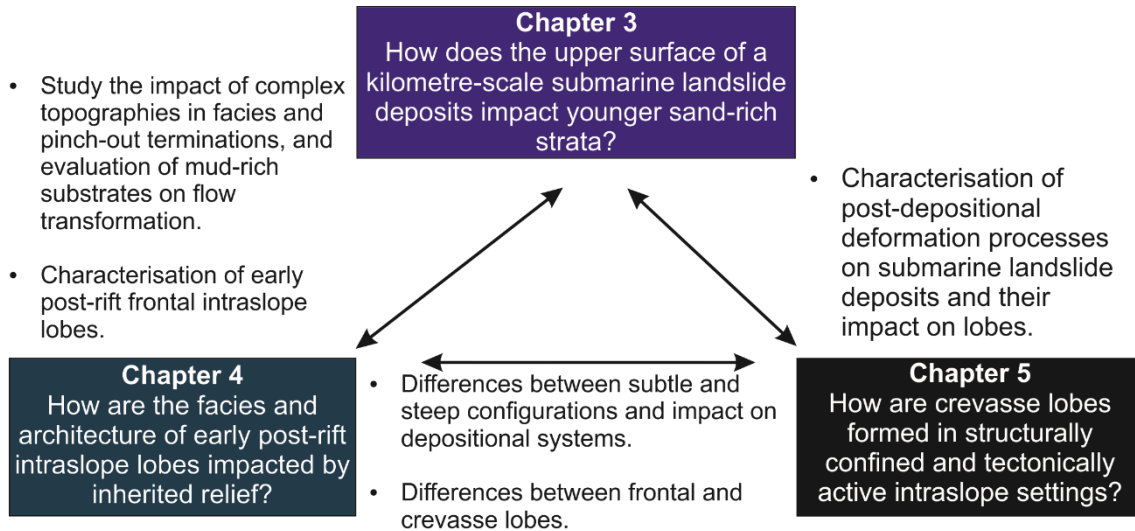


Figure 2.1. Diagram illustrating the main research question and the common objectives that link the different chapters.

2.1: How do submarine landslide deposits impact younger depositional systems?

Submarine landslide deposits can form from individual catastrophic emplacement events (Pelinovsky and Poplavsky, 1996; Nisbet and Piper, 1998; Fryer et al., 2004), from multiple mass failure episodes (e.g. Sobiesiak et al., 2016), or from slow-moving and long-lived motion (creeping; Butler and McCaffrey, 2010). Submarine landsliding is an effective mechanism for accommodation creation on continental slopes (e.g. Fairweather, 2014; Ortiz-Karpf et al., 2015; Kneller et al., 2016) because their deposits can produce gentler slope profiles than the equilibrium slope profile (Figure 2.2; Kneller, 2003; Kneller et al., 2016). Several features mark the upper surfaces of submarine landslides,

such as slide scars (Bugge et al., 1987; Moscardelli and Wood, 2008), megaclasts (Jackson, 2011; Nwoko et al., 2020a) and pressure ridges (Bull et al., 2009), developing complex seabed topography along their upper surfaces (Figure 2.2; e.g. Kneller et al., 2016). As turbidity currents are highly sensitive to topography, relief associated with submarine landslide deposits will dictate the sediment routing patterns, deposit distribution, and architecture (Kneller et al., 2016). Understanding this interaction is necessary to further evaluate the implications for deposition and burial of sediments and organic carbon, potential hydrocarbon reservoir development, and future carbon storage places.

While the kinematics and evolving morphology along the basal shear surface of submarine landslides have been the focus of several studies (Lucente and Pini, 2003; McGilvery and Cook, 2003; Moscardelli and Wood, 2008; Bull et al., 2009; Dykstra et al., 2011; Posamentier and Martinsen, 2011; Dakin et al., 2013; Sobiesiak et al., 2018), the dynamic evolution of the upper surface is less documented and understood. Furthermore, submarine landslide deposits can evolve through post-depositional deformation processes, which produce highly dynamic and inherently complex interactions with younger depositional systems (Butler and McCaffrey, 2010). Identifying upper kinematic boundary layers to submarine landslides is important because this will influence the behaviour of subsequent sediment gravity flows in more complex ways than simple passive healing of topography (Sinclair and Tomasso, 2002; Smith, 2004a). In addition, this may suggest that inferring emplacement processes from the relief of submarine landslides exposed on the seabed may be inappropriate if there has been significant and/or long-term modification of the top surface morphology.

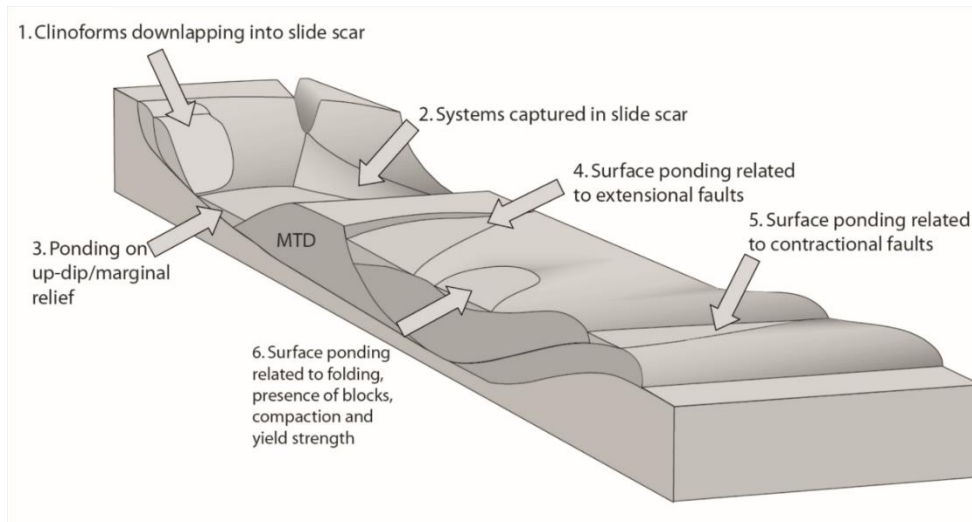


Figure 2.2. Schematic diagram illustrating styles of accommodation associated with MTDs (Kneller et al., 2016).

Due to the variable resolution of seismic reflection data and uncertainty of core-scale observations, it is not straightforward to differentiate syn- from post-depositional processes in subsurface examples. Here, I will use exhumed ancient systems with the aim of expanding the knowledge of the mechanisms responsible for the generation of relief on top of submarine landslide deposits, with a special emphasis on the post-depositional deformation processes along a dynamic upper surface, by investigating an exceptionally well-exposed axially-emplaced 9.6 km long debrite on an outcrop belt in Chacay Melehue Graben in West Central Argentina (Chapter 3). This investigation is augmented by a complementary study of a range of transversely-emplaced submarine landslide deposits in the exhumed Middle Eocene strata of the Banastón deep-water system in the Aínsa Basin, NE Spain (Chapter 5).

2.2 Are all intraslope lobes made equal?

Many ancient and modern continental slopes show stepped profiles (Pirmez et al., 2000; Prather et al., 2012), differing from 'simple' slope profiles characterised by gradual gradient changes (Brooks et al., 2018c). Apart from the mass wasting processes

mentioned in the previous section, several other geological processes can modify seafloor relief, such as tectonism (Sinclair and Tomasso, 2002; Joseph and Lomas, 2004), salt diapirism (Hodgson et al., 1992; Prather et al., 1998, 2017; Oluboyo et al., 2014) and mud diapirism (Prather et al., 2012; Jobe et al., 2017). Stepped slopes are characterised by higher gradient areas ($< 3^\circ$; ramps) and relatively low gradient areas ($< 0.2^\circ$; flats) (Barton, 2012; Deptuck et al., 2012; Hay, 2012; Jobe et al., 2017; Mignard et al., 2019). Changes in slope profile strongly affect the behaviour of sediment gravity flows, leading them to be more depositional in low gradient areas with subsequent development of intraslope lobes (Barton, 2012; Deptuck et al., 2012; Jobe et al., 2017) and more erosional and/or bypassing in higher gradient areas, associated with channel development (Barton, 2012; Hay, 2012; Wynn et al., 2012; Mignard et al., 2019). Therefore, the slope profile strongly controls the organisation of geomorphic elements down-dip (Figure 1.25). The abrupt modification of slope gradient is associated with localised erosional features such as knickpoint and spoon-shaped scours associated with channel-lobe transition zones (Kenyon et al., 1995; Wynn et al., 2002; Mignard et al., 2019) and in the distal end of the intraslope lobes (Figure 2.2; e.g. Deptuck et al., 2012; Jobe et al., 2017).

However, most studies are based on seafloor imagery and seismic-reflection datasets, with only limited information about the sub-seismic scale architectures and facies. Previous models of exhumed intraslope lobes highlight that they are smaller and comprise a higher sand percentage than terminal basin floor lobes (Figure 2.3; Figueiredo et al., 2010; Van der Merwe et al., 2014; Sychala et al., 2015; Brooks et al., 2018c). Developing accurate facies models is important because the sand-rich and proximal locations of intraslope lobes are targets for oil and gas reservoirs and will likely be targeted for carbon storage projects in the future. Therefore, understanding the range of

intraslope lobe types, and in particular, documenting their pinch-out configurations, will help to reduce risk and uncertainty in subsurface examples.

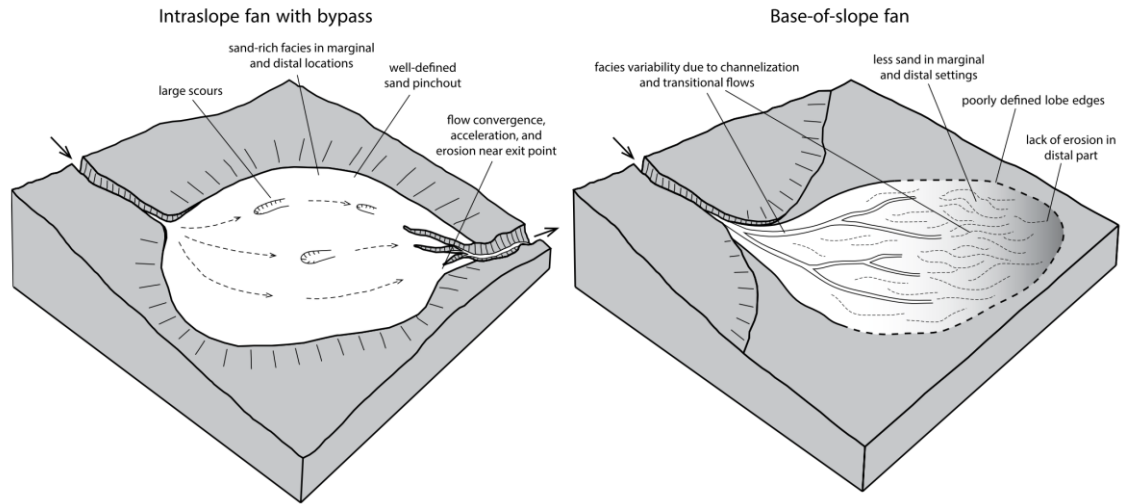


Figure 2.3. Schematic diagrams of an intraslope submarine fan (left) and base-of-slope submarine fan (right) highlight their differing geomorphological characteristics and facies distributions. Due to the bypass of muddy sediment and erosion at the distal parts of the intraslope step, intraslope submarine lobe deposits show more sand-rich facies architecture (left) than predicted by traditional base-of-slope lobe facies models (right) (Jobe et al., 2017).

These depositional models (e.g. Sychala et al., 2015; Jobe et al., 2017; Brooks et al., 2018c) associate the sandier nature of intraslope lobes (Figure 2.3 and Figure 2.4) with flow decoupling (Kneller and McCaffrey, 1999), where the concentrated basal divisions of high-density flow deposit sediment as a result of a reduction in slope gradient causing flow deceleration and loss of flow-capacity (Hiscott, 1994a). In contrast, the more dilute (parts of) flows transporting fine-grained sediments bypass basin-ward due to their higher flow efficiency (Stevenson et al., 2015). Current models also highlight the predominance of turbidites and the rare occurrence of transitional flow deposits (Figure 2.4; Sychala et al., 2015; Jobe et al., 2017). Structureless turbidites dominate the lobe axis, structured turbidites with abundant climbing-ripple lamination the lobe off-axis, and thin-bedded heterolithic packages the lobe fringe (Figure 2.4; Sychala et al., 2015; Brooks et al.,

2018c). The outcrop-based study documented in this thesis aims to broaden the scope of existing depositional models by studying the deposits and architecture of exhumed intraslope lobes in the Neuquén Basin (Argentina) from event bed- to lobe complex-scale in an early post-rift intraslope setting (Chapters 3 and 4).

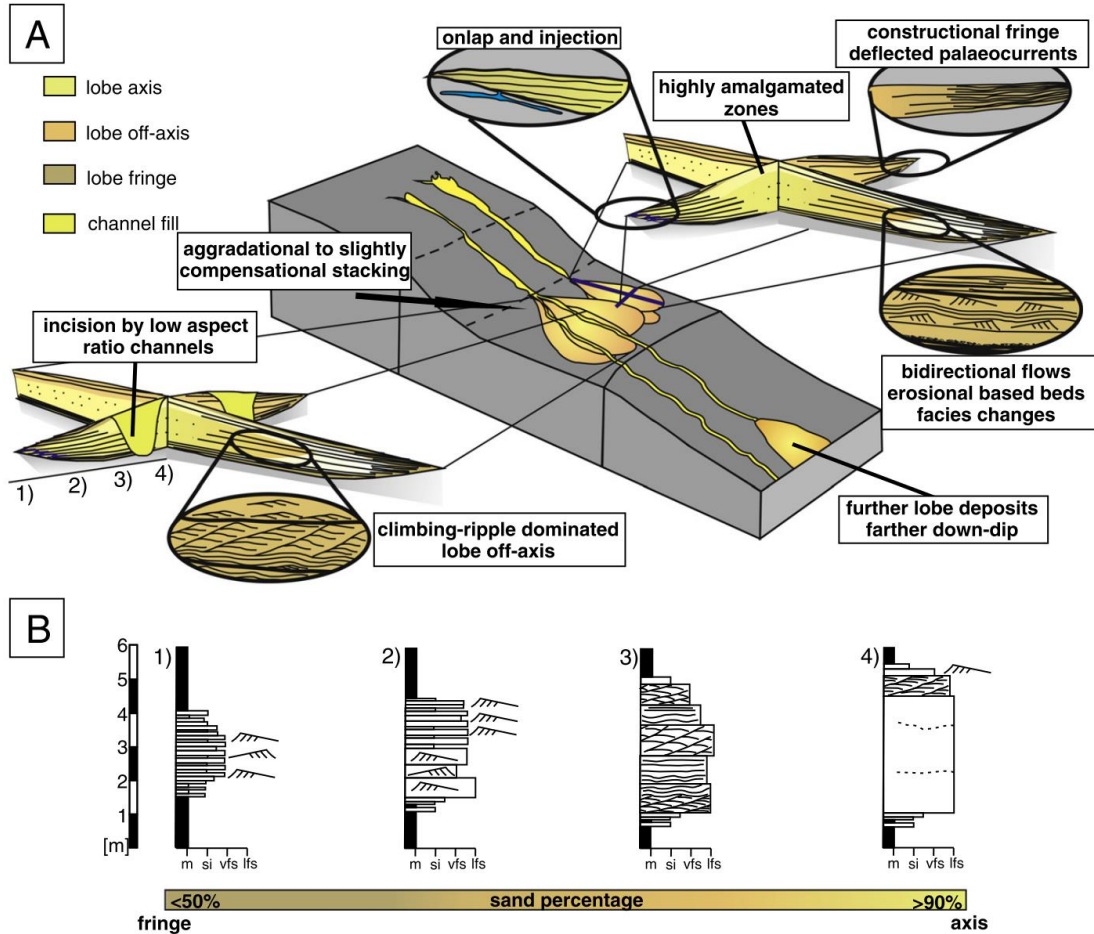


Figure 2.4. Block diagram showing the key recognition criteria for intraslope lobes according to Spychala et al. (2015). Compensational stacking patterns with a strong aggradational component; onlap terminations onto mud-prone slope combined with sandstone injectites; highly amalgamated deposits in lobe complex axis; lobe-off axis are dominated by climbing-ripple lamination; bidirectional ripple laminations dominate lobe fringes. Incision by their feeder channels as a result of the progradation and slope readjustment (B) Simplified logs of facies associations of intraslope lobes (Spychala et al., 2015).

2.3 How are crevasse lobes formed and preserved in structurally confined and tectonically active intraslope settings?

Crevasse lobes are important records of the morphodynamic evolution of submarine channels. Commonly, crevasse lobe development is linked to channel wall/ breaching on the outer bends of sinuous channels, which can ultimately result in avulsion of the channel system (Damuth et al., 1988; Posamentier and Kolla, 2003; Fildani and Normark, 2004; Armitage et al., 2012; Brunt et al., 2013; Maier et al., 2013; Morris et al., 2014a). Therefore, crevasse lobes can represent sand-rich bodies encased within fine-grained overbank deposits. Crevasse lobes could be targeted in exploration due to their connection to potential hydrocarbon-bearing channel belt sandstones, such as in the Puchkirchen foreland channel system (Figure 2.5; Molasse Basin, Austria), which represents the largest single-reservoir gas field in the basin (Haidach field; De Ruig and Hubbard, 2006; Hubbard et al., 2009). Crevasse lobes from the Puchkirchen channel system developed despite the limited accommodation space and the confinement exerted by the foreland basin's opposing lateral slopes (Figure 2.5; De Ruig and Hubbard, 2006; Hubbard et al., 2009).

Inspired by these studies based on seismic reflection datasets, Chapter 5 aims to investigate the bed-scale character of exhumed crevasse lobes in the Ainsa Basin (Spain) to improve our understanding of the relationship between active tectonism and crevasse lobe development and to assess whether these lobes are different to frontal lobes in intraslope settings (Chapters 3 and 4).

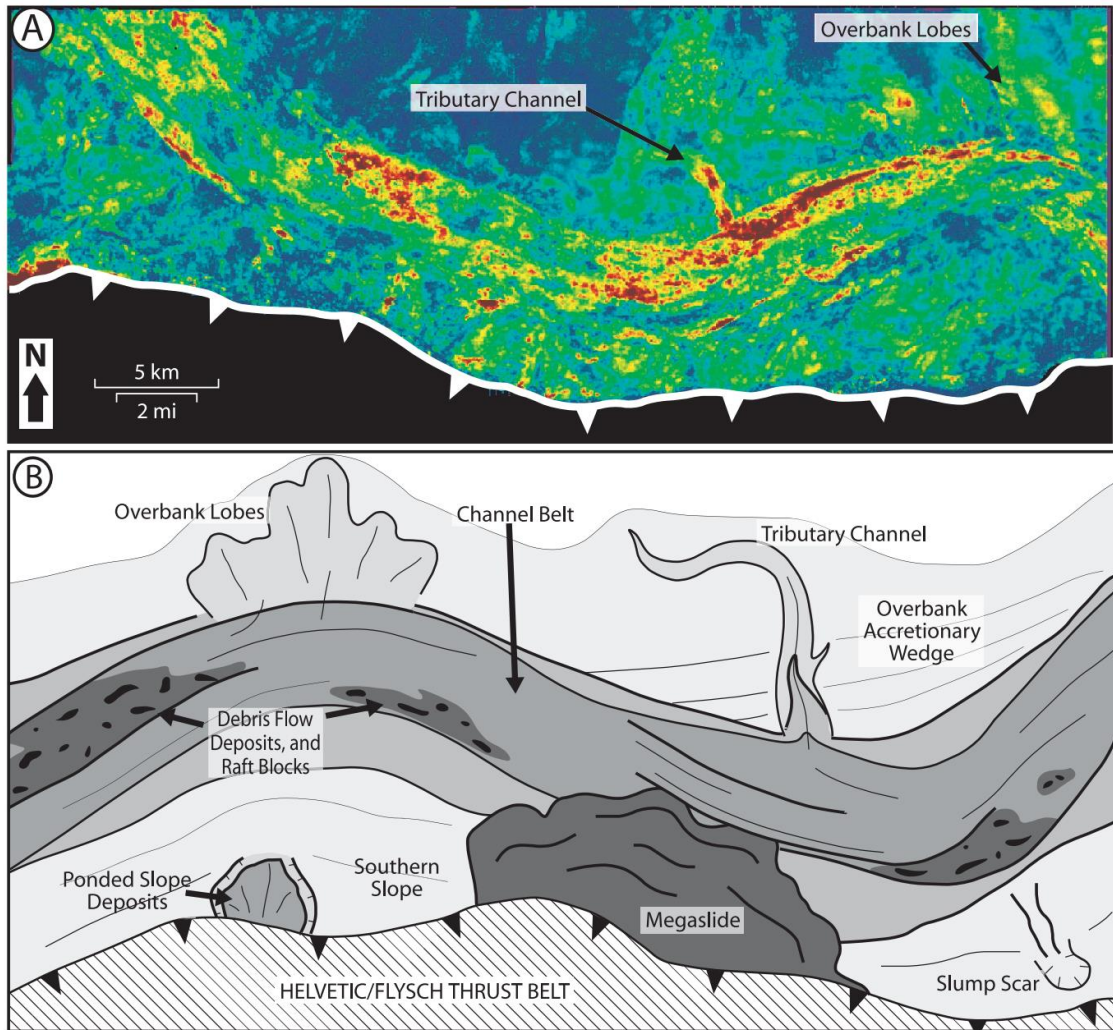


Figure 2.5. Seismic amplitude map of the Upper Puchkirchen interval. Note the high-amplitude of the W–E–trending channel belt with crevasse splay or overbank lobes on the outer bend of the main channel (top right) and small tributary channel (centre). Palaeoflow's direction was towards E. (B) A schematic diagram of the depositional system highlights the channel system's main elements in the Puchkirchen and basal Hall formations. The Channel belt is 3–5 km wide (De Ruig and Hubbard, 2006).

3. Substrate entrainment, depositional relief, and sediment capture: impact of a submarine landslide on flow process and sediment supply

Martínez-Doñate, A.¹, Privat, A. M-L. J.², Hodgson, D.M.², Jackson, C.A-L.¹, Kane, I.A.¹, Spychala, Y. T. ³, Duller, R.A.⁴, Stevenson, C.⁴, Keavney, E. ², Schwarz, E.⁵, Flint, S.S.¹

1. School of Earth and Environmental Sciences, University of Manchester, Manchester M13 9PL, UK.
2. School of Earth and Environment, University of Leeds, Leeds LS29JT, UK.
3. Institute for Geology, Leibniz University Hannover, Callinstraße 30, Hannover 30167, Germany.
4. Department on Earth, Ocean, and Ecological Sciences, University of Liverpool, 4 Brownlow Street, Liverpool L69 3GP, UK.
5. Centro de Investigaciones Geológicas (CIG), La Plata, Provincia de Buenos Aires, Argentina.

3.1 Abstract

Submarine landslides can generate complicated patterns of seafloor relief that influence subsequent flow behaviour and sediment dispersal patterns. In subsurface studies, the term ‘Mass Transport Deposit’ (MTD) is commonly used and covers a range of processes and resultant deposits. While the large-scale morphology of submarine landslide deposits can be resolved in seismic data, the nature of their upper surface and its impact on both facies distributions and stratal architecture of overlying deposits is rarely resolvable. However, field-based studies often allow a more detailed characterisation of the deposit. The early post-rift Middle Jurassic deep-water succession of the Los Molles Formation is exceptionally well-exposed along a dip-orientated WSW-ENE outcrop belt in the Chacay Melehue depocentre, Neuquén Basin, Argentina. Twenty-seven (27) sedimentary logs constrained by marker beds

were correlated to document the sedimentology and architecture of a > 47 m thick and at least 9.6 km long debrite, which comprises two different types of megaclasts. The debrite overlies ramps and steps, indicating erosion and substrate entrainment. Two distinct sandstone-dominated units overlie the debrite. The lower sandstone unit is characterised by: i) abrupt thickness changes, wedging and progressive rotation of laminae in sandstone beds associated with growth strata; and ii) detached sandstone load balls within the underlying debrite. The combination of these features suggests syn-sedimentary foundering processes due to density instabilities at the top of the fluid-saturated mud-rich debrite. The debrite relief controlled the spatial distribution of foundered sandstones. The upper sandstone unit is characterised by thin-bedded deposits, locally overlain by medium- to thick-bedded lobe axis/off-axis deposits. The thin beds show local thinning and onlapping onto the debrite, where it develops its highest relief. Facies distributions and stacking patterns record the progradation of submarine lobes and their complex interaction with long-lived debrite-related topography. The emplacement of a kilometre-scale debrite in an otherwise mud-rich basinal setting and accumulation of overlying sand-rich deposits suggests a genetic link between the mass-wasting event and transient coarse clastic sediment supply to an otherwise sand-starved part of the basin. Therefore, submarine landslides demonstrably impact the routing and behaviour of subsequent sediment gravity flows, which must be considered when predicting facies distributions and palaeoenvironments above MTDs in subsurface datasets.

3.2 Introduction

Submarine landslide deposits, or Mass Transport Deposits (MTDs) (Nardin et al., 1979), are sedimentary bodies that have been translated downslope from high to low gradient slopes as a result of mass failure and gravitational processes (Hampton et al., 1995; Moscardelli and Wood, 2008; Ogata et al., 2012; Festa et al., 2016; Kneller et al., 2016). The typically cohesive

nature of the flows enables the transportation of large clasts (> 4.1m; herein named megaclasts, *sensu* Blair and McPherson, 1999) (Labaume et al., 1987; Payros et al., 1999; McGilvery and Cook, 2003; Lee et al., 2004; Jackson, 2011; Ogata et al., 2012; Hodgson et al., 2019; Nwoko et al., 2020a). Megaclasts within MTDs are sourced either from headwall areas or entrained from the substrate (Festa et al., 2016; Ogata et al., 2019). These features, accompanied by syn- and post-depositional faulting (Dykstra, 2005; Dykstra et al., 2011), generate the topographically irregular upper surfaces of MTDs (Moscardelli et al., 2006; Bull et al., 2009).

Deep-water sediment gravity flows interact with the rugose topography of MTDs, which influences flow behaviour, deceleration and steadiness (Armitage et al., 2009; Jackson & Johnson, 2009; Fairweather, 2014; Ortiz-Karpf et al., 2015, 2017; Steventon et al., 2021), and therefore dispersal patterns and depositional architecture (Kneller et al., 2016). MTD surface relief has been shown to affect facies distribution and associated sedimentary architecture; this has been reported from both outcrop (Pickering and Corregidor, 2005; Armitage et al., 2009; Dykstra et al., 2011; Fallgatter et al., 2017; Valdez et al., 2019) and subsurface studies (Ortiz-Karpf et al., 2017; Nwoko et al., 2020b). However, MTDs may continue to deform after initial emplacement through creeping processes (e.g. Butler and McCaffrey, 2010) or secondary mass movements (Sobiesiak et al., 2016; Brooks et al., 2018a). Furthermore, the high water content within newly deposited MTDs promotes active dewatering at their upper surface (Mulder and Alexander, 2001; Talling et al., 2012; Browne et al., 2020) associated with local instabilities and movement (Iverson, 1997; Major and Iverson, 1999; Van der Merwe et al., 2009). Fluids can also generate overpressure along with the interface between MTDs and their sediment cover, exploiting pathways created by internal MTD deformation (Ogata et al., 2012; Migeon et al., 2014; Praeg et al., 2014). Therefore, the interaction between the initial topographic relief of MTDs, dewatering processes, post-depositional deformation and subsequent sediment

gravity flows (and their deposits) is highly dynamic and inherently complex (e.g. Alves, 2015).

A better understanding of sedimentary processes above MTDs can help subsurface predictions of facies distributions, which might have been overlooked due to variable seismic resolution and core coverage. Therefore, detailed field-based studies can help to bridge the resolution gap.

Here, an exceptionally well-exposed debrite and overlying sand-rich strata in the Bathonian Los Molles Formation are investigated and physically correlated over 9.6 km along a depositional dip transect in the Chacay Melehue depocenter (Figure 3.1; Neuquén Basin, Argentina). The objectives of this study are to i) document the anatomy and stratigraphic architecture of the debrite, ii) investigate the impact of the dynamic upper relief on the overlying heterolithic and sand-rich strata, and iii) discuss the role that mass-wasting processes may have played as a trigger for subsequent sand-rich sediment supply.

3.3 Geological setting

The Neuquén Basin is located in central-western Argentina and central-eastern Chile, covering an area of > 160,000 km² (Figure 3.1A). The basin is bounded to the north-east by the Sierra Pintada, to the south by the North Patagonian Massif, and since the Early Jurassic, by the early Andean magmatic arc to the west (Legarreta and Gulisano, 1989; Suárez and de la Cruz, 1997; Franzese and Spalletti, 2001; Howell et al., 2005). The Neuquén Basin contains a > 6 km-thick sedimentary succession that spans the Mesozoic to the Late Cenozoic and records several unconformities related to tectonic phases (Vergani et al., 1995; Legarreta and Uliana, 1996; Howell et al., 2005). Three key tectonic phases are recognised (Vergani et al., 1995; Franzese and Spalletti, 2001; Franzese et al., 2003): 1) Triassic-to-Early Jurassic rifting and the onset of subsidence; 2) Early Jurassic-to-Early Cretaceous post-rift thermal subsidence associated with the development of the Andean magmatic arc and back-arc basin; and 3) Late Cretaceous-to-

Early Cenozoic Andean compression and foreland basin development. In the western sector of the Central Neuquén Basin, the deep- to shallow-marine deposits of the early post-rift Cuyo Group (Lower-to-Middle Jurassic) (Gulisano et al., 1984) unconformably overlie the continental syn-rift volcano-sedimentary deposits of the Precuyano Group (Gulisano et al., 1984; Gulisano and Gutiérrez Pleimling, 1995; Legarreta and Uliana, 1996; Pángaro et al., 2009; Leanza et al., 2013) or the Palaeozoic basement of the Choiyoi Group (Llambías et al., 2003, 2007) (Figure 3.2A).

This investigation focuses on the Early Bathonian stratigraphy of the Upper Los Molles Formation, which forms a ~70 m thick interval characterised by ammonite-rich black shales and heterolithic successions comprising tuff layers with an intervening MTD and sandstone deposits (Figure 3.2B).

3.3.1. Study area: Chacay Melehue Graben

The succession in the Chacay Melehue area was deposited in a half-graben (~20 km long) (Maceda and Figueroa, 1995; Llambías et al., 2007; Leanza et al., 2013) that occupied the western and deepest part of a broader early post-rift depocentre in the Central Neuquén Basin (~65 km long) (Maceda and Figueroa, 1995; Veiga et al., 2013). The half-graben shows a strong asymmetry due to a steep western margin characterised by the development of the early Andean magmatic arc and the location of a major syn-rift fault (Maceda and Figueroa, 1995; Suárez and de la Cruz, 1997; Vicente, 2005), which contrasts with the stable and gently dipping eastern cratonic margin (Spalletti et al., 2012; Veiga et al., 2013). Deposition of the Los Molles Formation occurred during a period of thermal subsidence and regional transgression across complex inherited rift topography, which promoted the reduction of sediment supply and sand starvation in this part of the basin (Spalletti et al., 2012; Veiga et al., 2013). The proximity to

the volcanic arc (~30 km to the west), the abundant volcanoclastic deposits (Zöllner and Amos, 1973; Rosenfeld and Volldaeimer, 1980; Gulisano and Gutiérrez Pleimling, 1995; Suárez and de la Cruz, 1997; Vicente, 2005; Llambías et al., 2007), and palaeocurrent measurements in sandstones indicating southeastwards trend reveals that sediment supply feeding the Chacay Melehue area during the post-rift was sourced from the western magmatic arc (Gulisano et al., 1984; Vicente, 2005). The deep-marine deposits of the Los Molles Formation (Weaver, 1931) overlie shallow-marine tuffaceous clastic deposits (La Primavera Formation, Suárez and de la Cruz, 1997; Llambías and Leanza, 2005) and carbonate deposits of the Chachil Formation (Pliensbachian to Early Toarcian, Weaver, 1942; Kamo and Riccardi, 2009; Leanza et al., 2013; Riccardi and Kamo, 2014), deposited with the first marine incursion in the basin (Gulisano and Gutiérrez Pleimling, 1995; Leanza et al., 2013) (Figure 3.2A). Chronostratigraphic studies based on ammonite biostratigraphy (Gulisano and Gutiérrez Pleimling, 1995; Riccardi, 2008) and U-Pb radiometric dating (Kamo and Riccardi, 2009; Leanza et al., 2013; Riccardi and Kamo, 2014), place the Los Molles Formation in the Chacay Melehue region as Early Toarcian-to-Early Callovian in age (Gulisano and Gutiérrez Pleimling, 1995) (Figure 3.2C). The succession of the Los Molles Formation in the Chacay Melehue depocentre is 850 m thick (Figure 3.2B). A 55 m thick sandstone-prone interval in the lower succession represents an Aalenian turbidite system (interval II of Gulisano and Gutiérrez Pleimling, 1995). The overlying Bathonian section of the Los Molles Formation (up to 200 m thick) (Figure 3.2B) is mainly represented by mudstone and heterolithic successions, including a 70 m thick interval (study interval; Figure 3.2C) of deformed sand- and mud-rich deposits (interval IV of Gulisano and Gutiérrez Pleimling, 1995). The overlying Lower Callovian strata of the Los Molles Formation is characterised by a 300 m thick interval of thin-bedded mudstone. It is overlain by either the fluvial Lotena Formation (Gulisano and Gutiérrez Pleimling, 1995; Veiga et al., 2011) or evaporites (Tábanos Formation; Figure 3.2D), which

record a period of basin desiccation (Legarreta, 1991; Gulisano and Gutiérrez Pleimling, 1995; Legarreta and Uliana, 1996).

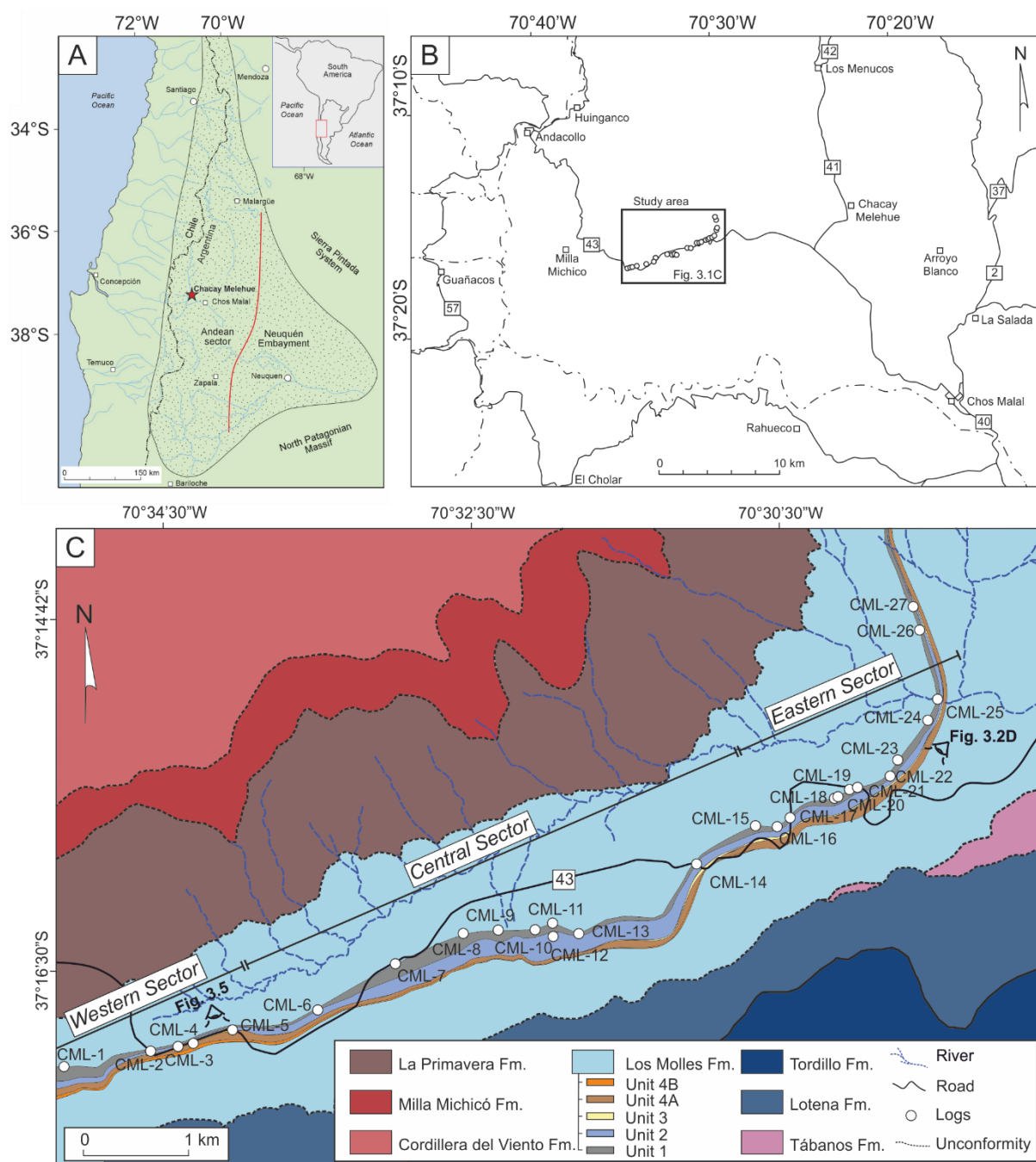


Figure 3.1. (A) Location map of the Neuquén Basin and the study area Chacay Melehue (red star). (B) Location map of the study area. (C) Map of the Chacay Melehue area with the formations (modified from Llambías et al. 2007) and the locations of the logs. See the studied units and their distribution.

Chapter 3: Substrate entrainment, depositional relief, and sediment capture: impact of a submarine landslide on flow process and sediment supply

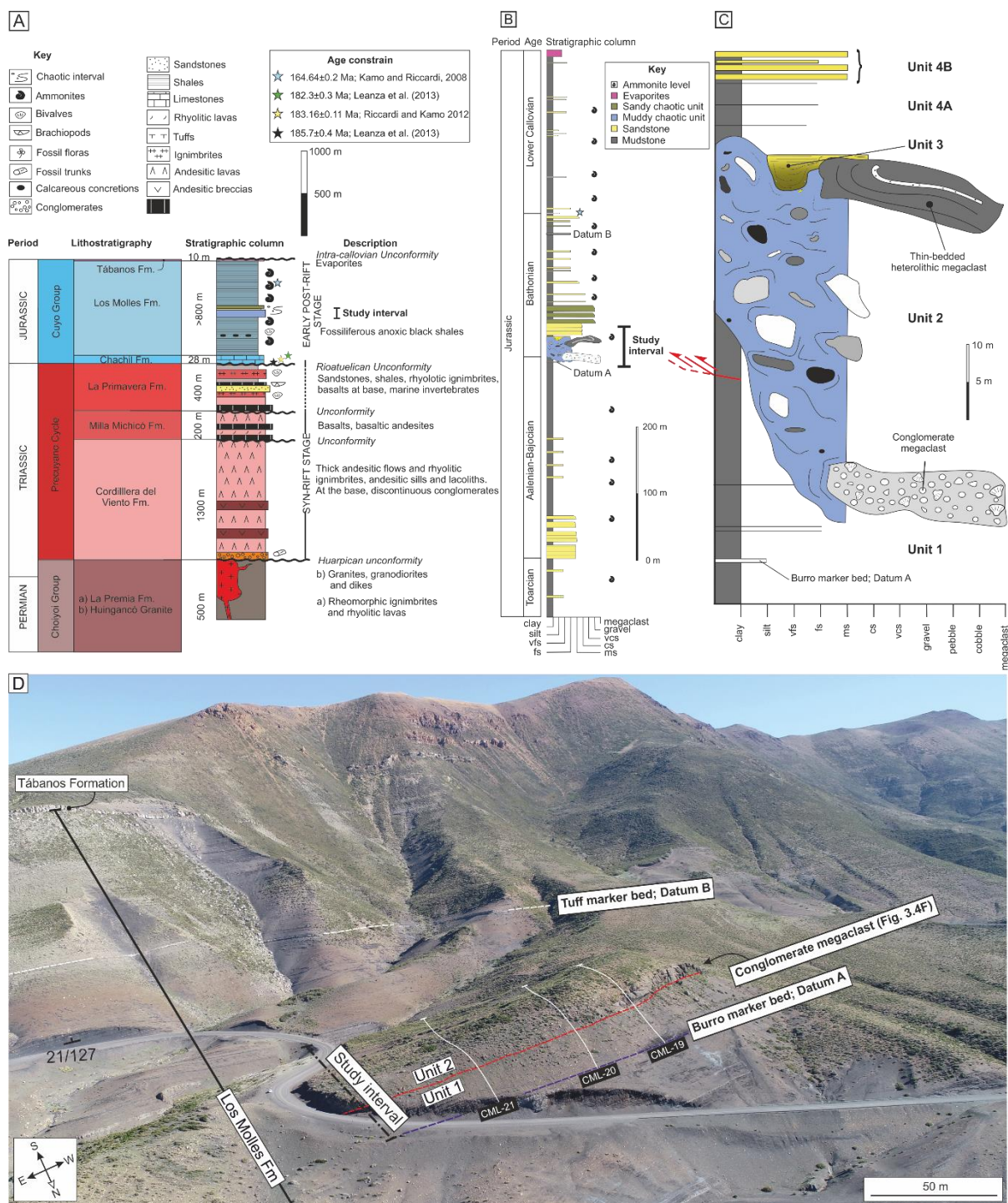


Figure 3.2. (A) General stratigraphic column of Chacay Melehue Graben (modified after Gulisano and Gutiérrez Pleimling (1995), Llambías et al. (2007) and Leanza et al. (2013)). (B) Stratigraphic column of Los Molles Formation and the Tábanos B Formation in the Chacay Melehue Graben (modified after Gulisano and Gutiérrez Pleimling (1995)). (C) Schematic log of the study interval. (D) Panoramic view from UAV photograph (car on the road for scale) showing the deep-water Los Molles Formation overlain by evaporitic deposits of the Tábanos Formation. The study interval and the two datums used to constrain the base and top of the correlation panel are shown. See the location of logs CML-19, -20 and -21 in Figure 3.1C.

3.4 Methodology

The sedimentology and stratigraphic architecture of a 70 m thick interval (Figure 3.1C and Figure 3.2C) within the Upper Los Molles Formation were investigated along a 9.6 km long and WSW-ENE orientated outcrop belt (Figure 3.1C). The succession dips 10-20° to the SE, with minimal structural overprint from the later tectonic inversion. Twenty-seven (27) sedimentary logs were measured at 1:25 to 1:40 scale along this transect (CML-1 to CML-27 from SW to NE) to document the broad depositional architecture of 4 different units (Unit 1, 2, 3, 4A and 4B) (Figure 3.2C). Ten detailed logs were measured at a 1:2 scale at specific locations to document fine-scale thickness and facies changes. Four marker beds were used to build a robust physical correlation between sedimentary logs (Figure 3.3). The marker beds are i) Datum A, or the 'Burro' marker bed, a light-grey indurated graded siltstone at the base of the study interval (Figure 3.2C, Figure 3.3 and Figure 3.4A); ii) a gravelly thin-bed (Figure 3.4I) and iii) a tuff layer (Figure 3.4J), both within one of the studied units (Unit 4A); and iv) Datum B, a tuff layer overlying the study interval (100-150 m above) across the study area (Figure 3.2D). Uncrewed Aerial Vehicle (UAV) photogrammetry (Figure 3.2D) was used in conjunction with standard field techniques, such as mapping and logging, to capture the micro- and macro-scale features of the investigated stratigraphic units. Fifty-eight (58) palaeocurrent measurements were collected, consisting of ripples, cross-bedding, flame structure and convolute lamination vergence from bed tops of sandstones, and plotted in rose diagrams.

3.5 Results: subdivision and characterisation of sedimentary Units 1-4

The study interval is subdivided informally into four different units (Figure 3.2C) based on their distinctive facies (Table 1) and stratal relationships.

3.5.1. Unit 1

Description: Unit 1 is 5.5-28 m thick and contains the Burro marker bed (Datum A) (Figure 3.2C), a graded siltstone bed that is sharply overlain by light-grey fine-grained, planar-parallel laminated sandstone (Figure 3.4A). This unit is truncated by the basal surface of Unit 2 and is thinnest in the central sector of the exposure (see sections CML-9 to CML-16 in Figure 3.3). Unit 1 comprises a heterolithic succession of planar-parallel laminated mudstones (F1) and thin-bedded (< 0.1 m thick) normally graded, well-sorted siltstones (F2) to very fine-grained sandstones (F3), and occasional medium-bedded structureless sandstones (F5) (Figure 3.4A, Figure 3.4B and Figure 3.4C). When traced from west to east, the thin-bedded sandstones show subtle lateral fining and thinning, transitioning from heterolithic succession to mudstone-prone succession. Unit 1 is rich in ammonites, belemnite rostrums and bivalves, as well as calcareous concretions (Damborenea, 1990; Gulisano and Gutiérrez Pleimling, 1995; Riccardi et al., 2011).

The central and eastern sectors contain a discrete stratigraphic interval that exhibits deformed bedding (Figure 3.4B). This interval is thickest (at least 10 m; Figure 3.3B) in the central sector, where, internally, it exhibits an array of imbricated decametre-scale east-verging thrusts (offset < 2 m) and associated drag folds (Figure 3.4B). The thrusts originate from a bed conformable surface, leaving the underlying bedding undeformed. In the eastern sector, a thin (~5 m thick) interval of intense deformation is characterised by open folds and minor thrusts (offset < 1 m). Unit 1 stratigraphy in the western sector lacks any deformation (Figure 3.3B)

Interpretation: The laminated mudstones, graded siltstones and thin sandstone beds are interpreted as deposits of low-density turbidity currents (Allen, 1982b; Trabucho-Alexandre et al., 2012; Könitzer et al., 2014), whereas the medium-bedded sandstones represent the deposits

of medium- to high-density turbidity current (Talling et al., 2012). The laterally extensive character, mudstone dominance, and overall eastward (downdip) fining and thinning trend of thin-bedded sandstones of Unit 1 suggest deposition from low-energy sediment gravity flows in distal areas (e.g. Mutti, 1977), with possible distal lobe fringe deposits (Boulestex et al., 2020). The discrete intervals of deformed bedding found in the upper parts of Unit 1 represent a post-depositional sheared zone linked to the overlying Unit 2.

3.5.2. Unit 2

Description: Unit 2 has an unconformable basal contact that truncates Unit 1 in the central sector (Figure 3.2 and Figure 3.3). The relief of the basal contact is characterised by down- and up-stepping segments (ramps, $> 2^\circ$) linked by bedding-parallel segments (flats). The average thickness of Unit 2 is 20-30 m but can locally reach up to > 47 m in the central sector and abruptly thins to < 8 m towards the eastern and western sectors (Figure 3.3). This change in thickness coincides with deeper erosion on the basal surface.

Unit 2 is characterised by a matrix-supported medium-grained muddy sandstone to sandy mudstone and is very poorly sorted throughout, ungraded, and with a chaotic distribution of outsized clasts (F14; Figure 3.4H). Clasts range in character and size from granular quartz grains and rounded volcanic epiclasts to much larger megaclasts (> 4.1 -140 m long) (Hodgson et al., 2019) of either conglomeratic or heterolithic lithology (Figure 3.2C, Figure 3.4F and Figure 3.5). The chaotic distribution of polymictic clast encased into a muddy sand matrix is responsible for the block-in-matrix fabric (e.g. Ogata et al., 2012). Typically, conglomeratic megaclasts are rounded, elongated and weakly deformed (Figure 3.4F and Figure 3.4G) and are clast-supported, with well-rounded to sub-angular clasts (0.03-1 m diameter) and fragments of thick-shelled bivalves (oysters; Figure 3.4G). These oyster-bearing conglomeratic

megaclasts are preferentially located near the base of Unit 2 (Figure 3.2C, Figure 3.2D and Figure 3.3B). In contrast, heterolithic megaclasts are angular and characterised by internally folded packages of planar laminated and normally graded thin-bedded material (Figure 3.5) and preferentially distributed toward the top of Unit 2 (Figure 3.2C, Figure 3.3B). This heterogeneity promotes a homogeneous matrix-rich texture in the middle division. Apart from the irregular basal contact of Unit 2, thickness changes within the unit are strongly controlled by the rugose upper surface. Kilometre-scale wavelength (1-3 km) and metre-scale amplitudes (0.5-8 m) are responsible for a complex supra-debrite topography.

Interpretation: The sedimentary characteristics of this unit, such as the chaotic distribution of (mega)clast floating onto a muddy sandstone to sandy mudstone matrix, suggest near-instantaneous deposition from a flow with high yield strength and buoyant support that could transport clasts up to 140 m long (Stow and Johansson, 2000; Mulder and Alexander, 2001). Using Datum A, the debrite formed a long-wavelength mounded top (Figure 3.3), attributed to the parental flow's cohesive nature and en-masse freezing. Unit 2 is interpreted as a cohesive debris flow deposit (Talling et al., 2012). The ramp and flat geometry at the base of Unit 2 indicate the debris flow's erosive nature (e.g. Lucente and Pini, 2003). The similarity in composition between the heterolithic megaclasts and underlying Unit 1 suggests entrainment of deep-marine substrate blocks due to the shear stress exerted by the overriding debris flow (Van der Merwe et al., 2009; Watt et al., 2012; Ogata et al., 2014a; Hodgson et al., 2019). In contrast, the sand content in the matrix and the oyster-bearing conglomerate megaclasts suggest a shallow marine origin of the mass failure (e.g. Ogata et al., 2012). Alternatively, the megaclasts bearing shells could come from the remobilization of older slope strata, including shallow-marine deposits (La Primavera Formation; Suárez and de la Cruz, 1997; Llambías and

Leanza, 2005). The two distinct megaclast sources suggest long-distance transport of clasts and flow bulking through local substrate entrainment (e.g. Sobiesiak et al., 2016).

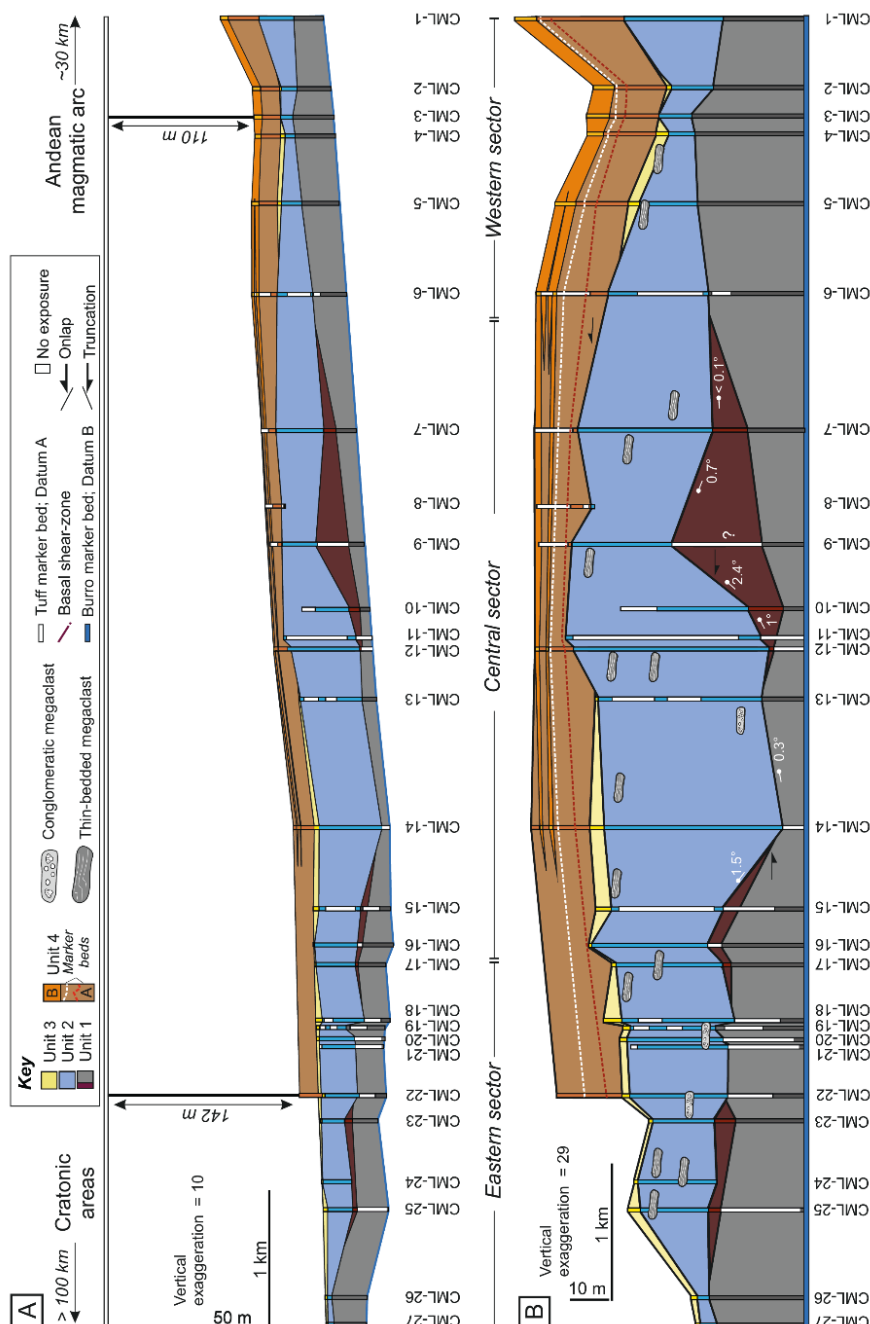


Figure 3.3. Correlation panels show the spatial relationship between stratigraphic units in the Bathonian succession of the Los Molles Formation and the different depositional architectures constrained by flattening on the top and basal datums. (A) Correlation panel including Units 1 to 4 with the Tuff marker as a datum (Datum B) showing stepped slope. (B) Correlation panel with the basal Burro marker bed (Datum A) as a datum showing the complex ramp-flat geometry and the basal-shear zone elements (brown coloured zone) at the base of Unit 2 and the correlation within Unit 4A based on two continuous sandstone marker beds. Note the heterogeneous distribution of Unit 3 and the pinching of Unit 4B in the central sector.

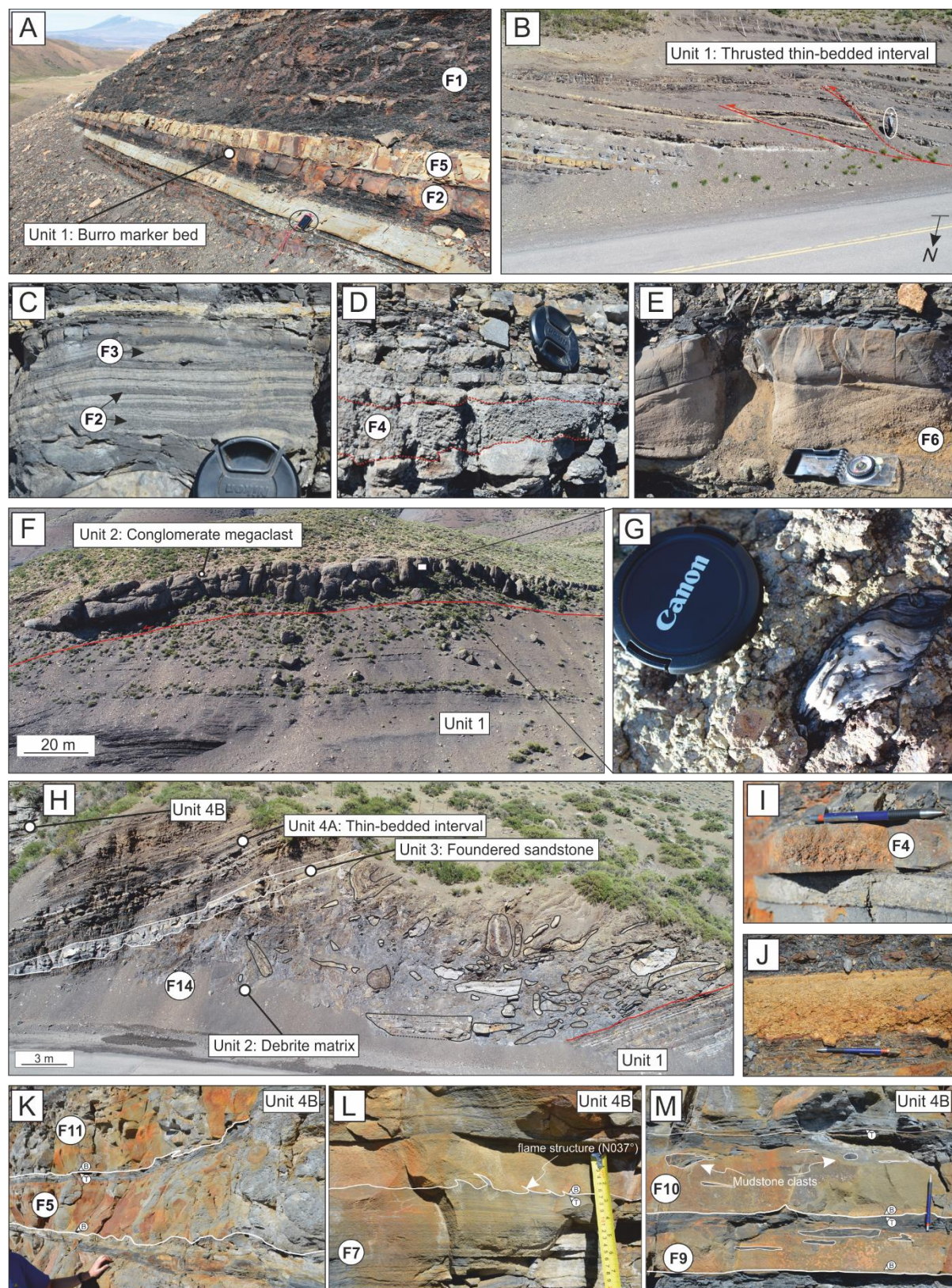


Figure 3.4. Representative sedimentary facies photos. (A) Unit 1: Planar-laminated mudstone (F1) with a few thin- to medium-bedded intercalated siltstone beds (F2) (Burro marker bed; Datum A) and sandstone beds (F5). (B) Unit 1: Basal shear-zone characterised by imbricated thrusts with drag folding. Geologist for scale. (C) Unit 4A: Heterolithic deposits consisting of the alternation between siltstones (F2) to (very) fine-grained sandstones (F3). (D) Unit 4A:

Gravelly thin bed (F4) locally eroded into fine-grained sandstones (F3). (E) Unit 4A: Medium-bedded sandstones with cross-bedding (F6). (F) Unit 2: 140 m long conglomerate megaclast, bearing oyster and belemnite fragments and sitting above Unit 1. See a fragment of an oyster in the inset (G). (H) Unit 2, 3 and 4A: Foundered sandstones onlapping the matrix-rich debrite (F14) with deformed heterolithic megaclasts draped by the thin-bedded deposits of Unit 4A. (I) Unit 4A: Gravelly and (J) Tuff-marker bed within 4A. See the correlation in Figure 3.3 and Figure 3.9 (red and white dashed lines). (K) Unit 4B: Amalgamated medium- (F6) to thick-bedded (F11) sandstones. (L) Unit 4B: Medium-bedded banded sandstone (F7) overlain by massive matrix-poor sandstones (F5). Note the vergent flame structures within the amalgamation surface. (M) Unit 4B: Thin- (F9) and medium-bedded (F10) hybrid event beds with a linked debrite consisting of matrix-rich sandy division with elongated mudstone clasts.

LITHOFACIES	LITHOLOGY	DESCRIPTION	THICKNESS	PROCESS INTERPRETATION
F1: Laminated mudstone.	Mudstone.	Dark-coloured planar parallel laminated mudstone with ammonites. Concretionary horizons are common.	0.1-3 cm	Deposits from dilute sediment gravity under relative dysoxic-anoxic conditions (Trabucho-Alexandre et al., 2012; Köntzer et al., 2014).
F2: Graded siltstone.	Graded siltstone.	Normally graded from silty bases to mud-rich tops. Usually structureless, although planar parallel-laminations are common.	1-5 cm	Deposition under low-density turbidity current (Allen, 1971b).
F3: Thin-bedded fine-grained sandstones.	Very fine-to fine-grained sandstones.	Normally graded, well-sorted thin-beds. Fine-grained bases and very fine-grained tops. Structureless at the base with planar laminated tops. Rare starved ripple lamination at bed tops.	1-10 cm	Deposition and tractional reworking by low-density turbidity current (Allen, 1971b, 1982b; Jobe et al., 2012).
F4: Thin-bedded granular sandstones.	Granular-to medium-grained sandstones.	Normally graded, well-sorted, coarse-grained to granular-sandstones. Sharp planar base and top.	1-10 cm	Deposition from partially bypassing turbidity currents (Stevenson et al., 2015).
F5: Medium-bedded	Very fine-to medium-	Structureless, normally graded sandstones. Bed bases are medium-grained,	10-50 cm	Deposition from high-density turbidity currents. High-aggradation rates inhibited the formation of

sandstones.	grained sandstone.	grading up until fine-grained.		sedimentary structures (Talling et al., 2012).
F6: Thin-bedded cross-stratified sandstones.	Granular to medium-grained sandstones.	Normally graded, well-sorted thin-beds. Foreset heights range from 5 to 7 cm, and angles vary between 10° and 35°. Erosional bases are common. Sharp contacts with planar base and undulatory top.	5-10 cm	Partially bypassing flow (Stevenson et al., 2015) that reworked the previously deposited coarse fraction. Cross-bedding is attributed to high-magnitude steady parental flow (Arnott, 2012; Talling et al., 2012).
F7: Medium-bedded banded sandstones.	Banded sandstones with sharp alternation between darker and lighter bands.	Sandstones comprise alternation between matrix-poor light bands and matrix-rich dark bands (0.2 to 2 cm thick). Similar grain size (fine to medium) along with different bands. The bed bases can be structureless.	10-50 cm	Deposits beneath mud-rich transitional plug flow formed by tractional reworking within the upper stage plane bed flow regime (Baas et al., 2009, 2011b; Baas et al., 2016; Stevenson et al., 2020).
F8: Thick-bedded banded sandstones with mudstone clast.	Banded sandstones with diffuse alternation between darker and lighter bands. Lighter bands are grain-supported, while darker bands are matrix-supported, with abundant mudstone clasts.	Sandstones comprise banding between matrix-poor light bands and matrix-rich mudstone clast (millimetric scale) bearing dark bands (0.5-2 cm). Banding is diffuse and can be developed throughout the bed or from the middle to the top of the bed, commonly overlaid by convolute lamination. Laminae show local tilting and increasing spacing between laminae.	50-150 cm	Rapid aggradation and episodic damping of near-bed turbulence due to clay flocs disaggregation (Lowe and Guy, 2000). Increasing spacing between laminae is attributed to growth strata due to foundering processes.
F9: Thin-bedded	Silty sandstone.	Structureless bases with linked argillaceous,	1-10cm	Distal deposits are the product of en masse deposition and potentially

hybrid event beds.		ungraded and poorly-sorted top divisions.		behave as transitional to laminar flows (Kane et al., 2017).
F10: Medium-bedded hybrid event beds.	Bipartite sandstones with matrix-poor basal divisions and upper argillaceous mudstone-clast prone division.	Bipartite sandstone beds are characterised by a matrix-poor structureless lower division passing gradually into linked mudstone clasts with matrix-rich upper division.	10-50 cm	Deposits formed under transitional flows. Erosion and incorporation of intrabasinal clasts. The entrained substrate was rapidly disaggregated within the flow resulting in clast-rich and clay-rich divisions at the bed top. The flows increased in concentration but had not developed stable density stratification (Haughton et al., 2003; Davis et al., 2009; Hodgson, 2009; Kane and Pontén, 2012; Kane et al., 2017).
F11: Thick-bedded sandstones.	Structureless sandstone.	Structureless, thick-bedded argillaceous sandstones, lacking mudstone clasts. High amalgamation ratios and erosional beds when lying above fine-grained intervals. Banding is locally developed at bed tops, alternating between matrix-poor light bands and matrix-rich dark bands (0.2 to 2 cm thick). Similar grain size (fine to medium) along with different bands. Heterolithic bedforms and pinch-and-swell geometries can be developed.	0.5-1.2 m	Deposition under high-density turbidity currents (<i>sensu</i> Lowe, 1982), formed by incremental layer-by-layer deposition with high aggradation rates (Kneller and Branney, 1995; Sumner et al., 2008; Talling et al., 2012). The banding represents planar lamination (Tb division) (Stevenson et al., 2020).
F12: Thick-bedded structureless matrix-poor sandstones with normal	Structureless sandstones with mudstone clasts at the base.	Structureless thick-bedded, medium- to coarse-grained, crudely normally graded sandstones with low-matrix content. They contain some mudstone clasts (0.1-1 m) with diffuse boundaries preferentially located at	0.5-2 m	Deposition under high-density turbidity currents (<i>sensu</i> Lowe, 1982), formed by incremental layer-by-layer deposition with very high aggradation rates (Kneller and Branney, 1995; Sumner et al., 2008; Talling et al., 2012). Mudstone clast is entrained due to erosion of

y graded mudstone clast.		the base, which show coarse tail grading. Mudstone diapirs along the basal interface are common.		an unconsolidated debris (Unit 2) and syn-sedimentary buoyancy product of density instabilities (Owen, 1987, 2003).
F13: Thick-bedded structureless matrix-rich sandstones with ungraded mudstone clast.	Argillaceous sandstone with abundant mudstone clasts.	Structureless thick-bedded, fine- to medium-grained, ungraded sandstones with very high-matrix content and abundant decimetric mudstone clasts (0.1-1 m) randomly distributed.	0.5-2 m	Moderate-strength cohesive debris flows derived from mudstone clast entrainment and disaggregation. Mudstone clasts are supported by their positive buoyancy with respect to the surrounding matrix and the matrix strength (Talling et al., 2012).
F14: matrix-supported conglomerates.	Mud-rich medium-grained sandstone to sandy mudstone.	Poorly sorted, ungraded with a chaotic distribution of outsized clasts (up to 140 m long). Irregular and sharp contacts. Bases can be erosive and undulatory tops.	7.4 – 47.9 m	Cohesive debris-flow deposits (Talling et al., 2012) with near-instantaneous deposition from a flow with high yield strength and buoyant support.

Table 3.1. Descriptions of the facies recognised in the Los Molles stratigraphy of the Chacay Melehue area, including lithologies, thicknesses, and interpretations of their depositional processes.

3.5.3. Unit 3

Description: Unit 3 (0-4 m thick) is composed of thick sandstone beds (0.5-2 m) with sharp, irregular concave-up bases and abrupt pinch-out terminations, which result in a disconnected distribution of packages of wedge-shaped sandstone bodies (Figure 3.3) (see architecture section). Unit 3 is only present where Unit 2 is relatively thin (in the eastern-central and western sectors) and is absent in the central region where Unit 2 shows its maximum thickness (Figure 3.3). Where Unit 3 is absent, Unit 4 overlies Unit 2 (Figure 3.3). Unit 3 comprises bed types characterised by two main amalgamated divisions (lower and upper divisions) with some grain-

size breaks lacking any mudstone- and siltstone-rich bounding intervals (Figure 3.6). The basal interface of these sandstone bodies shows centimetre-scale undulations characterised by abundant load casts, semi-detached ball structures, and mudstone intrusions (diapirs and injectites) originating from Unit 2 (Figure 3.6).

Two types of thick-bedded amalgamated sandstone facies dominate the lower division, which varies along the transect (Figure 3.6 Figure 3.8). Grain-size breaks define amalgamation surfaces within sandstones. In the western sector, and more rarely in the eastern sector, the lower divisions are thick-bedded (0.5-2 m thick), structureless, weakly normally graded, moderately- to poorly-sorted sandstones (F12). At bed bases, these sandstones comprise well-rounded (0.1-1 m diameter) mudstone clasts of low-sphericity and diffuse boundaries (mudstone clast type A), which show a coarse tail grading (Figure 3.6). Locally, in the eastern sector, lower divisions of these sandstone bodies comprise thick-bedded, structureless, very poorly-sorted, more argillaceous sandstones with abundant mudstone clasts (0.1 - 1 m diameter) with very diffuse boundaries (mudstone clast type A), which are ungraded and randomly orientated (F13) throughout the encasing matrix (Figure 3.6).

The lower division of Unit 3 sandstone bodies is overlain by an upper division (up to 2 m thick), which comprises coarse to very fine-grained, normally graded, moderately- to poorly-sorted sandstones (0.5-1.7 m) (Figure 3.6). Banding can be developed throughout the bed or overlying a structureless division (Figure 3.6). The banding is characterised by an alternation between lighter matrix-poor bands and darker matrix-rich bands that comprise bedding parallel millimetric mudstone clast with sharp boundaries (mudstone clast type B) (F8; Figure 3.6C). Contacts between bands are diffuse (Figure 3.6B and Figure 3.6F). The spacing between the individual bands (0.5-2 cm) increases from the margin to the central parts of the sandstone

body, commonly showing rotation (Figure 3.6E). These sandstones develop symmetrical and asymmetrical convolute lamination at bed tops (predominant vergence towards NE; Figure 3.6D). Decimetre-scale long and centimetre-scale thick mudstone injections can be observed within this division (Figure 3.6B).

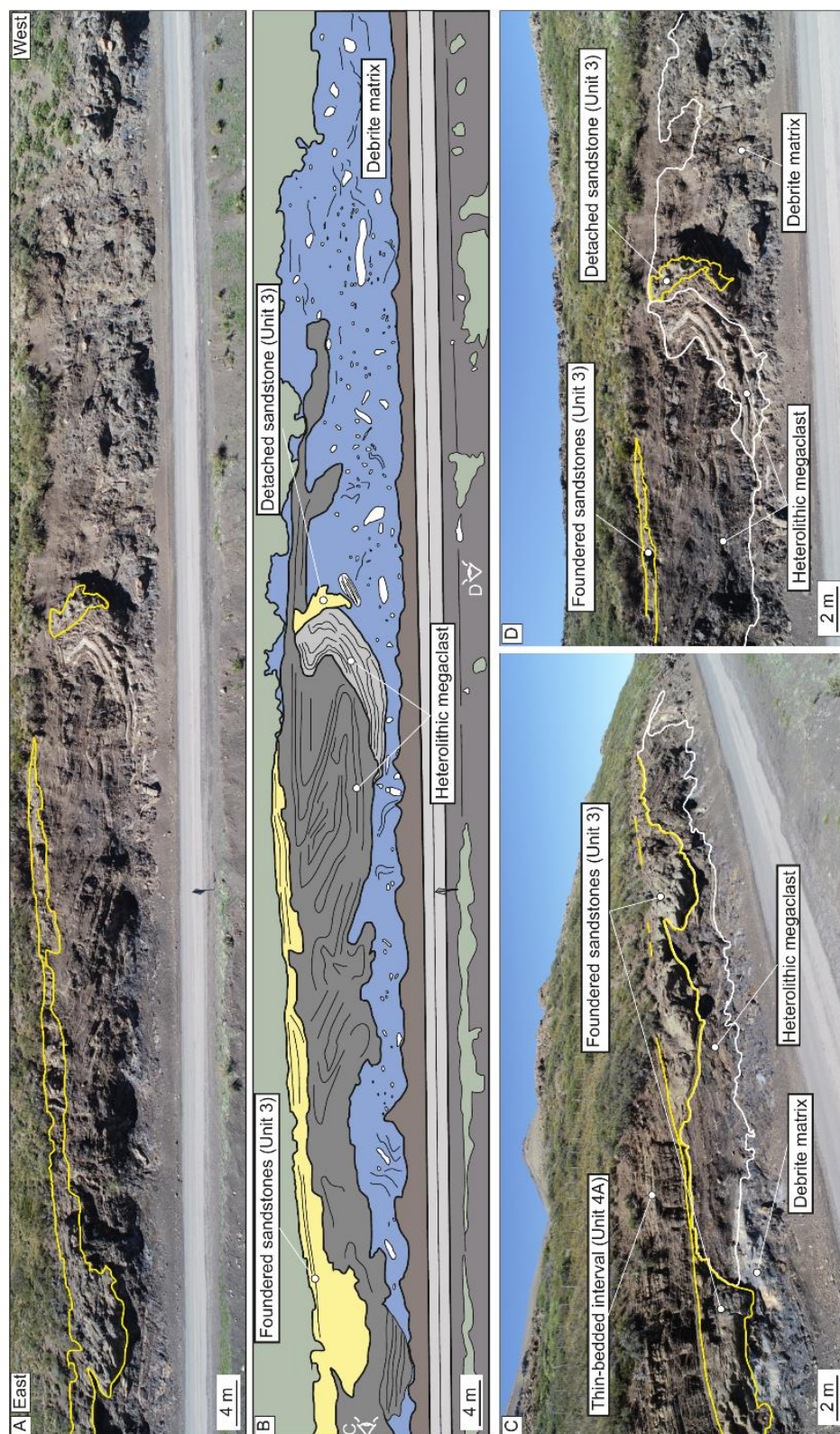


Figure 3.5. (A) Panorama of the exposure showing the upper division of Unit 2 overlaid by Unit 3 foundered sandstone. (B) Sketched exposure of A. Note the matrix-supported texture and the chaotic distribution of clasts. (C) and (D) the same exposure of (A) from a different perspective. Note the unconformable base and conformable flat top interface of Unit 3 sandstones.

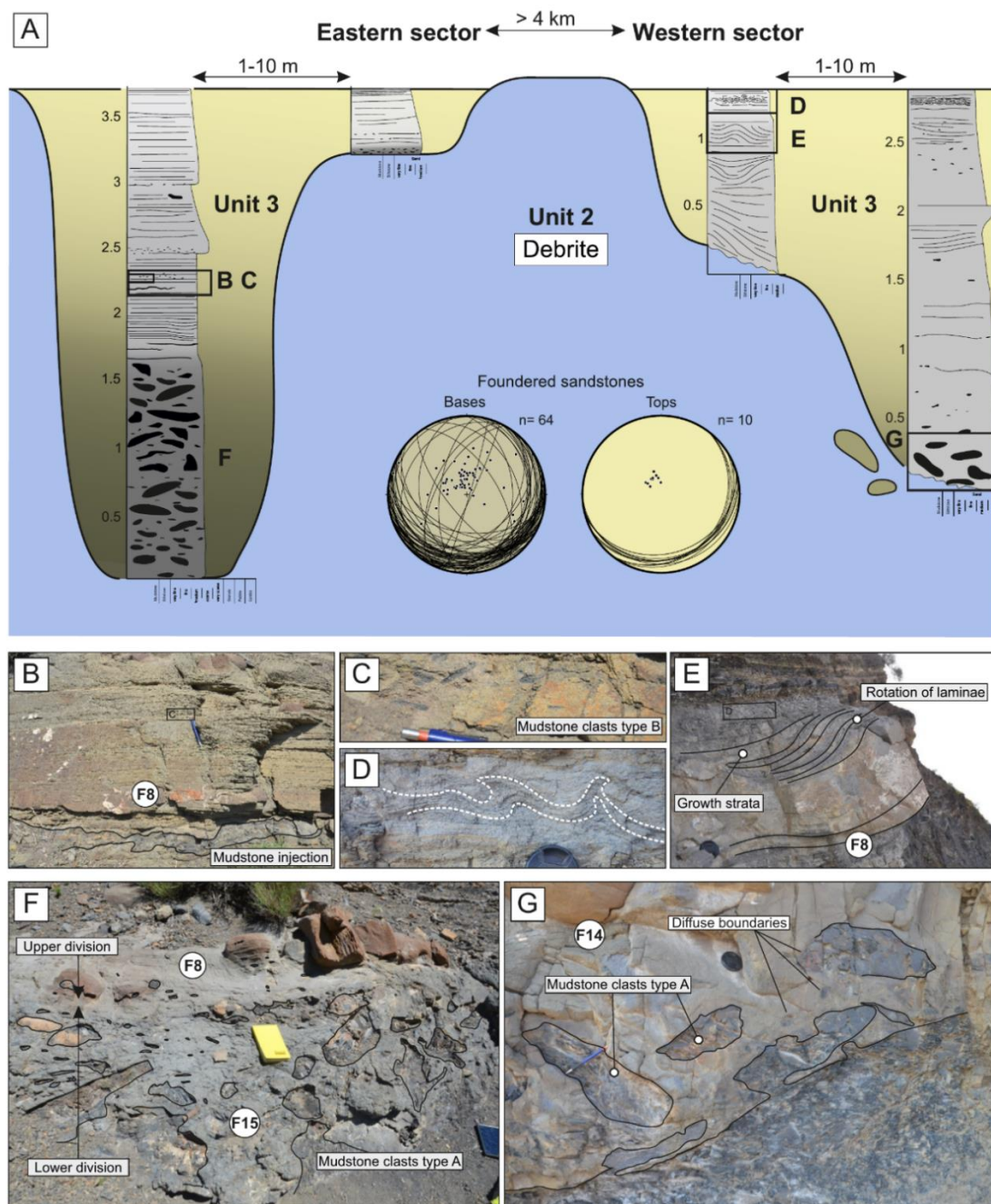


Figure 3.6. Foundered sandstones (Unit 3) diagram. (A) Illustrative correlation of sandstone foundering (Unit 3) into debrite (Unit 2). Note the difference between the conformable bed tops of matrix-poor and traction-dominated sandstones (right-hand stereonet) and the mudstone clast- and matrix-rich sandstone texture near the unconformable bed bases (left-hand stereonet), which shows the architecture of these sandstone bodies. (B) Thick-bedded banded sandstones with bedding-parallel sill injection (F8). See mudstone clasts (type B) in the inset (C). (D) Convolute-laminae with NE vergence. (E) Sandstones showing rotation and growth strata. (F) Lower division comprising thick-bedded structureless argillaceous (F13) sandstone division with a patchy and random distribution of mudstone clasts overlain by upper division comprising thick-bedded banded sandstones (F8). (G) Thick-bedded structureless sandstone with an undulating irregular base comprising decimetre-scale mudstone clasts (type A) (F12).

Interpretation: The wedge-shaped and deformed concave-up basal contacts of the sandstone bodies beds in Unit 3 are interpreted to reflect the interaction with the rugose upper surface and syn-sedimentary foundering of sand into the underlying mud-rich debrite (Figure 3.6). Foundering is driven by instability due to the density contrast between the sand deposited above a less dense debrite (density loading) and lateral changes in sediment load (uneven loading) (Owen, 1987, 2003) produced by the short-wavelength rugosity of the upper surface. The lack of sedimentary structures in the lower divisions of bed types recognised in Unit 3 is interpreted as a product of hindered settling from highly concentrated gravity flows, resulting in turbulence damping and rapid deposition (Talling et al., 2012), inhibiting any period of traction (Sumner et al., 2008). The normally graded lower divisions were produced by incremental layer-by-layer deposition from high concentration gravity flows, such as high-density turbidity currents (*sensu* Lowe, 1982). In contrast, the thick-bedded argillaceous sandstones with ungraded mudstone clasts observed in the distal areas (eastern sector) are interpreted as moderate-strength cohesive debrites (*sensu* Talling et al., 2012). The decimetre-scale mudstone clasts (type A) were transported due to the matrix strength of the debris flows and their positive buoyancy with respect to the encasing matrix.

The lateral facies transition from high-density turbidites to moderate-strength cohesive debrite suggests a flow transformation due to the entrainment of cohesive material from the underlying debrite (e.g. Kane and Pontén, 2012; Baker et al., 2017). The unconsolidated state of the debrite might have enhanced the substrate entrainment of decimetre-scale mudstone clasts (type A) and disaggregation (as indicated by the diffuse boundaries; Figure 3.6G), increasing the amount of mud and, therefore, the cohesiveness of the flow. Based on facies juxtaposition, the foundered sandstones can be subdivided into two different facies associations: 1) proximal and 2) distal, foundered sandstone facies associations (Figure 3.8). High-density turbidites and

moderate-strength cohesive debrites are characterised by rapid deposition (incremental deposition and en masse freezing, respectively), triggering the liquefaction of the fluid-saturated and unconsolidated upper surface of the debrite and foundering of sand. The undulations of the concave-up basal interface reflect complex interactions with the substrate: as the denser sand sank into the fluid-saturated muddy substrate, the buoyancy of mud promoted the syn- to post-depositional intrusion (mud diapirs and injectites) of the substrate into sandstones. The most advanced stage of foundering is observed when detached sand-balls develop (Figure 3.5; Owen, 2003; Tinterri et al., 2016).

In contrast, the banded sandstone characteristic of the upper divisions is interpreted to be formed under episodic near-bed turbulence damping at high deposition rates (Lowe and Guy, 2000). The juxtaposition of the banded sandstones over the mudstone-clast bearing sandstones of the lower divisions suggests highly stratified flows, mixing and upwards transfer of centimetre-scale mudstone clast (type B) and the cohesive material from the disaggregation of the entrained decimeter-scale mudstone clast (type A). This enrichment in cohesive clayey material triggered the periodic suppression of turbulence and, therefore, banding development. The banding passes into convolute laminations towards the top, indicating moderate deposition rates. The vergence of convoluted laminations suggests syn-sedimentary shear stress exerted by the overriding flow (McClelland et al., 2011; Butler et al., 2016) and flow-rebound produced by the underlying debrite relief (e.g. Tinterri et al., 2016).

3.5.4. Unit 4

Description: Unit 4 (10-27.3 m thick) has a sharp and concordant contact with the underlying Unit 2 and Unit 3 (Figure 3.2C). It comprises two sub-units: a lower heterolithic interval (Unit 4A) and an upper sandstone-prone interval (Unit 4B; Figure 3.2C and Figure 3.3). Unit 4A is

a thin- to medium-bedded (0.01-0.5 m; Figure 3.4H) heterolithic succession (F1, F2, F3 and F5) with a maximum thickness of 22 m, thinning to 8 m in the central sector above where Unit 2 is thickest (Figure 3.3 and Figure 3.9). Most thin beds (0.01-0.1 m thick) are fine- to medium-grained normally graded sandstones, matrix-poor, moderately well-sorted, and structureless with common planar-parallel lamination and/or starved-ripple lamination near bed tops (F3). Palaeocurrent measurement shows a consistent flow trend towards the NE (Figure 3.9). Unit 4A also comprises coarse- to granular normal-graded sandstones, relatively low matrix content with common grain-size breaks (0.07-0.2 m thick), erosive bases and sharp-planar tops (F4; Figure 3.4D) and two medium-bedded matrix-supported conglomerates with sandstone clasts (F14; 0.25 and 0.35 m thick, respectively) that pinch out towards the central sector (Figure 3.9). One of these thin gravelly beds, which lacks any lateral thinning or fining trend (Figure 3.4I), was traced across the exposure (gravelly marker bed; dashed red line in Figure 3.9). In addition, a 0.15 m thick tuff layer (Figure 3.4J) was also used for correlation purposes (tuff marker bed; dashed white line in Figure 3.9). The medium-bedded sandstones (0.1–0.5 m thick) are structureless, ungraded, with planar-parallel and convolute lamination at bed tops, except one that shows cross-bedding (F6; Figure 3.4E). These sandstones have sharp bed bases and tops and lack mudstone clasts. In the eastern sector, Unit 4A is dominated by thin- to medium-bedded heterolithic succession that lacks any gravelly (F5) or matrix-supported conglomerate beds (F14) (Figure 3.7 and Figure 3.9).

Unit 4B (5.7 m thick in the western sector) thins eastwards along a 4.3 km transect until it pinches out and a facies transition occurs, where Unit 2 is thickest (Figure 3.3 and Figure 3.9). In the western sector, it dominantly comprises medium- (F5; Figure 3.4K) to thick-bedded sandstones (F11; Figure 3.4K), with less common ‘bipartite’ sandstone beds (F9 and F10) composed of a matrix-poor lower division and a matrix-rich upper division with mudstone

clasts. Conformable bases and sharp tops characterise the thick-bedded sandstones (0.5-1.2 m). Where the thick-bedded sandstones are not amalgamated, they are intercalated with centimetre-thick beds of fine-grained material (F1 and F2), and bed bases are loaded locally. The thick-bedded sandstones are normally graded from medium to fine sand, well-sorted with rare centimetric mudstone clasts at the bed top. Soft-sediment deformation structures, such as centimetre-scale flames with NE vergence, are also common at bed bases and along amalgamation surfaces (Figure 3.4L). Banded sandstones are medium-bedded (0.1-0.5 m), fine- to medium-grained, and characterised by alternating between light- and dark-coloured bands, ranging from 0.2 to 2 cm thick (F7; Figure 3.4L). Both band types show a similar maximum grain size, although the darker bands are matrix-rich and light bands are matrix-poor. Banding is generally sub-parallel to bedding. Although banded sandstones are more commonly associated with thick-bedded structureless sandstones, the banded sandstones can be individual event beds, with banding above the structureless basal division. The medium-bedded bipartite sandstone beds (0.1-0.5 m) consist of a medium-grained, matrix-poor and structureless lower division, which is overlain by a fine-grained matrix-rich upper division characterised by poor sorting and abundant mudstone clasts (0.05-0.3 m) with low sphericity and variable roundness (F9 and F10; Figure 3.4M). The lower and upper divisions show a gradual upwards increase in matrix content rather than across a sharp boundary. When Unit 4B is traced eastwards towards the central sector, the sandstone package transitions into a few thin beds (0.1 m thick) of weakly graded, very poorly-sorted matrix-rich sandstone, lacking the mudstone clasts observed in western areas. Unit 4B is absent in the eastern sector (Figure 3.9).

Interpretation: In Unit 4A, the thin sandstone beds showing planar and cross ripple laminations support an interpretation as low- to medium-density turbidites (Talling et al., 2012). The starved-ripple lamination observed in thin-bedded sandstones is interpreted as the reworking

of sand deposited by dilute flows with low sedimentation rates (Talling et al., 2007; Jobe et al., 2012). The intercalation of thin-bedded sandstones with finer-grained deposits suggests a lobe fringe environment (Lobe fringe facies association; Figure 3.8) (Prélat et al., 2009; Sychala et al., 2017b). The abundant coarse-grained to gravelly thin-bedded sandstones in the western sector record intermittent energetic coarse-grained flows, suggesting sporadic sediment bypass processes (Stevenson et al., 2015). However, the low matrix content within the granular beds suggests a sediment source area where only coarse- to granular grain size was available. The intercalation of such different facies suggests the juxtaposition of depositional environments of contrasting energy and/or different sediment sources. Either scenario could be possible given the complex sediment routing patterns and multiple transverse or axial sources available in the Neuquén Basin during the early post-rift setting (Vicente, 2005; Privat et al., 2021) and by analogy to other post-rift settings (e.g. Lien, 2005; Fugelli and Olsen, 2007; Hansen et al., 2021). The mass failure would trigger a new coarse-grained source due to slide scar position and geometry, promoting intermittent sand supply to an otherwise sand-starved environment (see ‘Origin and role of the mass-wasting process as a trigger for turbidite systems development’ in discussion). The downdip variability in the thickness of Unit 4A (from 22 to 8.5 m thick), reduction in gravelly sandstone content, and the stratigraphic thinning between the granular marker bed (red dashed line in correlation) and the top debrite (Unit 2) reveal the existence of subtle relief on the debrite surface (Figure 3.9). Furthermore, the two poorly sorted, ungraded muddy sandstones, interpreted as debrites due to their chaotic distribution of clast within the argillaceous matrix, also pinch out towards the central sector. The ripples and convolute laminae with SW vergence (Figure 3.9) contrast with the consistent NE paleoflow, suggesting local flow deflection (cf. Tinterri et al., 2016) in the central sector, where the debrite relief is highest, indicating the interaction between sediment gravity-flows and the upper surface of the debrite.

Massive medium- to thick-bedded deposits of Unit 4B are interpreted as high-density turbidites formed by incremental layer-by-layer deposition with high aggradation rates (Kneller and Branney, 1995), interpreted to represent proximal lobe axis environments (lobe axis facies association; Figure 3.8) (e.g. Prélat et al., 2009; Kane et al., 2017). The location of these facies in the westernmost sector, and the palaeoflow measurements, suggest that the western sector was relatively proximal. Banded sandstones represent the deposits of mud-rich transitional flows formed by tractional reworking (Stevenson et al., 2020). The bipartite beds consisting of a basal structureless to planar laminated sandstone division, overlain by a linked mudstone clast-rich upper division, are interpreted as hybrid event beds (HEBs), formed from transitional flows deposited under high-deceleration rates (Haughton et al., 2009; Hodgson, 2009; Kane and Pontén, 2012) in more distal environments than the banded sandstones (Stevenson et al., 2020). The gradual and diffuse boundary between the basal turbidite and the upper debrite suggests vertical segregation of particles within the cohesive flow (Kane et al., 2017). The facies evolution of Unit 4B from proximal (western sector) to distal (eastern sector) of thick-bedded sandstones into hybrid event beds likely represents the downdip transition from lobe-axis/off-axis environments (lobe axis facies association: Figure 3.8) (*sensu* Prélat et al., 2009) into lobe-fringe environments (lobe fringe facies association; Figure 3.8) (e.g. Kane et al., 2017; Sychala et al., 2017a), persisting until the frontal/oblique pinch-out (e.g. Hansen et al., 2019).

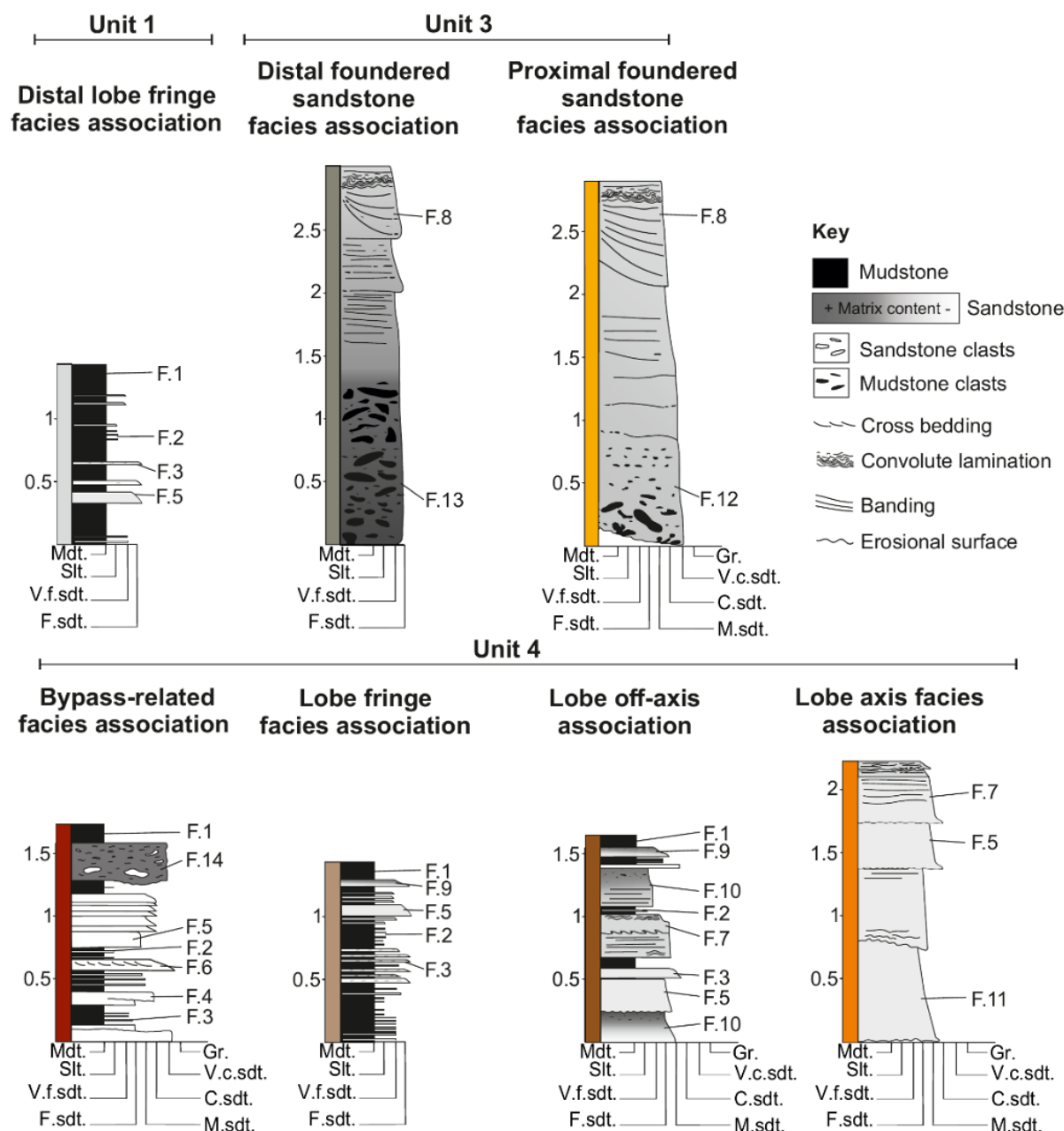


Figure 3.8. Facies associations of Units 1, 3 and 4. See Table 3.1, Figure 3.4 and Figure 3.6 for more detail. See Figure 3.9 for the lateral variability of each facies association.

3.6 Depositional architecture of the debrite and overlying units

3.6.1. Large scale architecture: debrite relief

Using Datum A ('Burro' marker bed), the upper surface of the > 9.6 km long debrite forms a broad convex-up relief that reaches a maximum in the central section coincident with the deepest incision (at least 22.5 m of erosional relief; Figure 3.3B). The spatial association of the

thickest part of the debrite with the deepest incision support a genetic link between the geometry of the flat-ramp-flat shaped basal shear zone and the mounded top. The morphology of the basal surface can buttress material translated downslope and develop positive topographic features, such as pressure ridges (Moscardelli et al., 2006; Bull et al., 2009). Bed-by-bed correlation within Unit 4A shows that where the upper surface of the debrite develops the highest relief (~8 m of positive relief with respect to the western sector), Unit 3 is absent, and it is overlain by Unit 4A, showing a laterally continuous stratigraphic interval with metre-scale thickness variations (Figure 3.9). Unit 4A thins from 22 m (CML-1) and 13 m (CML-2) to 6 m (CML-12) across the highest part of the debrite (Figure 3.9). The lower part of Unit 4A pinches out in the central sector, developing onlaps of individual beds, and supporting the existence of a gentle relief (Bakke et al., 2013; Soutter et al., 2019). In contrast, the upper part of Unit 4A shows tabular architecture with a lateral continuity of over 7 km (Figure 3.9).

Unit 4A is overlain by Unit 4B, which shows a progressive thinning of the submarine lobe from the western to the central sector over 5.6 km, from 5.7 m (CML-3) to 1.7 m (CML-12) and 1 m (CML-14) with a mean thinning rate of 0.9 m/km. The submarine lobe pinches out between CML-14 and CML-22 (< 2 km), interfingering with unit 4A (Figure 3.9). The lack of onlap geometries against underlying deposits and subtle thinning rates consistent with unconfined settings (e.g. Pr elat et al., 2009) suggests a lack of a pronounced pre-existing relief. However, the coincidence of lobe pinch-out in the area where the debrite relief is highest and where the underlying Unit 4A is thinnest (Figure 3.9) might reflect subtle residual relief.

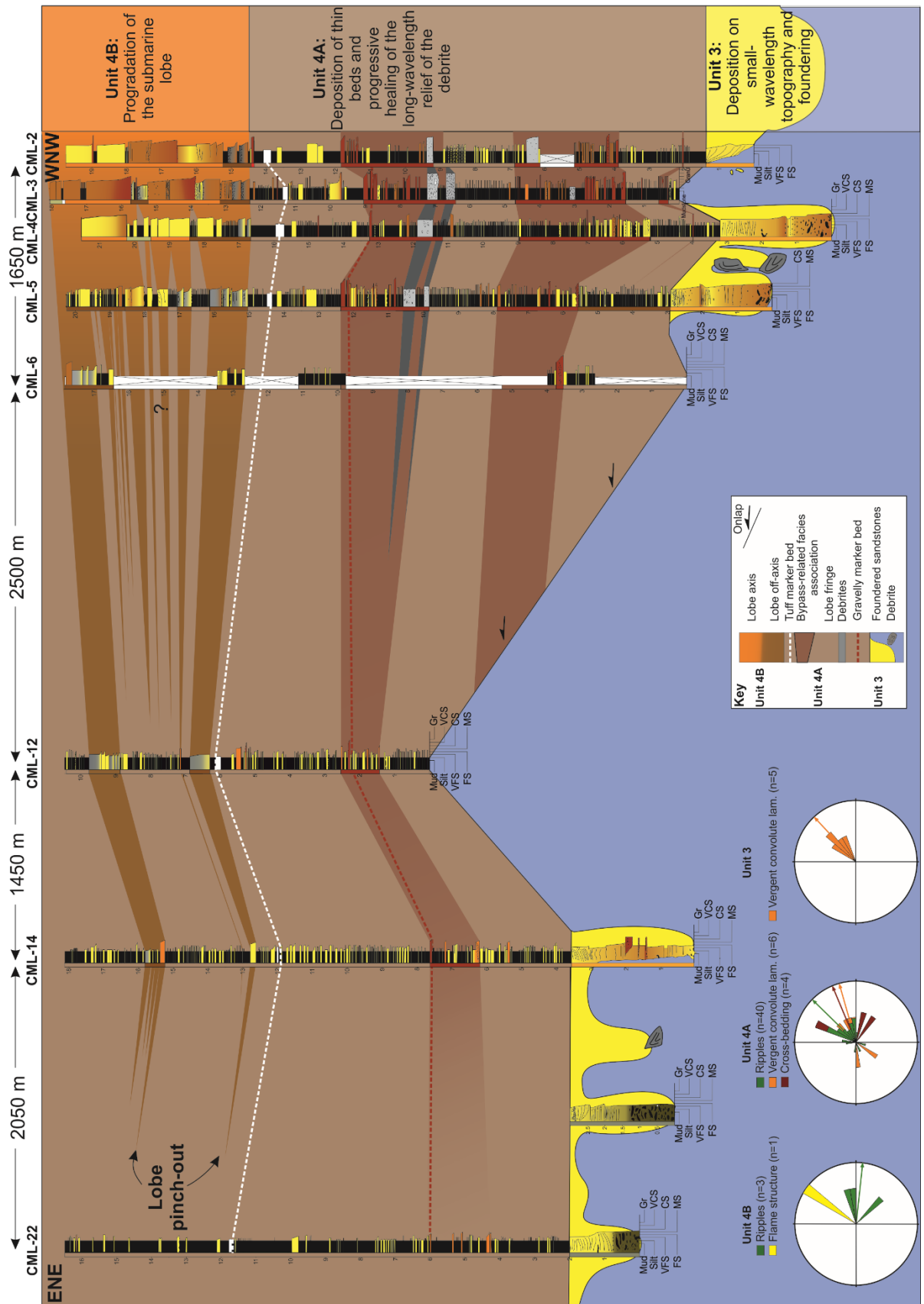


Figure 3.9. The correlation panel focuses on the strata (Unit 3 and 4) overlying the debrite (Unit 2). Note the colour bar next to each log representing the facies associations (see Figure 3.8). Unit 3 is only present in western and eastern sectors whilst absent in the debrite high (CML-

12). The lower part of Unit 4A thins and onlaps the debrite, while the upper one shows a larger lateral extent. Note the gravelly and tuff marker beds (red and white dashed lines, respectively). Unit 4A alternates between fine-grained lobe fringes and coarser healing lobe fringes in the western sector. Coarse-grained healing fringes pinch out, developing fine-grained lobe fringes in the eastern sector. Unit 4B consists of amalgamated thick-bedded sandstone of lobe axis, thinning into medium-bedded dominate lobe off-axis environment in the western sector. The sand-rich lobe thins and fines towards the east, pinching out in the central sector and interfingering with the lobe fringe deposits of Unit 4A. Note that the pinch-out terminations are developed where the debrite relief is highest. The rose diagram shows the details of ripples (green), vergent convolute lamination (orange), asymmetric flame structures (yellow) and cross-bedding (red). Mean vectors of each type are shown, all suggesting a NE trend, except in Unit 4B, where the ripples suggest an E-directed palaeoflow indicating deflection processes. The perimeter of the rose diagrams corresponds to 100% of the value.

3.6.2. Small-scale architecture: foundered sandstones

The steeply-dipping unconformable base, internal deformation and abrupt thickness changes of Unit 3 sandstones contrast with their flat and conformable tops (see stereoplots in Figure 3.9). These sandstone bodies can be subdivided into three different types by their architecture.

Type 1

Description: The thinner foundered sandstone bodies range between 0.5- 2 m thick and are only formed by the banded sandstones (Figure 3.10A and Figure 3.10B). They are characterised by 5-25 m wide lenticular shapes, with thickness/width ratios varying from 1:5 to 1:18. These sandstone bodies show relatively constant thinning rates (~0.25 cm/m) towards their pinch outs. They are characterised by: i) advancing onlap terminations onto Unit 2 at the base and a vertical change into; ii) progressive rotation of laminae and the wedging of the sandstones (Figure 3.10C).

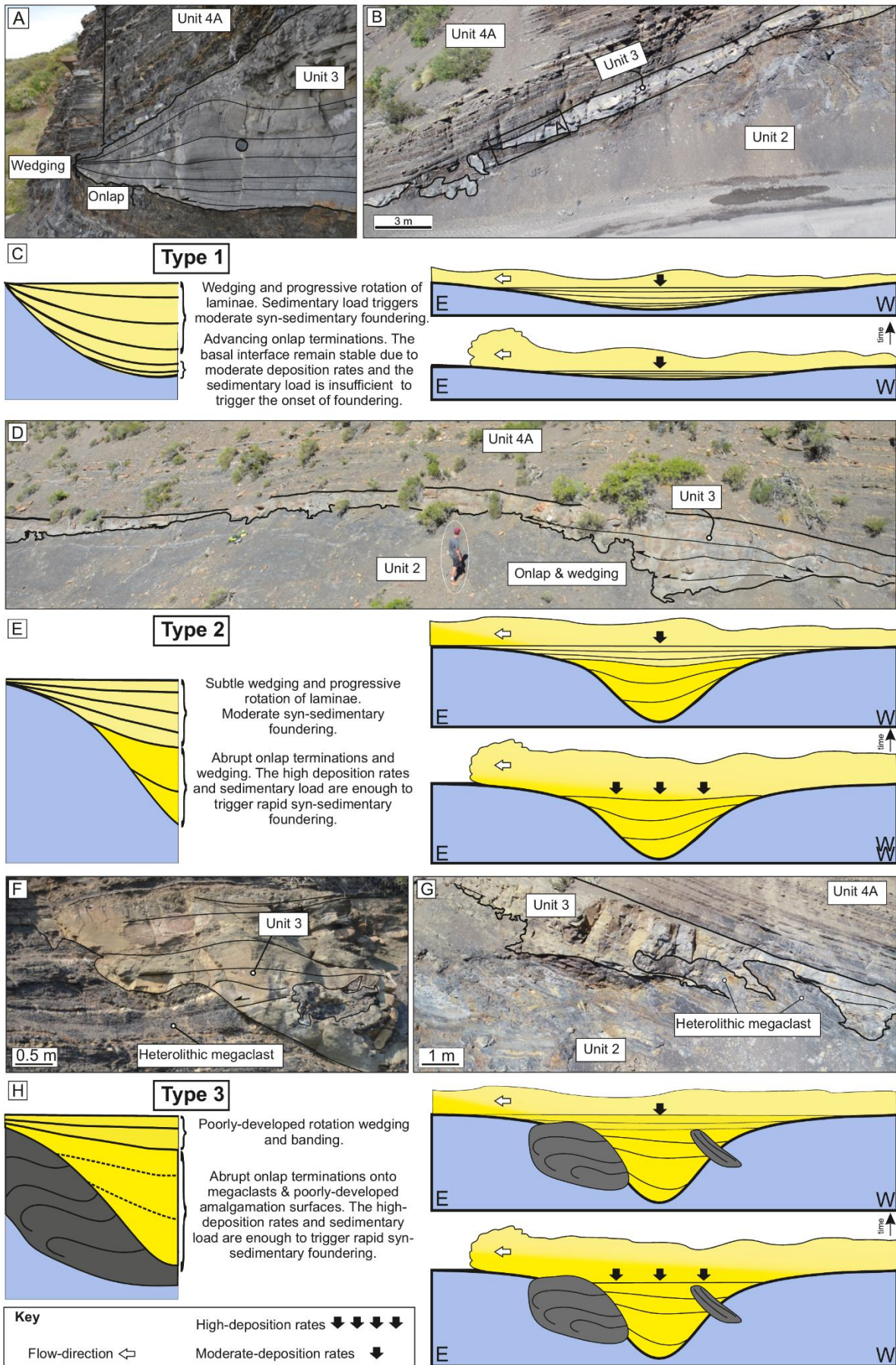


Figure 3.10. Illustrative diagram of foundered sandstone architecture and a model for their development.

Type 1: (A) Thin-bedded sandstone with onlap termination at the base, indicating interaction with inherited relief and wedging associated with the syn-depositional foundering. (B) Bodies wedge smoothly, forming lenticular bodies with flat tops. Note the location of A) indicated by a black rectangle. (C) Sketch of the architecture and evolutionary model of Type 1 architecture: Initial deposition is insufficient to trigger the foundering.

Type 2: (D) Thick-bedded foundered sandstones with associated thinner margins. Central parts are composed of sandstones deposited by high-density turbidity currents, whereas the thinner margins are sandstones interpreted as being deposited under more fluidal sediment gravity flows (Transitional flows). (E) Sketch of the architecture and evolutionary model of Type 2 architecture: Initial deposition is enough to trigger the foundering.

Type 3: (F) and (G) The shape of the thick-bedded sandstone bodies depends on the size and geometry of the thin-bedded megaclast. See Figure 3.5 for more detail. (H) Sketch of the architecture and evolutionary model of Type 2 architecture: While foundering, the sandstone might be protruded by the megaclast due to its higher competence than the surrounding debrite matrix.

Interpretation: The onlap termination indicates the interaction between the parental sediment gravity flow and pre-existing debrite-related relief (e.g. Bakke et al., 2013), and the sediment load was insufficient to trigger the soft-sediment deformation along the upper surface. In contrast, the overlying rotation and wedging represent growth strata associated with the syn-sedimentary foundering. This juxtaposition of terminations indicates that foundering did not start since the onset of deposition of sand due to insufficient stress to trigger the soft-sediment deformation. This termination style supports an incremental layer-by-layer deposition rather than en masse.

Type 2

Description: Thick-bedded foundered sandstones (up to 4 m thick) are characterised by irregular stepped bases and abrupt thickness variations (up to 2 m thinning over 1 m laterally) (Figure 3.10D). They are composed of the juxtaposition of two different divisions: i) lower and ii) upper divisions (Figure 3.10E). The lower divisions comprise structureless sandstones with poorly-developed amalgamation surfaces (F12 or F13). They rarely exceed 10 m laterally, and

3 m in thickness (thickness/width 1:2 to 2:1) and are characterised by both abrupt onlaps terminations and wedging. In contrast, the upper divisions are characterised by banded sandstones (F8), which are more laterally extensive than the underlying division, with a maximum length of 50 m and rarely exceeding 1 m in thickness, and thin laterally towards margins (thickness/width, 1:10).

Interpretation: The coexistence of onlap terminations and wedging indicate that the foundering began at the onset of deposition and the existence of pre-existing topography along the upper surface. The sediment load was enough to trigger the foundering because the debrite relief strongly influenced the initial high-concentration flows, which promoted a loss in flow capacity and deposition under high aggradation rates. The rapid deposition and foundering are responsible for the poorly-developed onlap terminations and amalgamation surfaces. The deposition of lower division deposits promoted a reduction in debrite rugosity due to the infilling of topographic lows, enabling the deposition of laterally more extensive deposits. The rotation and wedging in the banding of the upper division are less well developed than in Type 1 sandstone bodies. This suggests a progressive reduction in syn-sedimentary deformation and increased seafloor stability (e.g. Owen, 1987, 2003).

Type 3

Description: These sandstone bodies show similar facies juxtaposition as in Type 2. In this case, the sandstones terminate against heterolithic megaclasts (Figure 3.10F and Figure 3.10G) due to their preferential location towards the top of the debrite (Figure 3.2, Figure 3.3B and Figure 3.5). Type 3 foundered sandstones diverge from the concave-up geometry of types 1 and 2 as they also depend on the shape of the megaclast. Some megaclasts disconnect bodies

laterally (Figure 3.5), whereas others only impact the base, with the top part of the sandstones undisturbed (Figure 3.10G).

Interpretation: The fluid-saturated matrix and rigid megaclast respond differently to the shear stress exerted by the deposition of sand creating. This differential compaction (Ogata et al., 2014) controls the architecture of the foundered sandstones, creating complex bodies (Figure 3.10H).

3.7 Discussion

3.7.1. Basal shear zone and impact on the substrate

As submarine landslides travel across the seafloor, they exert shear stress on the substrate, coupled with significant over-pressure (Bull et al., 2009; Hodgson et al., 2019; Payros and Pujalte, 2019). This leads to substrate entrainment (Eggenhuisen et al., 2011; Hodgson et al., 2019) and/or deformation (Butler and McCaffrey, 2010; Watt et al., 2012; Dakin et al., 2013; Ogata et al., 2014). The debris flow (Unit 2) incised at least 22.5 m into the substrate (Unit 1; Figure 3.3B). In the central sector, the basal shear surface forms ramps (up to 800 m long, > 2°) and flats (up to 1550 km long; Figure 3.3B; between the logs CML-9 and CML-10) (see Lucente and Pini, 2003; Martinez et al., 2005 for flat-ramp-flat geometry). The stress applied to the substrate during the emplacement is accommodated by both stratigraphic intervals consisting of deformed packages (basal shear-zone) and interfaces consisting of a plane (basal shear-surface) (Alves and Lourenço, 2010), such as the discrete basal shear zone located in upper Unit 1. The absence of contractional features in the deposits underlying Unit 1 supports the deformation as the result of the shear stress produced by the emplacement of the debrite rather than tectonism. The basal shear zone has a variable thickness and deformation styles. It is absent in the western sector, whereas erosion and deformed intervals record high basal shear

stress in the central sector (Figure 3.3B). In the central sector, the deformed package (up to 10 m thick) is characterised by decametre-scale thrusts with metre-scale offsets and drag folding (Figure 3.4B). The predominance of imbricate thrusting over folding, and lack of internal disaggregation within the package, indicate competent substrate rheology (e.g. Van der Merwe et al., 2011). The eastward vergence of the compressional structures (Figure 3.4B) indicates an eastward emplacement direction for the debris flow (Twiss and Moores, 1992), consistent with the palaeoflow indicators in the bounding strata.

The thrusting is attributed to bulldozing by the entrenched debris flow (e.g. Jackson, 2011; Hodgson et al., 2019; Payros and Pujalte, 2019), representing the initial stage of substrate entrainment. Entrainment of megaclasts into a debris flow has been reported in other systems in the subsurface (Moscardelli et al., 2006; Alves and Cartwright, 2009; Sawyer et al., 2009; Dakin et al., 2013; Ortiz-Karpf et al., 2015; Soutter et al., 2018; Nwoko et al., 2020a) and more rarely at outcrop (Ogata et al., 2014; Sobiesiak et al., 2016; Hodgson et al., 2019; Cumberpatch et al., 2021). The progressive increase in thickness and degree of strain along the basal shear zone of Unit 2 and the enrichment in rafted heterolithic megaclasts (Figure 3.3B) suggest downdip evolution of the debris flow, which might have affected the parental debris flow rheology (e.g. Hodgson et al., 2019; Payros and Pujalte, 2019) and bulking of the flow (Gee et al., 2006; Alves and Cartwright, 2009; Butler and McCaffrey, 2010; Hodgson et al., 2019). The preferential location of heterolithic megaclast towards the top of Unit 2 might be related to internal granular convection cells created along with the debris flow, enhanced by the buoyancy of less dense rafted megaclast compared to debrite matrix (Sobiesiak et al., 2016; Hodgson et al., 2019) and kinetic sieving (Legros, 2002). In contrast, conglomerate megaclast are always found at the base of the debrite due to their higher density than the surrounding debrite matrix.

3.7.2. Dynamic debrite topography and impact on overlying strata

The absence of Unit 3 sandstones over the thickest part of the debrite suggests that the sediment gravity flows were strongly stratified and influenced by the debrite relief (Figure 3.3 and Figure 3.9). The sandstone bodies are also disconnected at finer scales, revealing short wavelength (metre-scale) and amplitude (decimetre-scale) rugosity on the debrite surface. The existence of simultaneous short wavelength and amplitude rugosity superimposed on a large-scale wavelength relief on the upper surface of an MTD has also been reported by Armitage et al. (2009), defined as 'surface-topography hierarchy', in the Cretaceous Tres Pasos Formation at the Sierra Contreras (Chile) and by Fairweather (2014) in Carboniferous Paganzo Basin at Cerro Bola (Argentina). In this study, the deposition of sand in pre-existing lows filled the short-wavelength rugosity and triggered the loading of individual sandstone bodies onto the mud-rich debrite (See 'Small-scale architecture: Foundered sandstones' sections), leaving the large-scale relief underfilled (Figure 3.9). The foundering process is evidence of substrate liquefaction and highlights the dynamic interface between the debrite and subsequent flows and their deposits. A similar scenario was proposed by Van der Merwe et al. (2009, 2011) in the Vischkuil Formation in the Laingsburg depocentre (Karoo Basin).

The ability of supra-MTD rugosity to pond turbidity currents travelling across their upper surface is a well-known phenomenon (Kneller et al., 2016). However, the presence of foundered sandstones up- and down-dip of the debrite high and its consistent NE paleocurrent trend suggest connected sediment transport routes across the debrite with no evidence of flow ponding or stripping (Figure 3.9) (e.g. Armitage et al., 2009; Fairweather, 2014). The highly-stratified grown-hugging parental flows of Unit 3 would have been ponded in proximal parts (western sector) if a fully enclosing topography existed, given their reduced ability to surmount obstacles (Al-Ja'Aidi et al., 2004; Bakke et al., 2013), resulting in sand starvation over the debrite in distal settings (Sinclair and Tomasso, 2002; Kneller et al., 2016). The overlying Unit

4A can be traced laterally across the study area, with metre-scale thinning where the debrite is thickest (see CML-12; Figure 3.9). Apart from this, the advancing onlap geometries of the thin beds and the divergence in the overall NE-orientated paleocurrents (rose diagram Unit 4; Figure 3.9) indicate the progressive healing of the large-scale wavelength debrite relief, with some deflection of turbidity currents.

The thin sandstone beds of the upper part of Unit 4A healed the debrite high. However, the gravelly beds thin and fine from proximal to distal areas (western to eastern sectors), and the two debrites pinch out in proximal areas (western sector), suggesting subtle remnant topography (Figure 3.9). The different lateral continuity of individual beds is explained by different rheologies of individual sediment gravity flows, which affect the flow efficiency (Al Ja'Aidi et al., 2004). Cohesive debris flows are more influenced by irregular relief, while low-density turbidity currents are less affected by seafloor topography (Bakke et al., 2013; Soutter et al., 2019). This suggests that laterally continuous thick accumulations of lobe fringes can develop on gentle topographies, while the submarine lobes' axial parts are restricted to lower relief areas. The interaction of thin-bedded turbidite successions with gentle topography has also been reported in other deep-water settings (i.e., 'aggradational lobe fringes'; Sychala et al., 2017c). The deposition of lobe fringe successions reduced confinement, which enabled the deposition of the Unit 4B submarine lobe.

The submarine lobe is characterised by a progressive thinning and fining, developing pinch-out geometries and interfingering with Unit 4A in the area where the relief of the debrite is highest. The development of pinch-out geometries over the areas where the debrite shows a mounded relief and where the Unit 4A onlaps and thins suggests that the relief was not wholly healed with the deposition of Unit 4A and affected the parental flows of Unit 4B.

One explanation is that the exposure exhumes the Unit 4B lobe obliquely, with the medium- to thick-bedded lobe axis deposits in the westernmost sector (CML-1 to CML-4) transitioning into an HEB-dominated fringe, being highly impacted by gentle seafloor topography (Figure 3.11). Alternatively, the seafloor relief could have promoted the modification of flow pathways and deflection of flows, thus changing the downdip orientation. All these scenarios suggest a confined and uncontained (see Southern et al., 2015) lobe-type depositional system. The precise dispersal pattern of the flows remains unknown due to the outcrop limitations. Nonetheless, the documented stratigraphic evolution reveals that long-lived debrite relief and progressive healing by deposition of aggradational lobe fringes enabled the progradation of sand-rich submarine lobe, albeit with changes in flow rheology, the bed style and element-scale pinch-out (Figure 3.11).

Another explanation is that the debrite relief in the central sector might have been rejuvenated through volume changes in the debrite due to differential compaction by loading the lobe itself in the proximal sector through fluid loss or fault-controlled mechanical subsidence. However, it seems unlikely that the deposition of a 5.7 m thick lobe could promote a volume loss in an 8 – 47 m thick debrite, given that both units are separated by an 8 – 22 m thick thin-bedded interval. In contrast, the other two hypotheses are more plausible. Fluid loss-controlled evacuation could have promoted the subsidence of the upper surface of the debrite and overlying units (e.g. Browne et al., 2020). Alternatively, given the early post-rift setting, mechanical subsidence by an east-facing and N-S striking fault (Manceda and Figueroa, 1995) could have generated more accommodation in the western part of the study area (see Cristallini et al., 2006). However, this implies a very localised and rapid reactivation, and no other evidence for post-rift tectonism is identified.

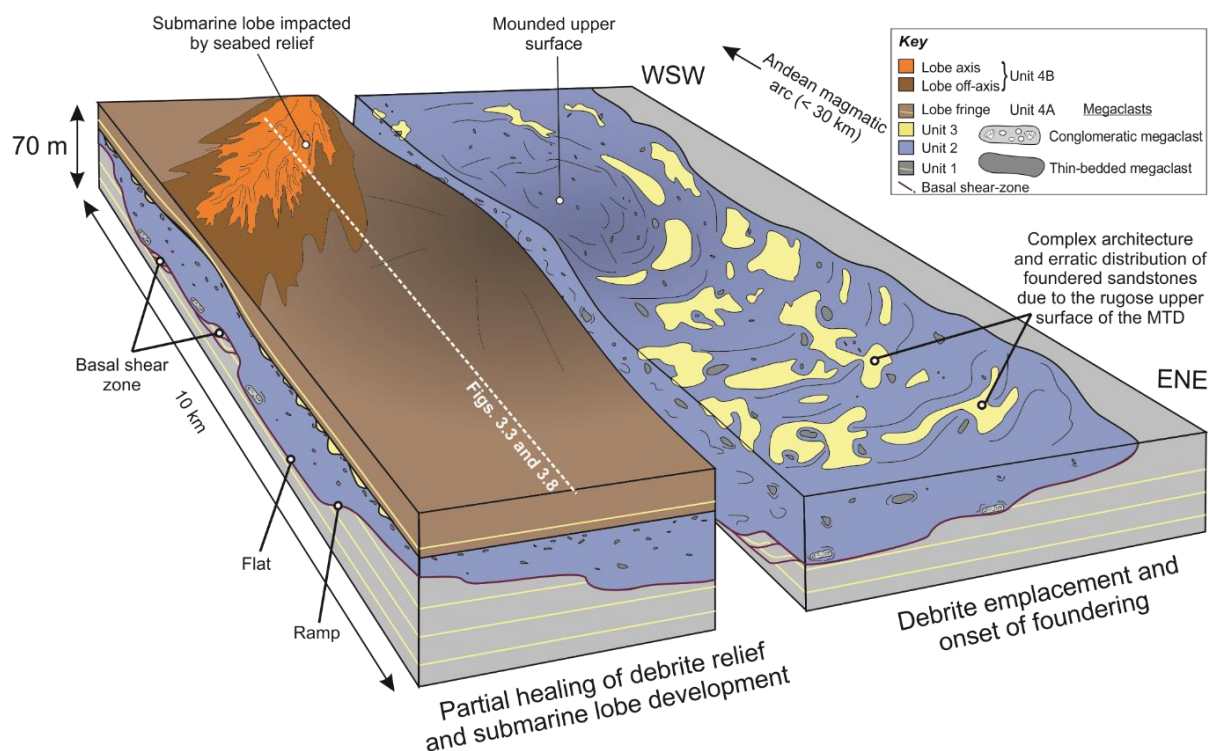


Figure 3.11. Down-dip oriented schematic diagram illustrating the relief created by the debrite and the impact on younger sand-rich units. Foundered sandstones fill the small-scale rugosity, leaving the kilometre-scale accommodation underfilled. The submarine gravity flows are deflected by long-lived subtle debrite-related relief (right block). Partial healing and draping of the debrite with the progradation of the lobe, which is gently impacted by the long-lived inherited relief. Note the white dashed line representing the correlation shown in Figure 3.3 and Figure 3.9.

3.7.3. Origin and role of the mass-wasting process as a trigger for turbidite system development

The emplacement of the > 9.6 km long and erosional debrite in the Chacay Melehue depocentre reflects an abrupt change in sedimentation patterns previously dominated by dilute mud-rich flows (Unit 1). The first significant sand influxes in the depocentre for ~6 Myr since the Aalenian (interval II of Gulisano and Gutiérrez Pleimling, 1995) are recorded by the sand-rich deposits (Unit 3) immediately overlying the debrite (Figure 3.2C). The juxtaposition of sand-rich turbidites over debrites (metres to hundreds of meters thick) have been reported in other systems (Kleverlaan, 1987; Labaume et al., 1987; Payros et al., 1999; Fallgatter et al., 2017).

These authors suggest that the debris flow underwent a period of mixing with ambient water, leading to the generation of an overriding co-genetic turbidity current. The foundering phenomenon reported here reveals a close spatiotemporal relationship between the debrite emplacement (Unit 2) and overlying sandstone deposition (Unit 3). An alternative mechanism is that the mass-failure event altered the basin margin physiography such that a sand source was captured. Mass-wasting processes responsible for the evacuation of material from shelf edge and upper slope areas alter the bathymetric configuration of basin margins and promote the funnelling of sediment stored in shallow marine environments through slide scars (e.g. Moscardelli and Wood, 2008; Kneller et al., 2016; Steventon et al., 2020) (Figure 3.12). The role played as a trigger mechanism for sand delivery to deep-water areas by the mass-wasting event is a plausible scenario given the sand-starvation recorded in the coeval deposits of Los Molles Formation along the eastern margin of the Chacay Melehue depocentre (Veiga et al., 2013)

Given the palaeoflow and kinematic indicators (Figure 3.4B), the thickness patterns of the studied units (Figure 3.3B), and previous studies on sediment supply from the volcanic arc (Vicente, 2005), it is proposed that the mass failure originated to the west of Chacay Melehue where a major syn-rift fault is located close to the volcanic arc (< 30 km; Manceda and Figueroa, 1995; De La Cruz and Suarez, 1997; Vicente, 2005). The role of the western volcanic arc as a source area for the early post-rift sediment supply in the Chacay Melehue depocentre is supported by the southeastwards directed paleocurrents measured in the Aalenian turbidite system at the base of the Los Molles Formation (Vicente, 2005; Figure 3.2) and the abundance of pyroclastic deposits within Los Molles Formation stratigraphy (Zöllner and Amos, 1973; Rosenfeld and Volldaeimer, 1980; Gulisano and Gutiérrez Pleimling, 1995; De La Cruz and Suarez, 1997; Llambías and Leanza, 2005). The oyster-bearing conglomerate megaclast and well-rounded volcanic epiclast within the matrix of the debrite indicate long-lived reworking

in shallow-marine settings prior to the mass failure, suggesting a shallow-water origin or remobilization of older slope strata, including shallow-marine deposits. This could represent the downslope transfer of sand following the collapse of reworked volcanoclastic deposits along the magmatic arc (Figure 3.12). The evolution from the initial mass-wasting sediment supply responsible for erratically distributed founder sandstone bodies (Unit 3) to a more mature system with the subtle distribution and diversity of lobe architectural elements (Unit 4) reflects the evolution to a more organised sediment supply system (Figure 3.11). This is abruptly superseded by a return to sand-starved conditions with dominant dilute mud-rich flows and hemipelagic deposition until the end of the Lower Callovian (Gulisano and Gutiérrez Pleimling, 1995).

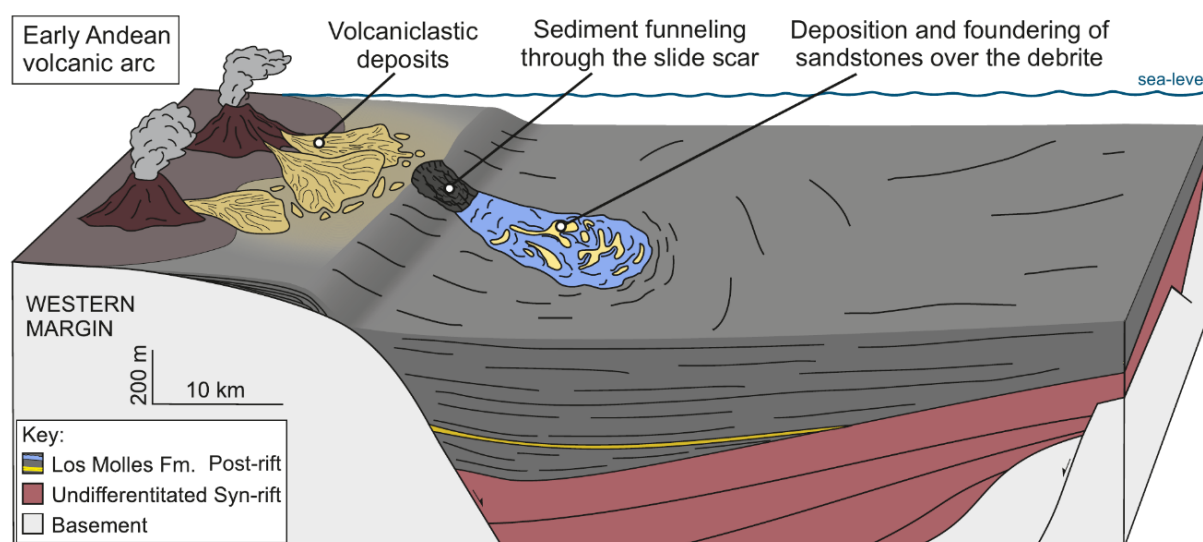


Figure 3.12. Schematic diagram illustrating the role of the mass failure recorded in the Chacay Mehue depocenter as the trigger for downslope remobilisation of sand from shallow-marine settings.

3.8 Conclusions

This study investigates the anatomy and architecture of a > 9.6 km long exhumed debrite. It shows how its twofold short- and long-wavelength relief and composition provided a likely input route for the subsequent sand-rich deep-water system and influenced flow behaviour

depositional patterns. The basal surface of the debrite forms ramps and steps, indicating deep incision and entrainment of the substrate that includes megaclasts. The foundering of overlying sands, their resultant geometry and spatial distribution, and the down-dip increase in mud content, indicate a dynamic and rugose upper surface to the debrite and complex flow-deposit interactions. The spatial distribution of the foundered sandstones indicates ground-hugging flows and the existence of debrite relief, which was progressively but not entirely healed by the submarine lobe. However, the architecture and facies distribution of the submarine lobe and their parental flows were still impacted by the long-lived, possibly rejuvenated, debrite-related topography.

The debrite emplacement coincided with an abrupt change in sediment supply to the Chacay Melehue depocentre from long-term mud-rich sedimentation to a transient sand-rich system. This change in depositional character is interpreted to have resulted from the funnelling of sediment stored in shallow marine environments to the west through a slide scar created by the debris flow, thus reconfiguring the sediment delivery pathway. Therefore, this study highlights that basin margin mass failures and their deposits play a key role in sediment dispersal patterns into deep-water settings and the behaviour of subsequent sediment gravity flows travelling across their upper surface.

4. Stratigraphic change in flow transformation processes recorded in early post-rift deep-marine lobe complexes in an intraslope setting

Martínez-Doñate, A.¹, Kane, I.A.¹, Hodgson, D.M.², Privat, A. M-L. J², Jackson, C.A-L.¹, Schwarz, E.³, Flint, S.S.¹

1. School of Earth and Environmental Sciences, University of Manchester, Manchester M13 9PL, UK.
2. School of Earth and Environment, University of Leeds, Leeds LS29JT, UK.
3. Centro de Investigaciones Geológicas (CIG), La Plata, Provincia de Buenos Aires, Argentina.

4.1. Abstract

The Early Jurassic Los Molles Formation in the Neuquén Basin of western Argentina is a rare example of well-exposed syn- to post-rift stratigraphy. In the Chachil Graben, the onset of the early-post-rift stage is marked by the drowning of a carbonate system and the development of two deep-marine intraslope lobe complexes. This field-based study involves correlating eleven stratigraphic logs, field mapping and petrographic analysis to document how grain size and texture within intraslope lobe sandstones change from the centre to the frontal pinch-out of the Chachil Graben. Eight different bed types are identified: two turbidites (Type A and B beds), four transitional flow deposits (Type C, D, E, F beds), and two chaotic deposits (Type G and H beds). Fifteen lobes are grouped into two stacked lobe complexes that show a stratigraphic evolution from a lower argillaceous sandstone-dominated lobe complex built by transitional flow deposits to an upper coarser-grained, cleaner lobe complex largely constructed by turbidites. The petrographic analysis quantified sandstone mineralogy, matrix content, grain size and sorting, revealing that both lobe complexes are volcanic arc-sourced. It is proposed that the differences in the character of the two lobe complexes are due to maturing of sediment

transport routes through progressive healing of the intraslope relief with a concomitant decrease in seabed erosion and flow bulking. A model for intraslope lobe complex development that accounts for the impact of flow confinement on sediment gravity flows by the early post-rift inherited topography is also proposed. The bed type distribution and stratigraphic evolution in both lobe complexes suggest that high-density and clay-rich flows terminate more abruptly against confining slopes and produce greater depositional variability than lower-density, clay-poor flows. Studying early post-rift submarine lobes and their interaction with inherited topography can help develop sedimentary models that consider a wide range of physiographic settings.

4.2. Introduction

Deep-water lobes formed by deposition from sediment gravity flows are a major component of submarine fans and are found in various tectonostratigraphic settings (e.g., Shanmugam and Muiola, 1988; Curray et al., 2002). Therefore, submarine lobes represent a crucial record of the interplay of climate, tectonics and eustasy (Sømme et al., 2009). Deep-marine lobes can form in a wide variety of tectonic settings, including syn-rift (e.g. Leppard and Gawthorpe, 2006; Strachan et al., 2013; Henstra et al., 2016; McArthur et al., 2016; Cullen et al., 2020) and post-rift stages of extensional basins (e.g. Haughton et al., 2003; Southern et al., 2017; Dodd et al., 2019; Hansen et al., 2021; Privat et al., 2021). Syn-rift depositional systems develop in isolated, normal fault-controlled depocentres that contain wedge-shaped packages of sediment fed by axial (i.e., fault-parallel) and transverse (i.e., fault-perpendicular) sediment supply systems (Ravnås and Steel, 1998). In contrast, post-rift depositional systems typically fill relief inherited from the preceding rift phase (Privat et al., 2021), with regional thermal subsidence providing additional accommodation (e.g. Zachariah et al., 2009). As a result, post-rift

sediment dispersal and resultant stratigraphic architecture can be highly variable and characterised by a range of stratal terminations onto intrabasinal topography (Prosser, 1993; Argent et al., 2000; Gabrielsen et al., 2001; Færseth and Lien, 2002; Dmitrieva et al., 2018). Sediment gravity flows interacting with topography can change both flow character (velocity, concentration) and direction (Kneller et al., 1991; Al Ja'Aidi et al., 2004; Soutter et al., 2021); the resultant deposits differ from those in unconfined settings, which generally have more predictable facies variability (e.g. Prélat et al., 2009; Spychala et al., 2017b). The influence of seafloor relief on bed types, facies transitions and the architecture of lobes bounded by steep slopes ($> 3^\circ$) has been well-documented in exhumed, highly confined settings (e.g. McCaffrey and Kneller, 2001; Sinclair and Tomasso, 2002; Patacci et al., 2014; Soutter et al., 2019). In contrast, there are fewer documented exhumed systems in which intraslope lobes developed above subtle slope changes (Smith, 2004; Burgreen and Graham, 2014; Spychala et al., 2017c; Privat et al., 2021). This is partially attributed to more subtle bed type changes and pinch-out terminations, which might have been under-recognised in exhumed and subsurface analogues. Petrographic analysis and bed-scale characterisation can help us to understand flow transformations at the event bed scale and the physiographic configurations of intraslope settings. Syn- and post-rift lobe systems are typically deeply buried, and outcrop analogues are rarely well-preserved due to later deformation during basin inversion. Therefore, our understanding of their bed types, facies transitions, and depositional architecture remains limited.

Early Jurassic strata in the Neuquén Basin (Figure 4.1A) provide a rare example of an exhumed, syn- to post-rift sedimentary succession that is well-preserved and well-exposed. In the Chachil Graben, located in the SW of the Neuquén Basin (Figure 4.1B and Figure 4.1C), the onset of the early-post rift stage is recorded by the drowning of a carbonate system and the subsequent

development of an intraslope lobe system in the Los Molles Formation (Figure 4.2; Privat et al., 2021). The objectives of this chapter are to 1) characterise the bed types of the early post-rift submarine lobe complexes and their variability towards pinch-outs; 2) document the petrography and texture of the different bed types in order to better understand the flow processes and environments of deposition; 3) discuss the stratigraphic evolution of deep-marine lobes deposited in a confined post-rift intraslope setting. A well-calibrated sedimentary and architectural model will improve our understanding of early post-rift intraslope lobes and potentially be used as an analogue for lobes in similar settings elsewhere.

4.3. Geological setting

The Neuquén Basin is located between 32°S and 40°S in central-western Argentina and central-eastern Chile, covering > 160,000 km². It was bounded to the northeast by the Sierra Pintada System, to the south by the North Patagonian Massif, and to the west by the Andean magmatic arc (Figure 4.1A; Legarreta and Uliana, 1996; Franzese and Spalletti, 2001). The stratigraphic record of the Neuquén Basin is characterised by Mesozoic (starting in the Late Triassic) to early Cenozoic, continental and marine siliciclastic, carbonate, evaporitic, and volcanic rocks (Legarreta and Uliana, 1996; Howell et al., 2005). Three tectonic phases are recognised in the development of the Neuquén Basin (Vergani et al., 1995; Franzese and Spalletti, 2001, 2003): i) Triassic-to-Early Jurassic rifting, characterised by the development of narrow and isolated depocentres; ii) Early Jurassic (Toarcian) to Early Cretaceous post-rift thermal subsidence, associated with the development of the back-arc basin; and iii) the Late Cretaceous to early Cenozoic formation of a foreland basin related to Andean compression. This chapter focus on the earliest Los Molles Formation (Toarcian) (Weaver, 1931), deposited during the early post-rift stage in the Chachil Graben.

Chapter 4: Stratigraphic change in flow transformation processes recorded in early post-rift deep-marine lobe complexes in an intraslope setting

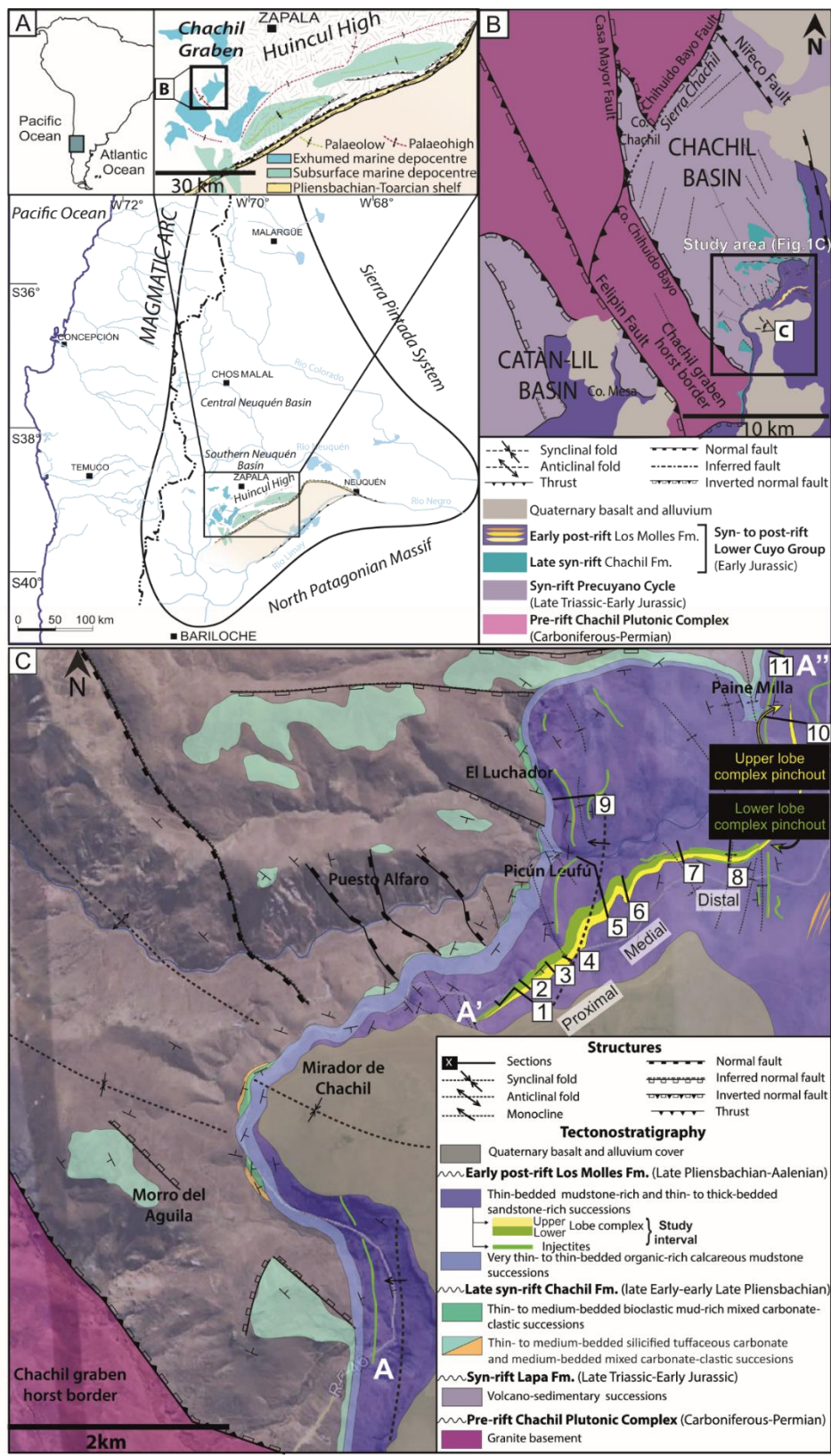


Figure 4.1. (A) Location map of the Neuquén Basin and the Chachil Graben. (B) Map of the Chachil Graben (Privat et al., 2021). (C) Detailed map of the Chachil Graben showing Los Molles Formation with the location of measured sections, adapted from Privat et al. (2021). See Figure 4.2 for A-A'-A'' cross-section.

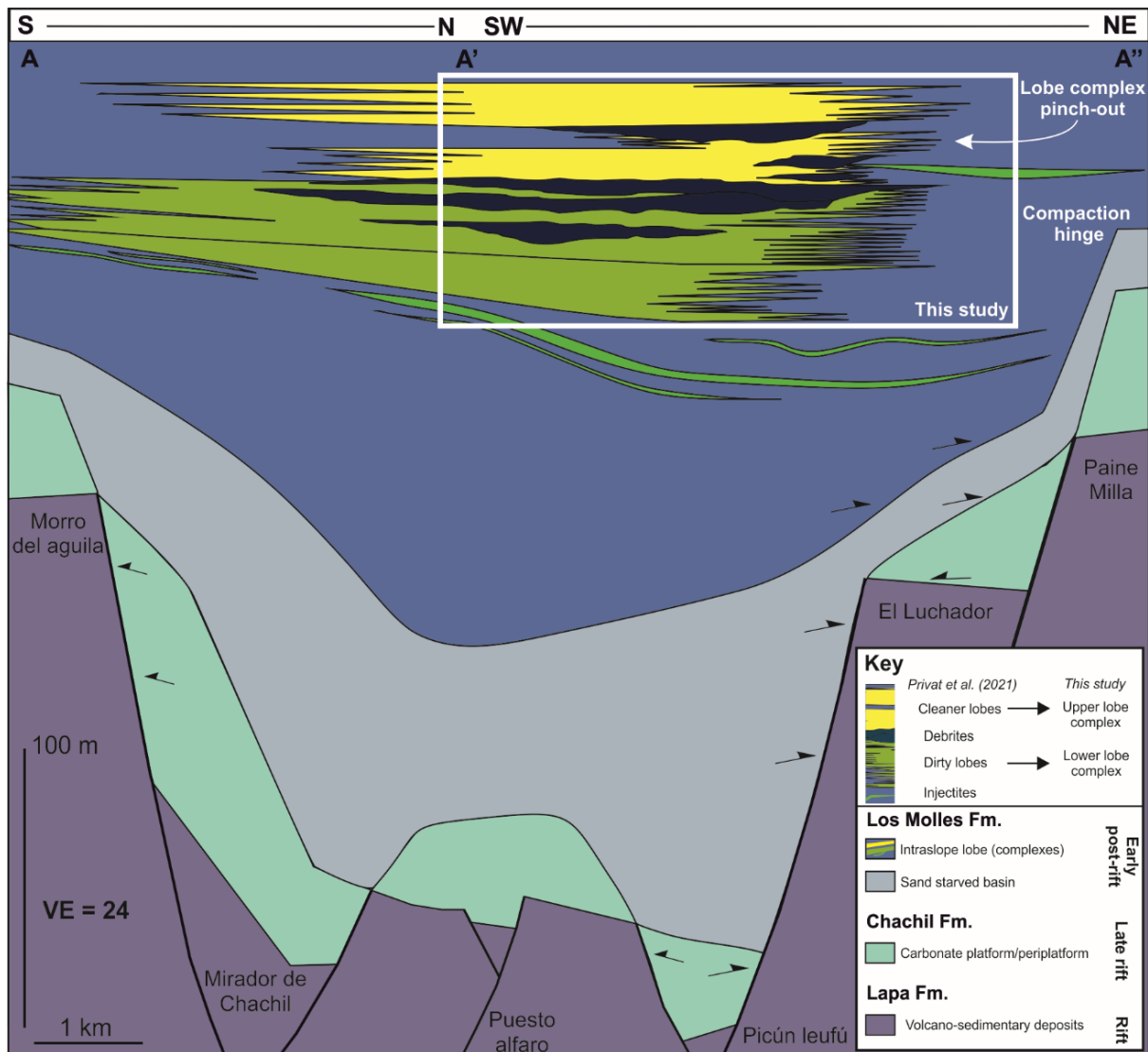


Figure 4.2. Schematic correlation shows the architecture of Lower and Upper Lobe Complexes and the debrites (modified from Privat et al., 2021). The onset of the early-post rift stage is recorded by the drowning and deepening of a carbonate system and the subsequent development of a deep-water lobe system. The palaeoflow direction is towards NE (from left to right) (see rose diagrams in Figure 4.13). Note that the debrites pinch out in a more proximal position than the lobe complexes, which show a progressive basinward advancement of their pinch-out from the base to the top (more detail in Figure 4.13).

4Study area: Chachil Graben

The Chachil Graben is a 15 km long, 10 km wide, NNW-SSE trending normal fault-controlled depocentre. It is bounded to the northwest and southwest by the SE and NW dipping Chihuido Bayo Fault system (Figure 4.1). The initial syn-rift volcano-sedimentary deposits (Lapa

Formation; Precuyano Cycle) thicken northwards from < 400 m at the basin margins to 2 km near its centre (Franzese et al., 2006). These thickness changes were controlled by fault systems striking parallel or oblique to the Chihuido Fault system, along the horst forming the southwestern border of the depocentre (Figure 4.1B). Late syn-rift extension promoted the development of footwall highs (Paine Milla, El Luchador, Puesto Alfaro and Morro del Aguila) and lows inside the Chachil Graben (Mirador de Chachil and Picún Leufú) (Figure 4.1C and Figure 4.2; Franzese et al., 2006; Privat et al., 2021). Regional subsidence associated with the late syn-rift phase led to the flooding of the rift depocentres, promoting the onset of carbonate sedimentation (Chachil Formation; Weaver, 1942; Leanza et al., 2013). Rapid basin deepening and drowning of the carbonate system led to the deposition of organic-rich, calcareous mudstones that draped inherited rift topography (basal Los Molles Formation) (Figure 4.2; Privat et al., 2021). Healing of rift topography and the onset of extra-basinal siliciclastic supply promoted the development of early post-rift intraslope lobe complexes (Privat et al., 2021).

Differential compaction of organic-rich mudstones over inherited rift topography promoted a long-lived seabed relief in the Chachil Graben (Figure 4.2; Privat et al., 2021). Similar differential compaction has also been documented in the subsurface (Cristallini et al., 2009) and exhumed depocentres elsewhere in the Neuquén Basin (Veiga et al., 2013; Sugawara & Nikaido, 2014). In the Chachil Graben, a S-dipping compaction hinge over the El Luchador fault block acted as an oblique counterslope to the NE-directed sediment gravity flows, controlling the architecture and pinch-out location of two submarine lobe complexes (Figure 4.2; dirty and cleaner lobe complexes, *sensu* Privat et al., 2021). Both lobe complexes are 6-8 km long, 5 km wide and < 50 m thick and are bound at their base and top by a > 4 m thick mudstone interval or an erosionally-based debrite (Figure 4.2; Privat et al., 2021). This study refers .3.1. to them as the Lower and Upper Lobe Complex, respectively (Figure 4.2). Their

constituent bed types (Figure 4.3) and stratigraphic architecture are described and compared as a basis for proposing an overall depositional model.

4.4. Data and methods

The dataset comprises 11 sedimentological logs 1:25 scale (Figure 4.1C), collected over a horizontal distance of 4 km. Logs were correlated, and the overall depositional architecture was constrained by walking out individual sandstone-rich packages and several stratigraphically distinct marker beds. Data collected included lithology, bed thickness and contacts, sedimentary structures, and palaeocurrent measurements from grooves, flutes, cross-bedding, flame structures, and ripple cross lamination. Uncrewed Aerial Vehicle (UAV) photogrammetry was used in conjunction with mapping and logging to capture the architecture of the sandstone and mudstone packages within the investigated stratigraphic interval.

Petrographic analysis was performed on 40 orientated and polished thin sections collected in 16 sandstone beds logged at a 1:2 scale (Figure 4.4-Figure 4.9). To understand the longitudinal character of flows, up to five samples were taken from the base to the top of the sandstone beds (see similar methods in Kane et al., 2017; Southern et al., 2017; Bell et al., 2018; Fildani et al., 2018). The long axes of 200 grains per thin section were measured (Appendix Table 2); this enabled the quantification and variations in sorting for each sample. Detrital components were quantified using the Gazzi-Dickinson point counting method (Gazzi, 1966; Dickinson, 1970; Zuffa, 1985). Percentage abundance was quantified by counting 400 points per thin section (Appendix Table 1) using an automated and motorised stepping stage controlled by PETROG software (PETROG System, Conwy Valley Systems Ltd., UK). The points were stochastically distributed across an aleatory grid, where the minimum interpoint distance was larger than the

coarsest grain fraction to avoid repetition (Van der Plas and Tobi, 1965). Point counting enabled the classifications of grains into 11 classes, matrix (particulate matter < 0.062 mm) and cement. The results were plotted on a matrix versus mean size grain diagram (Figure 4.10) and three ternary diagrams (Figure 4.11; Qm-F-Lt, Dickinson et al. (1983); Lm-Lv-Ls, Ingersoll and Suczek (1979); Qp-Lv-Lsm diagram, Dickinson (1985)) because combinations of specific end-members discriminate between different grain properties (Hulka and Heubeck, 2010; Ciccioli et al., 2014).

4.5. Bed types

The sandstone beds were divided into eight bed types (Figure 4.3; Type A-H beds) based on their thickness, texture (e.g., matrix content, grading, mudstone clast content), grading, and sedimentary structures. Petrographic analysis was used to quantify the mineralogy, matrix content, grain size range, and sorting (Type A-F beds; Figure 4.4-Figure 4.9) to support the outcrop-based interpretation. Samples with > 15 % matrix content were considered matrix-rich, with < 15% considered matrix-poor, based on the threshold of Pettijohn et al. (1972), which is similar to the one proposed in Sylvester and Lowe (2004) (~16%). The petrographic analysis did not differentiate between detrital and authigenic matrix, but the abundance of carbonaceous matter, micas, fine quartz and feldspar grains suggest that the matrix is predominantly detrital (Lowe and Guy, 2000). Deformation of weak detrital grains such as sedimentary lithoclasts (Ls) and devitrified volcanic clasts (Lv) contributed to the formation of the detrital matrix (pseudomatrix) (Dickinson, 1970). Two additional bed types had no petrographic analysis because they were not genetically related to the flows responsible for the formation of intraslope lobes (Type G beds) or do not represent depositional event beds (Type H beds) (Figure 4.3).

Chapter 4: Stratigraphic change in flow transformation processes recorded in early post-rift deep-marine lobe complexes in an intraslope setting


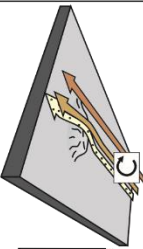



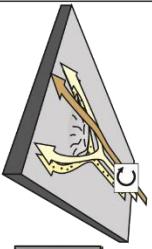

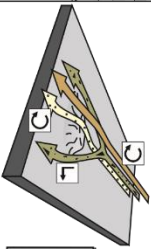



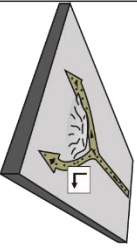




Bed Type	Process interpretation	Interaction with topography
<p>A</p>  <p>Bed thickness: ≤ 0.2 m Grain size: silt to fine sand Sedimentary structures: planar to ripple lamination Gradation: Normally graded</p>	<p>LDTC</p> <p>Deposition and tractional reworking by low-density turbidity current (Lowe, 1982; Best and Bridge, 1992; Hiscott, 1994a).</p>	 <p>Turbulent</p>
<p>B</p>  <p>Bed thickness: 0.2 - 1.2 m Grain size: fine sand to granular Sedimentary structures: Structureless with laminated tops, common grain size breaks and rare dune-scale cross lamination Gradation: Weakly normally graded to ungraded</p>	<p>HDTC, TETF or LTFP</p> <p>Deposition from high-density turbidity current (sensu Lowe, 1982) with high aggradation rates (Summer et al., 2008; Talling et al., 2012. Locally recording erosion (Kane et al., 2017) and bypass (Stevenson et al., 2015). Locally, turbulent flows can transform into turbulence-enhanced transitional flows or transitional plug flows (Baas et al., 2009, 2011, 2016).</p>	 <p>Turbulent</p>
<p>C</p>  <p>Bed thickness: 0.2-0.4 m Grain size: silt to fine sand Sedimentary structures: structureless base, banding in the middle and HCS, rounded ripple, or sinusoidal lamination Gradation: Weakly normally graded</p>	<p>LTPF</p> <p>Deposition from slow to moderately decelerating lower transitional plug flows (Baas et al., 2009, 2011, 2016). The banding is the result of tractional reworking (Baas et al., 2009, 2011, 2016, Stevenson et al., 2020), while ripple lamination indicates dilution from the mixing with ambient water.</p>	 <p>Hybrid</p>
<p>D</p>  <p>Bed thickness: < 0.2 m Grain size: silt to medium sand Sedimentary structures: structureless base, argillaceous bands and planar to ripple lamination Gradation: Weakly normally graded to ungraded</p>	<p>UTPF/QLPF</p> <p>Deposition from UPTF/QLPF (Baas et al., 2009, 2011, 2016). H1 divisions suggest shearing of mud flocs and mudstone clasts caused by a transitional flow with a turbulent component. The development of H3 division, and lack of H2, suggest abrupt deceleration rates (Baas et al., 2011, 2016; Stevenson et al., 2020) related to the distal collapse of the flow (Kane et al., 2017). The grooves at the base indicate that UPTF/QLTF were preceded by bypassing and forerunning debris head responsible for the entrainment of cohesive clay from the substrate (Baas et al., 2021).</p>	 <p>Hybrid</p>
<p>E</p>  <p>Bed thickness: 0.2-1 m Grain size: silt to medium sand Sedimentary structures: structureless and planar laminated tops Gradation: Weakly normally graded to ungraded</p>	<p>UTPF/QLPF</p> <p>The internal layering suggest a density stratification and different rheology within the same parental flow. The elevated matrix and abundant mudstone clast content suggest transitional flow behaviour (Kane and Ponten, 2012). H1 divisions suggest shearing of mud flocs and mudstone clasts caused by a transitional flow with a turbulent component. In contrast, ungraded and mudstone clast-rich division, represent transport by the matrix-strength of a cohesive and laminar flow, and deposition by cohesive freezing.</p>	 <p>Hybrid</p>
<p>F</p>  <p>Bed thickness: 0.2 - 1 m Grain size: fine to coarse sand Sedimentary structures: structureless and weakly laminated tops Gradation: Weakly normally graded to ungraded</p>	<p>UTPF/QLPF</p> <p>Deposition from UPTF/QLPF (Baas et al., 2009, 2011, 2016) characterised by an abrupt loss in capacity (Hiscott, 1994a), high sediment fallout and reduced tractional reworking (Talling et al., 2012). The crude normal grading and upwards increasing matrix suggest some turbulence at the base of the parental flow, although the dominant rheology was likely an intermediate yield strength laminar flow (Talling et al., 2012). However, the abundance of grooves suggest the development of the laminar plug at the base of these flows or being by a forerunning and bypassing debris flow (Baas et al., 2021), which led to flow bulking (sensu Haughton et al., 2009)</p>	 <p>Hybrid</p>
<p>G</p>  <p>Bed thickness: 0.2 - 5 m Grain size: clay to medium sand Sedimentary structures: Chaotic and structureless Gradation: Ungraded</p>	<p>QLPF/LPF</p> <p>Cohesive laminar debris flow deposition (Lowe, 1982; Sohn et al., 1997) of intermediate to high yield strength (Talling et al., 2012). The unconformable base and both sandstone and heterolithic clasts suggest an erosive nature and significant entrainment of compacted substrate (Dakin et al., 2013; Hodgson et al., 2019; Martinez-Doñate et al., 2021). The mixing of the cohesive laminar flow with ambient water might have diluted the basal part of the flow (Hampton, 1970; Mohrig et al., 1998; Marr et al., 2001)</p>	 <p>Laminar</p>
<p>H</p>  <p>Bed thickness: 0.1 - 4 m Grain size: fine- to medium-grained sand Sedimentary structures: Groove marks at both bed base and top</p>	<p>Postdepositional clastic injection</p> <p>Clastic injections associated with compaction-driven fluid expulsion (Hurst et al., 2011). Therefore, sub-horizontal thick sandstones are clastic sills with associated clastic dykes. Grooves at the base and top support laminar flow through lateral pressure transfer (Cobain et al., 2015).</p>	 <p>Laminar</p>

Figure 4.3. Bed type descriptions, depositional process interpretations and the generalised relationship between flow rheology and termination style (modified from Bakke et al., 2013).

4.5.1. Type A beds

Description: Thin-bedded (< 0.2 m thick), matrix-rich (> 15 %), planar- and ripple-laminated with sharp, planar bed bases and tops. Matrix content increases upwards within the bed (Figure 4.4; S13 sample bed: 17-33%). Beds are poorly to moderately sorted and normally graded, comprising very fine- to medium-grained sandstones. When analysed under the microscope, millimetre-scale mudchips are aligned along the laminae (Figure 4.4G; CH-26). Ripples show an overall NNE palaeocurrent. However, ripples show a broad divergence, even developing bidirectional ripple laminations. Near the pinch-outs, ripples are commonly replaced by convolute lamination.

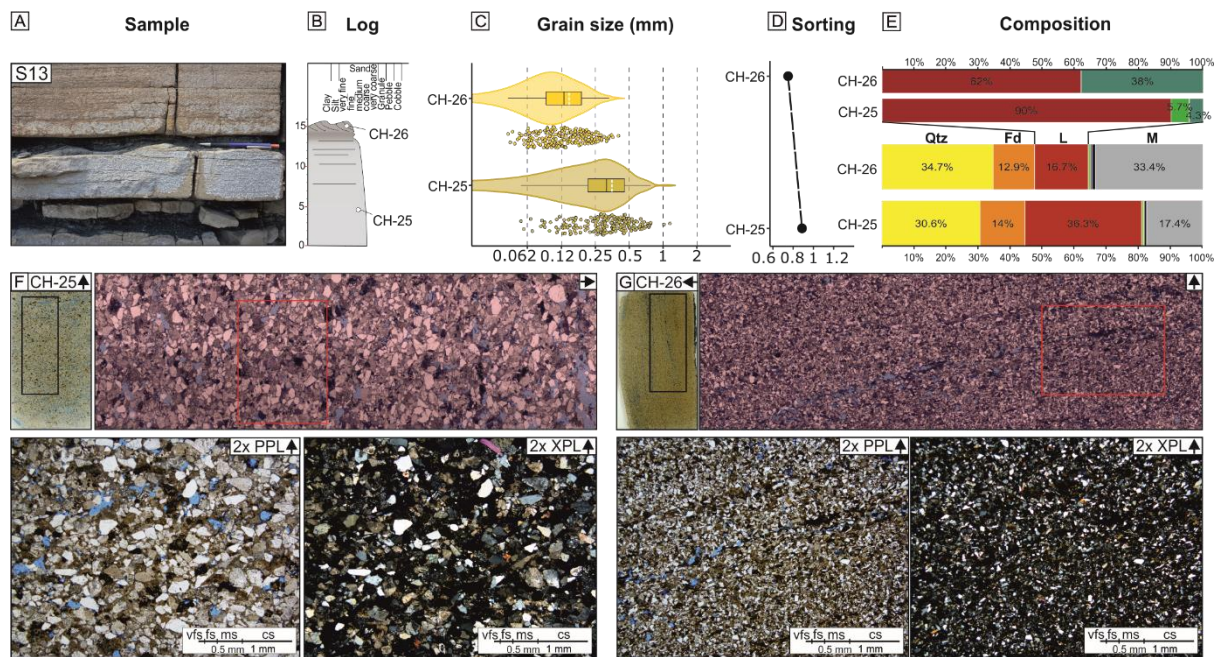


Figure 4.4. Summary diagrams illustrating Type A beds, (A) outcrop photo of the sampled bed, (B) detailed log (1:2 scale) of the sample bed, (C) grain size (200 measurements per sample), (D) sorting and (E) mineralogy (400 measurements per sample). Representative thin section (F; CH-25 and G; CH-26) scans, photomosaic and photomicrographs (PPL and XPL). Note black squares indicating the location of the photomosaic and red squares in the photomosaic indicating the position of the photomicrographs. The arrows in the top right show the top of the samples.

Interpretation: These bed types represent deposition from low-density turbidites (*sensu* Lowe, 1982). Grains are suspended due to flow turbulence and deposited under aggradation rates that are sufficiently slow to permit differential grain size settling and tractional reworking (Best and Bridge, 1992; Hiscott, 1994a; Sumner et al., 2008). Bidirectional ripple laminations suggest flow deflection and reflection against seafloor relief (Kneller et al., 1991; Edwards et al., 1994). Convolute lamination suggests high sedimentation rates and has been attributed to the development of reflected bores and internal waves, which might be related to interaction with seafloor relief (Tinterri et al., 2016). The upward increase in matrix content reflects the differential grain size settling from waning flows, which deposit coarser material near bed bases and finer material near bed tops (Mulder and Alexander, 2001).

4.5.2. Type B beds

Description: Medium- to thick-bedded (0.3-1.2 m thick), matrix-poor (< 15 %) sandstones, with sharp planar tops and sharp erosive bed bases with abundant multidirectional grooves with an ENE-WSW oriented dominant trend. Type B beds are poorly to moderately sorted and weakly normally graded, passing upwards from coarse-grained (locally very coarse and granular) to medium- to fine-grained sandstone (Figure 4.5; S6 sample bed). Overall, they show an upward decrease in centimetre-scale mudstone clast and matrix content (Figure 4.5; S4 sample bed: 17 - 4%), although subtle upward increasing trends are also documented (Figure 4.5; S14 sample bed: 9-13%). Locally, some beds show subtle inverse grading (T_{B-3} of Talling 2012) and grain-size breaks (coarse- to medium-grained), associated with a decrease in matrix content (Figure 4.5; S4 sample bed: 17% - 4%). Type B beds can be structureless and ungraded and contain weakly developed planar laminations (Figure 4.5; S6 sample bed). However, when these bed types overlie a scour, sigmoidal NE-dipping cross-stratifications are developed (Figure 4.5; S9 sample bed) (see Arnott and Al-Mufti, 2017).

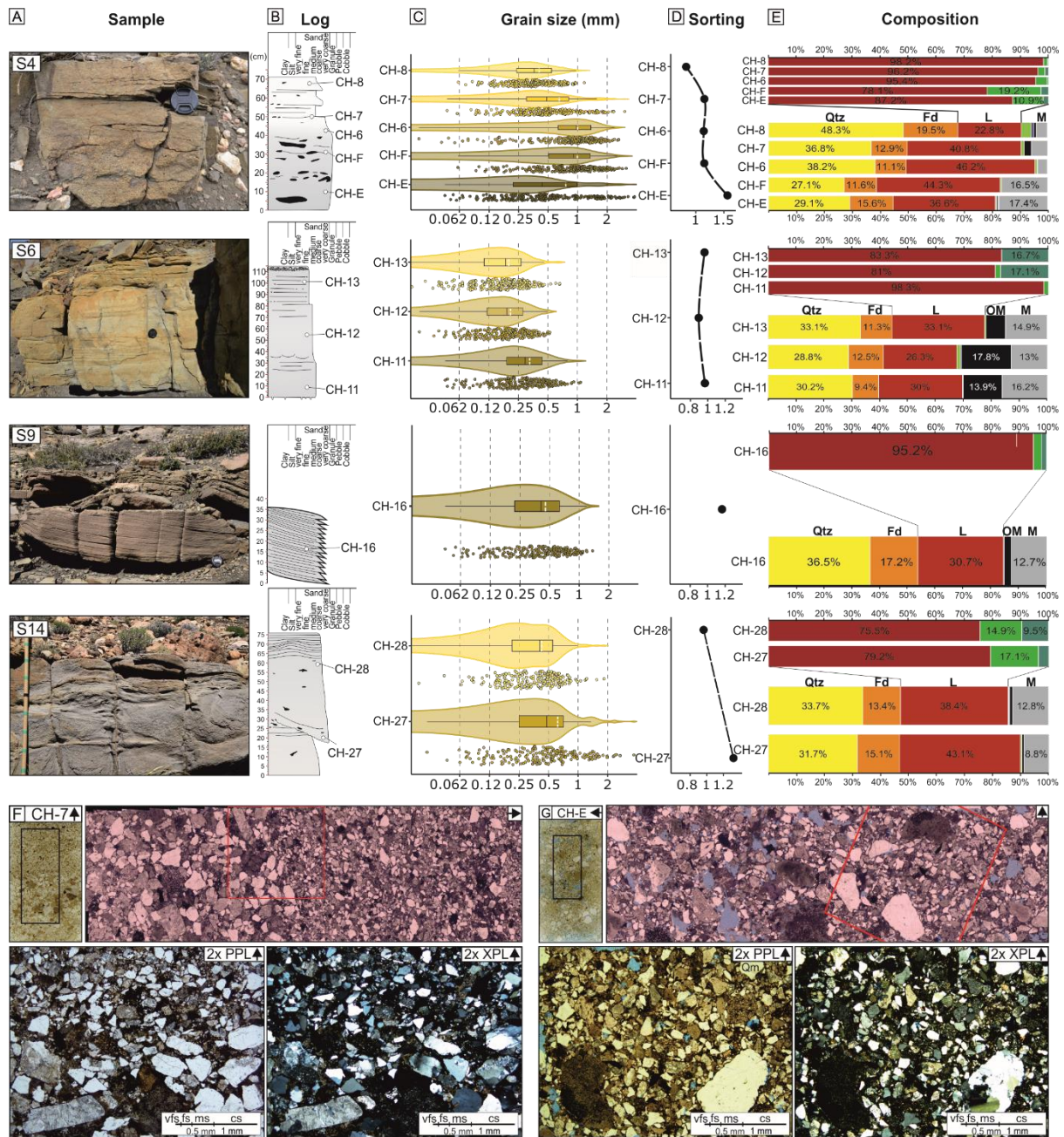


Figure 4.5. Summary diagrams illustrating Type B beds, (A) outcrop photo of the sampled bed, (B) detailed log (1:2 scale) of the sample bed, (C) grain size (200 measurements per sample), (D) sorting and (E) mineralogy (400 measurements per sample). Representative thin section (F; CH-7 and G; CH-E) scans, photomosaic and photomicrographs (PPL and XPL). Note black squares indicating the location of the photomosaic and red squares in the photomosaic indicating the position of the photomicrographs. The arrows in the top right show the top of the samples.

Interpretation: These sandstones were deposited from erosive high-concentration flows where particles are maintained in suspension by grain-to-grain interactions and fluid turbulence (Talling et al., 2012). Therefore, they are interpreted as high-density turbidites (*sensu* Lowe, 1982) deposited incrementally under aggradation rates high enough to suppress tractional reworking (Lowe, 1982). The tractional structures and normal grading observed at bed tops indicate a reduction in deposition rate, allowing differential grain settling and effective shearing (Sumner et al., 2008; Talling et al., 2012; Terlaky and Arnott, 2014). High-angle cross-bedding developed over scours supports scour-fill rather than dune formation (see pseudo-dunes of Arnott and Al-Mufti, 2017 and references therein). Inverse grading in the lower division (e.g. S4 sample bed) represents deposition under traction carpets (Lowe, 1982; Hiscott, 1994b; Sohn, 1997).

The upward increase in matrix content reflects differential grain size settling from waning flows, which deposit coarser material near the bed base and finer material near the bed top (Figure 4.5; S6 and S14 sample beds) (Mulder and Alexander, 2001). The high sediment fallout rate can prevent the segregation of flocs from returning into suspension, resulting in enhanced trapping of clay flocs at the flow and bed base (e.g. Middleton and Neal, 1989). Sand-sized mudstone clasts in intermediate positions within the sandstone beds suggest that either they remained in suspension for longer than particles of a similar size and density (e.g. quartz and feldspar grains) (Mulder and Alexander, 2001) or that they were entrained and deposited later in the lifespan of the flow. In contrast, deposits with an upward decrease in matrix content are associated with developing a cohesive viscous near-bed sublayer (near-bed laminar plug; Lowe and Guy, 2000). Grain-size breaks (Figure 4.5; S4 sample bed) suggest flow stratification developed between the cohesive viscous layer and the overlying turbulent flow division (Lowe

and Guy, 2000). The grooves represent tool-like clasts that gouged the substrate (Peakall et al., 2020) and indicate high-concentration flows. Groove development might be linked to the passage of a forerunning, fast-moving and bypassing debritic head, responsible for rafting mudstone clast and transferring them as bedload, developing grooves (Baas et al., 2021). Disaggregation of mudstone clasts could trigger the development of turbulence-enhanced transitional flows (TETFs) or even lower transitional plug flows (LTPFs) (Baas et al., 2009, 2011) over short distances.

4.5.3. Type C beds

Description: Medium-bedded (0.2-0.4 m), matrix-rich (> 15%) sandstones, forming tripartite deposits with sharp boundaries between constituent divisions (Figure 4.6; S11 sample bed). Bed bases are sharp and conformable and contain abundant ENE-WSW oriented discontinuous tool marks (skim marks) with high divergence. The lower division of Type C beds (5-20 cm thick) is structureless, weakly normally graded, moderately sorted, and matrix-rich (27%). The middle division (10-15 cm thick) is ungraded and poorly sorted, with the highest matrix content of the three divisions (37%), and characterised by low-amplitude, undulating microbanding (< 1 cm spacing; Stevenson et al., 2020), with alternating planar sub-parallel to undulatory, light (i.e., mud-poor) and dark (i.e., mud-rich) bands containing rare, millimetre-scale mudchips (Figure 4.6F; S11 sample bed). The dark argillaceous bands are responsible for the poor sorting within this division (Figure 4.6). The upper division (< 5 cm thick) is normally graded matrix-rich (30%) and moderately sorted. NNE-oriented ripple lamination is common, with millimetre-scale mudchips aligned within the ripple laminae (Figure 4.6).

Chapter 4: Stratigraphic change in flow transformation processes recorded in early post-rift deep-marine lobe complexes in an intraslope setting

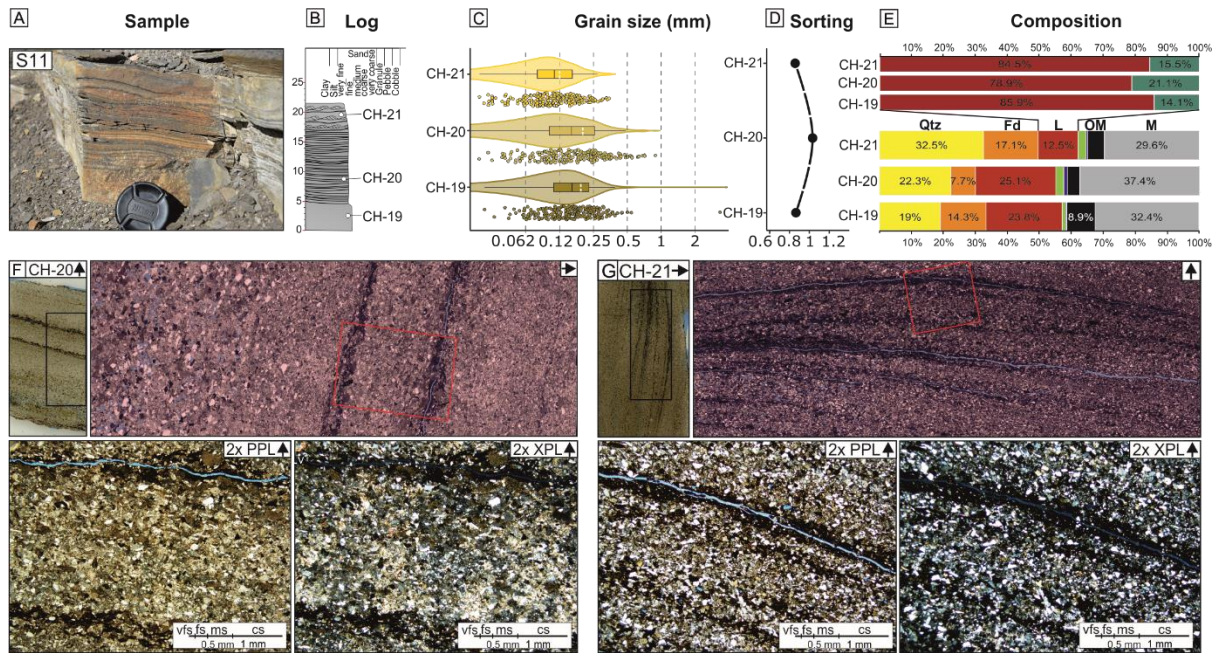


Figure 4.6. Summary diagrams illustrating Type C beds, (A) outcrop photo of the sampled bed, (B) detailed log (1:2 scale) of the sample bed, (C) grain size (200 measurements per sample), (D) sorting and (E) mineralogy (400 measurements per sample). Representative thin section (F; CH-20 and G; CH-21) scans, photomosaic and photomicrographs (PPL and XPL). Note black squares indicating the location of the photomosaic and red squares in the photomosaic indicating the position of the photomicrographs. The arrows in the top right show the top of the samples.

Interpretation: Due to its similar matrix content and lack of bounding fine-grained interval, the development of the three divisions is interpreted as being deposited from the same transitional flow. The normally graded lower division suggests deposition from a flow comprising a turbulent component to permit differential grain size settling (Best and Bridge, 1992; Hiscott, 1994a; Sumner et al., 2008). The lack of tractional structures and high matrix content suggest deposition from transitional flows under moderate to high aggradation rates. The banding in the intermediate division results from deposition and reworking from transitional flows, with a sustained traction period formed within the upper-stage plane bed flow regime (Baas et al., 2009, 2016; Stevenson et al., 2020). Lower structureless and intermediate banded divisions suggest deposition from lower transitional plug flows (LTPFs) (*sensu* Baas et al., 2009), where mixing with ambient water developed the ripple-bearing upper division. However the basal

skim marks suggest that a bypassing laminar and concentrated head could have preceded the LTPFs due to the incompatibility between the development of skim marks and the turbulence state (Peakall et al., 2020; Baas et al., 2021). This tripartite structure is comparable to the H1 (lower division), H2 (intermediate division) and H4 (upper division) described in Haughton et al. (2009). The lack of the linked debrite division (H3) suggests a high flow efficiency, and they neither decelerated rapidly nor were very cohesive (Stevenson et al., 2020). The divergence between the tool marks (ENE-WSW) and the ripples (NNE) suggests the existence of seabed relief where the forerunning bypassing head was more influenced by seabed relief than the more dilute depositional part of the flow, although it could be related to two different flows (Peakall et al., 2020).

4.5.4. Type D beds

Description: Thin-bedded (< 0.2 m thick), matrix-rich (> 15%) sandstone, forming bipartite deposits, with sharp boundaries between its constituent divisions (Figure 4.7; S2, S7A and S7B sample beds). The lower divisions (< 0.2 m thick) are matrix-rich (26-30%), structureless, fine- to medium-grained, weakly normally graded, and moderately sorted (Figure 4.7), and grooves with a wide range of directions. The upper divisions (~ 0.1 m thick) are massive and characterised by argillaceous sandstone comprising abundant mudstone clasts and plant fragments (0.5- 2 cm in length) (Figure 4.7). Upper divisions lack thin section observation due to the fissile character of the argillaceous sandstones.

Chapter 4: Stratigraphic change in flow transformation processes recorded in early post-rift deep-marine lobe complexes in an intraslope setting

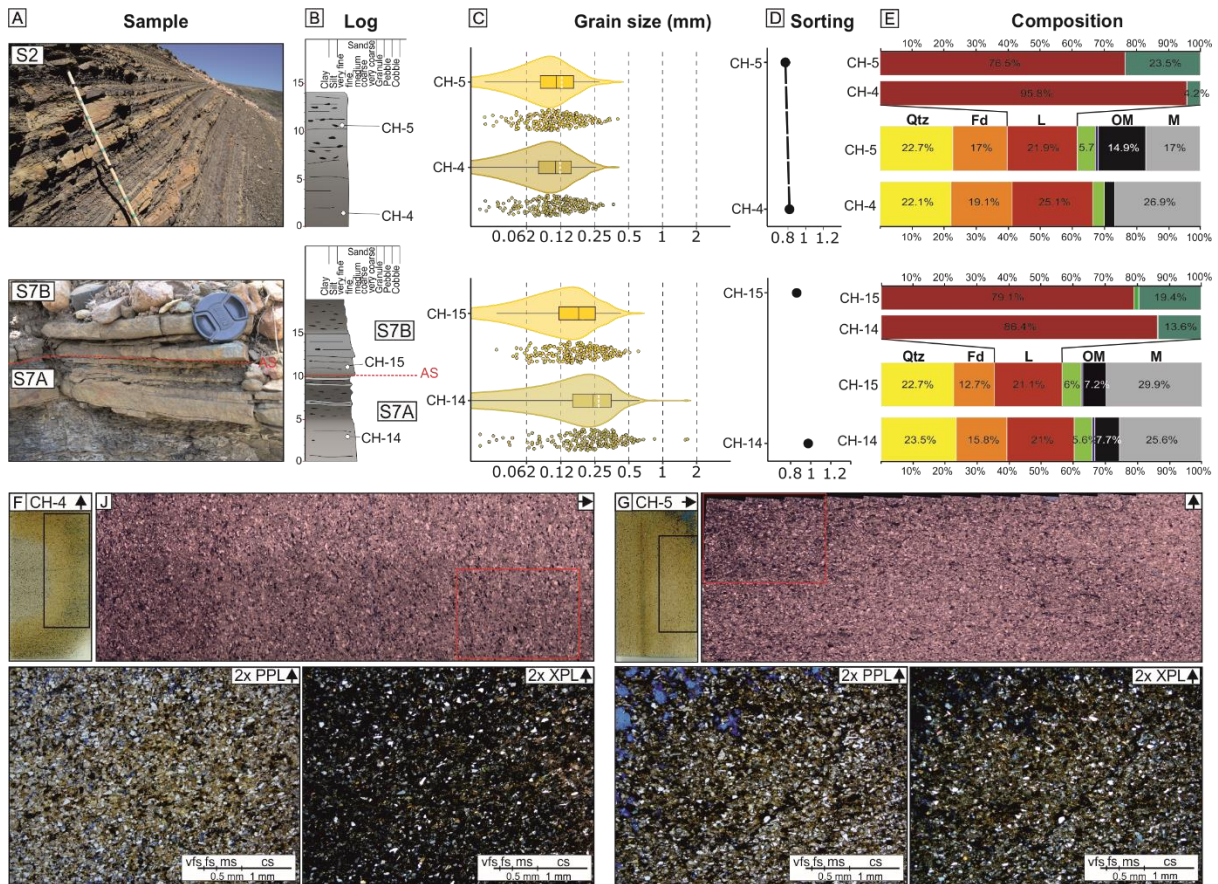


Figure 4.7. Summary diagrams illustrating Type D beds, (A) outcrop photo of the sampled bed, (B) detailed log (1:2 scale) of the sample beds (red line represents the amalgamation surface between them), (C) grain size (200 measurements per sample), (D) sorting and (E) mineralogy (400 measurements per sample). Representative thin section (F; CH-4 and G; CH-5) scans, photomosaic and photomicrographs (PPL and XPL). Note black squares indicating the location of the photomosaic and red squares in the photomosaic indicating the position of the photomicrographs. The arrows in the top right show the top of the samples.

Interpretation: The juxtaposition of the lower and upper divisions without an intervening mudstone layer suggests that they represent the H1 and H3 divisions of HEBs (see Haughton et al., 2009) genetically related to a single depositional event. The internal layering reflects discrete rheological changes within the source flow due to deceleration related to lateral spreading and/or increased near-bed flow concentration or cohesion (Kane et al., 2017). However, the lack of abrupt boundaries suggests that the flow did not develop stable internal stratification (Kane et al., 2017). The high matrix content (26-30%) and the crude normal

grading within the lower divisions (H1) suggest the shearing of mud flocs and mudstone clasts caused by a transitional flow with a turbulent component. The upper argillaceous divisions (H3) suggest deposition from intermediate to high yield strength debris flow divisions (Talling et al., 2012). The preservation of plant fragments supports the interpretation of a laminar state within the upper divisions (e.g. Hodgson, 2009; D2 Type). Therefore, Type D beds are interpreted as thin-bedded HEBs formed under upper transitional plug flows (UTPF) and quasi-laminar plug flow (QLPF) (*sensu* Baas et al., 2009, 2011, 2016). The development of H3 division, and lack of H2, suggest abrupt deceleration rates (Baas et al., 2011; Baas et al., 2016; Stevenson et al., 2020) related to the distal collapse of the flow (Kane et al., 2017). The grooves at the base indicate that UPTF/QLPFs were preceded by bypassing a forerunning debritic head responsible for incorporating cohesive clay from the substrate (Baas et al., 2021).

4.5.5. Type E beds

Description: Medium- to thick-bedded (0.2-1 m thick), matrix-rich (> 15%), tripartite beds with sharp and loaded bases containing abundant multidirectional grooves and sharp tops (Figure 4.8). The contacts between each division are gradual (Figure 4.8; S12 and S15 sample beds), and lower and intermediate divisions are structureless with abundant mudstone clasts. The lower divisions (10-40 cm thick) are medium-grained, matrix-rich (20-23%) (Figure 4.8; S15 and S8 sample beds) or matrix-poor (13%) (Figure 4.8; S12 sample bed), weakly normally graded, moderately sorted, and contain few deformed mudstone clasts (5-50 cm diameter) (Figure 4.8). The intermediate division (10-20 cm thick) is medium-grained, matrix-rich (19-23%), weakly normally graded and moderately sorted, and contains abundant, rounded mudstone clasts (0.1-5 cm diameter) (Figure 4.8). The uppermost division (5-15 cm thick) is fine-grained, matrix-rich (20-31%), normally graded, moderately sorted and structureless to weakly planar laminated, containing rare mudstone clasts (Figure 4.8).

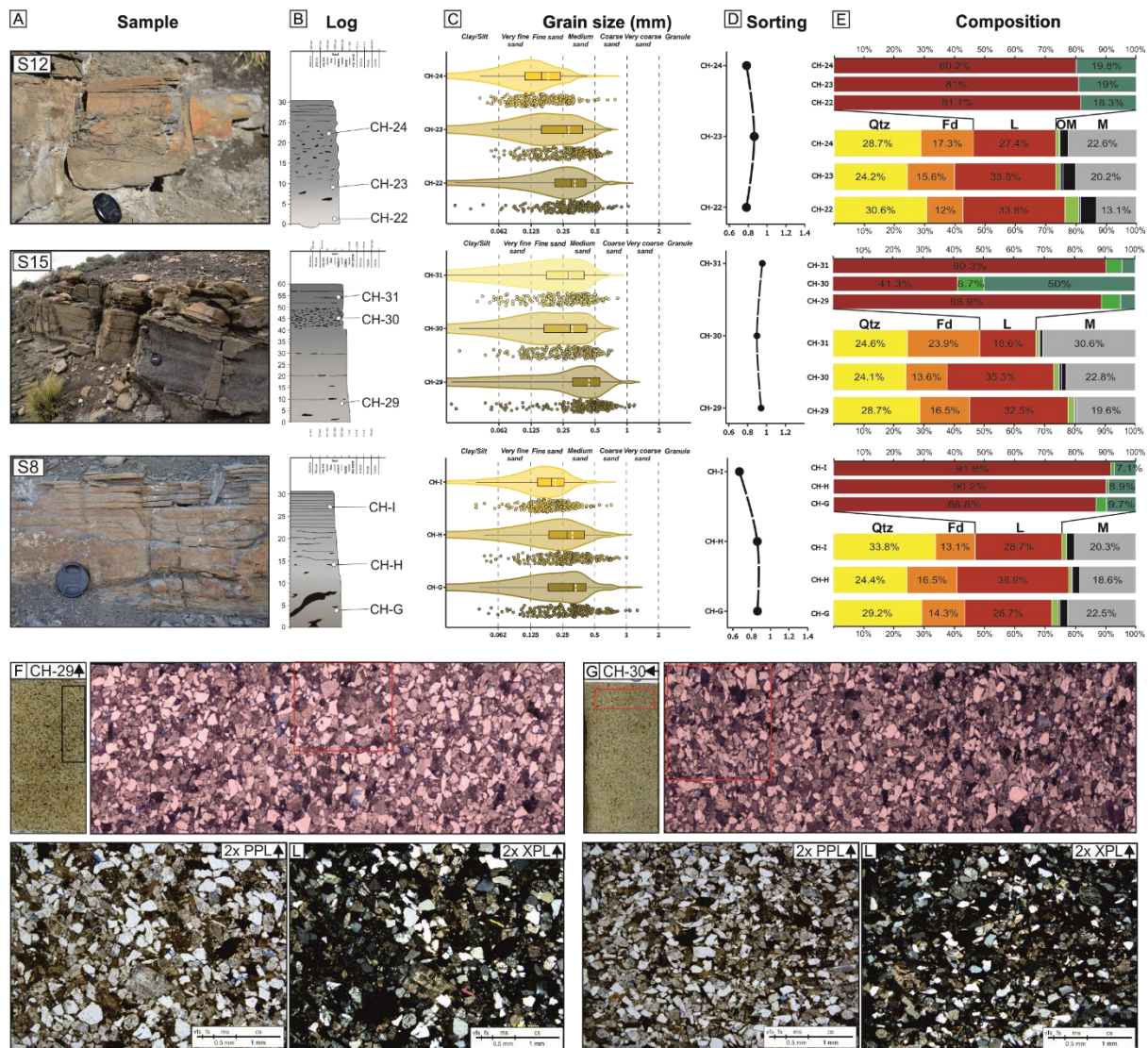


Figure 4.8. Summary diagrams illustrating Type E beds, (A) outcrop photo of the sampled bed, (B) detailed log (1:2 scale) of the sample bed, (C) grain size (200 measurements per sample), (D) sorting and (E) mineralogy (400 measurements per sample). Representative thin section (F; CH-29 and G; CH-30) scans, photomosaic and photomicrographs (PPL and XPL). Note black squares indicating the location of the photomosaic and red squares in the photomosaic indicating the position of the photomicrographs. The arrows in the top right show the top of the samples.

Interpretation: The internal layering suggests different rheologies related to HEB development (e.g. Lowe and Guy, 2000; Haughton et al., 2003, 2009; Talling et al., 2004; Barker et al., 2008; Kane and Pontén, 2012). The lack of abrupt boundaries suggests that the flow did not develop stable internal stratification (Kane et al., 2017). Loaded bases and mudstone rafts suggest shearing and entrainment of semi-consolidated substrate material into an undersaturated flow

(Terlaky and Arnott, 2014; Kane et al., 2017). The incorporation of clay-rich material resulted in flow bulking and increased flow concentration, promoting a transitional flow behaviour (Kane and Pontén, 2012). Normal grading within the lower division (H1) suggests that the basal layer was fluid and turbulent enough to allow particle settling of the denser/coarser-grained fraction according to grain size/density (Baas et al., 2009) or a low yield strength basal division (Kane et al., 2017). Therefore, these matrix-rich basal divisions are not comparable to the clean sandstone turbidite base of hybrid event beds in other systems (Haughton et al., 2003, 2009; Talling et al., 2004; Amy et al., 2006; Barker et al., 2008; Davis et al., 2009) suggesting a different style of flow transformation. The abundant grooves indicate that these flows were preceded by a highly erosive bypassing debris flow and later infilled by the deposition of H1. The weakly normally graded, matrix- and mudstone clast-rich intermediate divisions (H3) suggest hindered settling as a sediment transport mechanism (Mulder and Alexander, 2001) and capacity-driven deposition (Hiscott, 1994a) rather than transport as a result of the matrix-strength of a high yield strength debris flow division and cohesive freezing (Talling et al., 2012). The poorly-developed lamination on the upper divisions (H4) suggests high aggradation rates with poorly developed tractional reworking on the upper-stage plane bed. The H4 division in Type E beds seems unlikely to represent the deposition from the tails of these flows. Instead, they may be related to deposition from parts of the flow high enough not to incorporate enough substrate and develop debritic division (Hussain et al., 2020; Baas et al., 2021). Additionally, they can be caused by mixing ambient water (Marr et al., 2001; Talling et al., 2002; Sequeiros, 2012). Therefore, Type E beds are interpreted as thick-bedded hybrid event beds (HEBs) (e.g. Kane et al., 2017) deposited from UTPF to QLPFs under high deceleration rates (Baas et al., 2009, 2011, 2016).

4.5.6. Type F beds

Description: Medium- to thick-bedded (0.3-1 m thick) and generally matrix-rich (> 15%) sandstones. The matrix content increases upwards within a bed (Figure 4.9; S3 sample bed; 13-27%). Bed bases are sharp, loaded and erosive, comprising abundant ENE-WSW oriented grooves and planar to undulatory sharp tops. Beds are structureless, with poorly-developed diffuse planar lamination ('wispy lamination' of Lowe and Guy, 2000; Lowe et al., 2003) (Figure 4.9; e.g. S10 sample bed) that usually occupies the upper half of beds, although it can be developed from base to top. Beds are coarse-grained to medium- or fine-grained, weakly normally graded to ungraded, and poorly sorted, comprising a wide grain size range, especially at the lower half (Figure 4.9; from very fine to granule, S3 sample bed). Locally, faint planar laminations or hummock-like bedforms develop near bed tops (Figure 4.9; S5 sample bed).

Interpretation: The high matrix content (up to 40%) and poor sorting suggest deposition from UTPF/QLPFs (Baas et al., 2009, 2011, 2016) characterised by an abrupt loss in capacity (Hiscott, 1994a), high sediment fallout and reduced tractional reworking (Talling et al., 2012). The crude normal grading and upwards increasing matrix suggest some turbulence at the base of the parental flow, although the dominant rheology was likely an intermediate yield strength laminar flow (Talling et al., 2012). However, the abundance of grooves suggests the development of a laminar plug at the base of these flows or a forerunning and bypassing debris flow (Baas et al., 2021), which led to flow bulking (*sensu* Haughton et al., 2009). Structured tops, if present, suggest mixing with ambient water at the rear or upper parts of the flow, which reduces viscosity and yield strength (Talling et al., 2002; Sequeiros, 2012). Hummock-like bedforms are attributed to the development of combined flows with an oscillatory component, indicative of complex interaction between the parental flow and topography (Tinterri, 2011; Tinterri et al., 2016)

Chapter 4: Stratigraphic change in flow transformation processes recorded in early post-rift deep-marine lobe complexes in an intraslope setting

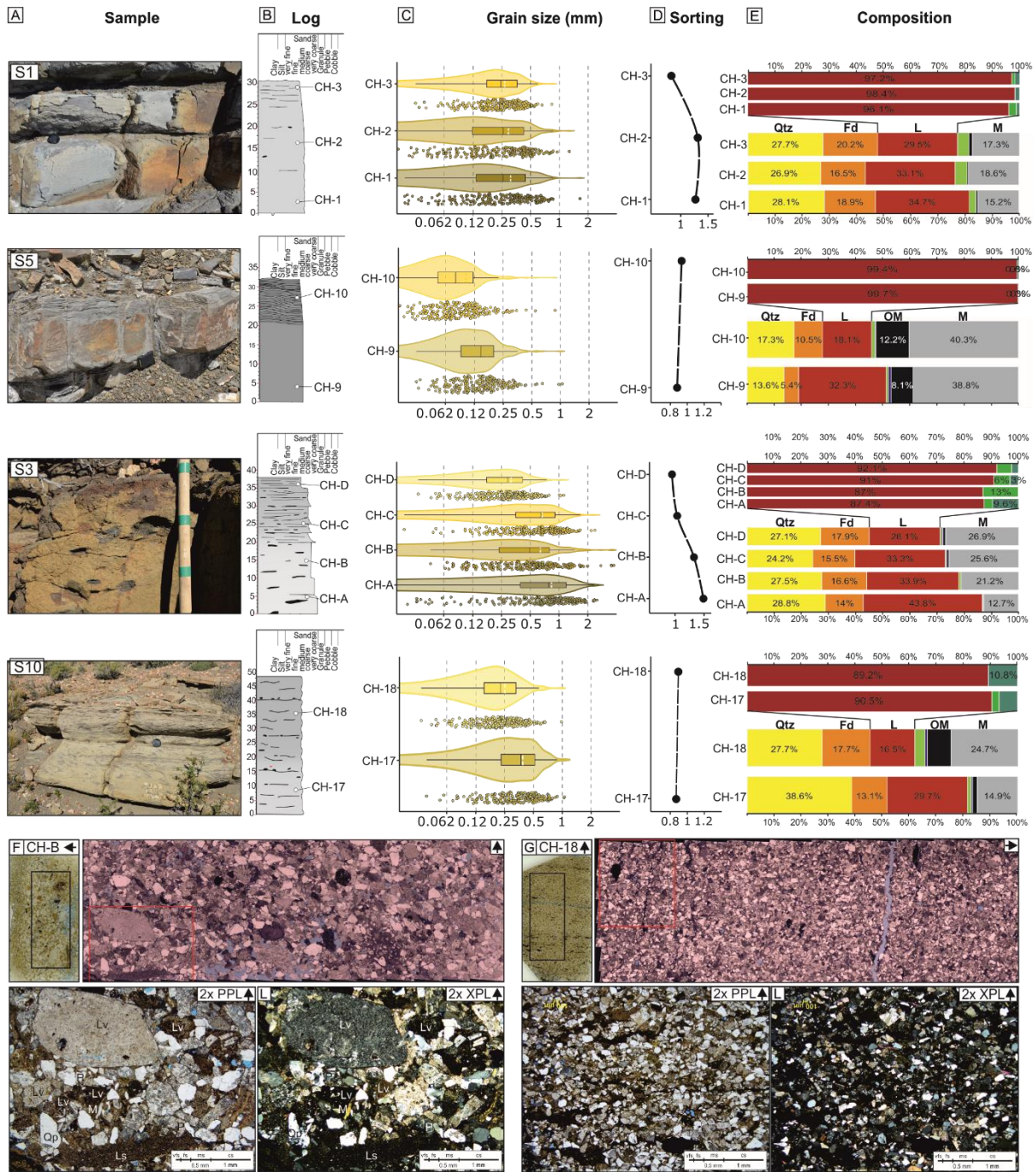


Figure 4.9. Summary diagrams illustrating Type F beds, (A) outcrop photo of the sampled bed, (B) detailed log (1:2 scale) of the sample bed, (C) grain size (200 measurements per sample), (D) sorting and (E) mineralogy (400 measurements per sample). Representative thin section (F; CH-B and G; CH-18) scans, photomosaic and photomicrographs (PPL and XPL). Note black squares indicating the location of the photomosaic and red squares in the photomosaic indicating the position of the photomicrographs. The arrows in the top right show the top of the samples.

4.5.7. Type G beds

Description: Thick-bedded (0.5-6 m) sandy mudstone with sharp, erosive bases and undulatory tops. Type G beds contain abundant outsized, subangular sandstone clasts (0.05–1 m) supported by a poorly sorted and argillaceous matrix (Figure 4.3). A medium-grained massive sandstone can locally underlie the argillaceous thick-bedded deposits with basal grooves containing deformed mudstone clasts (0.5-8 cm diameter) (Privat et al., 2021).

Interpretation: The outsized clasts supported within the argillaceous matrix suggest cohesive freezing from intermediate to high yield strength debris flows (Figure 4.3; Talling et al., 2012) (Sohn 1997). Erosive bed bases and the presence of sandstone clasts suggest the source flows entrained compacted substrate (Dakin et al., 2013; Hodgson et al., 2019; Martínez-Doñate et al., 2021). Alternatively, the debrites can also represent scour-fills post-dating previous erosive and bypassing flows. Mixing the cohesive laminar flow with ambient water might have diluted the basal part of the flow (Hampton, 1970; Mohrig et al., 1998; Marr et al., 2001). Therefore, both divisions are co-genetic (HEB type 1 of Privat et al., 2021), with the basal sandstone representing deposition from a flow cohesive enough to develop grooves (Peakall et al., 2020), such as lower to upper transitional plug flows (Baas et al., 2009). Due to their high matrix strength and to avoid confusion with other bed types (especially Type D, E and F beds), Type G beds are referred to as debrites, despite the local development of transitional flow behaviour near their base.

4.5.8. Type H beds

Description: Thin to thick-bedded (0.1–4 m) sandstones with sharp bases and tops, containing abundant grooves on both margins. These sandstones are massive, fine- to medium-grained and well-cemented, with rare parallel striations on blistered surfaces (1 cm high and < 2 cm

diameter; see Cobain et al., 2017). They contain abundant mudstone clasts (2-5 cm diameter) and angular heterolithic rafts (10 – 50 cm length) that are oriented parallel to the bedding contacts (Figure 4.3). Sub-horizontal thick-bedded sandstones cross-cut the stratigraphy at low angles (< 15°). Thick sandstone beds develop branching into thin-bedded sub-vertical bodies (< 0.2 m thick) of similar lithology that cross-cut the stratigraphy at various angles (15-90°).

Interpretation: These features are clastic injectites associated with compaction-driven fluid expulsion (Hurst et al., 2011). The sub-horizontal thick sandstones are clastic sills with associated clastic dykes.

4.6. Petrography

Petrological analysis of the 40 thin sections allowed to determine the matrix content, grain size and mineral composition of Type A-F beds (Figure 4.4-Figure 4.9). Matrix represents a significant component in the analysed samples, ranging from 3.5% to 40.3% and 19.8% on average. Most sampled beds show an increase in matrix content from base to top, with a few exceptions where the matrix content decreases upwards (Figure 4.5 and Figure 4.8; S4 and S8 sample beds). The thick-bedded sandstones, where point contacts dominate, contain less matrix than the thin-beds, which are matrix-supported. Samples are characterised by a wide grain size range, varying from silt to granular, with the mean and median grain size being fine- to medium-sand. Overall, bed bases are generally coarser, and the mean grain size decreases upwards within the same event bed. This effect is well-developed in low- and high-density turbidites (Type A and B; Figure 4.4 and Figure 4.5) and banded TFDs (Type C; Figure 4.6). In contrast, HEBs (Type D and E; Figure 4.7 and Figure 4.8) and thick-bedded TFDs (Type F; Figure 4.9) can show ungraded profiles. When traced laterally, the grain size also decreases across the vertical profile of the event beds, developing (very) fine-grained and matrix-rich

pinch-outs. High-density turbidites (Type B beds) and thick-bedded TFDs (Type F beds) are the deposits that comprise the coarsest grain sizes (medium to coarse sand), whereas the rest is finer (very fine to medium sand) (Figure 4.10).

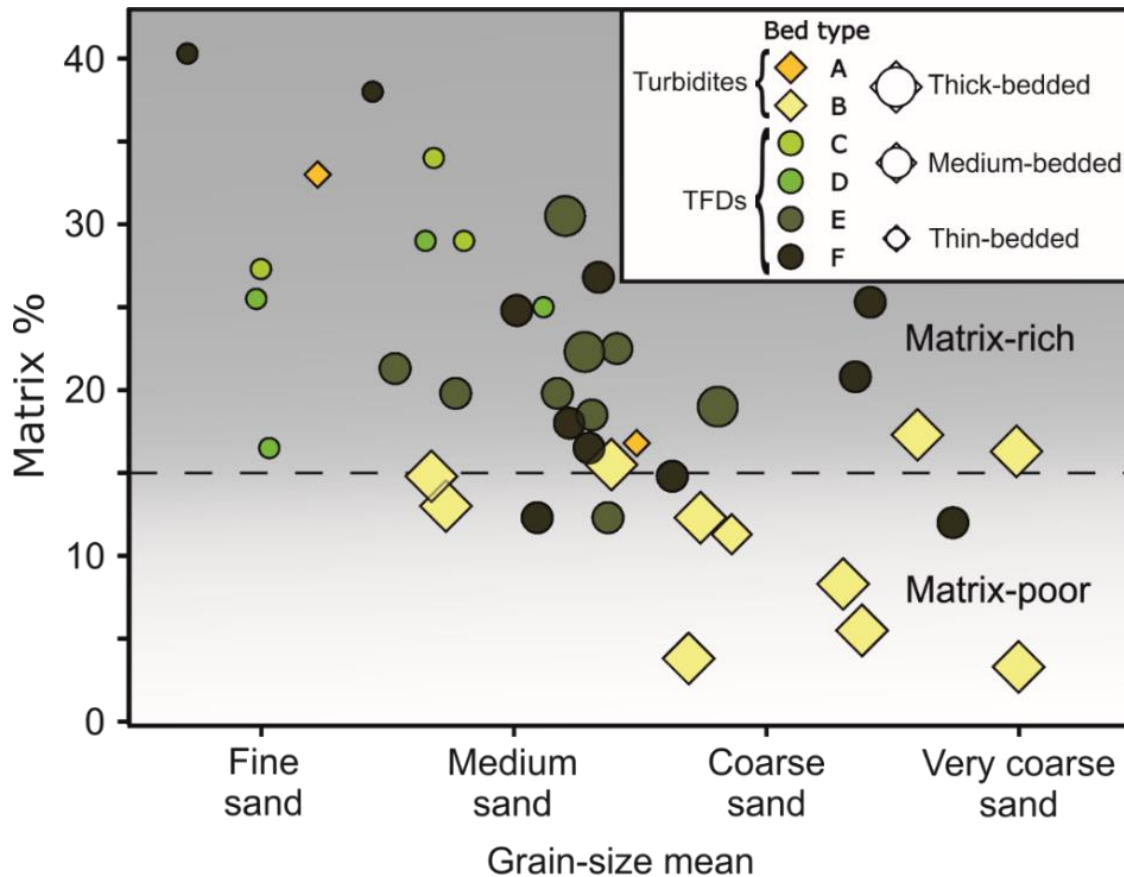


Figure 4.10. Graph showing matrix content as a function of the mean grain size of each sample (n= 40) according to the bed type. The dashed line at the 15% matrix represents the threshold for matrix-poor and matrix-rich intervals (Pettijohn et al., 1972). Note that the high-density turbidites (Type B beds) are the coarsest and less argillaceous, in contrast to most TFDs (Type C, D, E, and F beds) and low-density turbidites (Type A bed).

4.6.1. Compositional trends

Description: The analysed samples were plotted on standard Qm-F-Lt (Dickinson et al., 1983), Lv-Lm-Ls (Ingersoll and Suczek, 1979) and Qp-Lv-Lsm (Dickinson, 1985) ternary diagrams (Figure 4.11). In the Qm-F-Lt diagram (Dickinson et al., 1983), nine samples plot in the recycled orogenic field, nine in the mixed field, and twenty-two in the magmatic arc field

(Figure 4.11A). From those twenty-two samples, nineteen correspond to the dissected arc field, whereas three are in the transitional arc field. The Lv-Lm-Ls diagram (Ingersoll and Suczek, 1979) reveals the dominance of volcanic lithoclasts over the other two lithic fragment types by plotting thirty-seven samples on the back-arc basin field and three on the forearc basin field (Figure 4.11B). The Qp-Lv-Lsm diagram (Dickinson, 1985) plots twenty-seven samples on the magmatic arc field and thirteen on the mixed field (Figure 4.11C).

Interpretation: The petrographic work and later plotting of the collected samples into different ternary diagrams reveal a consistent provenance field for the Early Jurassic Los Molles Formation in the Chachil Graben corresponding to the magmatic arc (Burgess et al., 2000; Sugawara & Nikaido, 2014) and supported by the NE-directed palaeocurrents. Therefore, mixed source areas are unlikely to be responsible for the observed differences in depositional architecture and bed types within and between the Lower and Upper Lobe Complexes.

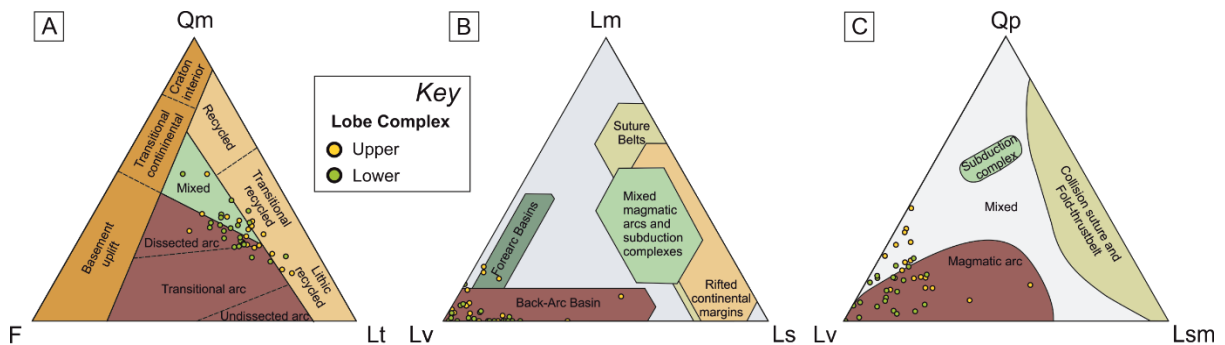


Figure 4.11. Ternary diagrams of the 40 analysed samples. (A) QmFLt (Dickinson et al., 1983) show a mixed and arc provenance. (B) Lv-Lm-Ls (Ingersoll and Suczek, 1979) show a volcanic arc source of the samples due to the dominance of volcanic lithoclasts (Lv) over sedimentary (Ls) and metamorphic (Lm) lithoclasts. (C) Qp-Lv-Lsm diagram (Dickinson, 1985) showing volcanic arc source.

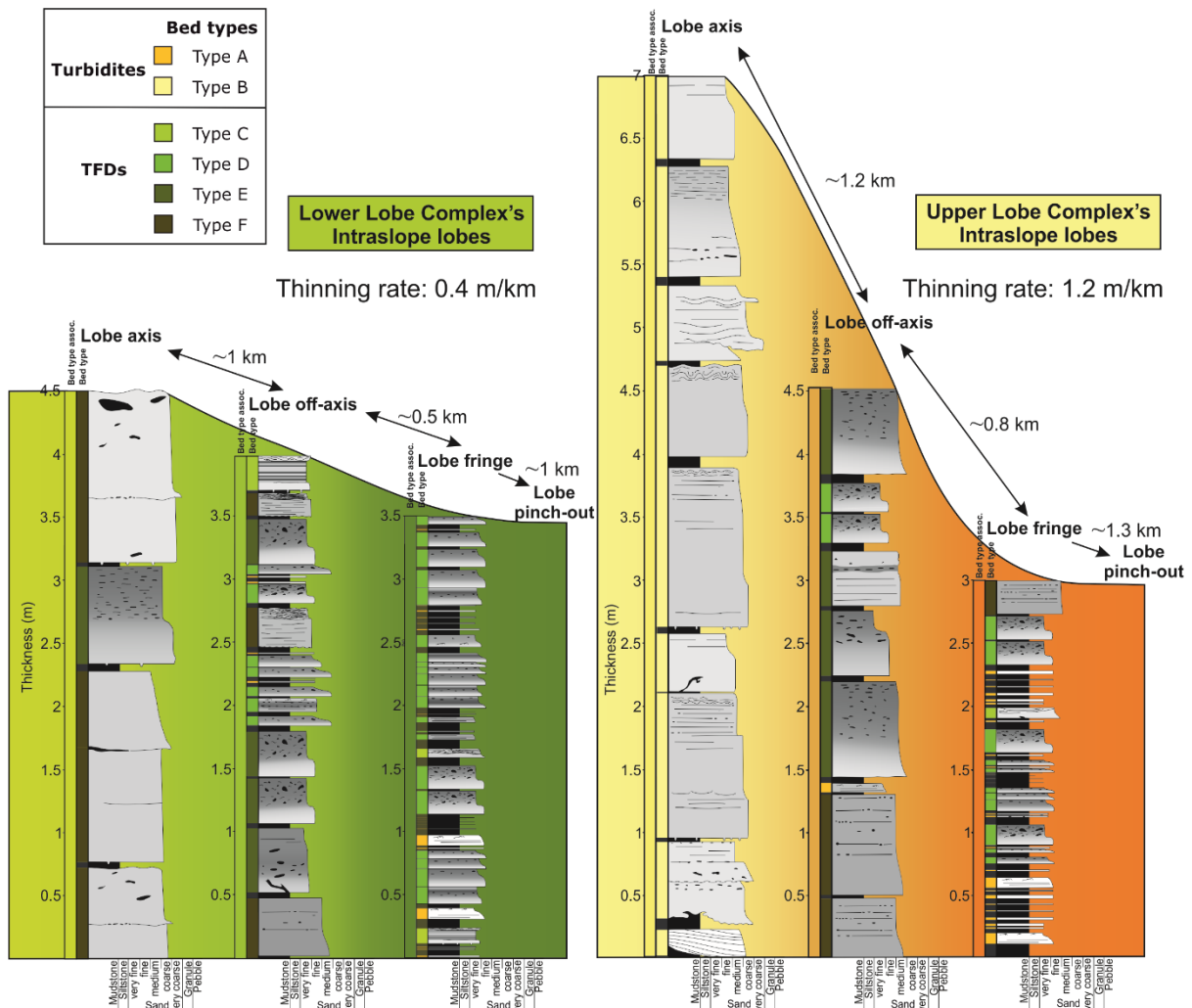


Figure 4.12. Bed type association representing lobe sub-environments: lobe axis, lobe off-axis and lobe fringe of Lower and Upper Lobe Complexes.

4.7. Lobe sub-environments

The studied bed types are stacked into 3-7 m-thick, composite stratal units, bounded at the base and top by 0.2-1 m thick regional mudstones. These sandstone-rich packages represent intraslope lobes (Privat et al., 2021). Three bed type associations are identified based on interpreted sedimentary processes and depositional environments (Figure 4.12). These bed type associations represent lobe sub-environments, including lobe axis, lobe off-axis and lobe fringe (*sensu* Pr elat et al., 2009). The lobes of each lobe complex show a different transition from axial to fringe sub-environments, which impacted the architecture of the individual lobes and

the lobe complexes. In the lower lobe complex lobes, the lobe axis passes to the lobe off-axis in ~1 km, into the lobe fringe over 0.5 km, and pinching out in ~1 km (Figure 4.12). In the lobes within the Upper Lobe Complex, these transitions are more gradual, passing from the lobe axis into the lobe off-axis over a horizontal distance of ~1.2 km and from off-axis to fringe environments over 0.8 km and pinching out in ~1.3 km (Figure 4.12).

4.7.1. Lobe axis

Description: This lobe sub-environment is characterised by amalgamated medium- to thick-bedded sandstones (< 1.2 m thick) forming stratal packages with rare mudstone intervals between the sandstone beds (< 0.1 m thick) (Figure 4.12). The lobe axes within the Lower Lobe Complex are ~4.5 m thick and dominated by TFDs, with Type F beds dominating over Type E beds (Figure 4.12). In contrast, the lobe axes of the Upper Lobe Complex are ~7 m thick and entirely dominated by thick-bedded, matrix-poor high-density turbidites (Type B beds) (Figure 4.12).

Interpretation: The highly amalgamated thick-bedded package represents a proximal environment dominated by deposition from energetic and high-concentration flows, supporting a lobe axis interpretation (Hodgson et al., 2006; Prélat et al., 2009; Sugawara & Nikaido, 2014; Spychala et al., 2015). In the Lower Lobe Complex, the elevated concentration, cohesiveness, and high-deceleration rates promoted capacity-driven deposition (Hiscott, 1994a), resulting in the development of the TFDs-dominated lobe axis comprising thick, amalgamated beds. In contrast, the axial parts of lobes in the Upper Lobe Complex were formed under erosional high-density turbidity currents. Despite the abundant mudstone clasts in Type B beds, no critical flow transformation developed due to the limited disaggregation of any contained clay, enabling preferential deposition of the coarsest grain fraction, and producing partial bypass of

the finer sediments to more distal, down-current areas (Kneller & McCaffrey, 2003; Stevenson et al., 2015).

4.7.2. Lobe off-axis

Description: Well-stratified, heterolithic successions of mudstones (< 0.1 m thick) and medium-bedded sandstones characterise the lobe off-axis sub-environment. The lobe off-axis shows a lower sandstone-mudstone proportion than the lobe axis due to the lower bed thickness and a reduced level of bed amalgamation (Figure 4.12). Sandstone beds in the Lower Lobe Complex are thinner (0.1- 0.5 m thick) than in the Upper Lobe Complex (0.1-0.7 m thick). The lobe off-axis deposits of lobes in the Lower Lobe Complex are ~4 m thick and dominated by thin to medium-bedded HEBs (Type D and E). However, subsidiary thick-bedded TFDs (Type F), banded TFDs (Type C), and low-density turbidites (Type A) are also observed. The lobe off-axis deposits of the lobes within the Upper Lobe Complex are ~4.5 m thick and shows less variability and thicker deposits. It is dominated by thick-bedded TFDs (Type F) and medium- to thick-bedded HEBs (Type E), and rare low-density turbidites (Type A).

Interpretation: The range of thin- to thick-bedded argillaceous deposits documented within the lobe off-axis suggests a sub-environment of deposition characterised by high-concentration flows with variable internal stratification and rheology. The dominance of TFDs with mudstone clasts indicates substrate entrainment and flow bulking (Haughton et al., 2009), which increases flow cohesion and concentration. Entrainment and disaggregation of clay promote the formation of oversaturated and cohesive flows (Kane et al., 2017) that could not transport their sediment load to distal parts of the lobe, thus promoting capacity-driven deposition (Hiscott, 1994a). Type C beds are interpreted as the product of a more moderate flow transformation

and deceleration rate, where the cohesive forces are not dominant enough to produce flow collapse (Stevenson et al., 2020). The differences between the lobe off-axis deposits of the Lower and Upper Lobe Complexes (amalgamation, thickness and variability of the deposits) lie in the behaviour of the source flows and their depositional character in the proximal sub-environment (lobe axis). In the Lower Lobe Complex, as the thick-bedded TFDs and HEBs were already deposited in the lobe axis, the flows reaching the lobe off-axis developed thinner deposits (Type C, D and E beds). In contrast, in the Upper Lobe Complex, the high-density turbidity currents transformed into transitional flows over longer distances, leading to high-density turbidite dominated (Type B beds) lobe axis and medium- to thick-bedded TFD-dominated (Type E and F beds) lobe off-axis.

4.7.3. Lobe fringe

Description: This lobe sub-environment is characterised by a well-stratified, fine-grained heterolithic succession composed of mudstones (< 0.25 m thick) and thin beds of sandstones (< 0.3 m thick). The sandstone-mudstone proportion is lower than the lobe axis and off-axis sub-environments (Figure 4.12). Overall, lobe fringes from the Lower and Upper Lobe Complex are similar, being ~3 m thick (Figure 4.12). Both comprise thin-bedded HEBs (Type D beds), banded TFDs (Type C beds) and low-density turbidites (Type A beds). However, the Lower Lobe Complex shows a higher proportion of thin-bedded HEBs (Type D beds), whereas the Upper Lobe Complex comprises a higher proportion of low-density turbidites (Type A beds) and rare medium-bedded HEBs (Type E beds).

Interpretation: The thin-bedded heterolithic packages and lack of bed amalgamation suggest deposition in distal lobe settings. Thin-bedded HEBs (Type D beds) support flow

transformation across the entire lobe, with flows that could not carry the sediment for a longer distance due to low flow cohesiveness, high deceleration rate, or both (Kane et al., 2017). The other fundamental deposit, the low-density turbidites (Type A beds), are related to the source flow's high flow efficiency and dilute nature, which largely bypasses proximal lobe sub-environments and are deposited in distal areas. Such flows are deflected and reflected from intrabasinal relief without collapsing, reworking the sediment and developing bidirectional ripple lamination (e.g. Kneller and McCaffrey, 1999). In these relatively distal sub-environments, banded TFDs (Type C beds) developed through flow deceleration, enhancing the cohesive forces over the turbulence (Stevenson et al., 2020). The rare presence of medium-bedded HEBs (Type E) in the Upper Lobe Complex is likely to represent flow transformation over a long distance from efficient high-density turbidity currents, enabling sediment transport and deposition in distal areas.

4.8. Intraslope lobe complex architecture and bed type distribution

The bed type associations described in the previous section are spatially and genetically related, representing different sub-environments within intraslope lobes. These intraslope lobes are stacked, forming two lobe complexes (Lower and Upper Lobe Complex), each bounded at the base and top by a > 4 m thick regional mudstone or an erosionally-based debrite (Type G beds) (Figure 4.13; log 1 to log 7). The sandstone-mudstone proportion was quantified for each bed type within each lobe for both lobe complexes in three different areas based on 764 sandstone beds (Figure 4.14A). Logs 1-4, 5-6, and 7-8 represent the proximal, medial, and distal locations, respectively (Figure 4.1C). Logs 9-11 were not included in this analysis due to limited coverage of the investigated stratigraphic interval.

Chapter 4: Stratigraphic change in flow transformation processes recorded in early post-rift deep-marine lobe complexes in an intraslope setting

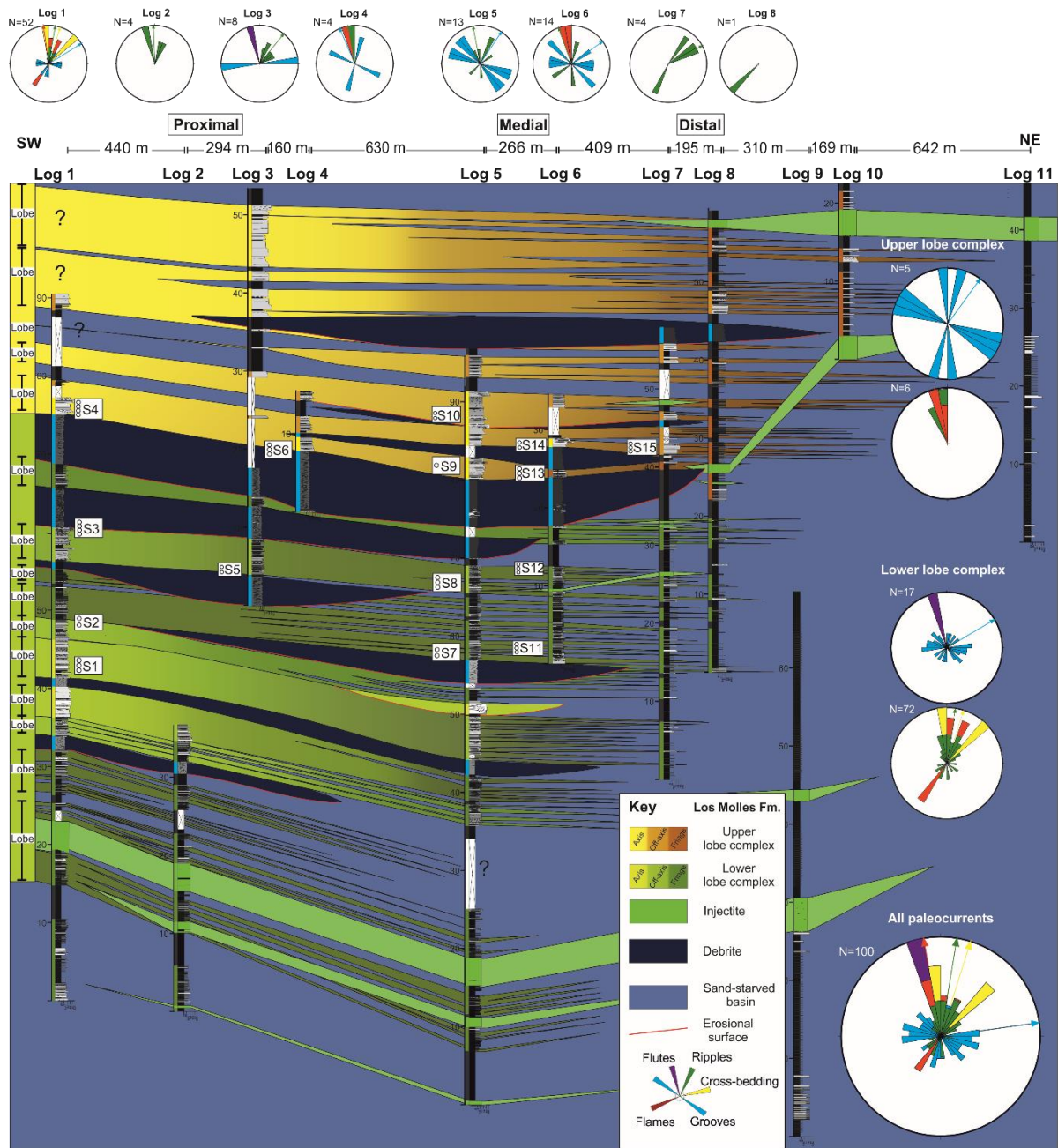


Figure 4.13. Detailed correlation panel showing the different lobe sub-environments, both lobe complexes' overall architecture and pinch-out positions. Rose diagrams show palaeocurrents for each lobe complex and log. Tool marks show higher divergence than ripples lamination as denser flows/divisions are more sensitive to intrabasinal topography than dilute flows/divisions.

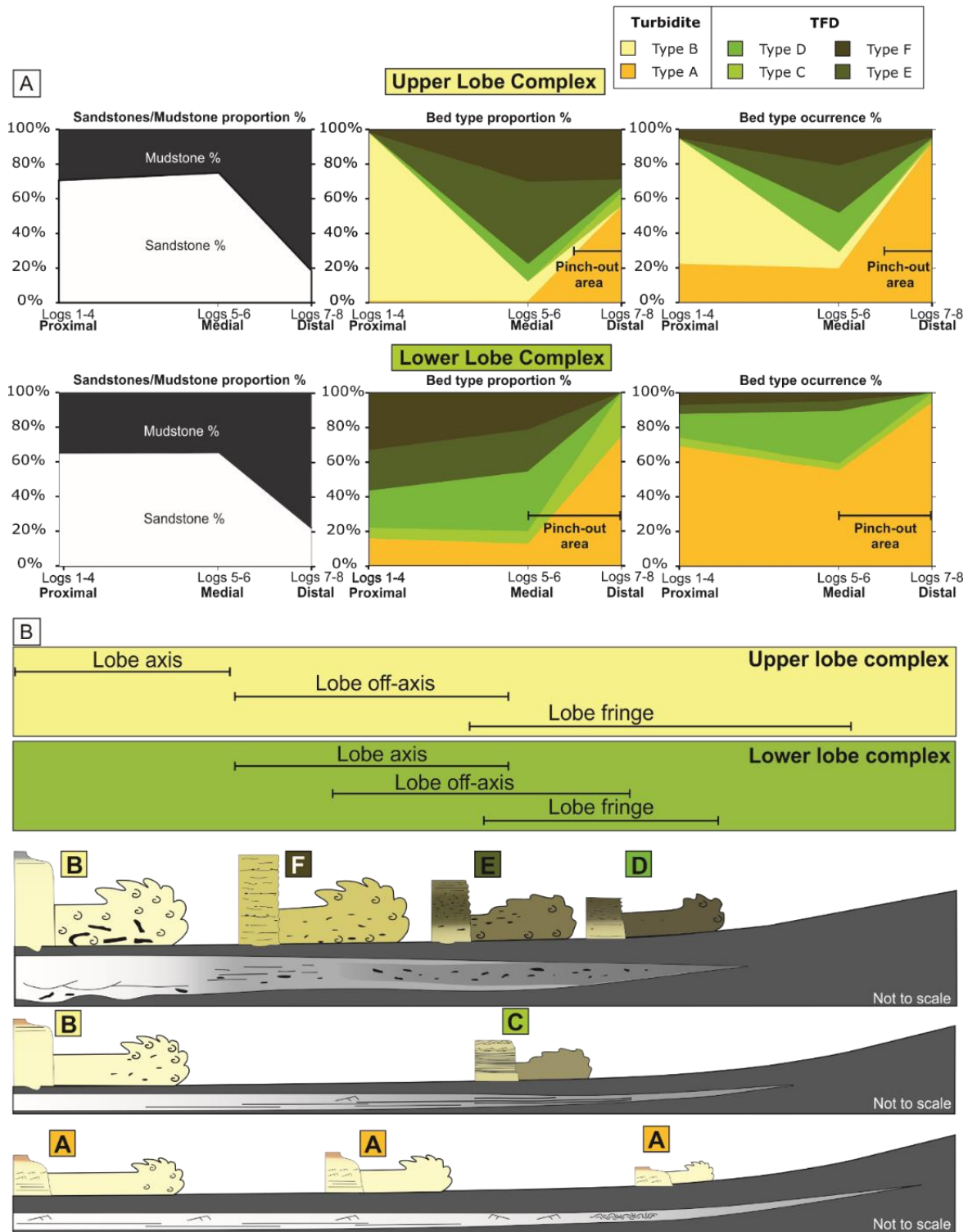


Figure 4.14. (A) Graphs showing sandstone-mudstone proportion (left), bed type proportion (centre) and bed type occurrence (right) from both Lower and Upper Lobe Complexes in proximal (Log 1-4), medial (Log 5-6), and distal (Logs 7-8) parts (see Figure 4.1C for location). (B) Summary diagram of different flow evolution showing deposit variability from proximal to pinch-out areas. Denser flows tend to decelerate more abruptly and produce strong deposit variability, unlike dilute flows, which can maintain their efficiency for longer distances. The

greater the incorporation of cohesive mud, the shorter the distance over which flows transform into low-efficiency cohesive flows, resulting in rapid flow collapse.

4.8.1. Lower Lobe Complex

The Lower Lobe Complex is ~45 m thick and contains 10 compensationally stacked intraslope lobes (see 'jig-saw architecture'; Marini et al., 2015) (Figure 4.13). Additionally, an overall basinward stepping stacking pattern of successive lobe pinch-outs is observed, recording the forestepping trend for the lobe complex (Figure 4.13). Lobes achieve a maximum thickness of 4.5 m and comprise the thickest (< 1 m thick) sandstone beds in their proximal parts (logs 1-4). These lobes are almost tabular, showing thinning rates of ~0.4 m/km (Figure 4.13). However, lobes pinch out abruptly north-eastwards (between logs 7-9) over a horizontal distance of 2.4-2.7 km (Picún Leufú; Figure 4.1C and Figure 4.13).

Apart from a complicated stacking pattern, the Lower Lobe Complex also records variability in sandstone content and bed type from proximal to distal (Figure 4.14A). When traced down-dip over 2.4 km, amalgamation and sandstone-mudstone proportion decrease from 65.0%-35.0% in proximal and medial areas to 21.7%-78.3% in distal areas (Figure 4.14A). In proximal (logs 1-4) and medial (logs 5-6) parts, TFDs (Type D, E and F) dominate over low-density turbidites (Type A bed) (proximal: 84%-16% and medial: 87%-13%). In the distal parts (logs 7-8), beyond the pinch-out of most HEBs and thick-bedded TFD (Type D, E, F), low-density turbidites (Type A bed) dominate over TFDs (75%-25%), with occasional thin-bedded banded sandstone (Type C bed) (Figure 4.14A).

4.8.2. Upper Lobe Complex

The Upper Lobe Complex is ~30 m thick and contains 5 aggradationally stacked intraslope lobes (Figure 4.13). The lobes are up to 7 m thick in proximal areas (logs 1-4), showing their

highest amalgamation ratio and the thickest beds (up to 1.2 m thick) (Figure 4.13). The lobes thin northeastward from ~7 m to ~3 m thick, showing thinning rates of 1.2 m/km (Figure 4.13) and pinch out over a horizontal distance of ~3.3 km between logs 10 and 11 (compaction hinge of El Luchador fault block; Figure 4.1C and Figure 4.13).

In proximal parts, the Upper Lobe Complex contains a sandstone-mudstone proportion of 66%-34% and is dominated by high-density turbidites (Type B beds; 98%) (Figure 4.14A). In medial areas, the sandstone-mudstone proportion is 75.1%-24.9%, and TFDs (Type E and F beds) dominate over turbidites (Type B beds) (87.7%-12.3%) (Figure 4.14A). In distal parts, there is an abrupt decrease in sandstone-mudstone proportion (18.3%-81.7%), and low-density turbidites dominate (Type A beds) over TFDs and HEBs (55.8%-44.2%) (Figure 4.14A).

4.9. Discussion

4.9.1. Controls on bed types and flow transformation

The flow transformations responsible for the reported variability in bed types are proposed to have been controlled by the incorporation of clay from the substrate and the flow deceleration rates (Figure 4.14B). It is suggested that the flow transformations observed here were characterised by the interplay between complex longitudinal and vertical flow segregation processes. Longitudinal flow processes are characterised by high concentration bypassing debris flow heads responsible for the bedload transfer of mudstone clasts to slower and more depositional parts of the flow (Baas et al., 2021). ‘Self-accelerating’ flow cells at the front of the flow have been reported in physical modelling (*sensu* Sequeiros et al., 2009, 2018) and are increasingly recognised in modern systems (Azpiroz-Zabala et al., 2017; Paull et al., 2018; Pope et al., 2022). However, in the rock record, evidence for the erosional and bypassing debris flow head is the abundance of grooves and high matrix content in Type B, C, D, E, F and G beds, as reported in this study. The formation of H1 divisions in Type C, D and E beds is

inferred to be a product of transitional flows (Baker and Baas, 2020; Hussain et al., 2020) rather than turbidites (Haughton et al., 2003, 2009; Davis et al., 2009). This evidence suggests that the internal structure is associated with vertical segregation processes (Baas et al., 2011, 2016, 2021; Kane et al., 2017) rather than a longitudinal process characterised by forerunning turbidity currents (Haughton et al., 2003, 2009). The gradual boundaries of the investigated HEBs reveal that the flow did not develop stable internal stratification (e.g. Kane et al., 2017), suggesting deposition from flows with high deceleration rates (Baas et al., 2011; Baas et al., 2016; Stevenson et al., 2020). Such high deceleration rates support the interpretation of lobes deposited within a complex intraslope topography. In this case, the inherited early post-rift topography (Figure 4.15A; Privat, 2019; Privat et al., 2021) led to the development of TFDs in proximal lobe sub-environments (Figure 4.15B; e.g. Fonnesu et al., 2015, 2018; Terlaky and Arnott, 2016; Brooks et al., 2018c, 2022; Mueller et al., 2021). In contrast, the non-erosional low-density turbidites remained almost tabular and without any transition into other bed types (Figure 4.14B), indicating more stable flow conditions and efficiency than in the denser transitional flows (Al Ja'Aidi et al., 2004).

4.9.2. Sediment routing pathways and mud availability

The mudstone-dominated substrate could have enhanced the development of matrix-rich deposits (Figure 4.14B). The >100 m thick mudstone package that draped the syn-rift topography (Figure 4.15A) was available for incorporation into the overriding flows, and the incorporation of this mud could have been enhanced by the immature sediment routing pathways (Privat et al., 2021), leading to poor channelisation. Well-developed sediment routing pathways remove part of the fines by flow striping and overspill (Peakall et al., 2000; Hodgson et al., 2016) and decrease the availability of muddy substrate (Fonnesu et al., 2015, 2018;

Mueller et al., 2021; Brooks et al., 2022). The first sediment-gravity flows arriving in the Chachil Graben (Figure 4.15A) passed over a semi-consolidated muddy substrate, which could have been easily entrained (Terlaky and Arnott, 2014; Kane et al., 2017; Martínez-Doñate et al., 2021) causing flow bulking (Haughton et al., 2009). This effect could explain the dominance of TFDs in the lobe axis of the Lower Lobe Complex (Figure 4.12, Figure 4.13 and Figure 4.15). This contrast with previous studies documenting the sandy nature of intraslope lobes (e.g. Spychala et al., 2015; Brooks et al., 2018c). These models highlight the preferential trapping of the coarser fraction of the sediment gravity flows, while the more dilute fine-grained tops of the turbidity currents bypass down-dip. However, flow decoupling (Kneller and McCaffrey, 1999) might have been reduced by the cohesive forces within the transitional flows during the development of lobes within the Lower Lobe Complex. In contrast, in the Upper Lobe Complex, the flows travelled over sandier deposits (Figure 4.13 and Figure 4.15A), which might have limited entrainment of the muddy substrate (Terlaky and Arnott, 2014). This interpretation is supported by the dominance of high-density turbidites in the lobe axis and TFDs and HEBs in lobe fringes (Figure 4.13 and Figure 4.15B). The bed type proportion in medial parts of the Upper Lobe Complex is comparable to the proportions in proximal parts of the Lower Lobe Complex (Figure 4.14A). A similar effect is observed at the lobe scale, with the lobe axes of the Lower complex and lobe off-axis deposits of the Upper Lobe Complex comprising similar bed type associations despite the different degrees of bed amalgamation (Figure 4.12). This study highlights the role that variable substrate entrainment can play in intraslope lobes with a similar source.

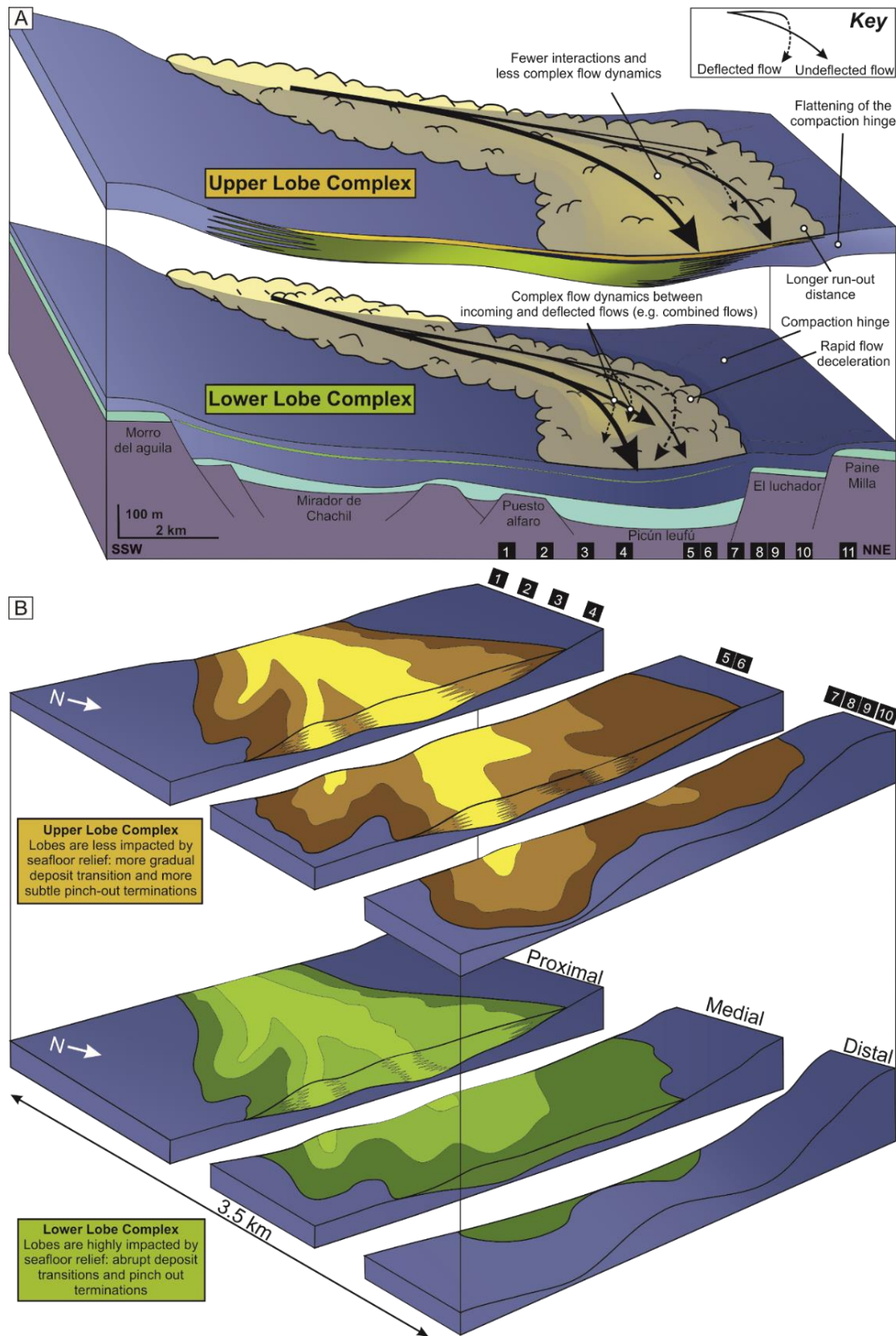


Figure 4.15. Schematic diagrams show (A) the response of parental sediment gravity flows interacting with the early post-rift seafloor relief (B) and a submarine lobe from Lower and Upper Lobe Complexes. The Lower Lobe Complex pinch-out is more proximal than the Upper Lobe Complex due to the flattening of the inherited early post-rift topography over time. Denser flows or parts of flows are restricted to the topographic lows, while the more dilute

ones can travel further into the compaction hinge, depositing low-density turbidites. Note the positions of the logs marked by black squares.

4.9.3. Impact of topography on the pinch-out pattern

Seafloor relief affects the deceleration rates of sediment gravity flows, impacting the character of deep-water deposits (e.g., Sumner et al., 2008; Baas et al., 2011; Stevenson et al., 2020). Depending on their flow properties, sediment gravity flows will respond differently when interacting with such relief (Kneller and McCaffrey, 1999; Al Ja'Aidi et al., 2004; Smith, 2004a; Bakke et al., 2013) and influence the distribution of bed types in the lobes (Figure 4.14 and Figure 4.15). The abruptness of pinch-out terminations (Bakke et al., 2013; Soutter et al., 2019) is strongly controlled by the yield strength of the source flow with limited flow efficiency (Hiscott, 1994a). This effect is observed in the Chachil Graben, where the lobe complex terminations offset the pinch-out of the contemporaneous debrites (Figure 4.13). This effect is not limited to laminar flows; it also impacts the transitional flows producing thin-bedded, matrix-rich HEBs (Type D beds) that pinch out abruptly against the frontal topography (Figure 4.14B). Denser flows are more sensitive to intrabasinal topography than dilute flows/divisions (e.g. Tóké and Patacci, 2018). This statement is supported by the high divergence in palaeoflow reported from the multidirectional grooves, indicative of the sensitivity of TFDs (Peakall et al., 2020) to obstacles (e.g. debrite rugosity; Muzzi Magalhaes and Tinterri, 2010) and basin-scale topography (e.g. compaction hinge) (Figure 4.15A). In contrast, the dilute (parts of) flows did not decelerate rapidly enough or failed to entrain enough substrate mud to suppress flow turbulence (Al Ja'Aidi et al., 2004; Talling et al., 2012). This results in extensive thin-bedded low-density turbidites (e.g. Smith, 2004) or banded TFDs offsetting the pinch-out of HEBs, depositing on relative topographic highs as seen with the pinch-out pattern documented in the study area (Figure 4.14B). The ripple and flame structures indicate that proximal areas (logs 1-4) show an overall NE trend, with deflection/reflection indicators

(Figure 4.13; Privat et al., 2021). Another indicator of complex flow behaviour resulting from the interaction between transitional flows and seafloor relief is the development of hummock-type structures (Figure 4.9; S5 sample bed). These structures are evidence of combined flows characterised by an oscillatory component produced by internal waves and reflected bores (Tinterri et al., 2016). Combined-flow bedforms are well-developed in the Lower Lobe Complex, where a higher degree of flow confinement and interaction with topography is inferred (Figure 4.15A).

4.9.4. The steepness of the confining slope and comparison with other systems

Intraslope lobe complexes of the earliest Los Molles Formation were deposited under the influence of a S-facing, oblique to frontal counterslope formed by a compaction hinge above the El Luchador fault block (Privat et al., 2021) (Figure 4.15). Reconstructing the steepness of the confining slope during this earliest post-rift stage is not straightforward where onlap terminations against basin margins are not developed. Deep-water systems interacting with gentle topography (i.e., a fraction of a degree) tend to produce a complex pinch-out of the sand-rich lobe component, characterised by an aggradational succession of tens of metres of thin-beds containing climbing ripples. Published examples include the Welsh Basin (Smith, 2004a) and Karoo Basin (Spychala et al., 2017c). In contrast, on steeper slopes (i.e., > 10 degrees), the characteristic termination style is onlap of sheet-like sandstone beds unconformably terminating directly onto the basin margin, such as in the Annot Basin, France (Kneller and McCaffrey, 1999; Sinclair, 2000; McCaffrey and Kneller, 2001; Bakke et al., 2013; Soutter et al., 2019) and the Laga Basin in Italy (Marini et al., 2015). In the Chachil Graben, the abruptness of pinch-outs, lack of climbing ripple lamination, and the bed types reported in this contribution suggest that the compaction hinge-related counterslope was steeper (> 1 degree)

than those reconstructed for the Welsh (Smith, 2004a) and Karoo Basin (Spychala et al., 2017c) but less steep than those reported in the Annot (Du Fornel et al., 2004; Soutter et al., 2019) or Laga Basin (Marini et al., 2015). Further quantifying the angle in the Chachil Graben is challenging due to the similarity between the organic-rich calcareous mudstones that draped the rift topography (Privat et al., 2021) and the high-efficiency silty, low-density turbidites offsetting the sandstones (distal fringe; Boulesteix et al., 2020). In addition, post-depositional compaction-driven deformation (burial-related) and the draping nature of the more distal deposits might lead to overestimating the counterslope angle (Pickering and Hilton, 1998; Bakke et al., 2013). Another indicator of seafloor relief is the presence of an injectite network (Figure 4.13 and Figure 4.15A; Cobain et al., 2017; Hansen et al., 2019). This suggests that early post-rift topography is not solely limited to inheritance from the previous extensional phase but can be locally enhanced by compaction-related deformation, promoting long-lived seabed relief that largely influenced the nature of the intraslope lobes.

4.9.5. Controls on stratigraphic architecture

The differential flow deceleration and deposition produced by the frontal topography in the Chachil Graben promoted a thicker accumulation of lobe-related deposits over the depocentre lows than on the topographic highs (Figure 4.14 and Figure 4.15) (Smith and Joseph, 2004). In the Lower Lobe Complex, the abruptness of the pinch-out terminations, the tabularity of the intraslope lobes (4.5 m thick and < 1m thinning), and the multidirectional grooves and ripples suggest that a complex frontal seafloor topography was a strong control on geometry and architecture. The Lower Lobe Complex (~45 m thick) is characterised by a progressive down dip advancement of the pinch-out position from base to top (Figure 4.13 and Figure 4.15A). This pinch-out pattern suggests infilling, flattening, and smoothing the complex inherited rift

topography over time (Figure 4.15) (e.g., Ross et al., 1994; Hay, 2012). The stacking of 10 intraslope lobes shows a compensational pattern (e.g. Mutti and Sonnino, 1981; Deptuck et al., 2008; Prélat et al., 2009) with a strong aggradational component, where topography confined the lobes frontally but enabled lateral compensation. The interpretation is that during the deposition of the Lower Lobe Complex, the deep-water system was confined (Winker, 1996; Sinclair, 2000; Southern et al., 2015) at the lobe scale but semi-confined (Marini et al., 2015; Dodd et al., 2019) at the lobe complex scale. In the Upper Lobe Complex (~30 m thick), the five intraslope lobes are thicker (7 m thick), show lower thinning rates, and can be traced over longer distances (> 3.3 km) than in the Lower Lobe Complex. This architecture and termination style suggest that seafloor topography impacted individual lobes less. Given that the pinch-out terminations developed over the compaction hinge, flows were likely to deflect towards the E(NE) after interacting with the south-dipping oblique-to-frontal oriented (see Kneller et al., 1991; Soutter et al., 2021) compaction hinge. The five intraslope lobes show an aggradational stacking pattern, juxtaposing similar sub-environments on top of one another. This reveals that even if the Upper Lobe Complex and its lobes recorded a reduction in frontal confinement (compared to the Lower Lobe Complex), the system was more confined laterally at the lobe complex scale, limiting lobe-scale compensational stacking. In other words, the stratigraphic evolution presented here shows an upward decrease in frontal confinement at both lobe and lobe complex scales; however, there is an increase in the degree of lateral confinement. It is postulated that the increasingly aggradational stacking pattern recorded from the Lower to the Upper Lobe Complex is unrelated to depocentre-scale topography modification but rather to an increase in sediment input and flow efficiency. Additionally, the continuous slope degradation and emplacement of debrites might have flattened the topography, favouring the connectivity along the slope and efficiency of the flows. This highlights that the concept of confinement is related to the balance between the accommodation and the size of the

depositional system and their source flows. Considering the two lobe complexes as a lobe complex set (Prélat et al., 2009), this larger unit shows a progradational stacking pattern (e.g. Hodgson et al., 2006; Grundvåg et al., 2014) related to the maturation of the sediment routing pathway (Hodgson et al., 2016) and smoothing of the inherited topography (Figure 4.15). This study highlights the impact of inherited early post-rift topography characterised by compaction hinge(s) development over syn-rift horsts could be more complex than previously reported, impacting deep-water systems from bed to bed to lobe-complex scale.

4.10. Conclusions

Two exhumed early post-rift intraslope lobe complexes show consistently different characteristics. Transitional flow deposits dominate the argillaceous Lower Lobe Complex, and beds pinch out more abruptly than in the overlying turbidite-dominated lobe complex. Both are volcanic arc sourced, and the source area was not responsible for the differences in bed types between the lobe complexes. The preferred interpretation is an autogenic response of the depositional system due to the progressive healing of intraslope relief, maturing of sediment transport routes, and reduction in muddy substrate entrainment. The compaction hinge(s) acted as a barrier for the denser and cohesive (parts of) flows, but the dilute turbidity currents could override and deposit on the intrabasinal slope. This study highlights the primary role of subtle inherited relief developed during the early post-rift stage of basin development. This model may provide new insights into how these systems act as hydrocarbon reservoirs, aquifers, and carbon storage sites. A better understanding of grain type and grain size segregation from proximal to distal parts of deep-water systems is critical for carbon sequestration and the CO₂ plume dynamics.

5. The impact of slope instabilities on submarine channels and development of crevasse lobes in tectonically active settings: an exhumed example from the Eocene Aínsa Basin (Spain)

Martínez-Doñate, A.¹, Soutter, E. L. ¹, Kane, I.A.¹, Poyatos-Moré, M. ², Hodgson, D.M.³, Flint, S.S.¹.

1. School of Earth and Environmental Sciences, University of Manchester, Manchester M13 9PL, UK.
2. Departament de Geologia, Universitat Autònoma de Barcelona, 08193 Cerdanyola del Vallés, Spain.
3. School of Earth and Environment, University of Leeds, Leeds LS29JT, UK.

5.1. Abstract

Tectonic deformation and associated submarine slope failures create seafloor relief that can strongly influence the pathways of subsequent sediment gravity flows and the resulting architecture of deep-water depositional systems. The exhumed Middle Eocene strata of the Banastón deep-water system in the Aínsa Basin, Spain, allow the investigation of the interplay between submarine slope channel systems and syn-depositional compressional tectonics. Previous studies have documented and mapped six sandstone-dominated sub-units (Banastón I-VI), interpreted as low-sinuosity and narrow channel-belt deposits confined by two tectonically-induced fine-grained opposing slopes. This study focuses on the Banastón II unit, exposed along a 1.5 km long dip-orientated (NW-SE) outcrop belt. Here detailed facies analysis is performed and physically correlated 10 measured sections over 1.5 km within a 111 m-thick stratigraphic interval. Results show the juxtaposition of overbank areas over channel belt deposits, displaying a stratigraphic evolution whereby the channel axes progressively migrated to the southwest, away from a growing structure in the northeastern part of the study area. Uplift of the active margin promoted mass-wasting events and the emplacement of submarine

landslides of different nature within the channel belt and overbank areas. These facilitated breaching of the active margin channel walls, leading to the development of crevasse scours and associated crevasse lobes deposited in the slide scar generated by the evacuation. The development of crevasse deposits on the active margin contrasts with other studies in similar foreland channel systems, where crevassing is only reported in the opposing, more stable slope. This phenomenon is interpreted as the result of accommodation generated by mass-wasting processes adjacent to the active basin margin, which impacted the sediment routing and depositional patterns of channelized gravity flows. Finally, the role of multiple mass failure events on channel avulsion in tectonically-active compressional margins is also explored and discussed.

5.2. Introduction

Submarine canyons and channel systems are conduits for the delivery of sediment (Mutti and Normark, 1991; Piper and Normark, 2001), nutrients (Heezen et al., 1955) and pollutants (Kane and Clare, 2019; Zhong and Peng, 2021) to deep-water, where associated deposits form archives of paleoenvironmental change (Prins and Postma, 2000; Castelltort et al., 2017; Läubli et al., 2021; Soutter et al., 2022). Channel belts result from the erosional degradation of the slope and/or the aggradation of constructional overbank deposits (Buffington, 1952; Menard, 1955; Normark, 1970). Sediment-gravity-flows travelling downslope are partially confined within the channel belts, with the more dilute and finer fraction of flows able to be flow stripped or overspill and deposit on the overbank areas (Piper and Normark, 1983; Peakall et al., 2000; Keevil et al., 2006; Kane et al., 2007; Kane and Hodgson, 2011; Hansen et al., 2017a). When these flows are unconfined, the construction of wedge-shaped deposits (Buffington, 1952), and are commonly termed external levees (Kane and Hodgson, 2011). However, limited accommodation in confined settings can hinder the development of external

levees, such as foreland basins (overbank wedges of De Ruig and Hubbard, 2006; Hubbard et al., 2009). Breaching of the channel margin or external levee can lead to crevasse lobe deposition and ultimately result in avulsion of the channel system (Damuth et al., 1988; Posamentier and Kolla, 2003; Fildani and Normark, 2004; Armitage et al., 2012; Brunt et al., 2013; Maier et al., 2013; Morris et al., 2014). The most commonly documented breaching mechanisms are enhanced bank erosion by downstream meander migration (sweep) and/or lateral meander growth (swing) (e.g. Peakall et al., 2000; Abreu et al., 2003; Deptuck et al., 2003), and mechanic weakening by overpressure leading to collapse of channel walls (e.g. Sawyer et al., 2014) or the external levee (Ortiz-Karpf et al., 2015).

The evolution of submarine channel systems in active compressional tectonic settings remains poorly understood compared to unconfined settings. The longitudinal profile, evolution and architecture of deep-water channels in active tectonic settings are strongly controlled by pre- or syn-depositional relief (e.g. Heiniö and Davies, 2007; Kane et al., 2010a; Georgiopoulou and Cartwright, 2013), halokinesis (e.g. Beaubouef and Friedmann, 2000; Gee and Gawthorpe, 2006) and emplacement of submarine landslides (Canals et al., 2000; Pickering & Corregidor, 2005; Fairweather, 2014; Kneller et al., 2016; Kremer et al., 2018; Nwoko et al., 2020b; Tek et al., 2020, 2021b; Steventon et al., 2021). Hereafter the term submarine landslide will refer to the product of a remobilized sedimentary body translated downslope due to gravitational instabilities and deposited en masse (Nardin et al., 1979; Hampton et al., 1995; Mulder and Alexander, 2001; Moscardelli and Wood, 2008; Bull et al., 2009; Talling et al., 2012; Kneller et al., 2016). Sediment routing and deep-water stratal patterns in active foreland basins largely depend on the basin physiography, which is often characterised by two or more opposing and confining slopes and influenced by the uplift/movement of compressional structures. Submarine channels in these settings are characterised by low sinuosity, and the mechanisms for avulsion are less understood than in highly sinuous, unconfined channel systems. While the

large-scale morphology of structurally confined submarine channel systems can be resolved with seismic reflection data, the distribution and decimetre- to the metre-scale architecture of sand-prone elements within otherwise mudstone-dominated stratal packages are rarely resolvable. Commonly, field-based studies are used to characterise these sub-seismic-scale elements, although deposits in active foreland basins are often highly deformed due to syn- and post-depositional compressional tectonics.

5.2.1. Study Area: San Vicente (Aínsa Basin)

The exhumed Eocene deep-water strata of the Aínsa Basin are well-preserved examples of submarine slope channel fill deposits in an active foreland basin setting (Figure 5.1A). Here, the growth and propagation of structures related to the Pyrenean orogeny controlled the formation and migration of successive deep-water systems (e.g., Pickering and Corregidor, 2005; Arbués et al., 2007; Pickering and Bayliss, 2009; Dakin et al., 2013; Cantalejo and Pickering, 2014; Bayliss and Pickering, 2015; Scotchman et al., 2015a; Castelltort et al., 2017; Bell et al., 2018; Tek et al., 2020). This field-based study focuses on one of the deep-water systems (the Banastón system) (Figure 5.1B) and involves ten (10) detailed sedimentary logs (measured at 1:20 scale) in the San Vicente area (north Aínsa Basin) (Figure 5.1C). The Banastón II sub-unit is well-exposed in a 111 m-thick succession along a 1.5 km long dip orientated (NW-SE) outcrop belt. The objectives of this study are to 1) improve our understanding of the different environments of deposition and architecture of foreland slope channels at bed scale; 2) document the controls and sedimentary processes involved in crevasse lobe development; 3) evaluate the role that active tectonism and mass wasting processes played in the general evolution and avulsion of the Banastón channel system.

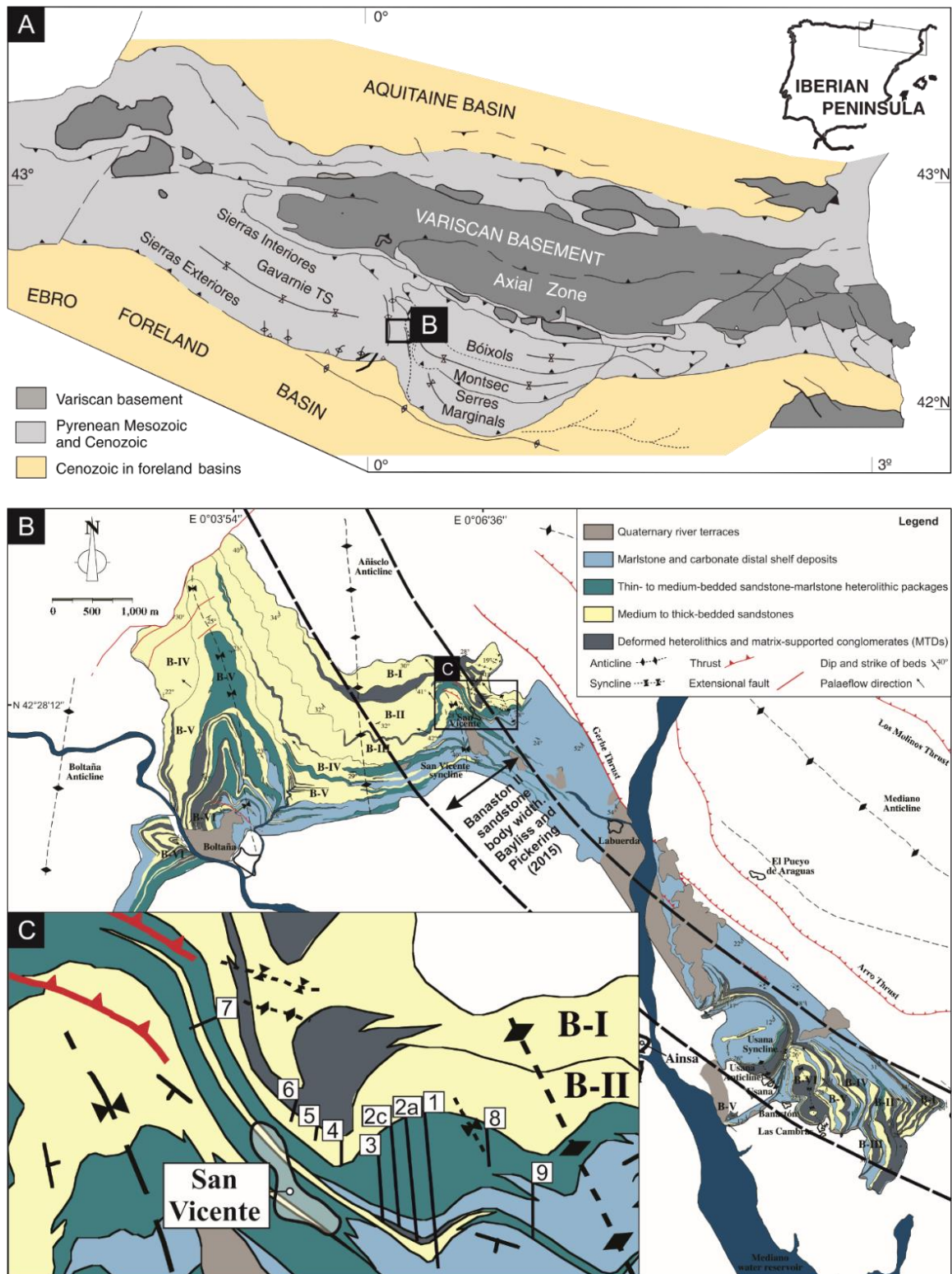


Figure 5.1. (A) Structural map of the Pyrenees (after Muñoz et al., 2013) and location of the Aínsa Basin (See black square). (B) Geologic map of the Banastón system and the main structures (after Bayliss and Pickering, 2015). Note the black square indicating the location of the study area. (C) Geologic map of the study area near the San Vicente town (after Pickering and Bayliss, 2009; Bayliss and Pickering, 2015) and the sedimentary logs collected in this study.

5.3. Geological setting

Late Cretaceous to Miocene convergence between Eurasian and Iberian continental plates resulted in the formation of the Pyrenees (Srivastava and Roest, 1991; Muñoz, 2002; Rosenbaum et al., 2002), and their related north and south Pyrenean foreland basins (Figure 5.1A). The southern foreland basin was characterised by a thin-skinned fold-and-thrust system with southward vergence, which led to the development of WNW-ESE orientated narrow and elongated piggyback basins (Muñoz, 2002), which deepen westwards (Dreyer et al., 1999). The south-central foreland basin is commonly subdivided into three main sectors, which formed a linked source-to-sink system during the Lower to Middle Eocene (Nijman, 1998; Payros et al., 2009; Chanvry et al., 2018): i) the Tremp-Graus depocentre in the east, with alluvial, fluvio-deltaic and shallow-marine deposits; ii) the Aínsa depocentre in the central part, dominated by submarine slope deposits; and iii) the Jaca depocentre in the west, where the basin floor deposits are found. The deep-water deposits of the Aínsa and Jaca depocentres are collectively known as the Hecho Group (Mutti et al., 1972) and have been the focus of several studies (e.g. Barnolas and Gil-Peña, 2002; Pickering and Corregidor, 2005; Arbués et al., 2007; Payros et al., 2009; Pickering and Bayliss, 2009; Clark and Cartwright, 2011; Pohl and Mccann, 2014; Cantalejo and Pickering, 2014; Scotchman et al., 2015a, b; Bayliss and Pickering, 2015; Castelltort et al., 2017; Läubli et al., 2021). The Hecho Group turbiditic systems were predominantly fed from the fluvio-deltaic environments in the east (Fontana et al., 1989; Gupta and Pickering, 2008; Caja et al., 2010; Thomson et al., 2017), supplying the Aínsa depocentre through a series of the tectonically-controlled submarine canyon and channel systems, well exposed in the southeast part of the depocentre (Mutti, 1977; Puigdefàbregas and Souquet, 1986; Millington and Clark, 1995).

In the Aínsa Basin, seven deep-water systems have been recognised: Fosado, Arro, Gerbe, Banastón, Aínsa, Morillo and Guaso (Burbank et al., 1992; Payros et al., 2009; Poyatos-Moré,

2014; Bayliss and Pickering, 2015; Scotchman et al., 2015; Castelltort et al., 2017; Clark et al., 2017). This study focuses on the Lutetian Banastón system, whose cumulative thickness ranges from ~500 m on the upper slope to ~700 m on the lower slope (Bayliss and Pickering, 2015). The channelized system was characterised by an axial supply (NNW directed paleoflow) with a lateral-offset stacking pattern towards the WSW (Figure 5.1B). This progressive channel axes' migration towards the WSW was controlled by the syn-depositional growth and propagation of NW-SE oriented oblique-lateral ramp structures related to more regional E-W thrust sheets. (Poblet et al., 1998; Fernández et al., 2012; Muñoz et al., 2013). Bayliss and Pickering (2015) mapped six channelized sandstone bodies within the Banastón system: BI (149 m thick and 2000 m wide), BII (98m thick and 1800 m wide), BIII (72 m thick and 1700 m wide), BIV (124 m thick and 2500 m wide), BV (97 m thick and 3300 m wide) and BVI (160 m thick and 2400 m wide) (Figure 5.1B). These six channelized sandstone bodies were subdivided into Stage I (BI-BIII) and Stage 2 (BIV-BVI) by Bayliss and Pickering (2015), where BI, BII and BIII were confined between the Mediano and Añisclo anticlines, and BIV, BV and BVI between the Añisclo and Boltaña anticlines, forming two NNW-oriented corridors ~5-8 km wide. This study focuses on the Banastón II sub-unit, whose deposition has been linked to a period of active tectonism (Läuchli et al., 2021).

5.4. Data and methods

The sedimentology and stratigraphic architecture of a 111 m-thick section in the Banastón II sub-unit over a 1.5 km SW-NE orientated outcrop belt were investigated. The bedding within the studied succession dips 30° to the SSW. Ten detailed sedimentary logs (Figure 5.1C) were collected at a 1:20 scale to document bed thicknesses, lithology, sedimentary structures, textures and palaeocurrent measurements (n=73) from ripples, flutes and grooves. Logs were correlated by walking individual sandstone packages, enabling the characterization of different

facies associations and the general stratigraphic evolution of the Banastón II system in the study area. Additionally, 7 detailed logs were collected at a 1:2 scale to document a specific stratigraphic interval's complexity and fine-scale thickness variability. Additionally, Uncrewed Aerial Vehicle (UAV) photogrammetry was used to capture the stratigraphic architecture of stratal packages and cover inaccessible areas.

5.5. Facies associations

Based on facies and outcrop analysis, 14 lithofacies in the Banastón II sub-unit are recognised (Figure 5.2, Figure 5.3, Figure 5.4, Table 5.1, Table 5.2 and Table 5.3). These lithofacies have been grouped into 5 facies associations (Figure 5.5), representing different depositional sub-environments.

5.5.1. FA1: Overbank deposits

Description: This facies association is characterised by thin-bedded heterolithic < 20 m thick successions (Figure 5.5A) dominated by alternating structureless carbonate mudstones (Lf1) and thin-bedded siltstones and sandstones (Figure 5.2A). Mudstones constitute 92.5% of FA1, while siltstones and sandstones constitute 7.5% (Figure 5.5A). Some thin siltstone and sandstone beds develop flat to loaded bases and lenticular tops, pinching out laterally (Lf2a) or are laterally extensive (Lf2b) at the outcrop scale (Figure 5.2A and Figure 5.2B). Lf2a is structureless or comprises starved-ripple cross-lamination (Figure 5.2A), while Lf2b shows planar lamination (Figure 5.2B). Locally, the conformable bedding of FA1 can be interrupted by unconformable 0.5-7 m thick deformed heterolithic packages, rotated above south-westwards dipping concave-up planes (LF7a and Lf7b; Figure 5.4A, Figure 5.4B and Figure 5.4C). LF7a is thinner than 5 m and shows limited disaggregation, with minor deformation in the bedding (Figure 5.4A and Figure 5.4B). However, Lf7b is 5-7 m thick, and the bedding is deformed and comprises metre-scale amplitude folds (Figure 5.4C).

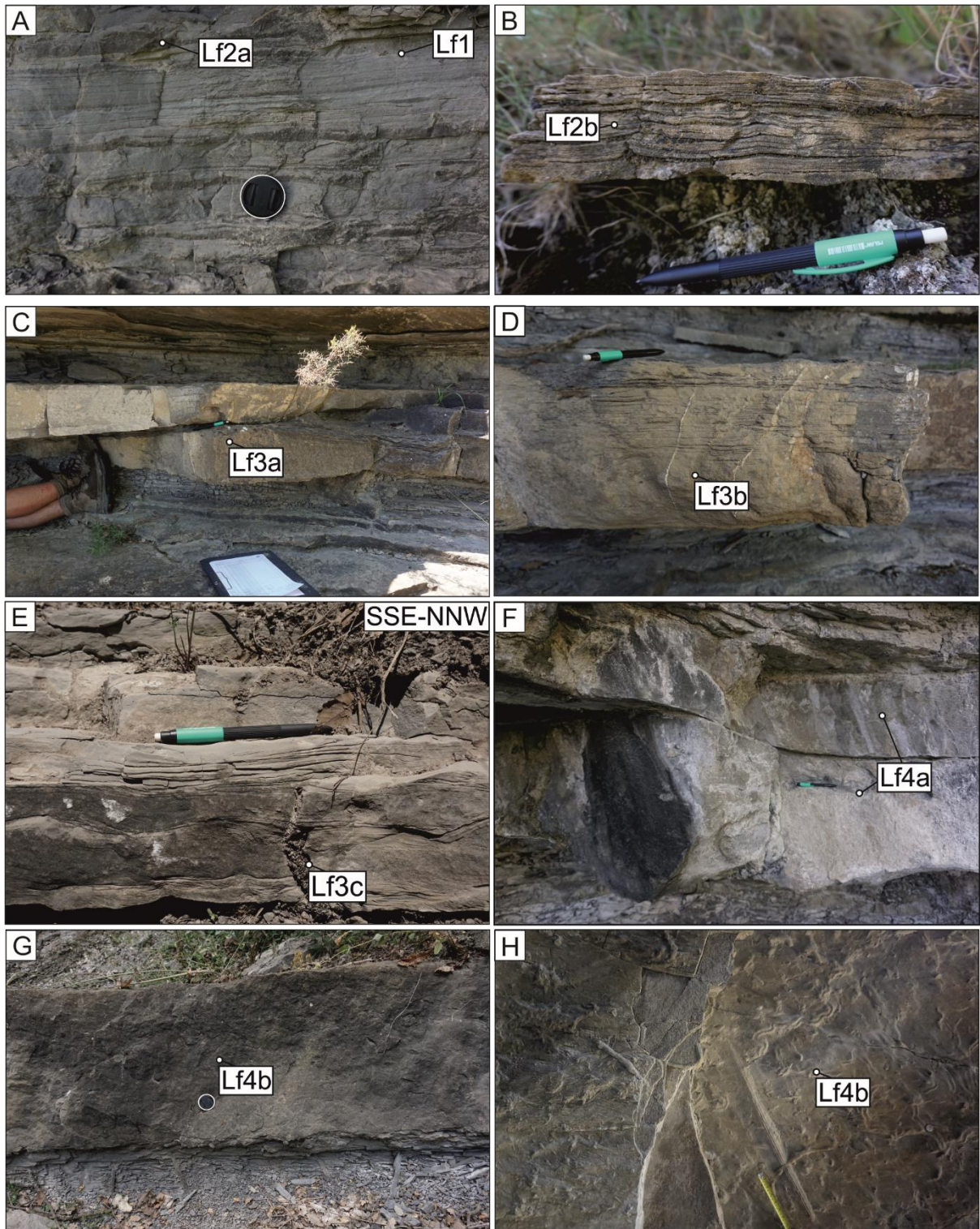


Figure 5.2. Outcrop photographs of Lf1-Lf4b lithofacies.

LITHOFACIES	LITHOLOGY	DESCRIPTION	THICKNESS	PROCESS INTERPRETATION	PHOTO
Lf1: Structureless mudstone	Carbonate mudstone	No gradation or structuration.	No clear bedding	Hemipelagic suspension fallout.	Figure 5.2A
Lf2a: Lenticular thin-bedded siltstones and sandstones	Siltstone to fine-grained sandstones	Sandstones with flat bases and convex tops. Lenses can be 5-20 cm long.	1-10 cm	Deposition from a partially bypassing flow and reworking by distal, sluggish and small volume low-density turbidity current (Allen, 1971b, 1982b; Jobe et al., 2012).	Figure 5.2A
Lf2b: Structured thin-bedded sandstones	Very fine to medium-grained sandstone	Normally graded, moderately-sorted thin-beds. Fine- to medium-grained bases and (very) fine-grained tops. Planar laminated from base to top.	1-10 cm	Deposition and tractional reworking by steady low-density turbidity current (Allen, 1971b).	Figure 5.2B
Lf3a: Lenticular medium-bedded sandstones	Very fine- to coarse-grained sandstones	Sandstones with flat bases and convex tops. Lenses can be 5-20 m long with 10-40 cm amplitudes. They are structureless at the base, overlain by planar or sinusoidal bedforms. Overlying deposits can onlap onto these sandstone bodies.	0-40 cm	Deposition from unsteady and unidirectional low- to medium-density turbidity currents (Allen, 1973; Kneller, 1995). Convex tops are associated with tractional reworking from bypassing and steady turbidity currents.	Figure 5.2C
Lf3b: Planar laminated argillaceous	Coarse to fine-grained argillaceous	Argillaceous sandstones with well-developed planar laminations	10-60 cm	Deposits beneath mud-rich transitional plug flow are formed by steady, unidirectional and	Figure 5.2D

us medium-bedded sandstone	s sandstones	and wavy tops. The bed bases can be structureless.		tractional reworking within the upper stage flow regime (Baas et al., 2009, 2011, Baas et al., 2016; Stevenson et al., 2020).	
Lf3c: Climbing-ripple and sinusoidal laminated medium-bedded argillaceous sandstone	Coarse to fine-grained argillaceous sandstones	Bipartite sandstones comprise a sandy basal division passing gradually into argillaceous division. Alternating structureless and supercritical climbing ripple lamination. Sinusoidal laminations are common near bed tops.	10-50 cm.	Deposition from long-lived surging flows under high-aggradation rates and tractional reworking (Jobe et al., 2012). The flows ultimately collapse, increasing the fallout rate and developing sinusoidal lamination (Tinterri, 2011; Jobe et al., 2012).	Figure 5.2E
Lf4a: Erosional mudstone clast-rich thick-bedded sandstones.	Coarse to fine-grained argillaceous sandstones	Highly amalgamated, crudely normally graded and structureless thick-bedded sandstones. Bed tops are silty, locally developing planar laminations towards bed tops. Bed bases are unconformable with abundant grooves and bioturbation. Mudstone-clast-rich horizons and grain-size breaks are common.	0.5-1.2 m	Deposition under high-density partially bypassing turbidity currents (<i>sensu</i> Lowe, 1982), formed by incremental layer-by-layer deposition with high aggradation rates (Sumner et al., 2008; Talling et al., 2012). Scouring and entrainment of the fine-grained substrate are common.	Figure 5.2F
Lf4b: Structurel	Coarse to fine-	Often amalgamated and	0.5-1.2 m	Deposition from high-density turbidity currents	Figure 5.2G

ess thick-bedded argillaceous sandstones	grained argillaceous sandstones	structureless thick-bedded sandstones that become gradually argillaceous towards bed tops. Bed bases are mostly conformable; however, not always. Decimetre-scale burrows from top to basal contacts, not limited to bed bases.	(<i>sensu</i> Lowe, 1982), formed by incremental layer-by-layer deposition with high aggradation rates (Kneller and Branney, 1995; Sumner et al., 2008; Talling et al., 2012). The upper argillaceous division reflects the fine-grained tail of the flow, which collapsed due to radial spreading and abrupt loss in flow capacity.	and Figure 5.2H
------------------------------------------	---------------------------------	---------------------------------------------------------------------------------------------------------------------------------------------------------------------------------------------------------------------------------	---------------------------------------------------------------------------------------------------------------------------------------------------------------------------------------------------------------------------------------------------------------------------------------------------------------------------------------	-----------------

Table 5.1. Description, process interpretation and photographs of the Lf1 – Lf4b lithofacies.

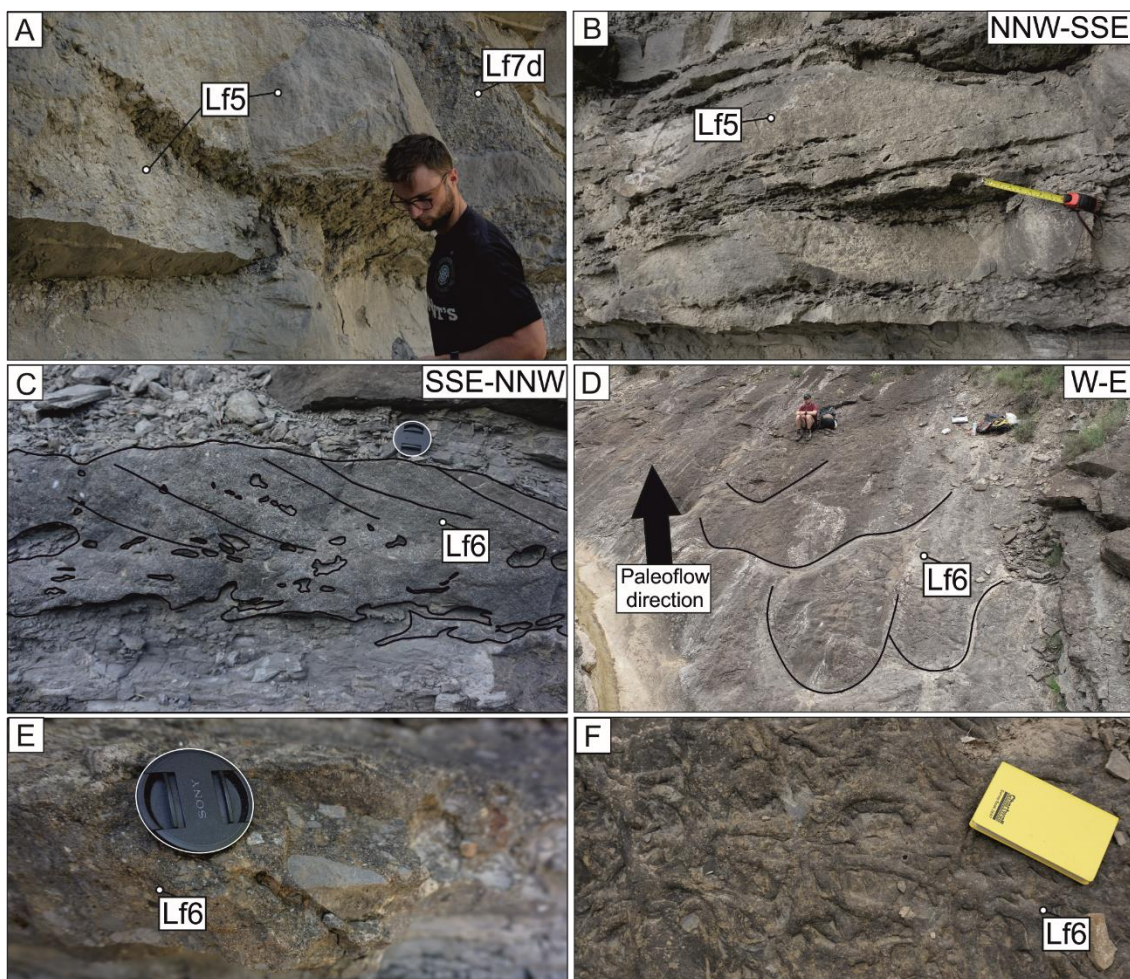


Figure 5.3. Outcrop photographs of Lf5 and Lf6 lithofacies.

LITH OFACIES	LITHOLOGY	DESCRIPTION	THICKNESSES	PROCESS INTERPRETATION	PHOTO
Lf5: Sand-filled scour	Argillaceous sandstone bearing abundant mudstone clasts along laminae	Medium- to thick-bedded sandstones with sharp unconformable concave-up (< 1 m) bases and flat tops. This lithofacies is structureless, planar laminated or dune-scale cross-bedded, bearing abundant mudstone clasts along laminae. Abundant burrows.	0.3-1 m	Deposition from high-density turbidity currents (<i>sensu</i> Lowe, 1982), formed by incremental layer-by-layer deposition with high aggradation rates (Kneller and Branney, 1995; Sumner et al., 2008; Talling et al., 2012). Planar and dune-scale cross-bedding bearing abundant mudstone clast along the laminae represent deposition from energetic, steady, and partially bypassing flows (Arnott, 2012; Talling et al., 2012; Stevenson et al., 2015).	Figure 5.3A and Figure 5.3B
Lf6: Medium-bedded granular sandstones	Medium to granular sandstone with mudstone clasts.	In plan view, medium-bedded granular sandstone with well-developed NW migrating dune-like bedforms with a crescentic shape. The cross-bedding is coarser-grained (granular to pebbly) than the surrounding sandstone (medium to very coarse). Rounded carbonate mudstone clasts are common.	20-50 cm	The abundant mudstone clasts suggest a partially bypassing flow (Stevenson et al., 2015) that reworked the previously deposited coarse fraction, forming dunes. Dune-like bedforms are attributed to high-magnitude steady parental flow (Arnott, 2012; Talling et al., 2012).	Figure 5.3C, Figure 5.3D, Figure 5.3E and Figure 5.3F.

Table 5.2. Description, process interpretation and photographs of the Lf5 and Lf6 lithofacies.

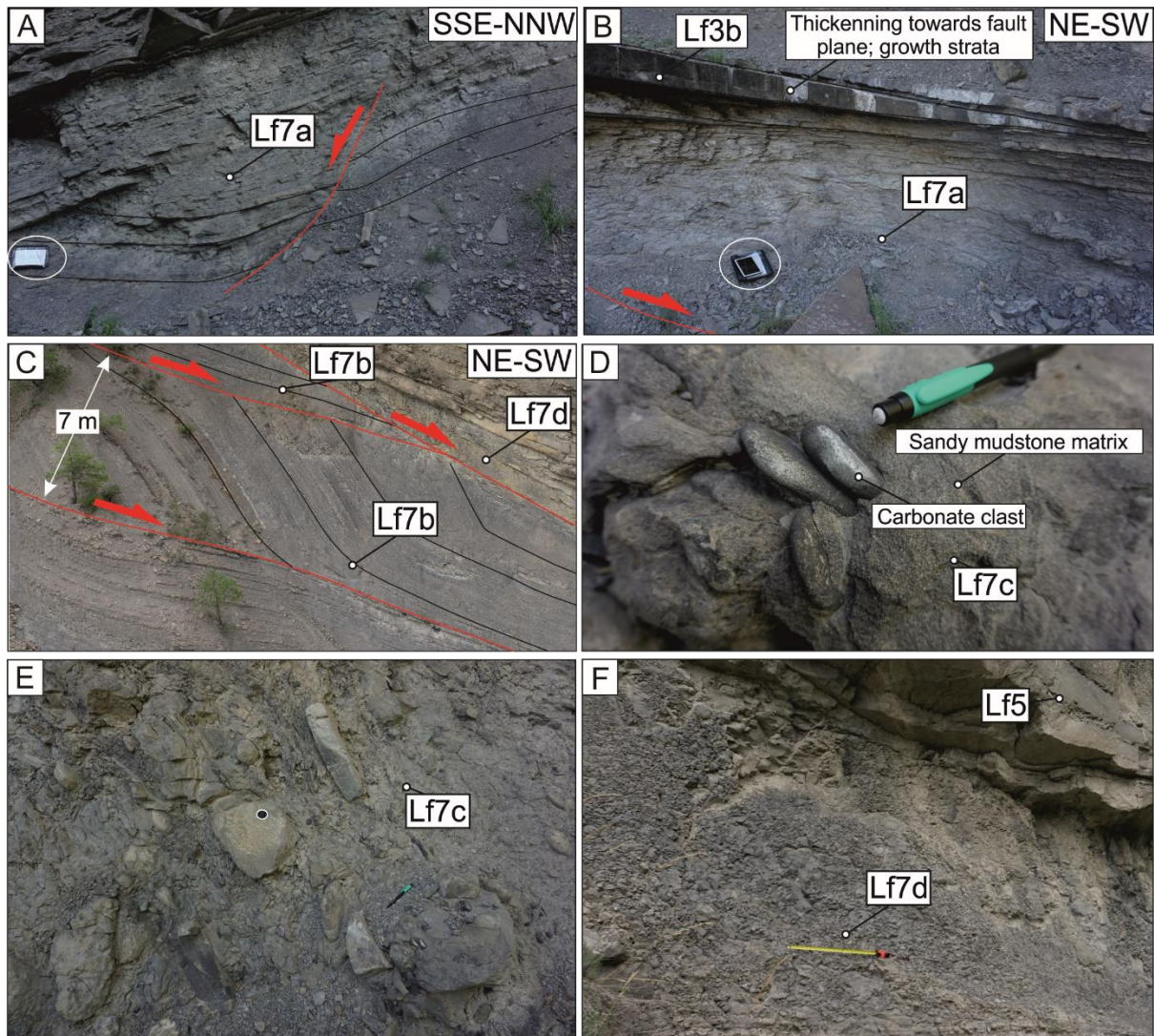


Figure 5.4. Outcrop photographs of Lf7a-Lf7d lithofacies.

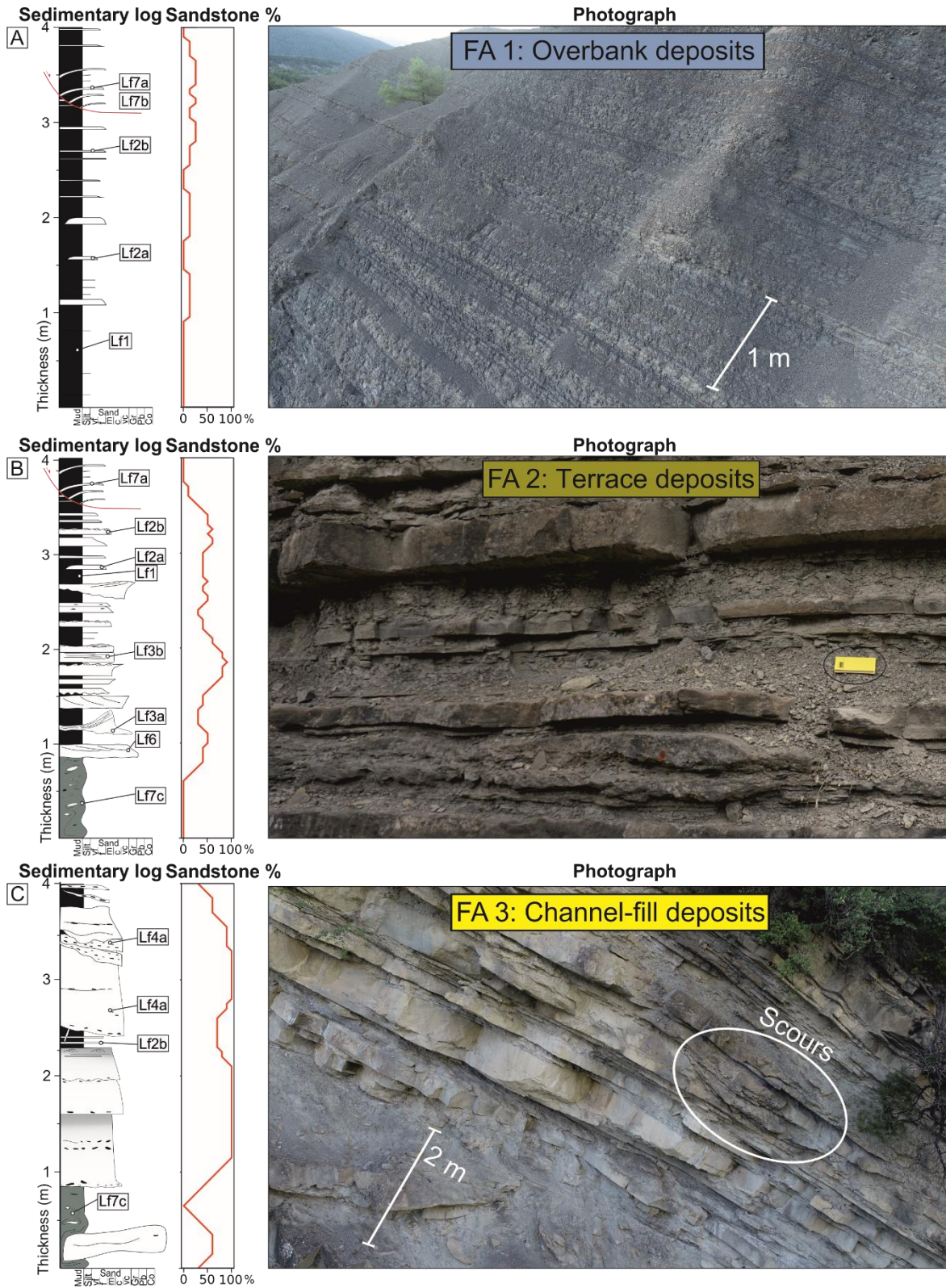
LIT HOF ACIES	LIT HOL OGY	DESCRIPTION	THI CKN ESS	PROCESS INTERPRETATION	PHOT O
LF7a: Rotated heterolithic	Thin-to medium-bedded heterolithic.	Rotated heterolithic (Lf1, Lf2a, LF2b) packages are characterised by decimetre-scale low-amplitude sinusoidal folding lacking internal disaggregation. Folding and normal faulting verge SW (perpendicular to paleoflow and parallel to the SW dipping active margin).	0.5-5 m	Local sliding of nearby stratigraphy (not disaggregated). Intraformational and non-erosional. The thickness changes of the top sandstone can be related to pre-depositional rugosity of the slide (e.g. Armitage et al., 2009) or	Figure 5.4A and Figure 5.4B

		The base of the deposit is often marked by a concave-up glide plane. At the top of this package, < 0.3 m thick sandstone beds showing localised thickness changes are common; thickening in the hangingwall towards the fault when the LF7a is thinnest and thinning or pinching out when Lf7a is thickest.		can be related to syn-depositional creeping/sliding (e.g. Ayckbourne et al., in press)	
LF7b: Folded heterolithics	Thin-to thick-bedded heterolithics.	Deformed heterolithic (Lf1, Lf2a, LF2b, LF4a, Lf4b, Lf5, Lf6, LF7c) package characterised by meter-scale amplitude open to recumbent folding. Normal faults and folds show SW vergence.	5-8 m	Local slumping of nearby stratigraphy (limited disaggregation). Intraformational and non-erosional. Equivalent to Type Ia MTCs of Pickering and Corregidor (2005).	Figure 5.4C
LF7c: Matrix-supported conglomerate	Mud-rich medium-grained sandstone to sandy mudstone.	Poorly sorted and ungraded with a chaotic distribution of clasts' floating' in a sandy mudstone matrix. Clasts show bimodal lithology: sub-rounded carbonate clast (> 15 cm) and sub-rounded to elongated sandstone clast (0.15 – 2 m). Irregular and sharp bases can be erosive, undulatory tops.	0.5-7 m	Cohesive debris-flow deposits (<i>sensu</i> Talling et al., 2012). The carbonate clasts are extraformational sediments eroded and reworked prior to their input to deep-water settings, while the sandstone clasts represent the rafting and incorporation of intraformational material into the debris flows. Equivalent to Type II MTCs of Pickering and Corregidor (2005).	Figure 5.4D and Figure 5.4E
LF7d: Sheared mudstone	Carbonate mudstone	Disaggregated and sheared carbonate mudstones, highly bioturbated	0.1-3 m	Local failure of nearby fine-grained stratigraphy. Bioturbation suggests that these deposits were overridden by nutrient- and oxygen-bearing flows	Figure 5.4F

				and proximity to channels.	
--	--	--	--	----------------------------	--

Table 5.2. Description, process interpretation and photographs of the Lf7a – Lf7d lithofacies.

Interpretation: The development of FA1 is the combined result of deposition from background sedimentation and low-density fine-grained turbidity currents. Here, background sedimentation refers to hemipelagic settling, and thin dilute sediment gravity flow deposits not visible to the naked eye in outcrop (see Boulesteix et al., 2020). These accumulations of thin beds are interpreted as the product of the flow-stripping and overspilling from the dilute upper parts of the channelized turbidity currents into the overbank areas (Piper and Normark, 1983; Peakall et al., 2000; Keevil et al., 2006; Kane et al., 2007; Kane and Hodgson, 2011; Hansen et al., 2017a). When these flows exit the confining channel belt, they are characterised by capacity-driven deposition as they become unconfined and decelerate (Hiscott, 1994a; Hübscher et al., 1997; Posamentier and Kolla, 2003; Kane et al., 2007, 2010b). The rotated stratigraphy is a common feature of overbank environments adjacent to channels (e.g. Kane et al., 2007; Kane et al., 2011; Dykstra et al., 2007; Hubbard et al., 2009; Hansen et al., 2015) representing localised submarine landslide deposits, product of the drapping and accretion on steep bounding slopes (Abreu et al., 2003; De Ruig and Hubbard, 2006; Hubbard et al., 2009) where the channel belt is confined.



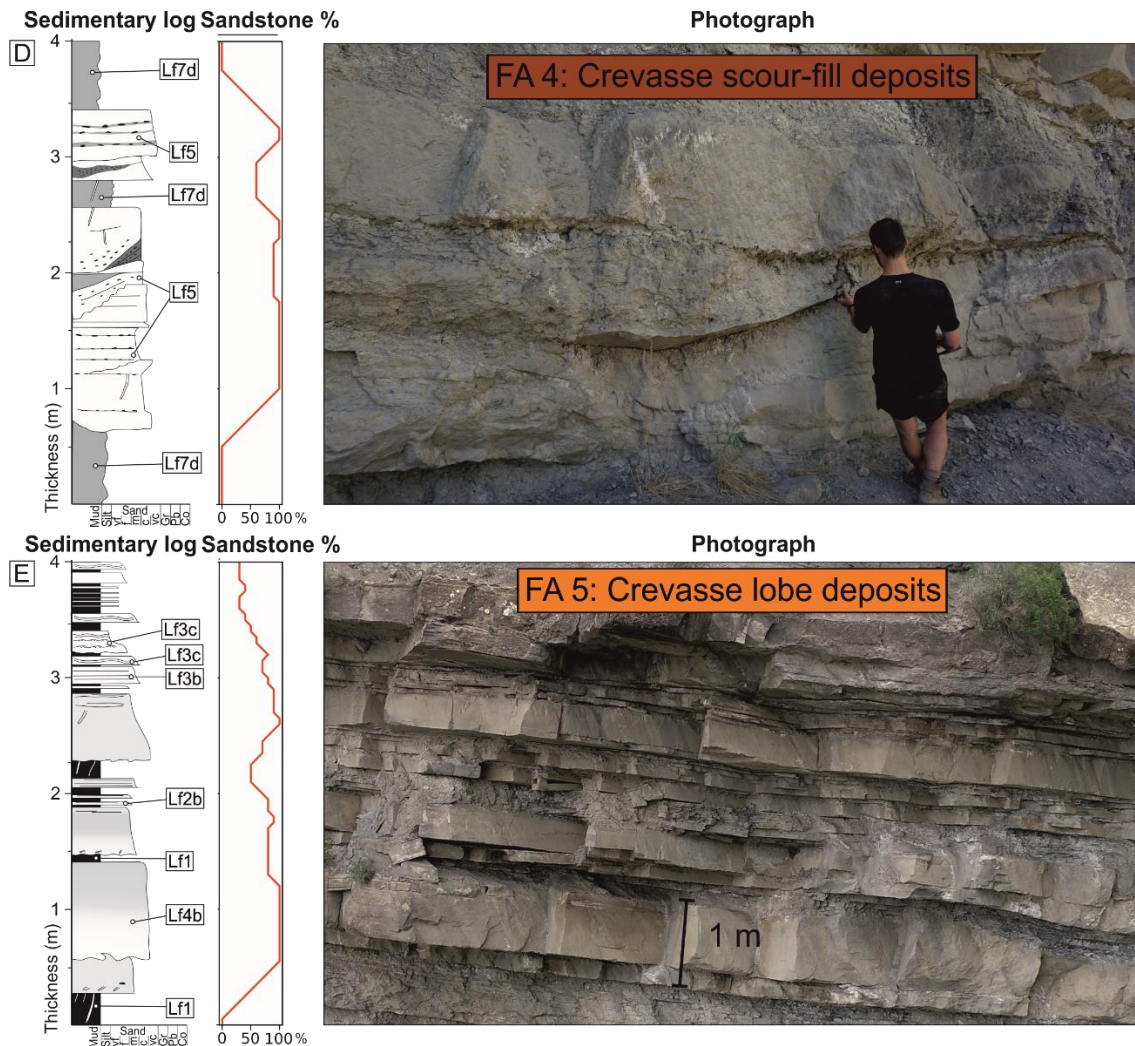


Figure 5.5. Representative sedimentary log, sandstone proportion and photograph of the stratal packages representing facies associations (A) FA1: Overbank deposits, (B) FA2: Terrace deposits, (C) FA3: Channel-fill deposits, (D) FA4: Crevasse scour-fill deposits and (E) FA5: Crevasse lobes deposit.

5.5.2. FA2: Terrace deposits

Description: This facies association is a medium-bedded heterolithic < 5 m thick succession (Figure 5.5B), with a basal matrix-supported conglomerate (Lf7c; Figure 5.4D and Figure 5.4E) and overlying alternating between carbonate mudstone (Lf1; Figure 5.2A), thin- to medium-bedded sandstones comprising a wide grain size range (fine-grained to pebbly) (Figure 5.5B). Laminated mudstones constitute 70% of FA2, while siltstones, sandstones and conglomerates constitute 30% (Figure 5.5B). Deformed heterolithic packages (Lf1, Lf2a and

Lf2b, and medium-bedded sandstones) rotated above concave-up planes are also observed (LF7a; Figure 5.4A and Figure 5.4B). Some medium thickness beds show a convex-shaped wavy top, developing positive relief up to 10 cm and pinching out laterally (LF3a; Figure 5.2C). This facies association also comprises medium-bedded tabular sandstones with sharp flat bases and sharp wavy tops (Lf3b; Figure 5.2D). Commonly, Lf3b is structureless at the base with well-developed planar laminations towards the top. In addition to the lithofacies described above, FA2 is differentiated from FA1 by the presence of dune-like, normally graded granular to pebbly sandstones (Lf6; Figure 5.3C, Figure 5.3D and Figure 5.3E) with intensely bioturbated top surfaces (Figure 5.3F). Lf6 overlie the matrix-supported conglomerate and become less frequent towards the top of the FA2 stratal package. The well-developed foresets contain abundant mudstone clasts and dip consistently towards the NW (Figure 5.3C). In plan-view, LF6 develops crescentic shapes (Figure 5.3D).

Interpretation: The variability in deposit thickness and grain size range suggest an environment of deposition dominated by mixed energy flows. The alternation of coarse-grained dune-like deposits and thin-bedded siltstones and sandstones reflect deposition from steady (Kneller and Branney, 1995) and bypassing high magnitude energetic flows, which reworked a previously deposited coarser fraction (Amy et al., 2000; Stevenson et al., 2015; Hansen et al., 2021). The thin beds are interpreted as the product of overspilling and flow stripping of lower magnitude flows (Peakall et al., 2000; Dennielou et al., 2006; Hansen et al., 2015). Furthermore, the lack of erosional features within these packages suggests that FA2 correspond to individual terrace deposits formed adjacent to the channel axis but within the channel belt (Babonneau et al., 2002, 2004, 2010; Hansen et al., 2015, 2017a, 2017b; Allen et al., 2022). The term terrace refers to a flat surface in an elevated position with respect to the active channel and inside the channel belt (Babonneau et al., 2004). The basal matrix-supported conglomerates (LF7c;

Figure 5.5B) are considered local deposits of cohesive debris flow (Talling et al., 2012), which might create a relative topographic high and promote the onset of the terrace. The preferential development of coarse-grained dune-like deposits immediately above the debrite suggests that the terrace was progressively elevated due to the progressive incision of the channel into the debrite. Furthermore, the deformed heterolithics (LF7a) are attributed to gravitational failures of the channel walls (Hansen et al., 2015, 2017b; Allen et al., 2022).

5.5.3. FA3: Channel-fill deposits

Description: This facies association comprises a 5-15 m thick package (Figure 5.5C) dominated by highly amalgamated thick-bedded sandstones overlying a muddy matrix-supported conglomerate (LF7c; Figure 5.4D and Figure 5.4E). Mudstones constitute 22.5% of FA3, while sandstones constitute 77.5% (Figure 5.5C). The thick sandstone beds are crudely normally graded and often structureless, locally developing planar and ripple laminations (Lf4a; Figure 5.2F). In the lower half of FA3, when they are not amalgamated, the thick beds of LF4a show silty tops and are bounded by heterolithic packages (< 0.3 m) of Lf1 and Lf2b (Figure 5.5C). In the upper half, they develop unconformable bases incising up to 0.5 m into the underlying stratigraphy, with abundant scours, mudstone clasts and grain-size breaks (Figure 5.5C).

Interpretation: The basal matrix-supported conglomerates represent deposition from cohesive debris flows. The amalgamation and normal crude grading within thick beds indicate deposition from high-density turbidity currents (*sensu* Lowe, 1982) under high aggradation rates (Kneller and Branney, 1995; Sumner et al., 2008). Furthermore, the silty tops of the thick beds in the lower half of FA3 suggest an abrupt loss in capacity and competence and deposition under high deceleration rates. In contrast, the scouring, abundance of mudstone clasts, and grain-size breaks reported in the upper half suggest sediment bypass and erosional flows

(Stevenson et al., 2015). These stratal packages are therefore interpreted deposits from channelized flows. However, the lack of major erosional surfaces (at outcrop scale) and minor bypass indicators suggest that FA3 is more closely related to channel backfilling than being representative of early channel formation, i.e. erosion and almost complete bypass (Hodgson et al., 2016), while the basal surface of the matrix-supported conglomerates (here interpreted as debrites) would indicate the base of the channel.

5.5.4. FA4: Crevasse scour-fill deposits

Description: This facies association comprises a < 5 m thick succession (Figure 5.5D) of highly amalgamated sandstone beds, interbedded with sheared mudstone intervals (LF7d;). Mudstones constitute 40% of FA4, while sandstones constitute 60% (Figure 5.5D). Medium- to thick-bedded sandstones (Lf5) with poor lateral continuity (< 100 m long) and low aspect ratios (5:1 to 10:1, width: thickness) characterise this facies association (Figure 5.3A and Figure 5.3B). Scours bound the base of LF5 and Lf7d (< 2 m thick), developing truncations with respect to the underlying beds (Figure 5.5D). Lf5 sandstone beds are planar or cross-bedded, medium- to coarse-grained with grain-size breaks, comprising abundant mudstone clasts orientated parallel to the laminae and centimetre-scale grooves at bed bases (Figure 5.3A and Figure 5.3B). Abundant centimetre- to decimetre-scale burrows are observed, preferentially at the base of the thick-bedded sandstone (Figure 5.3A) or elongated (5-50 cm long) from top to base at sheared mudstone intervals (LF7d; Figure 5.4).

Interpretation: Lf5 sandstone and Lf7d mudstone beds represent small-scale scour-fills (Arnott and Al-Mufti, 2017), while the truncation and low aspect ratio beds observed at their base support scouring of the substrate by previously bypassing flows (Pemberton et al., 2016; Terlaky and Arnott, 2016; Hofstra et al., 2018; Pohl et al., 2020). The deposition of crudely-

graded sandstone to ungraded (Lf5) over the scours is interpreted as deposited from high-density turbidity currents (Lowe, 1982). The development of grain-size breaks, cross-bedding and mudstone clast horizons in Lf5 indicates partial bypass by sustained flows (Kneller and McCaffrey, 2003; Stevenson et al., 2015). The sheared mudstones (LF7d) indicate localised, small-scale failure of nearby fine-grained stratigraphy. The intense burrowing suggests the recurrent input of oxygen and nutrients, suggesting proximity to channels.

5.5.5. FA5: Crevasse lobe deposits

Description: This facies association is a medium- to thick-bedded tabular sandstone package (1.5 – 5 m thick; Figure 5.5E) that overlies the crevasse scour-fill facies association (FA4). The dominant lithofacies are thick-bedded, structureless, crudely normally graded sandstones (Lf4b; Figure 5.2G). Lf4b is characterised by decimetre-scale abundant burrows and silty tops (Figure 5.2G and Figure 5.2H; e.g. Morris et al., 2014a). When not amalgamated, thick beds are bounded by mudstone intervals (Lf1) or thin- to medium-bedded planar laminated sandstones (Lf2b and Lf3b; Figure 5.2B and Figure 5.2D) or stoss-side preserved climbing ripples (Lf3c; Figure 5.2E).

Interpretation: The Lf4b lithofacies within this association suggest rapidly deposited medium- to high-density turbidity currents (*sensu* Lowe, 1982). Silty tops can be related to an abrupt loss in flow capacity (Hiscott, 1994a) due to the rapid loss of flow confinement as it exits the crevasse channel/scour. Planar laminations and stoss-side preserved climbing ripples reveal continued bedload traction with high aggradation rates (Sorby, 1859, 1908; Allen, 1973; Jobe, 2012). The intense bioturbation suggests proximity to channels, suggesting that these stratal packages are frontal or crevasse lobes (e.g. Morris et al., 2014a, b). The mapping of Bayliss and Pickering (2015) shows that these lobes are developed at the flanks of the channel rather

than its mouth. Furthermore, they overlie the Banastón II channel fills and terrace deposits, suggesting that they represent crevasse lobes rather than frontal (e.g. Beaubouef, 2004; De Ruig and Hubbard, 2006; Hubbard et al., 2009; Morris et al., 2014b).

5.6. Depositional architecture

The five facies associations (FA1-FA5) described above stack to form two major architectural elements: i) channel belts and ii) overbank deposits (Figure 5.6 and Figure 5.7).

5.6.1. Channel belt

Terrace deposits constitute 12.8% of the 111 m studied stratigraphic succession, while channel-fill deposits constitute 34.8% (Figure 5.6). Both terraces (FA2) and channel-fill deposits (FA3) suggest deposition within a partly confined/channelized environment, referred to as a channel belt. The basal debrites (Figure 5.5B and Figure 5.5C) suggest an association with submarine landslide emplacement. The abundance of debrites (17.5% of the studied section; Figure 5.6) and the mapping from Bayliss and Pickering (2015) suggest that channel belts occupy a topographic low within the foreland basin. Channel-fill deposits (FA3) are thicker-bedded, more amalgamated, and up to 3 times thicker than the terrace deposits (FA2) (15m vs 5 m), suggesting that the terrace surfaces formed elevated and adjacent areas to the channel (Babonneau et al., 2002, 2004, 2010; Hansen et al., 2015, 2017a, 2017b). The nature of the channel-fill and terrace deposits will vary according to the magnitude of flows along the channel thalweg (Babonneau et al., 2004; Dennielou et al., 2006). Low-magnitude flows are likely to be fully confined within the channels, and only the upper and more dilute parts of the flow will deposit onto the terraces, producing fine-grained thin beds (Hansen et al., 2015). In contrast, the basal part of high-magnitude flows will override both channel and terraces, the

flow only partially confined within the channel belt (Babonneau et al., 2004; Hansen et al., 2015, 2017a). High-magnitude flows are likely to result in bypass/erosion within the main channel, partial bypass and tractional reworking on the terrace, and deposition on the overbank areas if they overspill (Peakall et al., 2000; Kane et al., 2007; Hubbard et al., 2008; Kane and Hodgson, 2011; Hansen et al., 2017a). Variations in flow magnitude through time will produce highly variable bed thicknesses and grain sizes on the terrace, which are unlikely to be recorded in the channel axis. However, channel-fill deposits (FA3) lack major erosional surfaces (only minor scouring), indicating a more depositional phase than channel initiation, incision and bypass. Therefore, the channel-fill deposits recognized in the studied section are likely related to channel abandonment or backfilling (Morris and Normark, 2000; Hodgson et al., 2016).

5.6.2. Overbank

Overbank areas consist of three facies associations: the overbank (FA1), crevasse scour-fill (FA4) and crevasse lobe (FA5) deposits (Figure 5.6, Figure 5.7 and Figure 5.8), which are interpreted to represent depositional environments outside the channel belts. Overbank deposits are the most abundant facies association (38.2% in the studied interval) and include slumps and slides (16.1% and 12.2% of the studied interval; Figure 5.6). Crevasse scour-fills and crevasse lobes represent 3.6% and 10.6%, respectively (Figure 5.6). Together, they formed a 14-metre thick crevasse complex, interrupting the otherwise monotonous thin-bedded mudstone-dominated overbank deposition (). The crevasse complex comprises i) a 4 m thick basal crevasse scour-fill deposits characterised by poor lateral continuity (FA4) overlain by ii) a 10 m thick upwards-thinning laterally-continuous package, composed of 1.5 to 5 m thick and at least 1 km long aggradationally stacked crevasse lobes (Figure 5.8, Figure 5.9 and Figure 5.10). Bed thickness and amalgamation of sandstone beds decrease upward and laterally in the crevasse complex (Figure 5.1C, Figure 5.8 and Figure 5.10). Crevasse lobes are bounded by

centimetre-scale mudstone intervals (Lf1) and decimetre-scale sheared mudstones (LF7c). The sheared mudstone intervals represent 4.8% of the stratigraphic thickness and are only found within the crevasse complex (Figure 5.6). The lowermost and thickest (up to 5 m) crevasse lobe onlaps onto the underlying slump towards the NE (across strike), developing abrupt thinning rates (25 m/km) over tens of metres (Figure 5.7 and Figure 5.8). However, the slumps are truncated by an SW-dipping surface, interpreted to represent the slide scar of a younger mass failure (Figure 5.7 and Figure 5.8). Thinning rates within the crevasse lobe complex are lower towards NW (downdip), where the medium- to thick-bedded sandstones gradually thin (1m/km) into thin-bedded sandstones in 1 km (Figure 5.8). Due to the tabularity of crevasse lobe thin beds, no pinch-out terminations were documented along the downdip transect (Figure 5.8). Unlike the lowermost crevasse lobes, the uppermost thin-bedded crevasse lobes do not comprise any associated thick-bedded sandstones laterally, showing a tabular architecture (Figure 5.6 and Figure 5.8). The term overbank area is used here instead of the external levee (Kane and Hodgson, 2011) because depositional architecture is modified in narrow foreland channel systems where the distributary system is encased between two opposing slopes, as documented in the Puchkirchen system in the Austrian Molasse Basin (overbank wedges of De Ruig and Hubbard, 2006; Hubbard et al., 2009; Kremer et al., 2018). Tectonically-active margins can also promote overbank asymmetry (Kane et al., 2010b; Hansen et al., 2017a; Kneller et al., 2020), and it is expected that such a tectonic control resulted in an asymmetry between the northeastern and southwestern overbank deposits of the Banastón II sub-unit. Given that the southwestern overbank area of the Banastón II sub-unit does not crop out in the San Vicente area, this asymmetry cannot be proven.

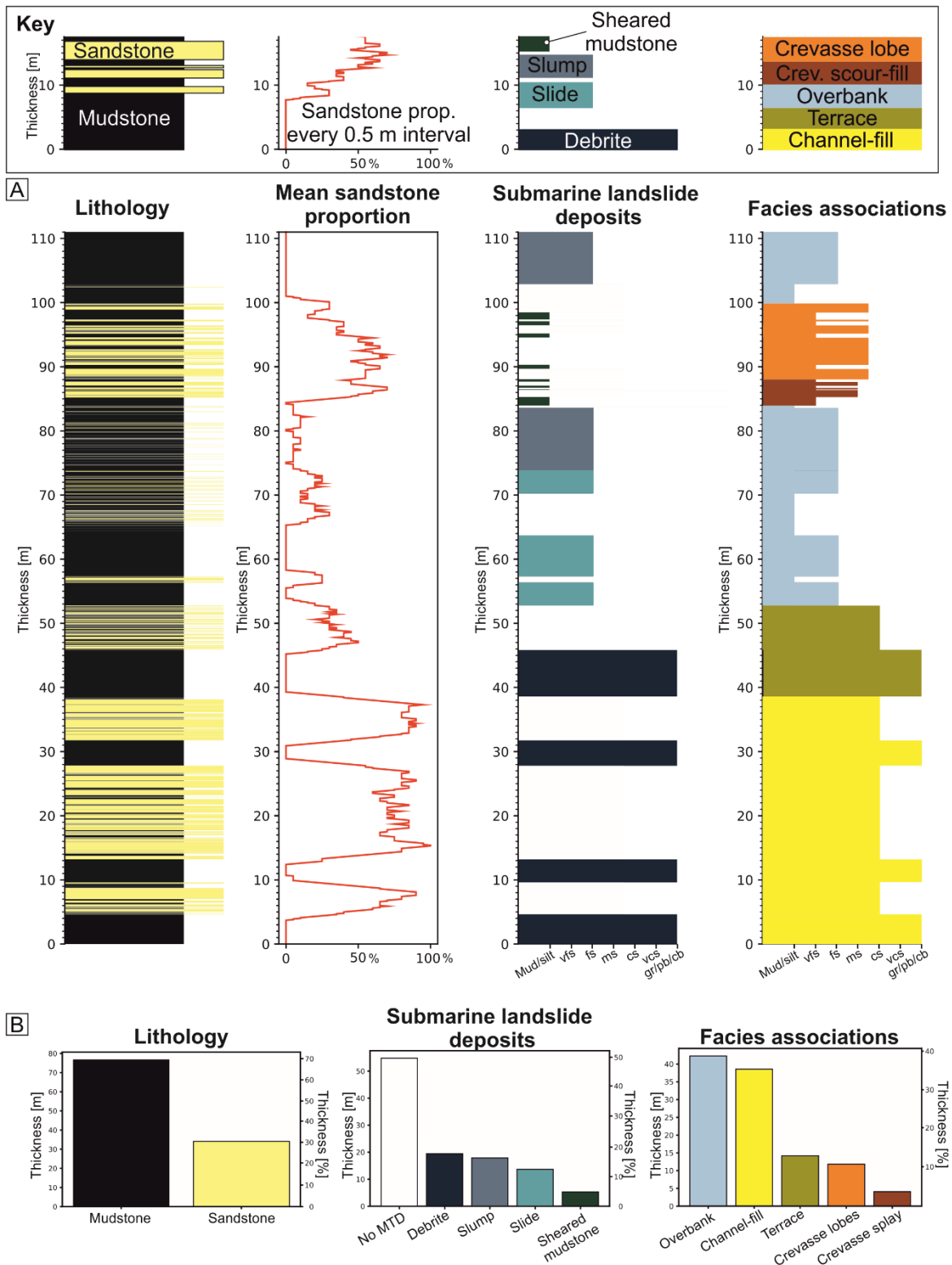


Figure 5.6. A) Logs and (B) Histograms showing the lithology, mean sandstone proportion, submarine landslide content and facies associations of the 111 m thick study interval. The section is mudstone-dominated, especially on the upper half where the overbank facies association overlies channel-fill and terrace deposits. Note the variation of submarine landslide deposits along the section.

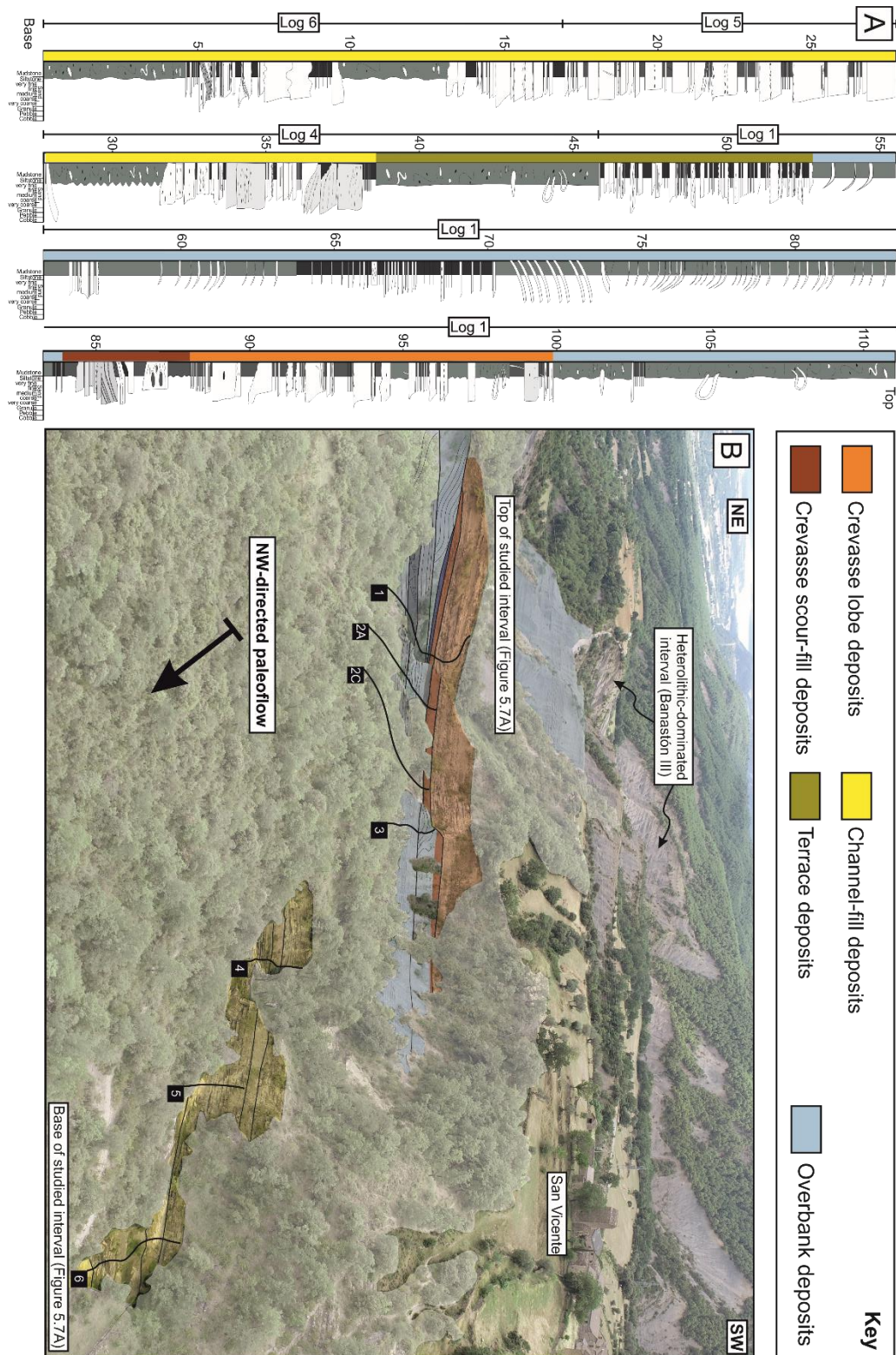


Figure 5.7. (A) General stratigraphic column of the investigated interval (111 m thick) of the Banastón II member and the different facies associations. Note that it is made of different sedimentary logs. (B) Interpreted UAV photographs with the different facies associations and sedimentary logs. Note the San Vicente town in the right top corner.

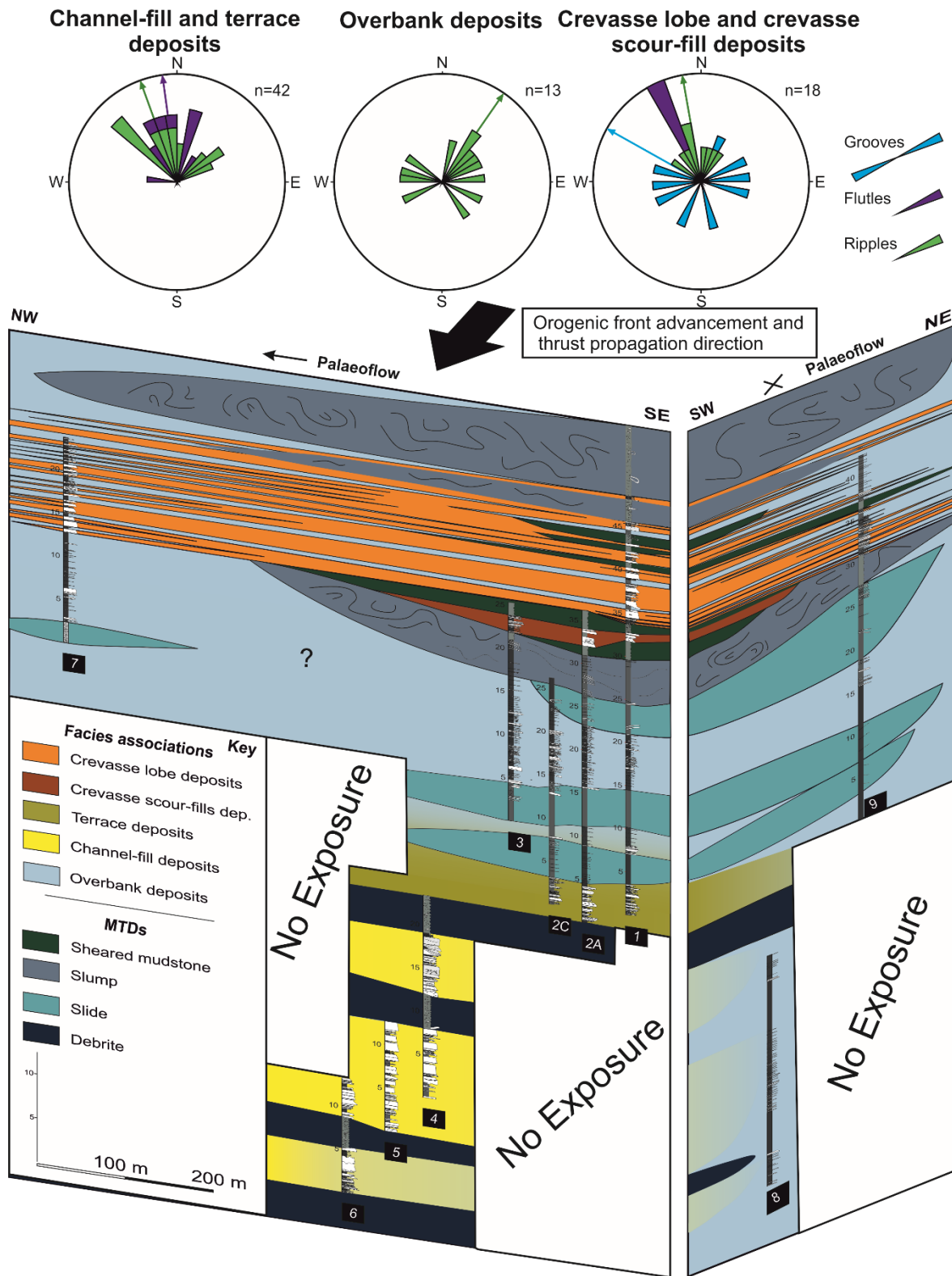


Figure 5.8. Correlation panel of the Banastón II member near the San Vicente town. See Figure 5.1C and Figure 5.7B for the location of the sedimentary logs. Note the rose diagrams of the palaeocurrents on crevasse lobes, overbank and channel belts (Channel-fill and terrace deposits).

5.7. Discussion

5.7.1. Channel wall collapse and crevasse complex development

Fine-grained sedimentation on the overbank areas was interrupted by the deposition of anomalously thick sandstone beds related to the development of the crevasse complex. Crevasse complexes result from breaching of the channel belt wall (Sawyer et al., 2007, 2014), allowing (parts of) high-density turbidity currents to escape channel-belt confinement (Posamentier and Kolla, 2003; De Ruig and Hubbard, 2006; Hubbard et al., 2009; Armitage et al., 2012; Brunt et al., 2013; Maier et al., 2013; Morris et al., 2014a). The breach can happen due to several mechanisms, including 1) overspilling due to excessive curvature in a submarine meander bend (e.g. Tek et al., 2021a), 2) lateral meander growth (swing) and/or downstream meander migration (sweep) (e.g. Peakall et al., 2000; Abreu et al., 2003; Deptuck et al., 2003), 3) collapse of the channel wall (e.g. Sawyer et al., 2014; Ortiz-Karpf et al., 2015). Given the low sinuosity of the Banastón channel, the onlap against a slide scar, and the juxtaposition of the crevasse complex over a slump, the channel wall collapse is considered the most plausible mechanism for the initiation of crevasse splays. The resulting breach is likely to be narrowest at the base and widen upwards due to the concave-up nature of both crevasse channels/scours and slide scars. This morphology is likely to promote localized flow constriction (Kneller, 1995), resulting in accumulative (Kneller and Branney, 1995; Kneller and McCaffrey, 1999; Soutter et al., 2021), waxing (Kneller, 1995; Mulder and Alexander, 2001) and partially bypassing turbidity currents (Talling et al., 2012; Stevenson et al., 2015). Localized acceleration of turbidity currents can produce incision, promoting further channelization (Gee et al., 2001; Eggenhuisen et al., 2011; De Leeuw et al., 2016). Another erosion mechanism can be explained by flow relaxation (*sensu* Pohl et al., 2020) due to the lateral spreading of the flow after the passage through the breach, which lowers the position of the downstream velocity maximum and increases shear stress near the substrate.

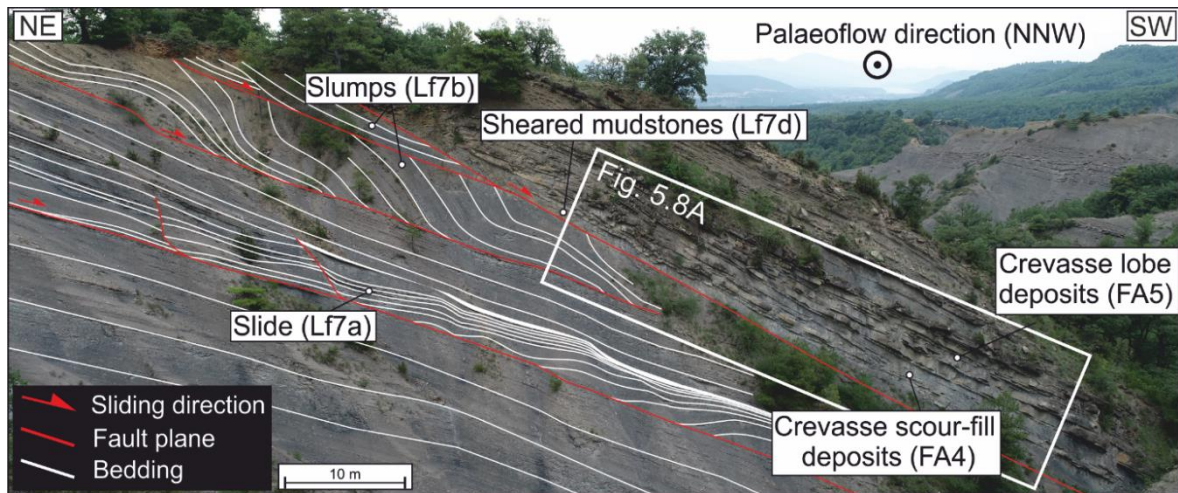


Figure 5.9. Interpreted UAV photographs of the multiple submarine landslides found within the overbank (FA1) and the crevasse scour-fills (FA4) and crevasse lobes deposits (FA5).

The crevasse scour-fill facies association is interpreted as the most proximal environment of the crevasse complex. The mixed erosional and depositional nature and intermediate position between the channel and the crevasse lobes can be analogous to other channel-lobe transition zones recognised in outcrops (Van der Merwe et al., 2014; Hofstra et al., 2015; Pemberton et al., 2016; Brooks et al., 2022; Hodgson et al., 2022). Substrate excavation can promote local mass failures from slide scar walls, as demonstrated by the interfingering of sand-fill scours (Lf5) and sheared mudstone intervals (Lf7c). This phenomenon has been reported in kilometre-scale submarine landslides, where sidewall fragmentation promotes secondary mass failures and reshapes the original slide scar (Richardson et al., 2011). This effect could reduce the aspect ratio (height/width) of the breach and, therefore, less flows constriction and progressive filling. This relationship is supported by the juxtaposition of crevasse lobes over crevasse scour-fills, representing a change from bypass to backfilling. Furthermore, the upward thinning and fining with increasing tabularity of sandstone beds within the crevasse lobes suggests progressive healing of the breach and/or the adjacent channel's abandonment.

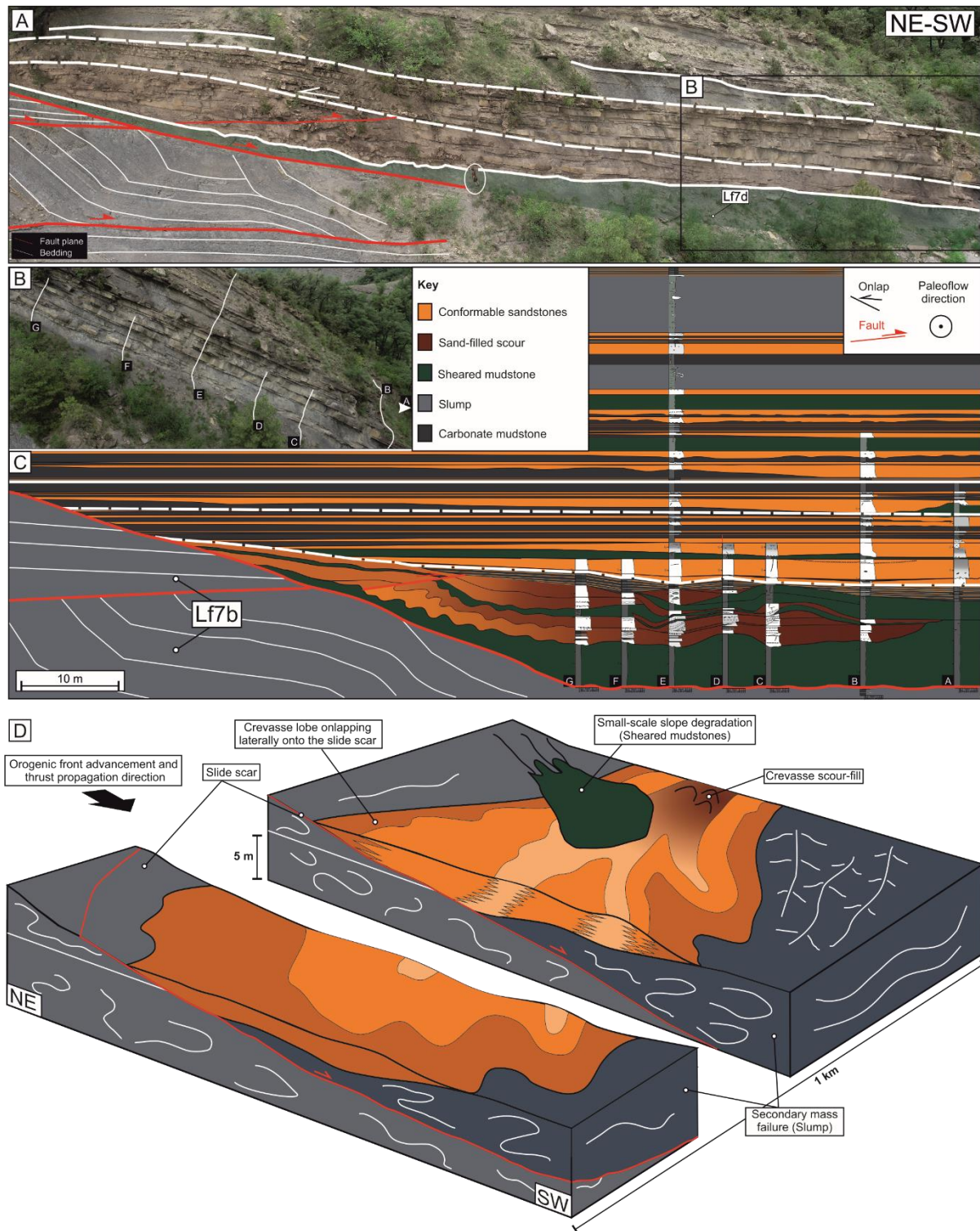


Figure 5.10. (A) Interpreted UAV photograph showing a basal slide overlain by the crevasse complex. (B) Location of the sedimentary logs of the crevasse complex. (C) Correlation panel of a crevasse complex showing the juxtaposition of crevasse lobes over the basal crevasse scour-fill deposits. (D) Model illustrating the crevasse lobe juxtaposed over a slump and laterally onlapping the slide scar.

Here it is proposed that the nature of the crevasse complex is controlled by the shape, development and healing of the breach, its stratigraphic evolution reflecting a re-establishment of the overbank areas after its breaching (Hubbard et al., 2009). Crevasse-lobe development has also been observed in the Puchkirchen Formation in the Austrian Molasse Basin (De Ruig and Hubbard, 2006; Hubbard et al., 2009). However, the crevasse lobes in the Austrian Molasse Basin are not identified on the active margin of the channel system. The abundance of slides and slumps in the studied section (16.1% and 12.2% cumulative thickness, respectively) suggest that they played a key role in creating the conditions to develop crevasse lobes near the active margin. The thickest part of slides (among other submarine landslides) is likely to be found at their lower, compressional domain. In contrast, the upper, extensional domain of submarine landslides is thinner and receives the deflected flows (Figure 5.10 and Figure 5.11A; Kremer et al., 2018; Ayckbourn et al., in press). Breaching by the collapse of the channel wall would leave behind some up-dip scours and concave topography susceptible to being exploited as a conduit for subsequent flows (Damuth et al., 1988; Posamentier and Kolla, 2003; Fildani and Normark, 2004; Armitage et al., 2012; Brunt et al., 2013; Maier et al., 2013; Morris et al., 2014a; Ayckbourn et al., in press). Slide and slump emplacement would also reduce the steepness of the active margin and, therefore, the 'valley-confinement'. Furthermore, flows can escape the channel belt, spreading and depositing sand on the otherwise mudstone-dominated overbank (Figure 5.11). This study highlights those small-scale submarine landslides (in this case < 10 m thick) and secondary mass failures can effectively induce crevasse lobe development on active margins and therefore provide a means of trapping sediment on the slope.

5.7.2. The impact of submarine landslides on channelised flows and terraces

Submarine landslides can be emplaced longitudinally (Bernhardt et al., 2012; Masalimova et al., 2015) and transversely (De Ruig and Hubbard, 2006; Hubbard et al., 2009; Kremer et al., 2018) in foreland basins. Despite the outcrop limitations and lack of kinematic indicators within the debrites (Bull et al., 2009), the position of submarine landslides within the palaeogeographic distribution in the Banastón sub-unit suggests that they were transversely emplaced (Bayliss and Pickering, 2015). Submarine landslides can disturb the slope equilibrium gradient (Corella et al., 2016; Kremer et al., 2018; Liang et al., 2020; Tek et al., 2020) and induce partial or full blockage (Posamentier and Kolla, 2003; Bernhardt et al., 2012; Corella et al., 2016; Kremer et al., 2018; Tek et al., 2020; Tek et al., 2021a). In highly sinuous and laterally migrating channel belts, the development of terrace surfaces is commonly related to meander-bend cut-off (Cronin, 1995; Mayall and Stewart, 2000; Deptuck et al., 2003; Babonneau et al., 2004; Janocko et al., 2013; Hansen et al., 2017b) or point bar accretion (Abreu et al., 2003; Deptuck et al., 2007; Dykstra and Kneller, 2009; Janocko et al., 2013). In contrast, narrow and confined foreland channels show less meandering (De Ruig and Hubbard, 2006; Hubbard et al., 2009; Masalimova et al., 2015; Kremer et al., 2018).

Sediment gravity flows travelling over debrites can show complex patterns due to the upper surface rugosity, which promotes channelization (Armitage et al., 2009; Fairweather, 2014; Kneller et al., 2016; Valdez et al., 2019; Tek et al., 2020; Martínez-Doñate et al., 2021; Allen et al., 2022). Flow channelization can promote positive feedback, with enhanced erosion in the channel further increasing confinement and channelization (Eggenhuisen et al., 2011; De Leeuw et al., 2016). Prolonged excavation will lead to the development of a conduit bounded laterally by elevated terraces (Hansen et al., 2017b; Tek et al., 2021a), as suggested by the fining upwards trend recorded in FA2 (Figure 5.5B). Recent studies based on high-resolution

bathymetry and shallow subsurface datasets (Tek et al., 2021a) and field-based studies (Allen et al., 2022) suggest that the clearance of the channel dammed by submarine landslides is more complex than previously thought due to the development of upstream-migrating knickpoints downstream of the submarine landslide. The high degree of bed amalgamation and lack of meter-scale erosional surfaces in the investigated channel-fill deposits indicate high aggradation rates rather than bypassing sediment gravity flows. I interpret this stratal architecture as indicative of channel backfilling (Pickering et al., 2001) due to channel damming induced by the debrite emplacement or tectonically-controlled upstream avulsion due to thrust propagation, as observed in older channel systems within the Aínsa Basin (Arro system; Tek et al., 2020). Therefore, it is suggested that the emplacement of submarine landslides within the channel belt impacts channelized flows and is the dominant mechanism for promoting terrace development in the Banastón II sub-unit.

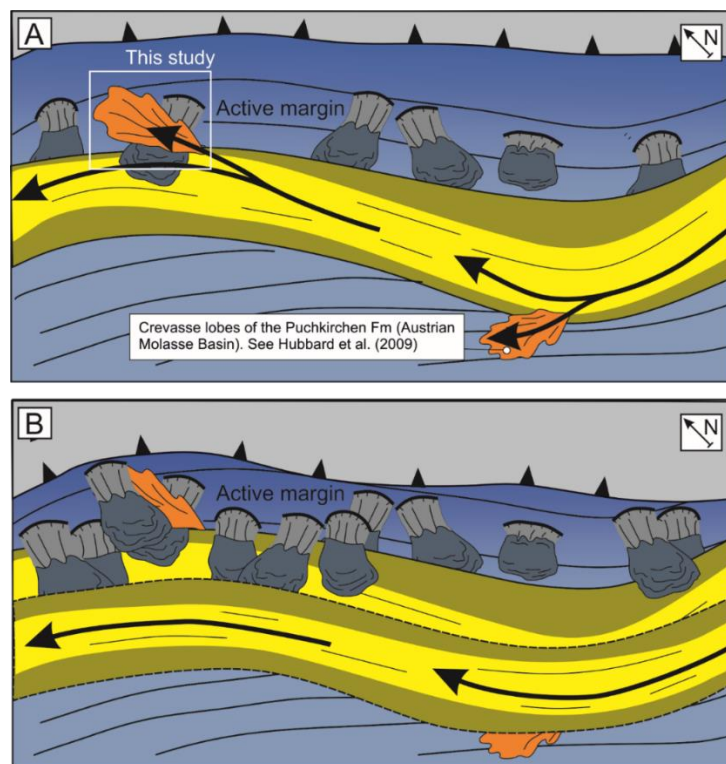


Figure 5.11. (A) Evolutionary model illustrating the crevasse lobe deposition on the active margin due to submarine landslide emplacement, deflecting channelised flows towards the slide scar and (B) how the continuous transversely-sourced submarine landsliding is a potential mechanism of avulsion of the Banastón II member.

5.7.3. Avulsion mechanism(s) in the Banastón II channel system

Long-lived breaching is associated with lateral meander growth (swing) and/or downstream meander migration (sweep) (e.g. Peakall et al., 2000; Abreu et al., 2003; Deptuck et al., 2003) and is common on the external levees of outer bends in sinuous channels (Damuth et al., 1988; Posamentier and Kolla, 2003; Fildani and Normark, 2004; Armitage et al., 2012; Brunt et al., 2013; Maier et al., 2013; Morris et al., 2014a). Such breaching is an effective mechanism for the avulsion of the channel system in unconfined settings, where deposition of crevasse lobes precedes avulsion (Damuth et al., 1988; Armitage et al., 2012; Brunt et al., 2013). However, crevasse lobe development in foreland basin settings is unlikely to represent the avulsion and re-routing of the entire channel belt (Flood et al., 1991) due to basin-scale structural confinement and low channel sinuosity (Hubbard et al., 2009). The lack of avulsion and related cannibalization of the channel-belt fill might explain why crevasse scour fills and lobes are preserved in the Banastón II system. It also seems unlikely that the emplacement of a few submarine landslides would result in the avulsion of the entire Banastón II deep-water channel system, given their small magnitude (< 10 m thick) compared to the scale of the channel system (98 m thick and 1800 m wide) and structural confinement (~5-8 km wide syncline). Recent work on stable isotopes within the Aínsa Basin indicates that the Banastón II sub-unit was strongly controlled by tectonism (Läuchli et al., 2021). As documented in this study, active tectonism in the foreland basin and related uplift and steepening of the active margin likely trigger abundant mass failure events. However, the progressive uplift and south-westward advancement of the active margin will promote the development of a belt of transverse submarine landslides running parallel to the strike of the active margin (Figure 5.11) that can enhance the SW-directed lateral migration of the channel belt (e.g. Posamentier and Kolla, 2003; Deptuck et al., 2007; Kane et al., 2010a; McHargue et al., 2011) as also suggested by Bayliss and Pickering (2015). Even if subsequent channelized sediment gravity flows are not

fully ponded after submarine landslide emplacement, they are likely to undergo constriction (Kneller, 1995) and deflection away from the active margin, producing punctuated channel migration (*sensu* Maier et al., 2012) and breaching. Therefore, it is proposed that repeated emplacement of submarine landslides, related to the syn-depositional growth of local structures adjacent to channel belts, determined the channel architecture and played a key role in the lateral offset of the Banastón system, in agreement with Bayliss and Pickering (2015).

5.8. Conclusions

The stratigraphic evolution of the Banastón II sub-unit near the San Vicente area records the lateral offset of a submarine channel system to the southwest, which I relate to the syn-depositional growth of local structures. The active tectonism promoted submarine landslides, which impacted the dynamics of the channel system. The interpretation is that the emplacement of debrites within channel belts resulted in channel damming and backfilling. Additionally, the modification of the slope gradient caused by the emplacement of debrites was the main mechanism for terrace formation. Furthermore, the emplacement of slides and slumps raised the channel base and left concave-up evacuation scars, forming a breach point that was exploited by subsequent flows to form a conduit and led to the development of crevasse lobes. Therefore, this study highlights that small-scale basin margin failures and their deposits can profoundly influence the dynamics of deep-water channels and their adjacent overbank areas on tectonically-confined submarine slopes.

6. Synthesis and conclusions

6.1 How do submarine landslide deposits impact younger depositional systems?

In Chapter 3 (Martínez-Doñate et al., 2021), the study of the 9.6 km long landslide deposit and underlying and overlying stratal units documented the juxtaposition of two scales of depositional topography along the upper surface (e.g. Armitage et al., 2009; Fairweather, 2014) characterised by: i) kilometre-scale wavelength and metre-scale amplitude relief, and ii) metre-scale wavelength and decimetre-scale amplitude (rugosity) (Figure 6.1). The buttressing of the debris flow against the ramps that formed along the basal shear zone was responsible for the larger-scale topography (Bull et al., 2009), while the smaller-scale rugosity was attributed to the yield strength of debris flows and their megaclast content (McGilvery and Cook, 2003; Kneller et al., 2016). Both scales of depositional topography were documented to influence the dispersal patterns of subsequent sediment gravity flows overriding the upper surface. The long-scale topography inhibited the deposition of sand-rich strata (foundered sandstones) in the central part of the submarine landslide, restricting deposition to areas of lower topography (Figure 6.1). The sedimentological study of the foundered sandstones concluded that such relief did not disconnect proximal and distal areas in 3D due to the development of tortuous corridors (Smith, 2004b) (Figure 6.1). On the other hand, the magnitude of the high-density turbidity currents was greater than the small-scale rugosity producing partial bypass and triggering the deposition of sand in their lows. The two scales of topography hindered the development of lobate-shaped architectures, producing sandstone bodies with concave-up bases and flat tops.

Chapter 3 (Martínez-Doñate et al., 2021) also documents the post-depositional and dynamic nature of the upper surface together with the syn-sedimentary foundering of sand. The characterisation of three types of architecture and terminations styles within

the foundered sandstones shows that foundering, as well as being a product of the density contrast between the debrite and sand, was triggered by the high sedimentation rates and lateral changes in sediment load (e.g. Owen, 2003), controlled by debrite rugosity. In contrast, the foundering phenomenon was not observed in the Chachil Graben (Chapter 4) despite the abundance of debrites. This is linked to the even load exerted by lobe deposits across their flat upper surface. In Chapter 3, the onlap and monotonous accumulation of aggradational lobe fringes (Unit 4A) revealed a long-lived debrite relief, culminating with the progradation of the sand-rich submarine lobe (Unit 4B) (Figure 6.1). The intraslope lobe is characterised by progressive down-dip thinning and fining. The area where the lobe pinches out coincides with where the underlying lobe fringes (Unit 4A) and smaller scalar debrites onlap the mounded relief of the debrite (Unit 2). This distribution suggests that the relief was not wholly healed with the deposition of the thin beds and continued to affect the flows forming the lobe.

An alternative is that the larger-scale topography was rejuvenated during the deposition of Unit 4 (Figure 6.1). The possible mechanisms for such a dynamic nature of the upper surface were discussed in Martinez-Donate et al. (2021) and include: 1) downslope creeping during the deposition of Unit 4; 2) mechanical subsidence associated with an east-dipping fault and subsequent rotation of the debrite or 3) fluid loss-controlled evacuation (Figure 6.1; see 'recommendation for future work' section). Post-depositional remobilisation associated with basinward-facing faults is not rare in submarine landslide deposits (see 'double slope failure' section in Sobiesiak et al., 2016).

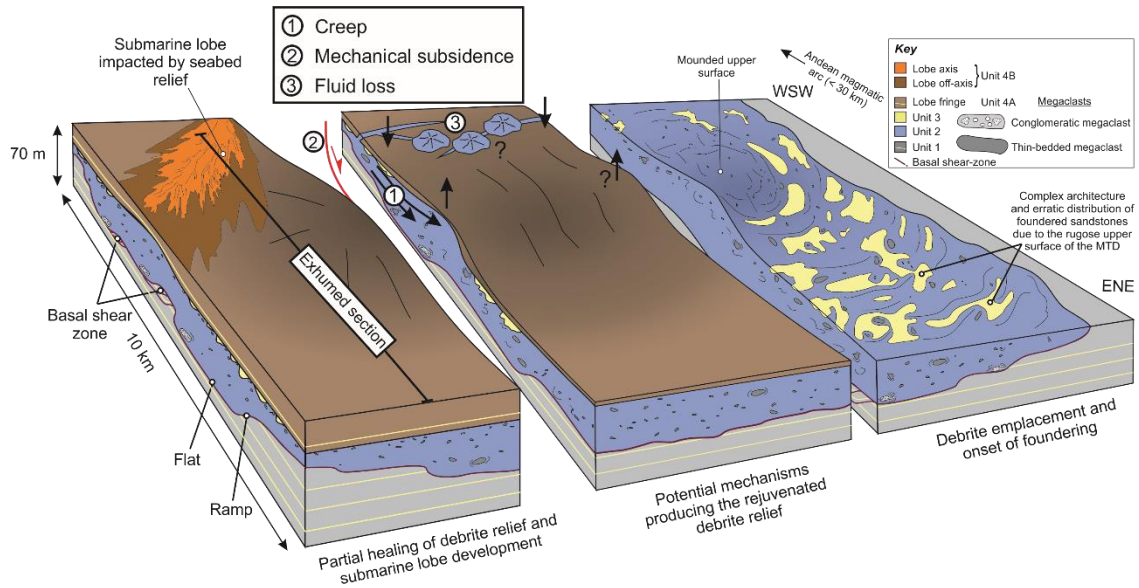


Figure 6.1. Down-dip oriented block diagram illustrating the relief created by the debrite and the impact on younger sand-rich units. The left block shows how foundered sandstones fill the small-scale rugosity, leaving the kilometre-scale accommodation underfilled. The middle block shows potential mechanisms that could have rejuvenated the debrite relief. The right block shows how the accumulation of thin beds draped the debrite, followed by the progradation of the intraslope lobe, which is gently impacted by the long-lived inherited relief. Modified from Martínez-Doñate et al. (2021).

A similar phenomenon was reported in the Ainsa Basin (Chapter 5), where a secondary failure of a slump was responsible for the development of crevasse lobes and their onlap onto the slide scar. This secondary failure suggests a less fluidal rheology submarine landslide, indicated by the preservation of original bedding (even if folded) in contrast to the debrite of Chacay Melehue, which showed more plastic rheology indicated by the high degree of internal disaggregation and excess pore pressure. Furthermore, in the Ainsa Basin, tertiary small-scale (< 1 m thick) mass failures from nearby stratigraphy also played an important role by flattening and widening the breach in the channel wall where the sediment gravity flows exited confinement highlighting that submarine landslide deposits can show multi-episode failures.

6.2 Are all intraslope lobes made equal?

The studies in Chacay Melehue (Chapter 3) and Chachil Graben (Chapter 4) enabled the characterisation of exhumed early post-rift intraslope lobes. The intraslope lobe of the Chacay Melehue Graben is 5.7 m thick and at least 4.3 km long. These intraslope lobes comprise a lobe axis dominated by argillaceous high-density turbidites with banded tops evolving down-dip into medium-bedded transitional flow deposit-dominated lobe off-axis and thin-bedded lobe fringe sub-environments. The intraslope lobes in Chachil Graben are 4.5 to 7 m thick and ~ 3 km long. Their dimensions are comparable to those reported in Sychala et al. (2015) and Brooks et al. (2018c) in the Karoo Basin but largely differ from the turbidite-dominated sub-environments: lobe axis is built by structureless thick-bedded turbidites, lobe off-axis by structured medium-bedded turbidites comprising wavy and climbing-ripple laminations and fringes show are built by thin sandstones beds characterised by bidirectional ripple lamination (Figure 6.2). The sandy nature of intraslope lobes is attributed to the preferential trapping of the coarser fraction of the sediment gravity flows while the more dilute fine-grained top of the turbidity currents bypasses (e.g. Sychala et al., 2015). Similar sedimentary facies were documented in the crevasse lobes of the Ainsa Basin (Chapter 5). However, the Early Jurassic intraslope frontal lobes of the Los Molles Formation are predominately built by deposits from transitional flows across all sub-environments (Figure 6.3), which inhibited effective grain size segregation and resulted in flow collapse as a result of flow deceleration, and, therefore very different pinch-out architectures.

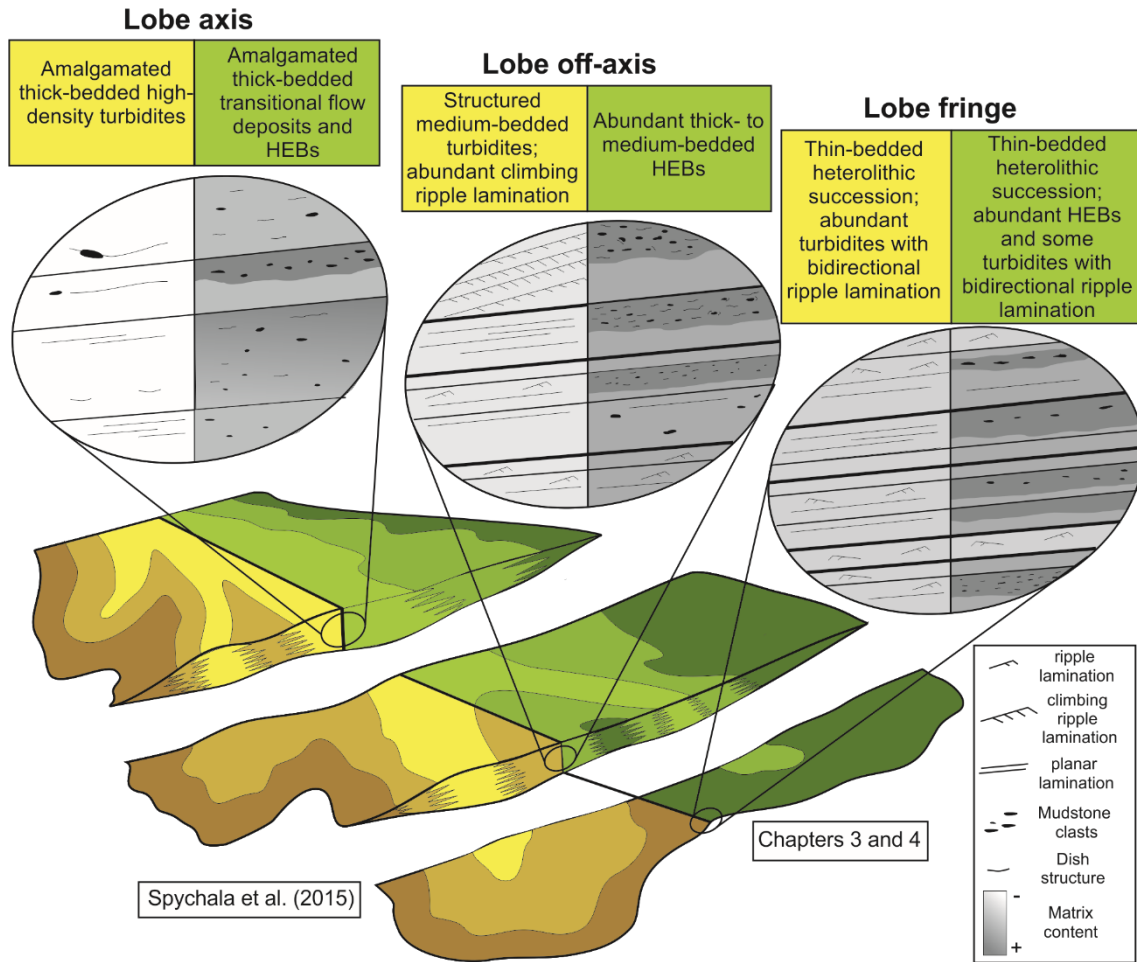


Figure 6.2. Schematic diagram comparing the facies in different lobe sub-environments in the intraslope lobes reported in the Karoo Basin (left, yellow- and brown coloured; Spychala et al., (2015)) and Neuquén Basin (right, green-coloured; Chapter 4).

Petrological work supports the interpretation of transitional flow behaviour due to the high-matrix content reported from axis to fringe sub-environments. Comparing the matrix content as a function of the mean grain size of Chachil Graben's early post-rift intraslope lobes to previous studies investigating matrix-rich deep-water deposits, the closest analogues are the 'slurry' flow deposits of the Britannia Formation of Lowe and Guy (2000) and the transitional flow deposits of the Forties Fan of Davis et al. (2009) (Figure 6.3), both of them also being deposited during their respective post-rift stages.

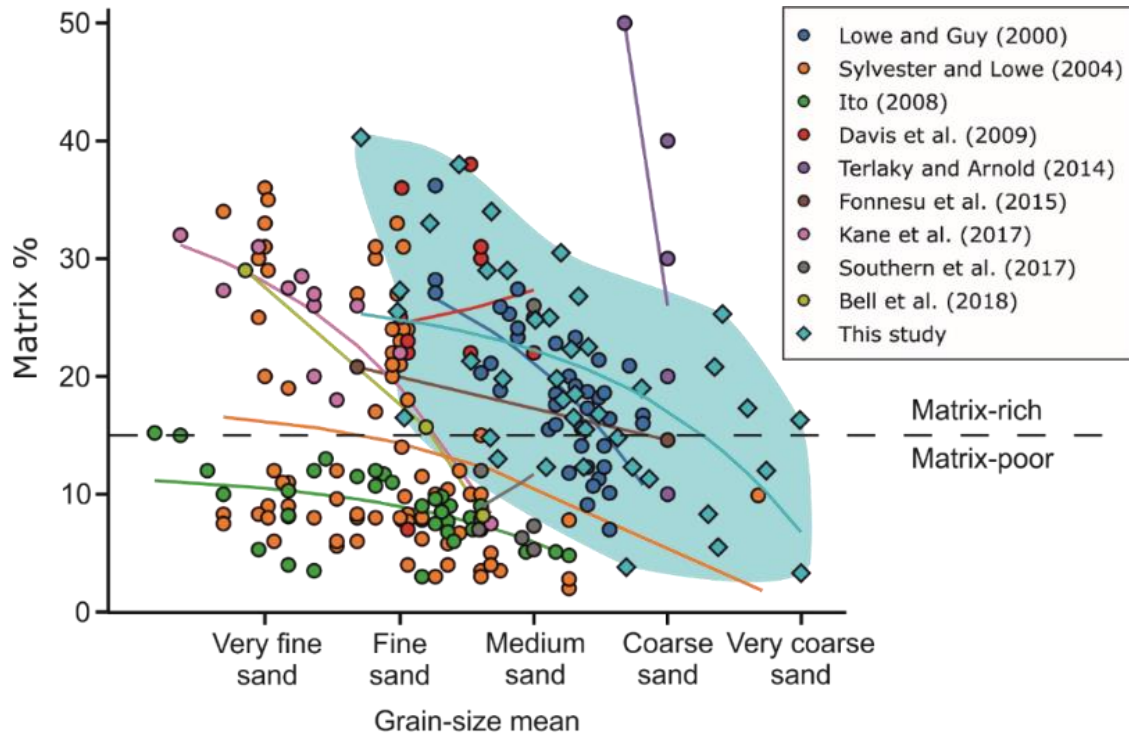


Figure 6.3. Graph showing matrix content as a function of the mean grain size of the intraslope lobes of the Chachil Graben (n=40; light blue coloured) and other published studies. The dashed line at the 15% matrix represents the threshold for matrix-poor and matrix-rich intervals (Pettijohn et al., 1972).

6.2.1. Why are the investigated intraslope lobes in the Neuquén Basin largely built by transitional flow deposits?

Petrological work in Chachil Graben Chapter and the NE-prograding submarine lobes from in Chacay Melehue Graben (Central W Neuquén Basin and Bathonian age) and Chachil Graben (SW Neuquén Basin and Toarcian age) indicate that both were fed from the volcanic arc, as previously suggested by Burgess et al. (2000). The growing volcanic arc at the southwestern basin margin most-likely produced a relatively narrow shelf configuration. Additionally, mass failures could have altered basin margin physiography by narrowing the shelf edge and promoting favour rapid sediment transfer downslope, as suggested in Chacay Melehue Graben (Chapter 3) (Figure 3.12). This palaeogeography and feeder system contrast with more mature basins with well-developed and mature drainage systems, where the sediment is transported for long distances and stored on the

shelf for longer before remobilisation to deep-water areas (Sømme et al., 2009). Furthermore, mature and well-developed channel systems, such as in the Ainsa Basin, are very effective at narrowing the grain-size range of flows (e.g. Hodgson et al., 2016). Back-arc settings with immature shelves are likely to develop multiple coeval entry points (e.g. slope incision or gullies; Carey and Schneider, 2011) and poorly-developed distributary systems where the removal of fines to overbanks areas via flow stripping is limited (Figure 6.4).

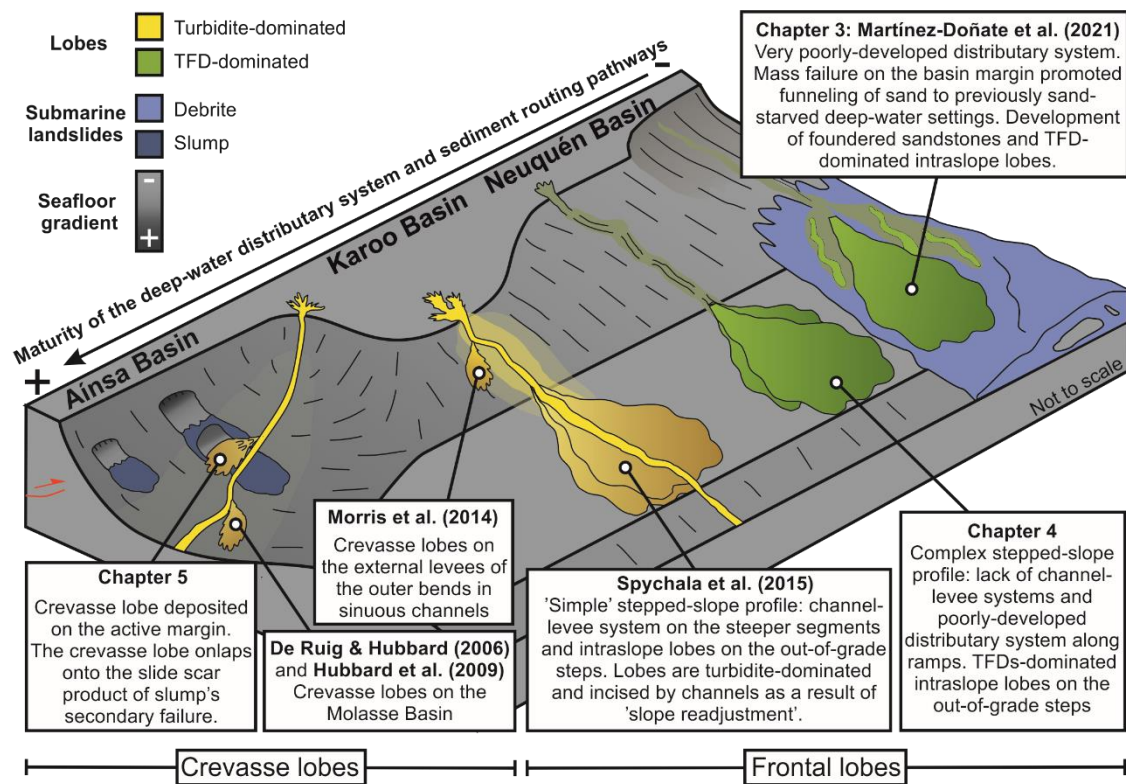


Figure 6.4. Block diagram illustrating turbidite-dominated (yellow coloured) crevasse lobes (Chapter 5 and Morris et al., 2014a); frontal intraslope lobes (Spychala et al., 2015) developed in simple stepped slope profiles and/or fed by a channel-levee system (see Jobe et al., 2017); TFD-dominated intraslope lobes (green coloured) developed over a submarine landslide (Chapter 3) and in structurally complex stepped slopes where distributary systems are poorly developed (Chapter 4).

Additionally, sediment gravity flows might have entrained large amounts of clay as they over-rode thick mudstone-dominated substrates rejuvenated through differential

compaction rather than static and/or sand-prone substrates. The role of well-developed channel systems and reduced interaction with clay-prone substrates is demonstrated by the turbidite-dominated crevasse lobes of the Ainsa Basin (Chapter 5). Here, the short distances travelled by the parental flows once they escaped channel confinement to their deposition (< 100 m) and the limited entrainment of marly and silty substrate material did not suppress flow turbulence due to the reduced tendency of these materials to form flocs or gel, in comparison to clays (Baas et al., 2009; Baker et al., 2017).

Therefore, this thesis concludes that the dimensions and depositional architecture of intraslope lobes are strongly controlled by accommodation and physiography, while the nature of their deposits is closely related to the parental flow properties and maturity of the distributary systems.

6.3. Influence of subtle seafloor topography on sediment gravity flow behaviour

The influence of steep seafloor relief on sediment gravity flow behaviour in highly confined settings has been well-documented from exhumed lobe succession, where abrupt thinning and onlap terminations are developed (Sinclair, 2000; McCaffrey and Kneller, 2001; Sinclair and Tomasso, 2002; Apps et al., 2004; Gardiner, 2006; Bakke et al., 2013; Patacci et al., 2014; Soutter et al., 2019); this has been documented in the crevasse lobes onlapping a slide scar in the Ainsa Basin (Chapter 5). However, recognition of subtle slope changes in exhumed lobe systems (Smith, 2004; Burgreen and Graham, 2014; Spsychala et al., 2017c; Privat et al., 2021) remains problematic due to subtle facies changes and pinch-outs that do not terminate against basin margins or topographic highs. This thesis provides evidence of subtle seafloor topography across

different observational scales based on the facies transitions, terminations and stacking patterns.

6.3.1. Event-bed scale

Sediment gravity flows will respond differently when interacting with seafloor topography according to their flow properties (Kneller and McCaffrey, 1999; Al Ja'Aidi et al., 2004; Smith, 2004b; Bakke et al., 2013). Studying the deposits of highly concentrated flows and their thinning patterns was particularly relevant to understanding the gentle seafloor configuration of the different study areas documented in this thesis. Due to the limited flow efficiency of medium to high-yield strength debris flows, debrites develop abrupt pinch-outs even on gentle slopes such as in the Chacay Melehue and Chachil Grabens (Chapters 3 and 4). High-density turbidites did not develop abrupt pinch-outs; instead, they evolved down-dip into poorly-sorted matrix-rich transitional flow deposits. The study of the systematic pinch-out of transitional flow deposits helped to understand the nature and evolution of the gentle topography related to the differential compaction of mudstones in Chachil Graben (Chapter 4) and the identification of the subtle remnant topography over the debrite in Chacay Melehue Graben (Chapter 3). The study of individual low-density turbidites in the thin-bedded package (Unit 4A) showed that some of the beds developed onlap terminations against the debrite; however, in most cases, low-density turbidites showed thinning rates that can be negligible over tens of metres in gently confined settings, as reported in Chacay Melehue Graben (Chapter 3) and Chachil Graben (Chapter 4).

6.3.2. Stratal packages

The characterisation of stratal packages and the stacking patterns provided the most useful information about the broader response of lobe systems and the nature of their bounding slopes. Highly confined deep-water successions commonly show tabular architectures

consisting of highly amalgamated sheet-like event beds onlapping onto steep slopes (see 'Class 1' onlap from Smith and Joseph, 2004). The resulting successions can show a bimodal deposit distribution, where lows comprise the thickest and coarser-grained deposits and mudstones dominate the steep slopes, as reported in the Ainsa Basin (Chapter 5) with the channels (regional low), crevasse lobes (local low) and overbank (slope). Such end-member stratal packages produce different aggradation rates between the lows and slopes, producing the climbing trajectory of onlapping thick beds over a diachronous confining surface. As a result, these stratal packages will show monotonous mudstone-prone accumulations characterised by abrupt upwards thickening and coarsening trends (Soutter et al., 2019).

In contrast, gently confined lobes are typically characterised by a more gradual thinning, decreasing bed amalgamation and sandstone-mudstone proportion towards the confining slopes. Unlike in mudstone-dominated slope successions of steep basin margins, sedimentation over gentle slopes is likely to be dominated by thin sandstone beds, promoting more balanced aggradation rates over the topographic lows and slopes such as documented in the thin-bedded interval overlying the debrite of Chacay Melehue Graben (Chapter 3), or lobe fringes in the Chachil Graben (Chapter 4). The resultant stratal packages will be characterised by progressive thickening and coarsening upward successions, as shown in the Chachil Graben (Chapter 4).

6.4. Recommendations for future work

One feature that requires further investigation in the western sector of Chacay Melehue Graben (Chapter 3) is the presence of large intrusive and extrusive mud-rich features (Figure 6.5 and Figure 6.6) related to fluid-loss controlled evacuation, which might have rejuvenated the larger-scale topography and affected the younger sandstone deposits that immediately overlie the studied interval (Figure 6.5A). Commonly these mud-rich features show discordant sub-vertical bodies that cross-cut the stratigraphy at various angles (15-90°) (Figure 6.5). One of the features shows a dome-like geometry (Figure 6.6), promoting the thinning and onlap of overlying sandstone beds, indicating that these features were on the seabed at the deposition time. In addition, at the base of the dome is a discordant mud-rich feature filled with clasts. Together, these observations support a mud volcano interpretation. Browne et al. (2020) documented similar features on outcrop- and subsurface examples north of the Taranaki Basin (New Zealand). These authors link the mud-rich features to fluid escape structures coming from basal MTDs, caused by sudden loading resulting from the emplacement of younger MTDs. Blanchard et al. (2019) also documented similar large-mud-rich features in the exhumed delta-front deposits in the Carboniferous of the Shannon Basin (County Clare, Ireland). In Chacay Melehue, it is not clear where the source of the mud is, but it could be sourced from overpressured parts of the debrite (Unit 2) that extruded onto the seabed. If in 3D, there is a mass evacuation of mud from the landslide body to the seabed, this could 'deflate' the deposit and lead to the observed dynamic nature of this feature (Figure 6.1).

Another aspect to consider for future works is evaluating whether large-scale foundered sandstones can be targeted during hydrocarbon exploration and for future carbon storage due to their connectivity and stratigraphic trapping potential. This study would require an

evaluation of the porosity and permeability of both foundered sandstones and underlying debrites.

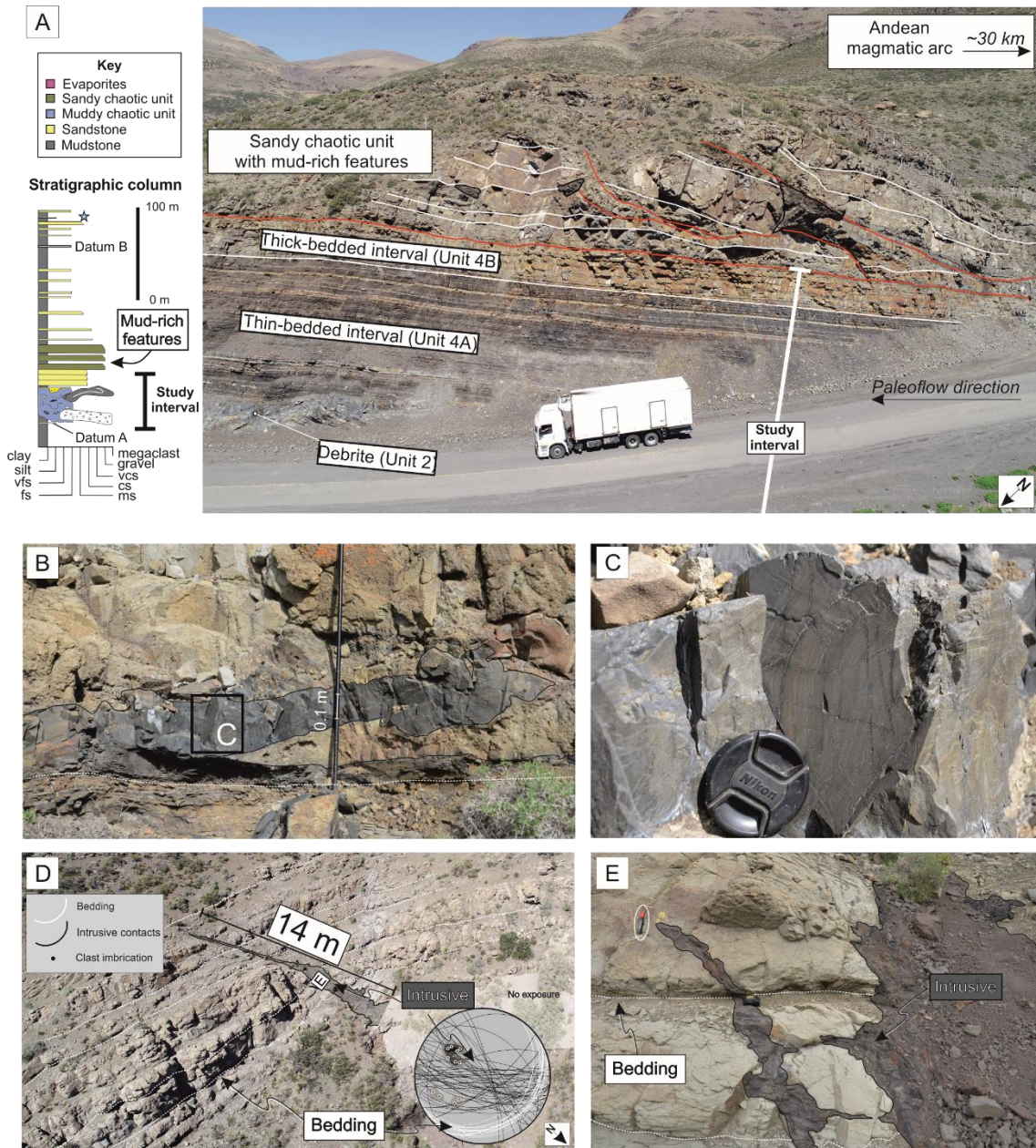


Figure 6.5. (A) The general stratigraphic column of the studied interval in the Chacay Melehue Graben (Chapter 3) is overlain by a 'chaotic sandy unit' showing a range of mud-rich features. (B) Discordant mudstone injection onto sandstone and (C) inset on the mudstone injection. (D) Discordant 14 m long mudstone injection. Note its discordant nature on the stereonet, which shows regional bedding gently dipping towards SE while the contacts of the mudstone injectite (measured every 50 cm on both sides from base top) and the long axis of some clast within it show a sub-vertical trend. (E) Inset on the contact between the mudstone injectite and the host sandstones.

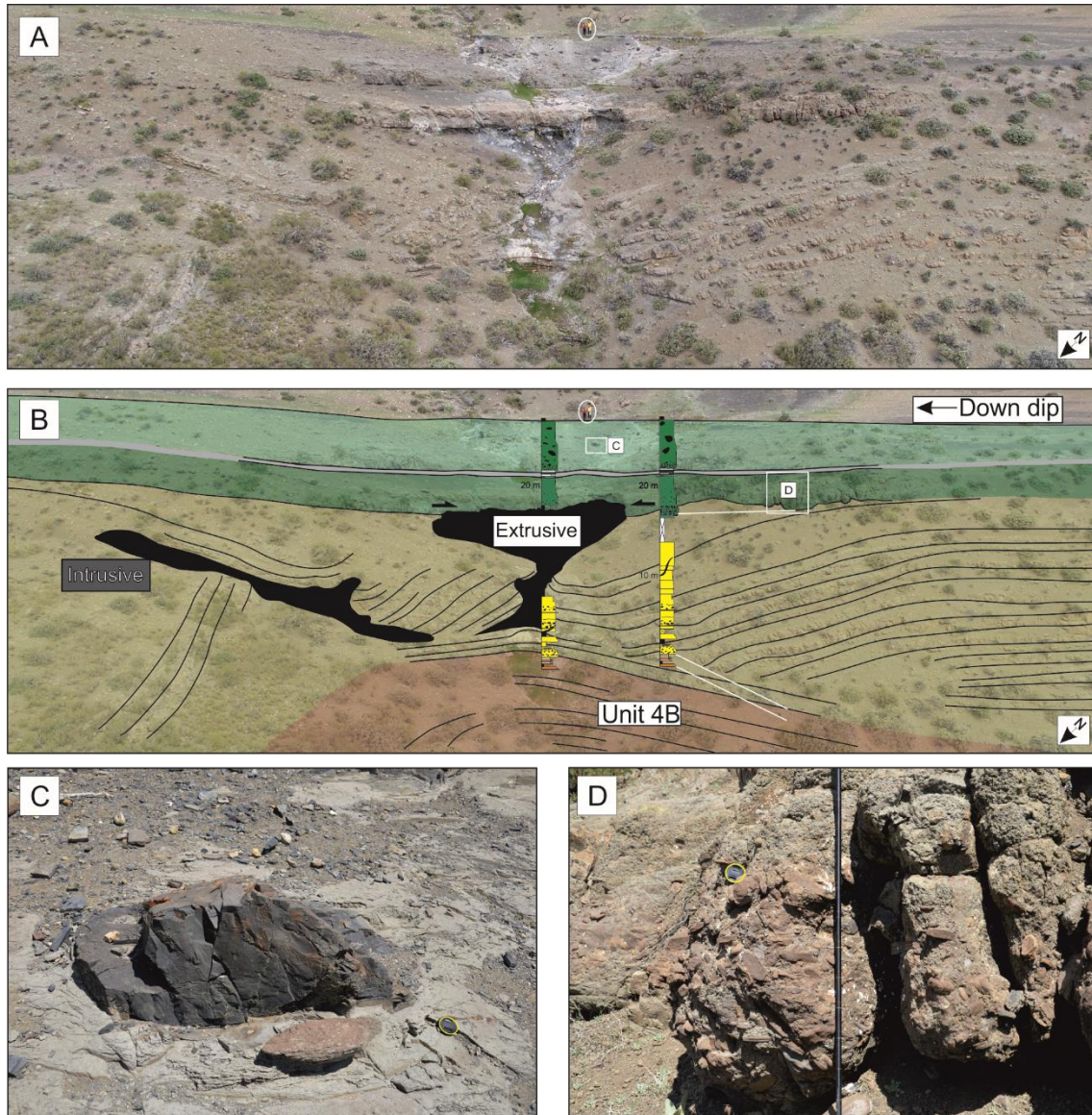


Figure 6.6. (A) Uninterpreted UAV photograph. Note that the white circle highlights two geologists for scale. (B) Interpreted UAV photograph highlighting the dome-like feature (centre) and a mudstone injection (left). Note discordant bedding of the yellow-coloured unit in contrast to the underlying Unit 4B (orange) and two overlying beds (green), which onlap and thin over the top of the dome-like feature indicating its extrusive nature. (C) and (D) Inset on the green-coloured units. Note that the mudstone clast in (C) eroded and incorporated into the gravity flow, supporting the extrusive nature.

Stratigraphic correlation, analysis of different pinchout styles, and the petrographic characterisation of sandstone bed types in the Chachil Graben (Chapter 4) raised the question of whether early post-rift lobe systems have potential as reservoirs for hydrocarbons and carbon storage. The grain size, sorting, matrix content and distribution

were quantified; these are key parameters controlling porosity and permeability values (e.g., Bell et al., 2018). Overall, the mean grain size, amalgamation and sandstone/mudstone proportions decrease from lobe axis to fringes, whereas matrix content and sorting increase. The deposits found at the lobe axis are likely to comprise the best reservoir properties of the lobes due to the abundance of high-density turbidites (only in the Upper Lobe complex) and the high amalgamation, which promotes communication between sandstone beds (Begg and King, 1985; Desbarats, 1987; Deutsch, 1989). In contrast, the decrease in amalgamation, grain size and the development of argillaceous deposits or divisions on the lobe-off axis and lobe fringes may result in decreasing permeability values (intrabed baffles; Porten et al., 2016; Southern et al., 2017; Bell, 2019).

On the other hand, the development of abrupt HEB-rich frontal pinch-outs, and confinement produced by compaction-related topography, suggests a high stratigraphic trapping potential with reduced leakage risk. The coarser grain sizes and less argillaceous deposits of the Upper Lobe complex suggest higher permeability values than the transitional flow deposit-dominated Lower Lobe complex (e.g. Southern et al., 2017). However, in the subsurface, the matrix content does not necessarily hinder the reservoir properties as the volume of clay coating around grains, such as chlorite, can inhibit quartz cement growth and, therefore, preserve primary porosity (Heald and Larese, 1974; Ehrenberg, 1993; Anjos et al., 2009; Dowey et al., 2012). Apart from the depositional reservoir quality (Marchand et al., 2015; Porten et al., 2016), the Early Jurassic intraslope lobes of the Los Molles Formation need an evaluation of the effects of post-depositional processes on texture. In addition, the development of injectites that pinch out within the mudstones suggests that they may form stratigraphic traps (post-depositional) (Hurst et

al., 2005, 2008; Scott et al., 2013), although they can also represent leakage paths (Monnier et al., 2014; Cobain et al., 2017). Further work in these or similar deposits is needed to improve our understanding of how these systems act as hydrocarbon reservoirs, aquifers, and carbon or hydrogen storage sites.

6.5. Conclusions

This thesis highlights that deep-water sedimentary systems are controlled by the interplay between the nature of sediment gravity flows and the receiving basin. The primary controls in facies and their transitions are dependent on the concentration of the flows, the amount of incorporated mud from the substrate and the bathymetrical configuration of the basin across different scales. Denser flows tend to decelerate more abruptly and produce strong deposit variability, unlike dilute flows, which can maintain their efficiency for longer distances. The greater the incorporation of cohesive mud, the shorter the distance over which flows transform into low-efficiency cohesive flows, resulting in rapid flow collapse.

The investigated early post-rift back-arc intraslope lobes are characterized by matrix-rich and transitional flow-dominated sedimentary bodies product of poorly-developed distributary systems, which enhanced mud availability and limited the overspilling of fine-grained sediments. In contrast to the lobes foreland basin are characterized by structured turbidites lacking transitional flow deposits, consequence of well-developed channel system.

This thesis concludes that facies and their transition, and terminations of early post rift lobes largely contrast with other subsurface and exhumed examples and raises the conclusions that each sedimentary system is its only analogue, despite the similarities between systems developed in similar tectonostratigraphic settings.

7. References

- Abreu, V., Sullivan, M., Pirmez, C. and Mohrig, D.** (2003) Lateral accretion packages (LAPs): An important reservoir element in deep water sinuous channels. *Mar. Pet. Geol.*, **20**, 631–648.
- Adeogba, A.A., McHargue, T.R. and Graham, S.A.** (2005) Transient fan architecture and depositional controls from near-surface 3-D seismic data, Niger Delta continental slope. *Am. Assoc. Pet. Geol. Bull.*, **89**, 627–643.
- Al Ja'Aidi, O.S., McCaffrey, W.D. and Kneller, B.C.** (2004) Factors influencing the deposit geometry of experimental turbidity currents: Implications for sand-body architecture in confined basins. *Geol. Soc. Spec. Publ.*, **222**, 45–58.
- Allen, C., Gomis-cartesio, L.E. and Hodgson, D.M.** Channel incision into a submarine landslide : an exhumed Carboniferous example from the Paganzo Basin , San Juan , Argentina Statement : This manuscript is a non-peer review preprint submitted to EarthArXiv and has been submitted for review at the open ac. 1–51.
- Allen, C., Gomis-Cartesio, L.E., Hodgson, D.M., Peakall, J. and Milana, J.P.** (2022) Channel incision into a submarine landslide on a Carboniferous basin margin, San Juan, Argentina: Evidence for the role of knickpoints.
- Allen, J.R.L.** (1971a) Mixing at turbidity current heads, and its geological implications. *J. Sediment. Res.*, **41**, 97–113.
- Allen, J.R.L.** (1971b) Instantaneous sediment deposition rates deduced from climbing-ripple cross-lamination. *J. Geol. Soc. London.*, **127**, 553–561.
- Allen, J.R.L.** (1973) Phase differences between bed configuration and flow in natural environments, and their geological relevance. *Sedimentology*, **20**, 323–329.
- Allen, J.R.L.** (1982a) Structures and sequences related to gravity-current surges. In: *Sedimentary Structures. Their Character and Physical Basis.*, Elsevier, Amsterdam, 395–431.
- Allen, J.R.L.** (1982b) Sedimentary structures, their character and physical basis Volume 1. Elsevier. 663 pp.
- Altinakar, M.S., Graf, W.H. and Hopfinger, E.J.** (1996) Flow structure in turbidity currents. *J. Hydraul. Res.*, **34**, 713–718.
- Alves, T.M.** (2015) Submarine slide blocks and associated soft-sediment deformation in deep-water basins: A review. *Mar. Pet. Geol.*, **67**, 262–285.
- Alves, T.M. and Cartwright, J.A.** (2009) Volume balance of a submarine landslide in the Espírito Santo Basin, offshore Brazil: Quantifying seafloor erosion, sediment accumulation and depletion. *Earth Planet. Sci. Lett.*, **288**, 572–580.
- Alves, T.M. and Lourenço, S.D.N.** (2010) Geomorphologic features related to gravitational collapse: Submarine landsliding to lateral spreading on a Late Miocene-Quaternary slope (SE Crete, eastern Mediterranean). *Geomorphology*, **123**, 13–33.
- Amy, L., Kneller, B. and McCaffrey, W.** (2000) Evaluating the Links Between Turbidite Characteristics and Gross System Architecture: Upscaling Insights from the Turbidite Sheet-System of Peïra Cava, SE France. *Deep. Reserv. World 20th*

- Annu.*, 1–15.
- Amy, L.A., McCaffrey, W.D. and Kneller, B.C.** (2004) The influence of a lateral basin-slope on the depositional patterns of natural and experimental turbidity currents. *Geol. Soc. Spec. Publ.*, **221**, 311–330.
- Amy, L.A., Talling, P.J., Edmonds, V.O., Sumner, E.J. and Lesueur, A.** (2006) An experimental investigation of sand-mud suspension settling behaviour: Implications for bimodal mud contents of submarine flow deposits. *Sedimentology*, **53**, 1411–1434.
- Anderson, K.S., Graham, S.A. and Hubbard, S.M.** (2006) Facies, architecture, and origin of a reservoir-scale sand-rich succession within submarine conyion fill: Insights from Wagon Caves Rock (Paleocene), Santa Lucia Range, California, U.S.A. *J. Sediment. Res.*, **76**, 819–838.
- Anjos, S.M.C., De Ros, L.F. and Silva, C.M.A.** (2009) Chlorite Authigenesis and Porosity Preservation in the Upper Cretaceous Marine Sandstones of the Santos Basin, Offshore Eastern Brazil. *Clay Miner. Cem. Sandstones*, 289–316.
- Apps, G., Peel, F. and Elliott, T.** (2004) The structural setting and palaeogeographical evolution of the Grès d’Annot Basin. *Geol. Soc. Spec. Publ.*, **221**, 65–96.
- Arbués, P., Mellere, D., Falivene, O., Fernández, O., Muñoz, J.A., Marzo, M. and Gibert, J.M. De** (2007) Context and Architecture of the Ainsa-1-Quarry Channel Complex, Spain. *Atlas Deep. outcrops*, 1–20.
- Argent, J.D., Stewart, S.A. and Underhill, J.R.** (2000) Controls on the Lower Cretaceous Punt Sandstone Member, a massive deep-water clastic deposystem, Inner Moray Firth, UK North Sea. *Pet. Geosci.*, **6**, 275–285.
- Armitage, D.A., McHargue, T., Fildani, A. and Graham, S.A.** (2012) Postavulsion channel evolution: Niger Delta continental slope. *Am. Assoc. Pet. Geol. Bull.*, **96**, 823–843.
- Armitage, D.A., Romans, B.W., Covault, J.A. and Graham, S.A.** (2009) The Influence of Mass-Transport-Deposit Surface Topography on the Evolution of Turbidite Architecture: The Sierra Contreras, Tres Pasos Formation (Cretaceous), Southern Chile. *J. Sediment. Res.*, **79**, 287–301.
- Arnott, R.W.C.** (2012) Turbidites, and the case of the missing dunes. *J. Sediment. Res.*, **82**, 379–384.
- Arnott, R.W.C. and Al-Mufti, O.** (2017) Deep-marine pseudo dune cross-stratification-similar, but completely different. *J. Sediment. Res.*, **87**, 312–323.
- Ayckbourn, A.J.M., Jerrett, R.M., Poyatos-Moré, M., Watkinson, M.P., Kane, I.A. and Taylor, K.G.** (2022) The Influence of creeping MTD topography on turbidity currents and their deposits: Examples from the Aínsa Basin (Spain).
- Azpiroz-Zabala, M., Cartigny, M.J.B., Talling, P.J., Parsons, D.R., Sumner, E.J., Clare, M.A., Simmons, S.M., Cooper, C. and Pope, E.L.** (2017) Newly recognized turbidity current structure can explain prolonged flushing of submarine canyons. *Sci Adv.* doi: 10.1126/sciadv.1700200
- Baas, J.H.** (2004) Conditions for formation of massive turbiditic sandstones by primary

- depositional processes. *Sediment. Geol.*, **166**, 293–310.
- Baas, J.H., Best, J. and Peakall, J.** (2016a) Predicting bedforms and primary current stratification in cohesive mixtures of mud and sand. *J. Geol. Soc. London.*, **173**, 12–45.
- Baas, J.H. and Best, J.L.** (2002) Turbulence modulation in clay-rich sediment-laden flows and some implications for sediment deposition. *J. Sediment. Res.*, **72**, 336–340.
- Baas, J.H., Best, J.L. and Peakall, J.** (2011) Depositional processes, bedform development and hybrid bed formation in rapidly decelerated cohesive (mud-sand) sediment flows. *Sedimentology*, **58**, 1953–1987.
- Baas, J.H., Best, J.L. and Peakall, J.** (2016b) Comparing the transitional behaviour of kaolinite and bentonite suspension flows. *Earth Surf. Process. Landforms*, **41**, 1911–1921.
- Baas, J.H., Best, J.L., Peakall, J. and Wang, M.** (2009) A phase diagram for turbulent, transitional, and laminar clay suspension flows. *J. Sediment. Res.*, **79**, 162–183.
- Baas, J.H., Tracey, N.D. and Peakall, J.** (2021) Sole marks reveal deep-marine depositional process and environment: Implications for flow transformation and hybrid-event-bed models. *J. Sediment. Res.*, **91**, 986–1009.
- Babonneau, N., Cremer, M. and Bez, M.** (2010) Sedimentary architecture in meanders of a submarine channel: Detailed study of the present congo turbidite channel (zaïango project). *J. Sediment. Res.*, **80**, 852–866.
- Babonneau, N., Savoye, B., Cremer, M. and Bez, M.** (2004) Multiple terraces within the deep incised Zaire Valley (ZaiAngo Project): Are they confined levees? *Geol. Soc. Spec. Publ.*, **222**, 91–114.
- Babonneau, N., Savoye, B., Cremer, M. and Klein, B.** (2002) Morphology and architecture of the present canyon and channel system of the Zaire deep-sea fan. *Mar. Pet. Geol.*, **19**, 445–467.
- Bagnold, R.A.** (1962) Auto-suspension of transported sediment; turbidity currents. *Proc. R. Soc. London. Ser. A. Math. Phys. Sci.*, **265**, 315–319.
- Baker, M.L. and Baas, J.H.** (2020) Mixed sand–mud bedforms produced by transient turbulent flows in the fringe of submarine fans: Indicators of flow transformation. *Sedimentology*, **67**, 2645–2671.
- Baker, M.L., Baas, J.H., Malarkey, J., Jacinto, R.S., Craig, M.J., Kane, I.A. and Barker, S.** (2017) The effect of clay type on the properties of cohesive sediment gravity flows and their deposits. *J. Sediment. Res.*, **87**, 1176–1195.
- Bakke, K., Kane, I.A., Martinsen, O.J., Petersen, S.A., Johansen, T.A., Hustoft, S., Jacobsen, F.H. and Groth, A.** (2013) Seismic modeling in the analysis of deep-water sandstone termination styles. *Am. Assoc. Pet. Geol. Bull.*, **97**, 1395–1419.
- Barker, S.P., Haughton, P.D.W., McCaffrey, W.D., Archer, S.G. and Hakes, B.** (2008) Development of rheological heterogeneity in clay-rich high-density turbidity currents: Aptian Britannia Sandstone Member, U.K. Continental shelf. *J. Sediment. Res.*, **78**, 45–68.

- Barnolas, A. and Gil-Peña, I.** (2002) Ejemplos de relleno sedimentario multiepisódico en una cuenca de antepaís fragmentada: La Cuenca Surpirenaica. *Bol. Geol. y Min.*, **112**, 17–38.
- Barton, M.D.** (2012) Evolution of an Intra-Slope Apron, Offshore Niger Delta Slope: Impact of Step Geometry on Apron Architecture. *Appl. of the Princ. Seism. Geomorphol. to Cont. Base-of-Slope Syst. Case Stud. From Seafloor Near-Seafloor Analog.* (Ed. by Prather B. E., Deptuck M. E., Mohrig D. C., B. van Hoorn Wynn R. B.), 181–197.
- Bayliss, N. and Pickering, K.T.** (2015) Transition from deep-marine lower-slope erosional channels to proximal basin-floor stacked channel-levée-overbank deposits, and syn-sedimentary growth structures, Middle Eocene Banastón System, Ainsa Basin, Spanish Pyrenees. *Earth-Science Rev.*, **144**, 23–46.
- Beaubouef, R.T.** (2004) Deep-water leveed-channel complexes of the Cerro Toro Formation, Upper Cretaceous, southern Chile. *Am. Assoc. Pet. Geol. Bull.*, **88**, 1471–1500.
- Beaubouef, R.T. and Friedmann, S.J.** (2000) High Resolution Seismic/Sequence Stratigraphic Framework for the Evolution of Pleistocene Intra Slope Basins, Western Gulf of Mexico: Depositional Models and Reservoir Analogs. *Deep. Reserv. World 20th Annu.*, 40–60.
- Begg, S.H. and King, P.R.** (1985) Modelling the effects of shales on reservoir performance: calculation of effective vertical permeability. In SPE Reservoir Simulation Symposium. OnePetro.
- Bell, D.** (2019) Prediction of reservoir properties from processes and architecture in deep-water clastic systems A thesis submitted to The University of Manchester for the degree of Doctor of Philosophy in the Faculty of Science and Engineering.
- Bell, D., Kane, I.A., Pontén, A.S.M., Flint, S.S., Hodgson, D.M. and Barrett, B.J.** (2018) Spatial variability in depositional reservoir quality of deep-water channel-fill and lobe deposits. *Mar. Pet. Geol.*, **98**, 97–115.
- Bernhardt, A., Stright, L. and Lowe, D.R.** (2012) Channelized debris-flow deposits and their impact on turbidity currents: The Puchkirchen axial channel belt in the Austrian Molasse Basin. *Sedimentology*, **59**, 2042–2070.
- Bertoni, C. and Cartwright, J.** (2005) 3D seismic analysis of slope-confined canyons from the Plio-Pleistocene of the Ebro Continental Margin (Western Mediterranean). *Basin Res.*, **17**, 43–62.
- Best, J. and Bridge, J.** (1992) The morphology and dynamics of low amplitude bedwaves upon upper stage plane beds and the preservation of planar laminae. *Sedimentology*, **39**, 737–752.
- Blair, T.C. and McPherson, J.G.** (1999) Grain-size and textural classification of coarse sedimentary particles. *J. Sediment. Res.*, **69**, 6–19.
- Blanchard, S., Matheson, E.J., Fielding, C.R., Best, J.L., Bryk, A.B., Howell, K.J., Monson, C.C., Mahoney, G. and Peakall, J.** (2019) Early burial mud diapirism and its impact on stratigraphic architecture in the Carboniferous of the Shannon Basin, County Clare, Ireland. *Sedimentology*, **66**, 329–361.

- Boulesteix, K., Poyatos-Moré, M., Hodgson, D.M., Flint, S.S. and Taylor, K.G.** (2020) Fringe or background: Characterizing deep-water mudstones beyond the basinfloor fan sandstone pinchout. *J. Sediment. Res.*, **90**, 1678–1705.
- Bouma, A.** (1962) Sedimentology of some Flysch Deposits: A Graphic Approach to Facies Interpretation. *Elsevier*, Amsterdam/New York, 168 pp.
- Bourget, J., Zaragosi, S., Mulder, T., Schneider, J.L., Garlan, T., Van Toer, A., Mas, V. and Ellouz-Zimmermann, N.** (2010) Hyperpycnal-fed turbidite lobe architecture and recent sedimentary processes: A case study from the Al Batha turbidite system, Oman margin. *Sediment. Geol.*, **229**, 144–159.
- Bradley, D. and Hanson, L.** (1998) Paleoslope analysis of slump folds in the devonian flysch of Maine. *J. Geol.*, **106**, 305–318.
- Britter, R.E. and Simpson, J.E.** (1978) Experiments on the dynamics of a gravity current head. *J. Fluid Mech.*, **88**, 223–240.
- Brooks, H.L., Hodgson, D.M., Brunt, R.L., Peakall, J. and Flint, S.S.** (2018a) Exhumed lateral margins and increasing flow confinement of a submarine landslide complex. *Sedimentology*, **65**, 1067–1096.
- Brooks, H.L., Hodgson, D.M., Brunt, R.L., Peakall, J., Hofstra, M. and Flint, S.S.** (2018b) Deep-water channel-lobe transition zone dynamics: Processes and depositional architecture, an example from the Karoo Basin, South Africa. *Bull. Geol. Soc. Am.*, **130**, 1723–1746.
- Brooks, H.L., Hodgson, D.M., Brunt, R.L., Peakall, J., Poyatos-Moré, M. and Flint, S.S.** (2018c) Disconnected submarine lobes as a record of stepped slope evolution over multiple sea-level cycles. *Geosphere*, **14**, 1753–1779.
- Brooks, H.L., Ito, M., Zuchuat, V., Peakall, J. and Hodgson, D.M.** (2022) Channel-lobe transition zone development in tectonically active settings: Implications for hybrid bed development. *Depos. Rec.*, 1–40.
- Browne, G.H., Bull, S., Arnot, M.J., Boyes, A.F., King, P.R. and Helle, K.** (2020) The role of mass transport deposits contributing to fluid escape: Neogene outcrop and seismic examples from north Taranaki, New Zealand. *Geo-Marine Lett.*, **40**, 789–807.
- Brunt, R.L., Hodgson, D.M., Flint, S.S., Pringle, J.K., Di Celma, C., Prélat, A. and Grecula, M.** (2013) Confined to unconfined: Anatomy of a base of slope succession, Karoo Basin, South Africa. *Mar. Pet. Geol.*, **41**, 206–221.
- Brunt, R.L., McCaffrey, W.D. and Kneller, B.C.** (2004) Experimental modeling of the spatial distribution of grain size developed in a fill-and-spill mini-basin setting. *J. Sediment. Res.*, **74**, 438–446.
- Buffington, E.C.** (1952) Submarine “Natural Levees”. *J. Geol.*, **60**, 473–479.
- Bugge, T., Befring, S., Belderson, R.H., Eidvin, T., Jansen, E., Kenyon, N.H., Holtedahl, H. and Sejrup, H.P.** (1987) A giant three-stage submarine slide off Norway. *Geo-Marine Lett.*, **7**, 191–198.
- Bull, S., Cartwright, J. and Huuse, M.** (2009) A review of kinematic indicators from mass-transport complexes using 3D seismic data. *Mar. Pet. Geol.*, **26**, 1132–1151.

- Bungum, H., Lindholm, C. and Faleide, J.I.** (2005) Postglacial seismicity offshore mid-Norway with emphasis on spatio-temporal-magnitudinal variations. *Mar. Pet. Geol.*, **22**, 137–148.
- Burbank, D.W., Puigdefabregas, C. and Anton Munoz, J.** (1992) The chronology of the Eocene tectonic and stratigraphic development of the eastern Pyrenean foreland basin, northeast Spain. *Geol. Soc. Am. Bull.*, **104**, 1101–1120.
- Burgess, P.M., Flint, S. and Johnson, S.** (2000) Sequence stratigraphic interpretation of turbiditic strata: An example from Jurassic strata of the Neuquén basin, Argentina. *Bull. Geol. Soc. Am.*, **112**, 1650–1666.
- Burgreen, B. and Graham, S.** (2014) Evolution of a deep-water lobe system in the Neogene trench-slope setting of the East Coast Basin, New Zealand: Lobe stratigraphy and architecture in a weakly confined basin configuration. *Mar. Pet. Geol.*, **54**, 1–22.
- Butler, R.W.H., Eggenhuisen, J.T., Haughton, P. and McCaffrey, W.D.** (2016) Interpreting syndepositional sediment remobilization and deformation beneath submarine gravity flows; a kinematic boundary layer approach. *J. Geol. Soc. London.*, **173**, 46–58.
- Butler, R.W.H. and McCaffrey, W.D.** (2010) Structural evolution and sediment entrainment in mass-transport complexes: Outcrop studies from Italy. *J. Geol. Soc. London.*, **167**, 617–631.
- Caja, M.A., Marfil, R., Garcia, D., Remacha, E., Morad, S., Mansurbeg, H., Amorosi, A., Martínez-Calvo, C. and Lahoz-Beltrá, R.** (2010) Provenance of siliciclastic and hybrid turbiditic arenites of the Eocene Hecho Group, Spanish Pyrenees: Implications for the tectonic evolution of a foreland basin. *Basin Res.*, **22**, 157–180.
- Canals, M., Casamor, J.L., Urgeles, R., Lastras, G., Calafat, A.M., Masson, D.G., Berné, S. and Alonso, B.** (2000) The Ebro Continental Margin, Western Mediterranean Sea: Interplay Between Canyon-Channel Systems and Mass Wasting Processes. *Deep. Reserv. World 20th Annu.*, 152–174.
- Cantalejo, B. and Pickering, K.T.** (2014) Climate forcing of fine-grained deep-marine systems in an active tectonic setting: Middle Eocene, Ainsa Basin, Spanish Pyrenees. *Palaeogeogr. Palaeoclimatol. Palaeoecol.*, **410**, 351–371.
- Carey, S.N. and Schneider, J.L.** (2011) Volcaniclastic processes and deposits in the deep-sea. In: *Developments in Sedimentology*, 1st edn., Heiko Hneke and Thierry Mulder, 63, 457–515.
- Carter, R.M.** (1975) A discussion and classification of subaqueous mass-transport with particular application to grain-flow, slurry-flow, and fluxoturbidites. *Earth Sci. Rev.*, **11**, 145–177.
- Cartigny, M.J.B., Postma, G., van den Berg, J.H. and Mastbergen, D.R.** (2011) A comparative study of sediment waves and cyclic steps based on geometries, internal structures and numerical modeling. *Mar. Geol.*, **280**, 40–56.
- Castelltort, S., Honegger, L., Adatte, T., Clark, J.D., Puigdefàbregas, C., Spangenberg, J.E., Dykstra, M.L. and Fildani, A.** (2017) Detecting eustatic and

- tectonic signals with carbon isotopes in deep-marine strata, Eocene Ainsa Basin, Spanish Pyrenees. *Geology*, **45**, 707–710.
- Chanvry, E., Deschamps, R., Joseph, P., Puigdefàbregas, C., Poyatos-Moré, M., Serra-Kiel, J., Garcia, D. and Teinturier, S.** (2018) The influence of intrabasinal tectonics in the stratigraphic evolution of piggyback basin fills: Towards a model from the Tremp-Graus-Ainsa Basin (South-Pyrenean Zone, Spain). *Sediment. Geol.*, **377**, 34–62.
- Ciccioli, P.L., Limarino, C.O., Friedman, R. and Marensi, S.A.** (2014) New high precision U-Pb ages for the Vinchina Formation: Implications for the stratigraphy of the Bermejo Andean foreland basin (La Rioja province, western Argentina). *J. South Am. Earth Sci.*, **56**, 200–213.
- Clark, I.R. and Cartwright, J.A.** (2011) Key controls on submarine channel development in structurally active settings. *Mar. Pet. Geol.*, **28**, 1333–1349.
- Clark, J., Puigdefàbregas, C., Castelltort, S. and Fildani, A.** (2017) Propagation of Environmental Signals Within Source-to-sink Stratigraphy. In: *Spanish Pyrenees, June 5th-9th, 2017. SEPM (Society for Sedimentary Geology)*.
- Cobain, S.L., Hodgson, D.M., Peakall, J. and Shiers, M.N.** (2017) An integrated model of clastic injectites and basin floor lobe complexes: implications for stratigraphic trap plays. *Basin Res.*, **29**, 816–835.
- Coleman, J.M. and Prior, D.B.** (1998) Mass wasting on continental margins. *Annu. Rev. Earth Planet. Sci.*, **16**, 101.
- Corella, J.P., Loizeau, J.L., le Dantec, N., Hilbe, M., Gerard, J., le Dantec, N., Stark, N., González-Quijano, M. and Girardclos, S.** (2016) The role of mass-transport deposits and turbidites in shaping modern lacustrine deepwater channels. *Mar. Pet. Geol.*, **77**, 515–525.
- Covault, J.A., Romans, B.W., Graham, S.A., Fildani, A. and Hilley, G.E.** (2011) Terrestrial source to deep-sea sink sediment budgets at high and low sea levels: Insights from tectonically active Southern California. *Geology*, **39**, 619–622.
- Cristallini, E., Bottesi, G., Gavarrino, A., Rodríguez, L., Tomezzoli, R. and Comeron, R.** (2006) Synrift geometry of the Neuquén Basin in northeastern Neuquén Province, Argentina. *Spec. Pap. Geol. Soc. Am.*, **407**, 147–161.
- Cristallini, E., Tomezzoli, R., Pando, G., Gazzera, C., Martínez, J.M., Quiroga, J., Marianso, B., Bechis, F., Barredo, S. and Zambrano, O.** (2009) Controls of the Precuyano in the structure of the Neuquén Basin. *Rev. la Asoc. Geol. Argentina*, **65**, 248–264.
- Cronin, B.T.** (1995) Structurally-controlled deep sea channel courses: Examples from the Miocene of southeast Spain and the Alboran Sea, southwest Mediterranean. *Geol. Soc. Spec. Publ.*, **94**, 115–135.
- Cullen, T.M., Collier, R.E.L., Gawthorpe, R.L., Hodgson, D.M. and Barrett, B.J.** (2020) Axial and transverse deep-water sediment supply to syn-rift fault terraces: Insights from the West Xylokastro Fault Block, Gulf of Corinth, Greece. *Basin Res.*, **32**, 1115–1149.
- Cumberpatch, Z.A., Soutter, E.L., Kane, I.A., Casson, M. and Vincent, S.J.** (2021)

- Evolution of a mixed siliciclastic-carbonate deep-marine system on an unstable margin: The Cretaceous of the Eastern Greater Caucasus, Azerbaijan. *Basin Res.*, **33**, 612–647.
- Curry, J.R., Emmel, F.J. and Moore, D.G.** (2002) The Bengal Fan: Morphology, geometry, stratigraphy, history and processes. *Mar. Pet. Geol.*, **19**, 1191–1223.
- Dakin, N., Pickering, K.T., Mohrig, D. and Bayliss, N.J.** (2013) Channel-like features created by erosive submarine debris flows: Field evidence from the Middle Eocene Ainsa Basin, Spanish Pyrenees. *Mar. Pet. Geol.*, **41**, 62–71.
- Dalla Valle, G., Gamberi, F., Foglini, F. and Trincardi, F.** (2015) The Gondola Slide: A mass transport complex controlled by margin topography (South-Western Adriatic Margin, Mediterranean Sea). *Mar. Geol.*, **366**, 97–113.
- Damborenea, S.E.** (1990) Middle Jurassic inoceramids from Argentina. *J. Paleontol.*, **736–759**.
- Damuth, J.E., Flood, R.D., Kowsmann, R.O., Belderson, R.H. and Gorini, M.A.** (1988) Anatomy and growth pattern of Amazon deep-sea fan as revealed by long-range side-scan sonar (GLORIA) and high-resolution seismic studies. *Am. Assoc. Pet. Geol. Bull.*, **72**, 885–911.
- Davis, C., Haughton, P., McCaffrey, W., Scott, E., Hogg, N. and Kitching, D.** (2009) Character and distribution of hybrid sediment gravity flow deposits from the outer Forties Fan, Palaeocene Central North Sea, UKCS. *Mar. Pet. Geol.*, **26**, 1919–1939.
- De La Cruz, R. and Suarez, M.** (1997) El Jurásico de la cuenca de Neuquén en lonquimay, Chile: formación nacientes del biobío (38–39°S). *Rev. Geol. Chile*, **24**, 3–24.
- De Leeuw, J., Eggenhuisen, J.T. and Cartigny, M.J.B.** (2016) Morphodynamics of submarine channel inception revealed by new experimental approach. *Nat. Commun.*, **7**, 1–7.
- De Pippo, T., Iardi, M. and Pennetta, M.** (1999) Main observations on genesis and morphological evolution of submarine valleys. *Zeitschrift fur Geomorphol.*, **43**, 91–111.
- De Ruig, M.J. and Hubbard, S.M.** (2006) Seismic facies and reservoir characteristics of a deep-marine channel belt in the Molasse foreland basin, Puchkirchen Formation, Austria. *Am. Assoc. Pet. Geol. Bull.*, **90**, 735–752.
- Dennielou, B., Huchon, A., Beaudouin, C. and Berné, S.** (2006) Vertical grain-size variability within a turbidite levee: Autocyclicity or allocyclicity? A case study from the Rhône neofan, Gulf of Lions, Western Mediterranean. *Mar. Geol.*, **234**, 191–213.
- Deptuck, M.E., Piper, D.J.W., Savoye, B. and Gervais, A.** (2008) Dimensions and architecture of late Pleistocene submarine lobes off the northern margin of East Corsica. *Sedimentology*, **55**, 869–898.
- Deptuck, M.E., Steffens, G.S., Barton, M. and Pirmez, C.** (2003) Architecture and evolution of upper fan channel-belts on the Niger Delta slope and in the Arabian Sea. *Mar. Pet. Geol.*, **20**, 649–676.

- Deptuck, M.E., Sylvester, Z. and O'byrne, C.** (2012) Pleistocene Seascape Evolution Above a "Simple" Stepped Slope—Western Niger Delta. In: *Application of the Principles of Seismic Geomorphology to Continental-Slope and Base-of-Slope Systems: Case Studies From Seafloor and Near-Seafloor Analogues* (Ed. by Prather B. E., Deptuck M. E., Mohrig D. C., B. van Hoorn & Wynn R. B.), 199–222.
- Deptuck, M.E., Sylvester, Z., Pirmez, C. and O'Byrne, C.** (2007) Migration-aggradation history and 3-D seismic geomorphology of submarine channels in the Pleistocene Benin-major Canyon, western Niger Delta slope. *Mar. Pet. Geol.*, **24**, 406–433.
- Desbarats, A.J.** (1987) Numerical estimation of effective permeability in sand-shale formations. *Water Resour. Res.*, **23**, 273–286.
- Deutsch, C.** (1989) Calculating effective absolute permeability in sandstone/shale sequences. *SPE Form. Eval.*, **4**, 343–348.
- Di Celma, C.N., Brunt, R.L., Hodgson, D.M., Flint, S.S. and Kavanagh, J.P.** (2011) Spatial and temporal evolution of a permian submarine slope channel-levee system, Karoo Basin, South Africa. *J. Sediment. Res.*, **81**, 579–599.
- Dickinson, W.R.** (1970) Interpreting detrital modes of graywacke and arkose. *J. Sediment. Res.*, **40**, 695–707.
- Dickinson, W.R.** (1985) Interpreting provenance relations from detrital modes of sandstones. Proven. arenites. Proc. Cetraro, Cosenza, 1984 333–361.
- Dickinson, W.R., Beard, L.S., Brakenridge, G.R., Erjavec, J., Ferguson, R., Inman, K., Knapp, R., Lindberg, F.A. and Ryberg, P.** (1983) Provenance of North American Phanerozoic sandstones in relation to tectonic setting. *Geol. Soc. Am. Bull.*, **94**, 222–235.
- Dmitrieva, E., Jackson, C.A.L., Huuse, M. and Kane, I.A.** (2018) Regional distribution and controls on the development of post-rift turbidite systems: Insights from the Paleocene of the eastern North Viking Graben, offshore Norway. *Pet. Geol. Conf. Proc.*, **8**, 147–170.
- Dodd, T.J.H., McCarthy, D.J. and Richards, P.C.** (2019) A depositional model for deep-lacustrine, partially confined, turbidite fans: Early Cretaceous, North Falkland Basin. *Sedimentology*, **66**, 53–80.
- Dorrell, R.M., Peakall, J., Sumner, E.J., Parsons, D.R., Darby, S.E., Wynn, R.B., Özsoy, E. and Tezcan, D.** (2016) Flow dynamics and mixing processes in hydraulic jump arrays: Implications for channel-lobe transition zones. *Mar. Geol.*, **381**, 181–193.
- Dott, R.H.** (1963) Dynamics of Subaqueous Gravity Depositional Processes'. *Am. Assoc. Pet. Geol. Bull.*, **47**, 104–128.
- Dowey, P.J., Hodgson, D.M. and Worden, R.H.** (2012) Pre-requisites, processes, and prediction of chlorite grain coatings in petroleum reservoirs: A review of subsurface examples. *Mar. Pet. Geol.*, **32**, 63–75.
- Dreyer, T., Corregidor, J., Arbues, P. and Puigdefabregas, C.** (1999) Architecture of the tectonically influenced Sobrarbe deltaic complex in the Ainsa Basin, northern

- Spain. *Sediment. Geol.*, **127**, 127–169.
- Droz, L., Jégou, I., Gillet, H., Dennielou, B., Bez, M., Canals, M., Amblas, D., Lastras, G. and Rabineau, M.** (2020) On the termination of deep-sea fan channels: Examples from the Rhône Fan (Gulf of Lion, Western Mediterranean Sea). *Geomorphology*, **369**, 107368.
- Du Fornel, E., Joseph, P., Desaubliaux, G., Eschard, R., Guillocheau, F., Lerat, O., Muller, C., Ravenner, C. and Sztrakos, K.** (2004) The southern Grès d'Annot outcrops (French Alps): an attempt at regional correlation. *Geol. Soc. London, Spec. Publ.*, **221**, 137–160.
- Dykstra, M.** (2005) Dynamics of Submarine Sediment Mass-Transport, from the Shelf to the Deep Sea. *PhD Thesis*, 159.
- Dykstra, M., Garyfalou, K., Kertznus, V., Kneller, B.C., Milana, J.P., Molinaro, M., Szuman, M. and Thompson, P.** (2011) Mass-transport deposits: combining outcrop studies and seismic forward modeling to understand lithofacies distributions, deformation, and their seismic expression. In: *Posamentier, H., Weimer P. & Shipp, C. SEPM Special Publication 95*, 295–310.
- Dykstra, M. and Kneller, B.** (2009) Lateral accretion in a deep-marine channel complex: Implications for channelized flow processes in turbidity currents. *Sedimentology*, **56**, 1411–1432.
- Edwards, D.A.** (1993) Turbidity currents: dynamics, deposits and reversals. *Berlin, Heidelberg: Springer Berlin Heidelberg*.
- Edwards, D.A., Leeder, M.R., Best, J.L. and Pantin, H.M.** (1994) On experimental reflected density currents and the interpretation of certain turbidites. *Sedimentology*, **41**, 437–461.
- Eggenhuisen, J.T., Mccaffrey, W.D., Haughton, P.D.W. and Butler, R.W.H.** (2011) Shallow erosion beneath turbidity currents and its impact on the architectural development of turbidite sheet systems. *Sedimentology*, **58**, 936–959.
- Ehrenberg, S.N.** (1993) Preservation of anomalously high porosity in deeply buried sandstones by grain-coating chlorite: examples from the Norwegian continental shelf. *Am. Assoc. Pet. Geol. Bull.*, **77**, 1260–1286.
- Elliott, T.** (2000) Megaflute erosion surfaces and initiation of turbidite channels. *Geology*, **28**, 119–122.
- Færseth, R.B. and Lien, T.** (2002) Cretaceous evolution in the Norwegian Sea - a period characterized by tectonic quiescence. *Mar. Pet. Geol.*, **19**, 1005–1027.
- Fagherazzi, S.** (2004) Modeling fluvial erosion and deposition on continental shelves during sea level cycles. *J. Geophys. Res.*, **109**, 1–16.
- Fairweather, L.** (2014) Mechanisms of supra MTD topography generation and the interaction of turbidity currents with such deposits. *PhD Thesis*, **1**, 242.
- Fallgatter, C., Kneller, B., Paim, P.S.G. and Milana, J.P.** (2017) Transformation, partitioning and flow–deposit interactions during the run-out of megafloes. *Sedimentology*, **64**, 359–387.
- Farre, J.A., McGregor, B.A., Ryan, W.B.F. and Robb, J.M.** (1983) Breaching the

- shelfbreak: passage from youthful to mature phase in submarine canyon evolution. In: *The Shelf Break: Critical Interface on Continental Margins*. (Ed. D.J. Stanley and G.T. Moore), *Society of Economic Paleontologists and Mineralogists Specialia*, 25–39.
- Farrell, S.G. and Eaton, S.** (1987) Slump strain in the Tertiary of Cyprus and the Spanish Pyrenees. Definition of palaeoslopes and models of soft-sediment deformation. *Geol. Soc. Spec. Publ.*, **29**, 181–196.
- Felix, M.** (2001) A Two-Dimensional Numerical Model for a Turbidity Current. *Part. Gravity Curr.*, 71–81.
- Felix, M. and Peakall, J.** (2002) Transformation of Debris Flows Into Turbidity Currents: a key Process for Hazard Prediction. In: *AGU Fall Meeting Abstracts*,
- Felix, M. and Peakall, J.** (2006) Transformation of debris flows into turbidity currents: Mechanisms inferred from laboratory experiments. *Sedimentology*, **53**, 107–123.
- Ferguson, R.A., Kane, I.A., Eggenhuisen, J.T., Pohl, F., Tilston, M., Spychala, Y.T. and Brunt, R.L.** (2020) Entangled external and internal controls on submarine fan evolution: an experimental perspective. *Depos. Rec.*, **6**, 605–624.
- Fernández, O., Muñoz, J.A., Arbués, P. and Falivene, O.** (2012) 3D structure and evolution of an oblique system of relaying folds: The Ainsa basin (Spanish Pyrenees). *J. Geol. Soc. London.*, **169**, 545–559.
- Festa, A., Ogata, K., Pini, G.A., Dilek, Y. and Alonso, J.L.** (2016) Origin and significance of olistostromes in the evolution of orogenic belts: A global synthesis. *Gondwana Res.*, **39**, 180–203.
- Field, M.E. and Hall, R.K.** (1982) Sonographs of submarine sediment failure caused by the 1980 earthquake off northern California. *Geo-Marine Lett.*, **2**, 135–141.
- Figueiredo, J.J.P., Hodgson, D.M., Flint, S.S. and Kavanagh, J.P.** (2010) Depositional environments and sequence stratigraphy of an exhumed permian mudstone-dominated submarine slope succession, KAROO BASIN, SOUTH AFRICA. *J. Sediment. Res.*, **80**, 97–118.
- Fildani, A., Clark, J., Covault, J.A., Power, B., Romans, B.W. and Aiello, I.W.** (2018) Muddy sand and sandy mud on the distal Mississippi fan: Implications for lobe depositional processes. *Geosphere*, **14**, 1051–1066.
- Fildani, A. and Normark, W.R.** (2004) Late Quaternary evolution of channel and lobe complexes of Monterey Fan. *Mar. Geol.*, **206**, 199–223.
- Flood, R.D., Manley, P.L., Kowsmann, R.O., Appi, C.J. and Pirmez, C.** (1991) Seismic facies and late Quaternary growth of Amazon submarine fan. In: *Seismic facies and sedimentary processes of submarine fans and turbidite systems*, Springer, New York, 415–433.
- Fonnesu, M., Felletti, F., Haughton, P.D.W., Patacci, M. and McCaffrey, W.D.** (2018) Hybrid event bed character and distribution linked to turbidite system sub-environments: The North Apennine Gottero Sandstone (north-west Italy). *Sedimentology*, **65**, 151–190.
- Fonnesu, M., Haughton, P., Felletti, F. and McCaffrey, W.** (2015) Short length-scale

- variability of hybrid event beds and its applied significance. *Mar. Pet. Geol.*, **67**, 583–603.
- Fontana, D., Zuffa, G.G. and Garzanti, E.** (1989) The interaction of eustacy and tectonism from provenance studies of the Eocene Hecho Group Turbidite Complex (south-central Pyrenees, Spain). *Basin Res.*, **2**, 223–237.
- Franzese, J. and Spalletti, L.** (2003) Tectonic and paleoenvironmental evolution of Mesozoic sedimentary basins along the Andean foothills of Argentina (32°S–54°S). **16**, 81–90.
- Franzese, J., Spalletti, L., Gomez, I. and Macdonald, D.** (2003) Tectonic and paleoenvironmental evolution of Mesozoic sedimentary basins along the Andean foothills of Argentina (32°S–54°S). **16**, 81–90.
- Franzese, J.R. and Spalletti, L.A.** (2001) Late triassic–Early jurassic continental extension in SouthWestern Gondwana: Tectonic segmentation and pre-break-up rifting. *J. South Am. Earth Sci.*, **14**, 257–270.
- Franzese, J.R., Veiga, G.D., Schwarz, E. and Gómez-Pérez, I.** (2006) Tectonostratigraphic evolution of a Mesozoic graben border system: The Chachil depocentre, southern Neuquén Basin, Argentina. *J. Geol. Soc. London.*, **163**, 707–721.
- Friend, F., Slater, M.J. and Williams, R.C.** (1979) Vertical and lateral building. *J. Geol. Soc. London.*, **136**, 39–46.
- Fryer, G.J., Watts, P. and Pratson, L.F.** (2004) Source of the great tsunami of 1 April 1946: A landslide in the upper Aleutian forearc. *Mar. Geol.*, **203**, 201–218.
- Fugelli, E.M. and Olsen, T.R.** (2007) Delineating confined slope turbidite systems offshore mid-Norway: The Cretaceous deep-marine Lysing Formation. *Am. Assoc. Pet. Geol. Bull.*, **91**, 1577–1601.
- Gabrielsen, R.H., Kyrkjebø, R., Faleide, J.I., Fjeldskaar, W. and Kjennerud, T.** (2001) The Cretaceous post-rift basin configuration of the northern North Sea. *Pet. Geosci.*, **7**, 137–154.
- Garcia, M. and Parker, G.** (1989) Experiments on Hydraulic Jumps in Turbidity Currents near a Canyon-Fan Transition. *Science (80-)*, **245**, 393–396.
- Garcia, M.H.** (1994) Depositional turbidity currents laden with poorly sorted sediment. *J. Hydraul. Eng.*, **120**, 1240–1263.
- García, M.H.** (1993) Hydraulic jumps in sediment-driven bottom currents. *J. Hydraul. Eng.*, **119**, 1094–1117.
- Gardiner, A.R.** (2006) The variability of turbidite sandbody pinchout and its impact on hydrocarbon recovery in stratigraphically trapped fields. *Geol. Soc. London, Spec. Publ.*, **254**, 267–287.
- Garziglia, S., Migeon, S., Ducassou, E., Loncke, L. and Mascle, J.** (2008) Mass-transport deposits on the Rosetta province (NW Nile deep-sea turbidite system, Egyptian margin): Characteristics, distribution, and potential causal processes. *Mar. Geol.*, **250**, 180–198.
- Gazzi, P.** (1966) Le arenarie del flysch sopracretaceo dell'Appennino modenese;

- Correlazioni con flysch di Monghidoro. *Min. Petrogr. Acta*, **12**, 69–97.
- Gee, M.J., Masson, D.G., Watts, A.B. and Mitchell, N.C.** (2001) Passage of debris flows and turbidity currents through a topographic constriction: seafloor erosion and deflection of flow pathways. *Sedimentology*, **48**, 1389–1409.
- Gee, M.J.R. and Gawthorpe, R.L.** (2006) Submarine channels controlled by salt tectonics: Examples from 3D seismic data offshore Angola. *Mar. Pet. Geol.*, **23**, 443–458.
- Gee, M.J.R., Gawthorpe, R.L. and Friedmann, S.J.** (2006) Triggering and Evolution of a Giant Submarine Landslide, Offshore Angola, Revealed by 3D Seismic Stratigraphy and Geomorphology. *J. Sediment. Res.*, **76**, 9–19.
- Georgiopoulou, A. and Cartwright, J.A.** (2013) A critical test of the concept of submarine equilibrium profile. *Mar. Pet. Geol.*, **41**, 35–47.
- Gervais, A., Savoye, B., Mulder, T. and Gonthier, E.** (2006) Sandy modern turbidite lobes: A new insight from high resolution seismic data. *Mar. Pet. Geol.*, **23**, 485–502.
- Goldfinger, C., Kulm, L.D., McNeill, L.C. and Watts, P.** (2000) Super-scale failure of the southern Oregon Cascadia margin. *Pure Appl. Geophys.*, **157**, 1189–1226.
- Grundvåg, S.A., Johannessen, E.P., Helland-Hansen, W. and Plink-Björklund, P.** (2014) Depositional architecture and evolution of progradationally stacked lobe complexes in the Eocene Central Basin of Spitsbergen. *Sedimentology*, **61**, 535–569.
- Gulisano, C. and Gutiérrez Pleimling, A.R.** (1995) Field Guide. The Jurassic of the Neuquén Basin. a) Neuquén Province: Asociación Geológica Argentina. *Série E*, **2**, 1–111.
- Gulisano, C.A., Gutiérrez Pleimling, A.R. and Digregorio, J.H.** (1984) Esquema estratigráfico de la secuencia jurásica del oeste de la provincia del Neuquén. IX Congr. Geológico Argentino 1:236–259.
- Gupta, K. Das and Pickering, K.T.** (2008) Petrography and temporal changes in petrofacies of deep-marine Ainsa-Jaca basin sandstone systems, Early and Middle Eocene, Spanish Pyrenees. *Sedimentology*, **55**, 1083–1114.
- Gupta, S., Underhill, J.R., Sharp, I.R., Gawthorpe, R.L. and Ract, A.** (1999) Gupta.suez.pdf. 167–189.
- Hampton, M.A.** (1970) Subaqueous debris flow and generation of turbidity currents. Stanford University.
- Hampton, M.A.** (1975) Competence of Fine-grained Debris Flows. *SEPM J. Sediment. Res.*, **Vol. 45**, 834–844.
- Hampton, M.A., Lee, H.J. and Locat., J.** (1995) Submarine Landslides. *Rev. Geophys.*, **34**, 33–59.
- Hansen, L.A.S., Callow, R., Kane, I.A. and Kneller, B.** (2017a) Differentiating submarine channel-related thin-bedded turbidite facies: Outcrop examples from the Rosario Formation, Mexico. *Sediment. Geol.*, **358**, 19–34.

- Hansen, L.A.S., Callow, R.H.T., Kane, I.A., Gamberi, F., Rovere, M., Cronin, B.T. and Kneller, B.C.** (2015) Genesis and character of thin-bedded turbidites associated with submarine channels. *Mar. Pet. Geol.*, **67**, 852–879.
- Hansen, L.A.S., Hodgson, D.M., Pontén, A., Bell, D. and Flint, S.** (2019) Quantification of basin-floor fan pinchouts: Examples from the Karoo Basin, South Africa. *Front. Earth Sci.*, **7**, 1–20.
- Hansen, L.A.S., Hodgson, D.M., Pontén, A., Thrana, C. and Obradors Latre, A.** (2021) Mixed axial and transverse deep-water systems: The Cretaceous post-rift Lysing Formation, offshore Norway. *Basin Res.*, 1–23.
- Hansen, L.A.S., Janocko, M., Kane, I. and Kneller, B.** (2017b) Submarine channel evolution, terrace development, and preservation of intra-channel thin-bedded turbidites: Mahin and Avon channels, offshore Nigeria. *Mar. Geol.*, **383**, 146–167.
- Harris, P.T. and Whiteway, T.** (2011) Global distribution of large submarine canyons: Geomorphic differences between active and passive continental margins. *Mar. Geol.*, **285**, 69–86.
- Haughton, P., Davis, C., McCaffrey, W. and Barker, S.** (2009) Hybrid sediment gravity flow deposits - Classification, origin and significance. *Mar. Pet. Geol.*, **26**, 1900–1918.
- Haughton, P.D.W.** (1994) Deposits of deflected and ponded turbidity currents, Sorbas Basin, southeast Spain. *J. Sediment. Res. A Sediment. Petrol. Process.*, **64 A**, 233–246.
- Haughton, P.D.W., Barker, S.P. and McCaffrey, W.D.** (2003) “Linked” debrites in sand-rich turbidite systems - Origin and significance. *Sedimentology*, **50**, 459–482.
- Hay, D.C.** (2012) Stratigraphic Evolution of a Tortuous Corridor From The Stepped Slope of Angola. *Appl. Princ. Seism. Geomorphol. to Cont. Base-of-Slope Syst. Case Stud. from Seafloor Near-Seafloor Analog.*, 163–180.
- Heald, M.T. and Larese, R.E.** (1974) Influence of coatings on quartz cementation. *J. Sediment. Res.*, **44**, 1269–1274.
- Heezen, B.C., Ewing, M. and Menzies, R.J.** (1955) The Influence of Submarine Turbidity Currents on Abyssal Productivity. *Oikos*, **6**, 170–182.
- Heezen, B.C., Menzies, R.J., Schneider, R.J., Ewing, W.M. and Granelli, N.C.L.** (1964) Congo Submarine Canyon. *Am. Assoc. Pet. Geol. Bull.*, **48**, 1126–1149.
- Heijnen, M., Mienis, F., Gates, A., Bett, B., Hall, R., Hunt, J., Kane, I., Pebody, C., Huvenne, V., Soutter, E. and Clare, M.** (2022) Challenging the highstand-dormant paradigm for land-detached submarine canyons.
- Heiniö, P. and Davies, R.J.** (2007) Knickpoint migration in submarine channels in response to fold growth, western Niger Delta. *Mar. Pet. Geol.*, **24**, 434–449.
- Henstra, G.A., Grundvåg, S.A., Johannessen, E.P., Kristensen, T.B., Midtkandal, I., Nystuen, J.P., Rotevatn, A., Surlyk, F., Sæther, T. and Windelstad, J.** (2016) Depositional processes and stratigraphic architecture within a coarse-grained rift-margin turbidite system: The Wollaston Forland Group, east Greenland. *Mar. Pet. Geol.*, **76**, 187–209.

- Hessler, A.M. and Fildani, A.** (2019) Deep-sea fans: Tapping into Earth's changing landscapes. *J. Sediment. Res.*, **8**, 1171–1179.
- Hiscott, R.N.** (1995) Traction-Carpet Stratification in Turbidites--Fact or Fiction?: REPLY.
- Hiscott, R.N.** (1994a) Loss of capacity, not competence, as the fundamental process governing deposition from turbidity currents. *J. Sediment. Res.*, **64**, 209–214.
- Hiscott, R.N.** (1994b) Traction-carpet stratification in turbidites; fact or fiction? *J. Sediment. Res.*, **64**, 204–208.
- Hodgson, D.M.** (2009) Distribution and origin of hybrid beds in sand-rich submarine fans of the Tanqua depocentre, Karoo Basin, South Africa. *Mar. Pet. Geol.*, **26**, 1940–1956.
- Hodgson, D.M., Brooks, H.L., Ortiz-Karpf, A., Spsychala, Y., Lee, D.R. and Jackson, C.A.L.** (2019) Entrainment and abrasion of megaclasts during submarine landsliding and their impact on flow behaviour. *Geol. Soc. Spec. Publ.*, **477**, 223–240.
- Hodgson, D.M., Flint, S.S., Hodgetts, D., Drinkwater, N.J., Johannessen, E.P. and Luthi, S.M.** (2006) Stratigraphic evolution of fine-grained submarine fan systems, Tanqua depocenter, Karoo Basin, South Africa. *J. Sediment. Res.*, **76**, 20–40.
- Hodgson, D.M., Kane, I.A., Flint, S.S., Brunt, R.L. and Ortiz-Karpf, A.** (2016) Time-transgressive confinement on the slope and the progradation of basin-floor fans: Implications for the sequence stratigraphy of deep-water deposits. *J. Sediment. Res.*, **86**, 73–86.
- Hodgson, D.M., Peakall, J. and Maier, K.L.** (2022) Submarine Channel Mouth Settings: Processes, Geomorphology, and Deposits. 1–38 pp.
- Hodgson, N.A., Farnsworth, J. and Fraser, A.J.** (1992) Salt-related tectonics, sedimentation and hydrocarbon plays in the Central Graben, North Sea, UKCS. *Geol. Soc. Spec. Publ.*, **67**, 31–63.
- Hofstra, M., Hodgson, D.M., Peakall, J. and Flint, S.S.** (2015) Giant scour-fills in ancient channel-lobe transition zones: Formative processes and depositional architecture. *Sediment. Geol.*, **329**, 98–114.
- Hofstra, M., Peakall, J., Hodgson, D.M. and Stevenson, C.J.** (2018) Architecture and morphodynamics of subcritical sediment waves in an ancient channel-lobe transition zone. *Sedimentology*, **65**, 2339–2367.
- Howell, D.G. and Normark, W.R.** (1982) Sedimentology of submarine fans. In: *American Association of Petroleum Geologists Memoir*, 365–404.
- Howell, J.A., Swcharz, E., Spalletti, L.A. and Veiga, G.D.** (2005) The Neuquén Basin, Argentina: A case study in sequence stratigraphy and basin dynamics. *Geol. Soc. London, Spec. Publ.*, **252**, 1–14.
- Hubbard, S.M., Covault, J.A., Fildani, A. and Romans, B.W.** (2014) Sediment transfer and deposition in slope channels: Deciphering the record of enigmatic deep-sea processes from outcrop. *Bull. Geol. Soc. Am.*, **126**, 857–871.
- Hubbard, S.M., de Ruig, M.J. and Graham, S.A.** (2009) Confined channel-levee

- complex development in an elongate depo-center: Deep-water Tertiary strata of the Austrian Molasse basin. *Mar. Pet. Geol.*, **26**, 85–112.
- Hubbard, S.M., Jobe, Z.R., Romans, B.W., Covault, J.A., Sylvester, Z. and Fildani, A.** (2020) The stratigraphic evolution of a submarine channel: linking seafloor dynamics to depositional products. *J. Sediment. Res.*, **90**, 673–686.
- Hubbard, S.M., Romans, B.W. and Graham, S.A.** (2008) Deep-water foreland basin deposits of the Cerro Toro Formation, Magallanes basin, Chile: Architectural elements of a sinuous basin axial channel belt. *Sedimentology*, **55**, 1333–1359.
- Hübscher, C., Spieß, V., Breitzke, M. and Weber, M.E.** (1997) The youngest channel-levee system of the Bengal Fan: Results from digital sediment echosounder data. *Mar. Geol.*, **141**, 125–145.
- Hughes-Clarke, J.E., Shor, A.N., Piper, D.J. and Mayer, L.A.** (1990) Large-scale current-induced erosion and deposition in the path of the 1929 Grand Banks turbidity current. *Sedimentology*, **37**, 613–629.
- Hughes Clarke, J.E.** (2016) First wide-angle view of channelized turbidity currents links migrating cyclic steps to flow characteristics. *Nat Commun.* doi: 10.1038/ncomms11896
- Hulka, C. and Heubeck, C.** (2010) Composition and provenance history of late cenozoic sediments in southeastern boliva: Implications for Chaco foreland basin evolution and Andean uplift. *J. Sediment. Res.*, **80**, 288–299.
- Hurst, A., Cartwright, J. and Cartwright, J.A.** (2008) Sand Injectites: Implications for Hydrocarbon Exploration and Production. *AAPG Mem.*, **87**, 34–49.
- Hurst, A., Cartwright, J.A., Duranti, D., Huuse, M. and Nelson, M.** (2005) Sand injectites: an emerging global play in deep-water clastic environments. *Geol. Soc. London, Pet. Geol. Conf. Ser.*, **6**, 133–144.
- Hurst, A., Scott, A. and Vigorito, M.** (2011) Physical characteristics of sand injectites. *Earth-Science Rev.*, **106**, 215–246.
- Hurst, A., Verstralen, I., Cronin, B. and Hartley, A.** (1999) Sand-Rich Fairways in Deep-Water Clastic Reservoirs: Genetic Units, Capturing Uncertainty, and a New Approach to Reservoir Modeling. *Am. Assoc. Pet. Geol. Bull.*, **83**, 1096–1118.
- Hussain, A., Haughton, P.D.W., Shannon, P.M., Turner, J.N., Pierce, C.S., Obradors-Latre, A., Barker, S.P. and Martinsen, O.J.** (2020) High-resolution X-ray fluorescence profiling of hybrid event beds: Implications for sediment gravity flow behaviour and deposit structure. *Sedimentology*, **67**, 2850–2882.
- Ingersoll, R. V. and Suczek, C.** (1979) Petrology and provenance of Neogene sand from Nicobar and Bengal fans, DSDP sites 211 and 218. *J. Sediment. Petrol.*, **49**, 1217–1228.
- Ito, M.** (2008) Downfan transformation from turbidity currents to debris flows at a channel-to-lobe transitional zone: The lower Pleistocene Otadai Formation, Boso Peninsula, Japan. *J. Sediment. Res.*, **78**, 668–682.
- Iverson, R.M.** (1997) The physics of debris flows. *Rev. Geophys.*, **35**, 245–296.
- Iverson, R.M., Logan, M., LaHusen, R.G. and Berti, M.** (2010) The perfect debris

- flow? Aggregated results from 28 large-scale experiments. *J Geophys Res.* doi: 10.1029/2009jf001514
- Jackson, C.A.L.** (2011) Three-dimensional seismic analysis of megaclast deformation within a mass transport deposit; Implications for debris flow kinematics. *Geology*, **39**, 203–206.
- Jackson, C.A.L.** and **Johnson, H.D.** (2009) Sustained turbidity currents and their interaction with debrite-related topography; Labuan Island, offshore NW Borneo, Malaysia. *Sediment. Geol.*, **219**, 77–96.
- Janocko, M., Nemec, W., Henriksen, S. and Warchol, M.** (2013) The diversity of deep-water sinuous channel belts and slope valley-fill complexes. *Mar. Pet. Geol.*, **41**, 7–34.
- Jegou, I., Savoye, B., Pirmez, C. and Droz, L.** (2008) Channel-mouth lobe complex of the recent Amazon Fan: The missing piece. *Mar. Geol.*, **252**, 62–77.
- Jobe, Z.R., Howes, N., Romans, B.W. and Covault, J.A.** (2018) Volume and recurrence of submarine-fan-building turbidity currents. *Depos. Rec.*, **4**, 160–176.
- Jobe, Z.R., Lowe, D.R. and Morris, W.R.** (2012) Climbing-ripple successions in turbidite systems : depositional environments , sedimentation rates and accumulation times. 867–898.
- Jobe, Z.R., Sylvester, Z., Howes, N., Pirmez, C., Parker, A., Cantelli, A., Smith, R., Wolinsky, M.A., O’Byrne, C., Slowey, N. and Prather, B.** (2017) High-resolution, millennial-scale patterns of bed compensation on a sand-rich intraslope submarine fan, western Niger Delta slope. *Bull. Geol. Soc. Am.*, **129**, 23–37.
- Joseph, P. and Lomas, S.A.** (2004) Deep-water sedimentation in the Alpine Foreland Basin of SE France: New perspectives on the Grès d’Annot and related systems - An introduction. *Geol. Soc. Spec. Publ.*, **221**, 1–16.
- Kamo, S.L. and Riccardi, A.C.** (2009) A new U-Pb zircon age for an ash layer at the Bathonian-Callovian boundary, Argentina. *Gff*, **131**, 177–182.
- Kane, I.A., Catterall, V., McCaffrey, W.D. and Martinsen, O.J.** (2010a) Submarine channel response to intrabasinal tectonics: The influence of lateral tilt. *Am. Assoc. Pet. Geol. Bull.*, **94**, 189–219.
- Kane, I.A. and Clare, M.A.** (2019) Dispersion, accumulation, and the ultimate fate of microplastics in deep-marine environments: A review and future directions. *Front Earth Sci.* doi: 10.3389/feart.2019.00080
- Kane, I.A. and Hodgson, D.M.** (2011) Sedimentological criteria to differentiate submarine channel levee subenvironments: Exhumed examples from the Rosario Fm. (Upper Cretaceous) of Baja California, Mexico, and the Fort Brown Fm. (Permian), Karoo Basin, S. Africa. *Mar. Pet. Geol.*, **28**, 807–823.
- Kane, I.A., Kneller, B.C., Dykstra, M., Kassem, A. and McCaffrey, W.D.** (2007) Anatomy of a submarine channel-levee: An example from Upper Cretaceous slope sediments, Rosario Formation, Baja California, Mexico. *Mar. Pet. Geol.*, **24**, 540–563.
- Kane, I.A., McCaffrey, W.D., Peakall, J. and Kneller, B.C.** (2010b) Submarine

- channel levee shape and sediment waves from physical experiments. *Sediment. Geol.*, **223**, 75–85.
- Kane, I.A. and Pontén, A.S.M.** (2012) Submarine transitional flow deposits in the Paleogene Gulf of Mexico. *Geology*, **40**, 1119–1122.
- Kane, I.A., Pontén, A.S.M., Vangdal, B., Eggenhuisen, J.T., Hodgson, D.M. and Spychala, Y.T.** (2017) The stratigraphic record and processes of turbidity current transformation across deep-marine lobes. *Sedimentology*, **64**, 1236–1273.
- Keevil, G.M., Peakall, J., Best, J.L. and Amos, K.J.** (2006) Flow structure in sinuous submarine channels: Velocity and turbulence structure of an experimental submarine channel. *Mar. Geol.*, **229**, 241–257.
- Kenyon, N.H., Millington, J., Droz, L. and Ivanov, M.K.** (1995) Scour holes in a channel-lobe transition zone on the Rhône Cone. *Atlas Deep Water Environ.*, 212–215.
- Kleverlaan, K.** (1987) Gordo megabed: a possible seismite in a tortonian submarine fan, tabernas basin, province almeria, southeast spain. *Sediment. Geol.*, **51**, 165–180.
- Kneller, B.** (1995) Beyond the turbidite paradigm: Physical models for deposition of turbidites and their implications for reservoir prediction. *Geol. Soc. Spec. Publ.*, **94**, 31–49.
- Kneller, B., Bozetti, G., Callow, R., Dykstra, M., Hansen, L., Kane, I., Li, P., McArthur, A., Catharina, A.S., Dos Santos, T. and Thompson, P.** (2020) Architecture, process, and environmental diversity in a late cretaceous slope channel system. *J. Sediment. Res.*, **90**, 1–26.
- Kneller, B., Edwards, D., McCaffrey, W. and Moore, R.** (1991) Oblique reflection of turbidity currents. *Geology*, **19**, 250–252.
- Kneller, B.C.** (2003) The influence of flow parameters on turbidite slope channel architecture. *Mar. Pet. Geol.*, **20**, 901–910.
- Kneller, B.C., Bennett, S.J. and McCaffrey, W.D.** (1997) Velocity and turbulence structure of density currents and internal solitary waves: Potential sediment transport and the formation of wave ripples in deep water. *Sediment. Geol.*, **112**, 235–250.
- Kneller, B.C., Bennett, S.J. and McCaffrey, W.D.** (1999) Velocity structure, turbulence and fluid stresses in experimental gravity currents. *J. Geophys. Res. Ocean.*, **104**, 5381–5391.
- Kneller, B.C. and Branney, M.J.** (1995) Sustained high-density turbidity currents and the deposition of thick massive sands. *Sedimentology*, **42**, 607–616.
- Kneller, B.C. and Buckee, C.** (2000) The structure and fluid mechanics of turbidity currents: A review of some recent studies and their geological implications. *Sedimentology*, **47**, 62–94.
- Kneller, B.C., Dykstra, M., Fairweather, L. and Milana, J.P.** (2016) Mass-transport and slope accommodation: implications for turbidite sandstone reservoirs. *Am. Assoc. Pet. Geol. Bull.*, **100**, 213–235.

- Kneller, B.C. and McCaffrey, W.D.** (2003) The interpretation of vertical sequences in turbidite beds: The influence of longitudinal flow structure. *J. Sediment. Res.*, **73**, 706–713.
- Kneller, B.C. and McCaffrey, W.D.** (1999) Depositional effects of flow nonuniformity and stratification within turbidity currents approaching a bounding slope: deflection, reflection, and facies variation. *J. Sediment. Res.*, **69**, 980–991.
- Könitzer, S.F., Davies, S.J., Stephenson, M.H. and Leng, M.J.** (2014) Depositional controls on mudstone lithofacies in a basinal setting: Implications for the delivery of sedimentary organic matter. *J. Sediment. Res.*, **84**, 198–214.
- Kremer, C.H., McHargue, T., Scheucher, L. and Graham, S.A.** (2018) Transversely-sourced mass-transport deposits and stratigraphic evolution of a foreland submarine channel system: Deep-water tertiary strata of the Austrian Molasse Basin. *Mar. Pet. Geol.*, **92**, 1–19.
- Kuenen, P.H.** (1966) Matrix of Turbidites: Experimental Approach. *Sedimentology*, **7**, 267–297.
- Labaume, P., Mutti, E. and Seguret, M.** (1987) Megaturbidites : A Depositional Model From the Eocene. *Geo-Marine Lett.*, **7**, 91–101.
- Lamb, M.P., Toniolo, H. and Parker, G.** (2006) Trapping of sustained turbidity currents by intraslope minibasins. *Sedimentology*, **53**, 147–160.
- Läuchli, C., Garcés, M., Beamud, E., Valero, L., Honegger, L., Adatte, T., Spangenberg, J.E., Clark, J., Puigdefàbregas, C., Fildani, A., de Kaenel, E., Hunger, T., Nowak, A. and Castelltort, S.** (2021) Magnetostratigraphy and stable isotope stratigraphy of the middle-Eocene succession of the Ainsa basin (Spain): New age constraints and implications for sediment delivery to the deep waters. *Mar Pet Geol.* doi: 10.1016/j.marpetgeo.2021.105182
- Leanza, H.A., Mazzini, A., Corfu, F., Llambías, E.J., Svensen, H., Planke, S. and Galland, O.** (2013) The Chachil Limestone (Pliensbachian-earliest Toarcian) Neuquén Basin, Argentina: U-Pb age calibration and its significance on the Early Jurassic evolution of southwestern Gondwana. *J. South Am. Earth Sci.*, **42**, 171–185.
- Lee, C., Nott, J.A., Keller, F.B. and Parrish, A.R.** (2004) Seismic expression of the cenozoic mass transport complexes deepwater Tarfaya-Agadir Basin offshore Morocco. *Proc. Annu. Offshore Technol. Conf.*, **3**, 1891–1908.
- Lee, H.J.** (2009) Timing of occurrence of large submarine landslides on the Atlantic Ocean margin. *Mar. Geol.*, **264**, 53–64.
- Legarreta, L.** (1991) Evolution of a Callovian-Oxfordian carbonate margin in the Neuquén Basin of west-central Argentina: facies, architecture, depositional sequences and global sea-level changes. *Sediment Geol.* doi: 10.1016/0037-0738(91)90142-Z
- Legarreta, L. and Gulisano, C.A.** (1989) Análisis estratigráfico secuencial de la Cuenca Neuquina (Triásico superior-Terciario inferior). In: *Cuencas sedimentarias argentinas.*, 221–243.
- Legarreta, L. and Uliana, M.A.** (1996) The Jurassic succession in west-central

- Argentina: Stratal patterns, sequences and paleogeographic evolution. *Palaeogeogr. Palaeoclimatol. Palaeoecol.*, **120**, 303–330.
- Legros, F.** (2002) Can dispersive pressure cause inverse grading in grain flows? *J. Sediment. Res.*, **72**, 166–170.
- Leppard, C.W. and Gawthorpe, R.L.** (2006) Sedimentology of rift climax deep water systems; Lower Rudeis Formation, Hammam Faraun Fault Block, Suez Rift, Egypt. *Sediment. Geol.*, **191**, 67–87.
- Lewis, K.B.** (1971) Slumping on a Continental Slope Inclined At 1°–4°. *Sedimentology*, **16**, 97–110.
- Liang, C., Xie, X., He, Y., Chen, H., Yu, X., Zhang, W., Mi, H., Lu, B., Tian, D., Zhang, H., Li, M. and Zhou, Z.** (2020) Multiple sediment sources and topographic changes controlled the depositional architecture of a palaeoslope-parallel canyon in the Qiongdongnan Basin, South China Sea. *Mar. Pet. Geol.*, **113**, 104161.
- Lien, T.** (2005) From rifting to drifting: Effects on the development of deep-water hydrocarbon reservoirs in a passive margin setting, Norwegian Sea.
- Liu, Q., Kneller, B., Fallgatter, C., Valdez Buso, V. and Milana, J.P.** (2018) Tabularity of individual turbidite beds controlled by flow efficiency and degree of confinement. *Sedimentology*, **65**, 2368–2387.
- Llambías, E.J. and Leanza, H.A.** (2005) Depósitos laháricos en la formación los molles en chacay melehue, neuquén: Evidencia de volcanismo jurásico en la cuenca neuquina. *Rev. la Asoc. Geol. Argentina*, **60**, 552–558.
- Llambías, E.J., Leanza, H.A. and Carbone, O.** (2007) Evolución Tectono-magmática durante el pérmico al Jurásico temprano en la Cordillera del Viento (37°05'S - 37°15'S): Nuevas evidencias geológicas y geoquímicas Del Inicio de la Cuencas Neuquina. *Rev. la Asoc. Geol. Argentina*, **62**, 217–235.
- Llambías, E.J., Quenardelle, S. and Montenegro, T.** (2003) The Choiyoi Group from central Argentina: A subalkaline transitional to alkaline association in the craton adjacent to the active margin of the Gondwana continent. *J. South Am. Earth Sci.*, **16**, 243–257.
- Lowe, D.R.** (1988) Suspended-load fallout rate as an independent variable in the analysis of current structures. *Sedimentology*, **35**, 765–776.
- Lowe, D.R.** (1982) Sediment gravity flows; II, Depositional models with special reference to the deposits of high-density turbidity currents. *J. Sediment. Res.*, **52**, 279–297.
- Lowe, D.R. and Guy, M.** (2000) Slurry-flow deposits in the Britannia Formation (Lower Cretaceous), North Sea: A new perspective on the turbidity current and debris flow problem. *Sedimentology*, **47**, 31–70.
- Lowe, D.R., Guy, M. and Palfrey, A.** (2003) Facies of slurry-flow deposits, Britannia Formation (Lower Cretaceous), North Sea: Implications for flow evolution and deposit geometry. *Sedimentology*, **50**, 45–80.
- Lucente, C.C. and Pini, G.A.** (2003) Anatomy and emplacement mechanism of a large

- submarine slide within a miocene foredeep in the Northern Apennines, Italy: A field perspective. *Am. J. Sci.*, **303**, 565–602.
- Macauley, R. V. and Hubbard, S.M.** (2013) Slope channel sedimentary processes and stratigraphic stacking, Cretaceous Tres Pasos Formation slope system, Chilean Patagonia. *Mar. Pet. Geol.*, **41**, 146–162.
- Macdonald, H.A., Peakall, J., Wignall, P.B. and Best, J.** (2011) Sedimentation in deep-sea lobe-elements: Implications for the origin of thickening-upward sequences. *J. Geol. Soc. London.*, **168**, 319–331.
- Machado, L.C.R.B. de C. modelo para heterogeneidades, Kowsmann, R.O., Almeida-Jr, W.D., Murakami, C.Y., Schreiner, S., Miller, D.J. and Piauilino, P.O. V.** (2004) Geometria da porção proximal do sistema deposicional turbidítico moderno da Formação Carapebus, de reservatório. *Bol. Geociências da Petrobras*, **12**, 287–315.
- Maier, K.L., Fildani, A., McHargue, T.R., Paull, C.K., Graham, S.A. and Caress, D.W.** (2012) Punctuated deep-water channel migration: High-resolution subsurface data from the Lucia Chica channel system, offshore California, U.S.A. *J. Sediment. Res.*, **82**, 1–8.
- Maier, K.L., Fildani, A., Paull, C.K., McHargue, T.R., Graham, S.A. and Caress, D.W.** (2013) Deep-sea channel evolution and stratigraphic architecture from inception to abandonment from high-resolution Autonomous Underwater Vehicle surveys offshore central California. *Sedimentology*, **60**, 935–960.
- Maier, K.L., Paull, C.K., Caress, D.W., Anderson, K., Nieminski, N.M., Lundsten, E., Erwin, B.E., Gwiazda, R. and Fildani, A.** (2020) Submarine-fan development revealed by integrated high-resolution datasets from La Jolla fan, offshore California, U.S.A. *J. Sediment. Res.*, **90**, 468–479.
- Maier, K.L., Roland, E.C., Walton, M.A.L., Conrad, J.E., Brothers, D.S., Dartnell, P. and Kluesner, J.W.** (2018) The tectonically controlled San Gabriel Channel-lobe transition zone, Catalina Basin, Southern California Borderland. *J. Sediment. Res.*, **88**, 942–959.
- Major, J.J. and Iverson, R.M.** (1999) Debris-flow deposition: Effects of pore-fluid pressure and friction concentrated at flow margins. *Bull. Geol. Soc. Am.*, **111**, 1424–1434.
- Manceda, R. and Figueroa, D.** (1995) Inversion of the Mesozoic Neuquen Rift in the Malague fold and thrust belt, Mendoza, Argentina. *Pet. basins South Am.*, **62**, 369–382.
- Mansor, H.E. and Amir Hassan, M.H.** (2021) Facies and bed type characteristics of channel-lobe transition deposits from the Oligocene-Miocene Tajau Sandstone Member, Kudat Formation, Sabah, Malaysia. *Geol. J.*, **56**, 5642–5672.
- Marchand, A.M.E., Apps, G., Li, W. and Rotzien, J.R.** (2015) Depositional processes and impact on reservoir quality in deepwater Paleogene reservoirs, US Gulf of Mexico. *Am. Assoc. Pet. Geol. Bull.*, **99**, 1635–1648.
- Marchand, A.M.E., Smalley, P.C., Haszeldine, R.S. and Fallick, A.E.** (2002) Note on the importance of hydrocarbon fill for reservoir quality prediction in sandstones.

- AA, **86**, 1561–1571.
- Marini, M., Milli, S., Ravnås, R. and Moscatelli, M.** (2015) A comparative study of confined vs. semi-confined turbidite lobes from the Lower Messinian Laga Basin (Central Apennines, Italy): Implications for assessment of reservoir architecture. *Mar. Pet. Geol.*, **63**, 142–165.
- Marr, J.G., Shanmugam, G. and Parker, G.** (2001) Experiments on subaqueous sandy gravity flows: The role of clay and water content in flow dynamics and depositional structures. *Bull. Geol. Soc. Am.*, **113**, 1377–1386.
- Martínez-Doñate, A., Privat, A.M.L.J., Hodgson, D.M., Jackson, C.A.L., Kane, I.A., Spychala, Y.T., Duller, R.A., Stevenson, C., Keavney, E., Schwarz, E. and Flint, S.S.** (2021) Substrate Entrainment, Depositional Relief, and Sediment Capture: Impact of a Submarine Landslide on Flow Process and Sediment Supply. *Front. Earth Sci.*, **9**, 1–23.
- Martinez, J.F., Cartwright, J. and Hall, B.** (2005) 3D seismic interpretation of slump complexes: Examples from the continental margin of Israel. *Basin Res.*, **17**, 83–108.
- Masalimova, L.U., Lowe, D.R., McHargue, T.I.M.O.T.H.Y. and Derksen, R.** (2015) Interplay between an axial channel belt, slope gullies and overbank deposition in the puchkirchen formation in the Molasse basin, Austria. *Sedimentology*, **62**, 1717–1748.
- Mayall, M., Jones, E. and Casey, M.** (2006) Turbidite channel reservoirs-Key elements in facies prediction and effective development. *Mar. Pet. Geol.*, **23**, 821–841.
- Mayall, M. and Stewart, I.** (2000) The architecture of turbidite slope channels. In: *Weimer, P., Slatt, R.M., Coleman, J., Rosen, N.C., Nelson, H., Bouma, A.H., Styzen, M.J., Lawrence, D.T. (Eds.), Deep-Water Reservoirs of the World: GCSSEPM Foundation 20th*,
- McArthur, A., Kane, I., Bozetti, G., Hansen, L. and Kneller, B.C.** (2019) Supercritical flows overspilling from bypass-dominated submarine channels and the development of overbank bedforms. *Depos. Rec.*, **6**, 21–40.
- McArthur, A.D., Hartley, A.J., Archer, S.G., Jolley, D.W. and Lawrence, H.M.** (2016) Spatiotemporal relationships of deep-marine, axial, and transverse depositional systems from the synrift Upper Jurassic of the central North Sea. *Am. Assoc. Pet. Geol. Bull.*, **100**, 1469–1500.
- McCaffrey, W. and Kneller, B.** (2001) Process controls on the development of stratigraphic trap potential on the margins of confined turbidite systems and aids to reservoir evaluation. *Am. Assoc. Pet. Geol. Bull.*, **85**, 971–988.
- McClelland, H.L.O., Woodcock, N.H. and Gladstone, C.** (2011) Eye and sheath folds in turbidite convolute lamination: Aberystwyth Grits Group, Wales. *J. Struct. Geol.*, **33**, 1140–1147.
- McGilvery, T.A. and Cook, D.L.** (2003) The Influence of Local Gradients on Accommodation Space and Linked Depositional Elements Across a Stepped Slope Profile, Offshore Brunei. Shelf Margin Deltas Linked Down Slope Pet. Syst. 23rd

- Annu. 387–419.
- McHargue, T., Pyrcz, M.J., Sullivan, M.D., Clark, J.D., Fildani, A., Romans, B.W., Covault, J.A., Levy, M., Posamentier, H.W. and Drinkwater, N.J.** (2011) Architecture of turbidite channel systems on the continental slope: Patterns and predictions. *Mar. Pet. Geol.*, **28**, 728–743.
- Menard, H.W.** (1955) Deep-Sea Channels, Topography, and Sedimentation. *Am. Assoc. Pet. Geol. Bull.*, **39**, 236–255.
- Middleton, G. V.** (1993) Sediment deposition from turbidity currents. *Annu. Rev. Earth Planet. Sci.*, **21**, 89–114.
- Middleton, G. V.** (1966a) Experiments on density and turbidity currents: I. Motion of the head. *Can. J. Earth Sci.*, **4**, 523–546.
- Middleton, G. V.** (1966b) Experiments on Density and Turbidity Currents: II. Uniform Flow of Density Currents. *Can. J. Earth Sci.*, **3**, 627–637.
- Middleton, G. V. and Hampton, M. a.** (1973) Sediment gravity flows: mechanics of flow and deposition. In: *Turbidity and Deep Water Sedimentation* (Ed. G.V. Middleton and A.H. Bouma), *SEPM, Pacific Section, Short Course Lecture Notes*, 1–38.
- Middleton, G. V. and Neal, W.J.** (1989) Experiments on the thickness of beds deposited by turbidity currents. *J. Sediment. Petrol.*, **59**, 297–307.
- Migeon, S., Ceramicola, S., Praeg, D., Ducassou, E., Dano, A., Ketzer, J.M., Mary, F. and Mascle, J.** (2014) Post-failure Processes on the Continental Slope of the Central Nile Deep-Sea Fan: Interactions Between Fluid Seepage, Sediment Deformation and Sediment-Wave Construction. In: *Submarine Mass Movements and Their Consequences. Advances in Natural and Technological Hazards Research, vol 37*. Springer, Cham. https://doi.org/10.1007/978-3-319-00972-8_11, 201–212.
- Mignard, S., Mulder, T., Martinez, P. and Garlan, T.** (2019) The Ogooue Fan (offshore Gabon): A modern example of deep-sea fan on a complex slope profile. *Solid Earth*, **10**, 851–869.
- Millington, J.J. and Clark, J.D.** (1995) The Charo/Arro canyon-mouth sheet system, south-central Pyrenees, Spain: a structurally influenced zone of sediment dispersal. *J. Sediment. Res. B Stratigr. Glob. Stud.*, 443–454.
- Mohrig, D., Whipple, K.X., Hondzo, M., Ellis, C. and Parker, G.** (1998) Hydroplaning of subaqueous debris flows. *Bull. Geol. Soc. Am.*, **110**, 387–394.
- Monnier, D., Imbert, P., Gay, A., Mourgues, R. and Lopez, M.** (2014) Pliocene sand injectites from a submarine lobe fringe during hydrocarbon migration and salt diapirism: A seismic example from the Lower Congo Basin. *Geofluids*, **14**, 1–19.
- Morris, E.A., Hodgson, D.M., Brunt, R.L. and Flint, S.S.** (2014a) Origin, evolution and anatomy of silt-prone submarine external levées. *Sedimentology*, **61**, 1734–1763.
- Morris, E.A., Hodgson, D.M., Flint, S.S., Brunt, R.L., Butterworth, P.J. and Verhaeghe, J.** (2014b) Sedimentology, stratigraphic architecture, and depositional

- context of submarine frontal-lobe complexes. *J. Sediment. Res.*, **84**, 763–780.
- Morris, S.A., Kenyon, N.H., Limonov, A.F. and Alexander, J.** (1998) Downstream changes of large-scale bed forms in turbidites around the Valencia channel mouth, north-west Mediterranean: Implications for palaeoflow reconstruction. *Sedimentology*, **45**, 365–377.
- Moscardelli, L. and Wood, L.** (2008) New classification system for mass transport complexes in offshore Trinidad. 73–98.
- Moscardelli, L., Wood, L. and Mann, P.** (2006) Mass-transport complexes and associated processes in the offshore area of Trinidad and Venezuela. *Am. Assoc. Pet. Geol. Bull.*, **90**, 1059–1088.
- Mueller, P., Patacci, M. and Di Giulio, A.** (2021) Hybrid event bed distribution in a mixed siliciclastic-calcareous turbidite succession: A cross-current perspective from the Bordighera Sandstone, Ligurian Alps, NW Italy. *Ital. J. Geosci.*, **140**, 255–274.
- Mulder, T. and Alexander, J.** (2001a) The physical character of subaqueous sedimentary density flows and their deposits. *Sedimentology*, **48**, 269–299.
- Mulder, T. and Alexander, J.** (2001b) The physical character of subaqueous sedimentary density flow and their deposits. *Sedimentology*, **48**, 269–299.
- Mulder, T. and Etienne, S.** (2010) Lobes in deep-sea turbidite systems: State of the art. *Sediment. Geol.*, **229**, 75–80.
- Muñoz, J.A.** (2002) The Pyrenees. In: *The Geology of Spain* (Ed. W. Gibbons and T. Moreno), *Geological Society, London*, 370–385.
- Muñoz, J.A., Beamud, E., Fernández, O., Arbués, P., Dinarès-Turell, J. and Poblet, J.** (2013) The Ainsa Fold and thrust oblique zone of the central Pyrenees: Kinematics of a curved contractional system from paleomagnetic and structural data. *Tectonics*, **32**, 1142–1175.
- Mutti, E.** (1977) Distinctive thin-bedded turbidite facies and related depositional environments in the Eocene Hecho Group (South-central Pyrenees, Spain). *Sedimentology*, **24**, 107–131.
- Mutti, E., Luterbacher, H.P., Ferrer, J. and Rosell, J.** (1972) Schema stratigrafico e lineamenti di facies del Paleogene marino della zona centrale sudpirenaica tra temp (Catalogna) e Pamplona (Navarra). *Mem. della Soc. Geol. Ital.*, **11**, 391–416.
- Mutti, E. and Normark, W.R.** (1991) An integrated approach to the study of turbidite systems. In: *Seismic facies and sedimentary processes of submarine fans and turbidite systems*, Springer, New York, NY., 75–106.
- Mutti, E. and Normark, W.R.** (1987) Comparing Examples of Modern and Ancient Turbidite Systems: Problems and Concepts. *Mar. Clastic Sedimentol.*, 1–38.
- Mutti, E. and Sonnino, M.** (1981) Compensation cycles: a diagnostic feature of turbidite sandstone lobes. In: *International Association of Sedimentologists—European regional meeting.*, 120–123.
- Muzzi Magalhaes, P. and Tinterri, R.** (2010) Stratigraphy and depositional setting of slurry and contained (reflected) beds in the Marnosoarenacea Formation

- (LanghianSerravallian) Northern Apennines, Italy. *Sedimentology*, **57**, 1685–1720.
- Nardin, T.R., Hein, F.J., Gorsline, D.S. and Edwards, B.D.** (1979) A review of mass movement processes, sediment and acoustic characteristics, and contrasts in slope and base-of-slope systems versus canyon- fan- basin floor systems. *Geol. Cont. slopes*, 61–73.
- Navarro, L. and Arnott, R.W.C.** (2020) Stratigraphic record in the transition from basin floor to continental slope sedimentation in the ancient passive-margin Windermere turbidite system. *Sedimentology*, **67**, 1710–1749.
- Nichols, G.** (2009) *Sedimentology and Stratigraphy*.
- Nijman, W.** (1998) Cyclicity and basin axis shift in a piggybank basin: towards modelling of the Eocene Tresp-Ager Basin, South Pyrenees, Spain. 135–162 pp.
- Nisbet, E.G. and Piper, D.J.W.** (1998) Giant submarine landslides. *Nature*, **392**, 329–330.
- Nittrouer, C.A. and Wright, L.D.** (1994) Transport of particles across continental shelves. *Rev. Geophys.*, **32**, 85–113.
- Normark, W.R.** (1970) Growth patterns of deep- sea fans. *Am. Assoc. Pet. Geol. Bull.*, **54**, 2170–2195.
- Normark, W.R.** (1978) Fan Valleys, Channels, and Depositional Lobes on Modern Submarine Fans: Characters for Recognition of Sandy Turbidite Environments. *Am. Assoc. Pet. Geol. Bull.*, **62**, 912–931.
- Nugraha, H.D., Jackson, C.A.L., Johnson, H.D., Hodgson, D.M. and Clare, M.** How erosive are submarine landslides?
- Nwoko, J., Kane, I. and Huuse, M.** (2020a) Megaclasts within mass-transport deposits: Their origin, characteristics and effect on substrates and succeeding flows. *Geol. Soc. Spec. Publ.*, **500**, 515–530.
- Nwoko, J., Kane, I. and Huuse, M.** (2020b) Mass transport deposit (MTD) relief as a control on post-MTD sedimentation: Insights from the Taranaki Basin, offshore New Zealand. *Mar. Pet. Geol.*, **120**, 104489.
- Ogata, K., Festa, A., Pini, G.A. and Alonso, J.L.** (2019) Submarine landslide deposits in orogenic belts: olistostromes and sedimentary mélanges. In: *Submarine Landslides: Subaqueous Mass Transport Deposits from Outcrops to Seismic Profiles*, 1–26.
- Ogata, K., Mountjoy, J.J., Pini, G.A., Festa, A. and Tinterri, R.** (2014a) Shear zone liquefaction in mass transport deposit emplacement: A multi-scale integration of seismic reflection and outcrop data. *Mar. Geol.*, **356**, 50–64.
- Ogata, K., Mutti, E., Pini, G.A. and Tinterri, R.** (2012) Mass transport-related stratal disruption within sedimentary mélanges: Examples from the northern Apennines (Italy) and south-central Pyrenees (Spain). *Tectonophysics*, **568–569**, 185–199.
- Ogata, K., Pogačnik, Z., Pini, G.A., Tunis, G., Festa, A., Camerlenghi, A. and Rebesco, M.** (2014b) The carbonate mass transport deposits of the Paleogene Friuli Basin (Italy/Slovenia): Internal anatomy and inferred genetic processes. *Mar. Geol.*, **356**, 88–110.

- Oluboyo, A.P., Gawthorpe, R.L., Bakke, K. and Hadler-Jacobsen, F.** (2014) Salt tectonic controls on deep-water turbidite depositional systems: Miocene, southwestern Lower Congo Basin, offshore Angola. *Basin Res.*, **26**, 597–620.
- Ortiz-Karpf, A., Hodgson, D.M., Jackson, C.A.-L. and McCaffrey, W.D.** (2017) Influence of Seabed Morphology and Substrate Composition On Mass-Transport Flow Processes and Pathways: Insights From the Magdalena Fan, Offshore Colombia. *J. Sediment. Res.*, **87**, 189–209.
- Ortiz-Karpf, A., Hodgson, D.M. and McCaffrey, W.D.** (2015) The role of mass-transport complexes in controlling channel avulsion and the subsequent sediment dispersal patterns on an active margin: The Magdalena Fan, offshore Colombia. *Mar. Pet. Geol.*, **64**, 58–75.
- Owen, G.** (1987) Deformation processes in unconsolidated sands. *Geol. Soc. Spec. Publ.*, **29**, 11–24.
- Owen, G.** (2003) Load structures: Gravity-driven sediment mobilization in the shallow subsurface. *Geol. Soc. Spec. Publ.*, **216**, 21–34.
- Pángaro, F., Pereira, D.M. and Micucci, E.** (2009) El sinrift de la dorsal de Huincul, Cuenca Neuquina: Evolución y control sobre la estratigrafía y estructura del área. *Rev. la Asoc. Geol. Argentina*, **65**, 265–277.
- Patacci, M., Haughton, P.D.W. and McCaffrey, W.D.** (2014) Rheological complexity in sediment gravity flows forced to decelerate against a confining slope, Braux, SE France. *J. Sediment. Res.*, **84**, 270–277.
- Paull, C.K., McGann, M., Sumner, E.J., Barnes, P.M., Lundsten, E.M., Anderson, K., Gwiazda, R., Edwards, B. and Caress, D.W.** (2014) Sub-decadal turbidite frequency during the early Holocene: Eel Fan, offshore northern California. *Geology*, **42**, 855–858.
- Paull, C.K., Mitts, P., Ussler, W., Keaten, R. and Greene, H.G.** (2005) Trail of sand in upper Monterey Canyon: Offshore California. *Bull. Geol. Soc. Am.*, **117**, 1134–1145.
- Paull, C.K., Talling, P.J., Maier, K.L., Parsons, D., Xu, J., Caress, D.W., Gwiazda, R., Lundsten, E.M., Anderson, K., Barry, J.P., Chaffey, M., O'Reilly, T., Rosenberger, K.J., Gales, J.A., Kieft, B., McGann, M., Simmons, S.M., McCann, M., Sumner, E.J., Clare, M.A. and Cartigny, M.J.** (2018) Powerful turbidity currents driven by dense basal layers. *Nat. Commun.*, **9**, 1–9.
- Payros, A. and Pujalte, V.** (2019) Eocene Mass-Transport Deposits in the Basque Basin (Western Pyrenees, Spain). 155–170.
- Payros, A., Pujalte, V. and Orue-Etxebarria, X.** (1999) The South Pyrenean Eocene carbonate megabreccias revisited: New interpretation based on evidence from the Pamplona Basin. *Sediment. Geol.*, **125**, 165–194.
- Payros, A., Tosquella, J., Bernaola, G., Dinarès-Turell, J., Orue-Etxebarria, X. and Pujalte, V.** (2009) Filling the North European Early/Middle Eocene (Ypresian/Lutetian) boundary gap: Insights from the Pyrenean continental to deep-marine record. *Palaeogeogr. Palaeoclimatol. Palaeoecol.*, **280**, 313–332.
- Peakall, J., Best, J., Baas, J.H., Hodgson, D.M., Clare, M.A., Talling, P.J., Dorrell,**

- R.M. and Lee, D.R.** (2020) An integrated process-based model of flutes and tool marks in deep-water environments: Implications for palaeohydraulics, the Bouma sequence and hybrid event beds. *Sedimentology*, **67**, 1601–1666.
- Peakall, J., McCaffrey, B. and Kneller, B.** (2000) A process model for the evolution, morphology, and architecture of sinuous submarine channels. *J. Sediment. Res.*, **70**, 434–448.
- Pelinovsky, E. and Poplavsky, A.** (1996) Simplified model of tsunami generation by submarine landslides. *Phys. Chem. Earth*, **21**, 13–17.
- Pemberton, E.A.L., Hubbard, S.M., Fildani, A., Romans, B. and Stright, L.** (2016) The stratigraphic expression of decreasing confinement along a deep-water sediment routing system: Outcrop example from southern Chile. *Geosphere*, **12**, 114–134.
- Pettijohn, F.J., Potter, P.E. and Siever, R.** (1972) Petrographic Classification and Glossary. In: *Sand and Sandstone. Springer Study Edition. Springer, New York, NY., Springer Science & Business Media.*, 512.
- Pickering, K.T. and Bayliss, N.J.** (2009) Deconvolving tectono-climatic signals in deep-marine siliciclastics, Eocene Ainsa basin, Spanish Pyrenees: Seesaw tectonics versus eustasy. *Geology*, **37**, 203–206.
- Pickering, K.T. and Corregidor, J.** (2005) Mass-transport complexes (MTCs) and tectonic control on basin-floor submarine fans, middle Eocene, South Spanish Pyrenees. *J. Sediment. Res.*, **75**, 761–783.
- Pickering, K.T. and Hilton, V.C.** (1998) Turbidite systems of southeast France: application to hydrocarbon prospectivity. Vallis Press.
- Pickering, K.T. and Hiscott, R.N.** (1989) Contained (reflected) turbidity currents from the Middle Ordovician Cloridorme Formation, Quebec, Canada: an alternative to the antidune hypothesis. *Sedimentology*, **32**, 373–394.
- Pickering, K.T., Hodgson, D.M., Platzman, E., Clark, J.D. and Stephens, C.** (2001) A new type of bedform produced by backfilling processes in a submarine channel, late miocene, Tabernas-Sorbas Basin, se Spain. *J. Sediment. Res.*, **71**, 692–704.
- Picot, M., Droz, L., Marsset, T., Dennielou, B. and Bez, M.** (2016) Controls on turbidite sedimentation: Insights from a quantitative approach of submarine channel and lobe architecture (Late Quaternary Congo Fan). *Mar. Pet. Geol.*, **72**, 423–446.
- Piper, D.J.W., Hiscott, R.N. and Normark, W.R.** (1999) Outcrop-scale acoustic facies analysis and latest Quaternary development of Hueneme and Dume submarine fans, offshore California. *Sedimentology*, **46**, 47–78.
- Piper, D.J.W. and Normark, W.R.** (2009) Processes that initiate turbidity currents and their influence on turbidites: A marine geology perspective. *J. Sediment. Res.*, **79**, 347–362.
- Piper, D.J.W. and Normark, W.R.** (1983) Turbidite depositional patterns and flow characteristics, Navy submarine fan, California Borderland. *Sedimentology*, **30**, 681–694.

- Piper, D.J.W. and Normark, W.R.** (2001) Sandy fans—from Amazon to Hueneme and beyond. *Am. Assoc. Pet. Geol. Bull.*, **85**, 1407–1438.
- Piper, D.J.W., Pirmez, C., Manley, P.L., Long, D., Flood, R.D., Normark, W.R. and Showers, W.** (1997) Mass-transport deposits of the Amazon Fan. Proc Ocean Drill Program, 155 Sci Results. doi: 10.2973/odp.proc.sr.155.212.1997
- Piper, D.J.W., Shor, A.N. and Hughes Clarke, J.E.** (1988) The 1929 Grand Banks earthquake, slump, and turbidity current. *Spec. Pap. Geol. Soc. Am.*, **229**, 77–92.
- Pirmez, C., Beaubouef, R., Friedmann, S. and Mohrig, D.** (2000) Equilibrium profile and baselevel in submarine channels: examples from Late Pleistocene systems and implications for the architecture of deepwater reservoirs.
- Poblet, J., Muñoz, J.A., Travé, A. and Serra-Kiel, J.** (1998) Quantifying the kinematics of detachment folds using three-dimensional geometry: Application to the Mediano anticline (Pyrenees, Spain). *Bull. Geol. Soc. Am.*, **110**, 111–125.
- Pohl, F., Eggenhuisen, J.T., Cartigny, M.J.B., Tilston, M.C., de Leeuw, J. and Hermidas, N.** (2020) The influence of a slope break on turbidite deposits: An experimental investigation. *Mar Geol.* doi: 10.1016/j.margeo.2020.106160
- Pohl, F., Eggenhuisen, J.T., Tilston, M. and Cartigny, M.J.B.** (2019) New flow relaxation mechanism explains scour fields at the end of submarine channels. *Nat. Commun.*, **10**, 1–8.
- Pohl, F. and Mccann, T.** (2014) Architecture and depositional development of the Eocene deep-marine Morillo and Coscojuela Formations, Aínsa Basin, Spain. *Geol. J.*, **49**, 221–238.
- Pope, E.L., Cartigny, M.J., Clare, M.A., Talling, P.J., Lintern, D.G., Vellinga, A., ... and Vendettuoli, D. O.** (2022) First source-to-sink monitoring shows dense head controls sediment flux and runout in turbidity currents.
- Porten, K.W., Kane, I.A., Warchol, M.J. and Southern, S.J.** (2016) A sedimentological process-based approach to depositional reservoir quality of deep-marine sandstones: An example from the springar formation, northwestern Vøring Basin, Norwegian Sea. *J. Sediment. Res.*, **86**, 1269–1286.
- Posamentier, H. and Martinsen, O.** (2011) The character and genesis of submarine mass-transport deposits: insights from outcrop and 3D seismic data. In: *Mass-transport deposits in deepwater settings.*, *SEPM, Special Publication*, 7–38.
- Posamentier, H.W.** (2003) Depositional elements associated with a basin floor channel-levee system: Case study from the Gulf of Mexico. *Mar. Pet. Geol.*, **20**, 677–690.
- Posamentier, H.W. and Kolla, V.** (2003) Seismic geomorphology and stratigraphy of depositional elements in deep-water settings. *J. Sediment. Res.*, **73**, 367–388.
- Posamentier, H.W. and Walker, R.G.** (2006) Deep-Water Turbidites and Submarine Fans. In: *Facies Models Revisited*, *SEPM Special Publication*, 399–520.
- Postma, G., Cartigny, M. and Kleverlaan, K.** (2009) Structureless, coarse-tail graded Bouma Ta formed by internal hydraulic jump of the turbidity current? *Sediment. Geol.*, **219**, 1–6.

- Poyatos-Moré, M.** (2014) Physical Stratigraphy and Facies Analysis of the Castissent Tecto-Sedimentary Unit. Universitat Autònoma de Barcelona.
- Praeg, D., Ketzer, J.M., Adolpho Herbert, A., Migeon, S., Ceramicola, S., Alexandre, D., Emmanuelle, Ducassou Stéphanie, D., Jean, M. and Rodrigues, L.F.** (2014) Fluid seepage in relation to seabed deformation on the central Nile deep-sea fan, part 2: evidence from multibeam and sidescan imagery. In: *Submarine Mass Movements and Their Consequences. Advances in Natural and Technological Hazards Research. 6th International Symposium. Volume 37*. https://doi.org/10.1007/978-3-319-00972-8_11, 37, 141–150.
- Prather, B.E., Booth, J.R., Steffens, G.S. and Craig, P.A.** (1998) Classification, lithologic calibration, and stratigraphic succession of seismic facies of intraslope basins, deep-water Gulf of Mexico. *Am. Assoc. Pet. Geol. Bull.*, **82**, 701–728.
- Prather, B.E., Keller, F.B. and Chapin, M.A.** (2000) Hierarchy of Deep-Water Architectural Elements With Reference to Seismic Resolution: Implications for Reservoir Prediction and Modeling. *Deep. Reserv. World 20th Annu.*, 817–835.
- Prather, B.E., O’Byrne, C., Pirmez, C. and Sylvester, Z.** (2017) Sediment partitioning, continental slopes and base-of-slope systems. *Basin Res.*, **29**, 394–416.
- Prather, B.E., Pirmez, C., Sylvester, Z. and Prather, D.S.** (2012) Stratigraphic Response to Evolving Geomorphology in a Submarine Apron Perched on the Upper Niger Delta Slope. In: *Application of the Principles of Seismic Geomorphology to Continental-Slope and Base-of-Slope Systems: Case Studies from Seafloor and Near-Seafloor Analogues*, 145–161.
- Pratson, L.F. and Coakley, B.J.** (1996) A model for the headward erosion of submarine canyons induced by downslope-eroding sediment flows. *Bull. Geol. Soc. Am.*, **108**, 225–234.
- Pratson, L.F., Ryan, W.B.F., Mountain, G.S. and Twichell, D.C.** (1994) Submarine canyon initiation by downslope-eroding sediment flows: evidence in late Cenozoic strata on the New Jersey continental slope. *Geol. Soc. Am. Bull.*, **106**, 395–412.
- Prélat, A., Covault, J.A., Hodgson, D.M., Fildani, A. and Flint, S.S.** (2010) Intrinsic controls on the range of volumes, morphologies, and dimensions of submarine lobes. *Sediment. Geol.*, **232**, 66–76.
- Prélat, A., Hodgson, D.M. and Flint, S.S.** (2009) Evolution, architecture and hierarchy of distributary deep-water deposits: a high-resolution outcrop investigation from the Permian Karoo Basin, South Africa. *Sedimentology*, **56**, 2132–2154.
- Prins, M.A. and Postma, G.** (2000) Effects of climate, sea level, and tectonics unraveled for last deglaciation turbidite records of the Arabian Sea. *Geology*, **28**, 375–378.
- Privat, A.M.J., Hodgson, D.M., Jackson, C.A., Schwarz, E. and Peakall, J.** (2021) Evolution from syn-rift carbonates to early post-rift deep-marine intraslope lobes: The role of rift basin physiography on sedimentation patterns. *Sedimentology*, 0–2.
- Prosser, S.** (1993) Rift-related linked depositional systems and their seismic expression. *Geol. Soc. Spec. Publ.*, **71**, 35–66.

- Puigdefàbregas, C. and Souquet, P.** (1986) Tecto-sedimentary cycles and depositional sequences of the Mesozoic and Tertiary from the Pyrenees. *Tectonophysics*, **129**, 173–203.
- Ravnås, R. and Steel, R.J.** (1998) Architecture of marine rift-basin successions. *Am. Assoc. Pet. Geol. Bull.*, **82**, 110–146.
- Riccardi, A. and Kamo, S.** (2014) Biostratigraphy and Geochronology of the Pliensbachian-Toarcian Boundary in Argentina. *XIX Congr. Geológico Argentino, Junio 2014, Córdoba, Actas T1-4*, 9–11.
- Riccardi, A.C.** (2008) The marine Jurassic of Argentina: A biostratigraphic framework. *Episodes*, **31**, 326–335.
- Riccardi, A.C., Damborenea, S.E., Manceñido, M.O. and Leanza, H.A.** (2011) Megainvertebrados del Jurásico y su importancia geobiológica. *Relat. del XVIII Congr. Geológico Argentino, Neuquén*, 441–464.
- Richardson, S.E.J., Davies, R.J., Allen, M.B. and Grant, S.F.** (2011) Structure and evolution of mass transport deposits in the South Caspian Basin, Azerbaijan. *Basin Res.*, **23**, 702–719.
- Rosenbaum, G., Lister, G.S. and Duboz, C.** (2002) Relative motions of Africa, Iberia and Europe during Alpine orogeny. *Tectonophysics*, **359**, 117–129.
- Rosenfeld, U. and Volldaeimer, W.** (1980) Turbidite und andere Rhythmite im tieferen Jura des Neuquén-Beckens (Argentinien). 379–421.
- Ross, W.C., Halliwell, B.A., May, J.A., Watts, D.E. and Syvitski, J.P.M.** (1994) Slope readjustment: a new model for the development of submarine fans and aprons. *Geology*, **22**, 511–514.
- Samuel, A., Kneller, B., Raslan, S., Sharp, A. and Parsons, C.** (2003) Prolific deep-marine slope channels of the Nile Delta, Egypt. *Am. Assoc. Pet. Geol. Bull.*, **87**, 541–560.
- Sawyer, D.E., Flemings, P.B., Dugan, B. and Germaine, J.T.** (2009) Retrogressive failures recorded in mass transport deposits in the Ursa Basin, Northern Gulf of Mexico. *J. Geophys. Res. Solid Earth*, **114**, 1–20.
- Sawyer, D.E., Flemings, P.B. and Nikolinakou, M.** (2014) Continuous deep-seated slope failure recycles sediments and limits levee height in submarine channels. *Geology*, **42**, 15–18.
- Sawyer, D.E., Flemings, P.B., Shipp, R.C. and Winker, C.D.** (2007) Seismic geomorphology, lithology, and evolution of the late Pleistocene Mars-Ursa turbidite region, Mississippi Canyon area, northern Gulf of Mexico. *Am. Assoc. Pet. Geol. Bull.*, **91**, 215–234.
- Scotchman, J.I., Bown, P., Pickering, K.T., BouDagher-Fadel, M., Bayliss, N.J. and Robinson, S.A.** (2015a) A new age model for the middle Eocene deep-marine Ainsa Basin, Spanish Pyrenees. *Earth-Science Rev.*, **144**, 10–22.
- Scotchman, J.I., Pickering, K.T., Sutcliffe, C., Dakin, N. and Armstrong, E.** (2015b) Milankovitch cyclicity within the middle eocene deep-marine guaso system, Ainsa Basin, Spanish Pyrenees. *Earth-Science Rev.*, **144**, 107–121.

- Scott, A., Hurst, A. and Vigorito, M.** (2013) Outcrop-based reservoir characterization of a kilometer-scale sand-injectite complex. *Am. Assoc. Pet. Geol. Bull.*, **97**, 309–343.
- Sequeiros, O.E.** (2012) Estimating turbidity current conditions from channel morphology: A Froude number approach. *J. Geophys. Res. Ocean.*, **117**, 1–19.
- Sequeiros, O.E., Mosquera, R. and Pedocchi, F.** (2018) Internal Structure of a Self-Accelerating Turbidity Current. *J. Geophys. Res. Ocean.*, **123**, 6260–6276.
- Sequeiros, O.E., Naruse, H., Endo, N., Garcia, M.H. and Parker, G.** (2009) Experimental study on self-accelerating turbidity currents. *J. Geophys. Res. Ocean.*, **114**, 1–26.
- Shanmugam, G.** (1996) High-density turbidity currents; are they sandy debris flows? *J. Sediment. Res.*, **66**, 2–10.
- Shanmugam, G.** (2006) Deep-water processes and facies models: Implications for sandstone petroleum reservoirs. *Elsevier*.
- Shanmugam, G. and Moiola, R.J.** (1988) Submarine fans: Characteristics, models, classification, and reservoir potential. *Earth Sci. Rev.*, **24**, 383–428.
- Shanmugam, G. and Moiola, R.J.** (1995) Reinterpretation of depositional processes in a classic flysch sequence (Pennsylvanian Jackfork Group), Ouachita Mountains, Arkansas and Oklahoma. *Am. Assoc. Pet. Geol. Bull.*, **79**, 672–695.
- Shanmugam, G. and Moiola, R.J.** (1991) Types of submarine fan lobes: models and implications. *Am. Assoc. Pet. Geol. Bull.* **75**:156–179.
- Simpson, J.E.** (1999) Gravity currents: In the environment and the laboratory. *Cambridge University Press*.
- Simpson, J.E.** (1969) A comparison between laboratory and atmospheric density currents. *Q. J. R. Meteorol. Soc.*, **95**, 758–765.
- Simpson, J.E. and Britter, R.E.** (1979) The dynamics of the head of a gravity current advancing over a horizontal surface. *J. Fluid Mech.*, **94**, 477–495.
- Sinclair, H.D.** (2000) Delta-fed turbidites infilling topographically complex basins: A new depositional model for the Annot sandstones, SE France. *J. Sediment. Res.*, **70**, 504–519.
- Sinclair, H.D.** (1994) The influence of lateral basinal slopes on turbidite sedimentation in the Annot sandstones of SE France. *J. Sediment. Res.*, **64**, 42–54.
- Sinclair, H.D. and Tomasso, M.** (2002) Depositional evolution of confined turbidite basins. *J. Sediment. Res.*, **72**, 451–456.
- Skene, K.I., Piper, D.J.W. and Hill, P.S.** (2002) Quantitative analysis of variations in depositional sequence thickness from submarine channel levees. *Sedimentology*, **49**, 1411–1430.
- Smith, R.** (2004a) Turbidite systems influenced by structurally induced topography in the multi-sourced Welsh Basin. *Geol. Soc. Spec. Publ.*, **222**, 209–228.
- Smith, R.** (2004b) Silled sub-basins to connected tortuous corridors: Sediment

- distribution systems on topographically complex sub-aqueous slopes. *Geol. Soc. Spec. Publ.*, **222**, 23–43.
- Smith, R. and Joseph, P.** (2004) Onlap stratal architectures in the Grès d'Annot: Geometric models and controlling factors. *Geol. Soc. Spec. Publ.*, **221**, 389–399.
- Sobiesiak, M.S., Alsop, G.I., Kneller, B. and Milana, J.P.** (2017) Sub-seismic scale folding and thrusting within an exposed mass transport deposit: A case study from NW Argentina. *J. Struct. Geol.*, **96**, 176–191.
- Sobiesiak, M.S., Kneller, B., Alsop, G.I. and Milana, J.P.** (2018) Styles of basal interaction beneath mass transport deposits. *Mar. Pet. Geol.*, **98**, 629–639.
- Sobiesiak, M.S., Kneller, B., Alsop, G.I. and Milana, J.P.** (2016) Internal deformation and kinematic indicators within a tripartite mass transport deposit, NW Argentina. *Sediment. Geol.*, **344**, 364–381.
- Sohn** (1997) On traction-carpet sedimentation. *J. Sediment. Res.*, **67**, no **3**, 502–509.
- Sohn, Y.K.** (1995) Traction-Carpet Stratification in Turbidites--Fact or Fiction?: DISCUSSION.
- Sømme, T.O., Helland-hansen, W., Martinsen, J. and Thurmond, J.B.** (2009) Relationships between morphological and sedimentological parameters in source-to-sink systems: a basis for predicting semi-quantitative characteristics in subsurface systems. *Basin Res.*, **21**, 361–387.
- Southard, J.B.** (1991) Experimental determination of bed-form stability. *Annu. Rev. Earth Planet. Sci.*, **19**, 423.
- Southard, J.B. and Boguchwal, L.A.** (1990) Bed configuration in steady unidirectional water flows; Part 2, Synthesis of flume data. *J. Sediment. Res.*, **60**, 658–679.
- Southern, S.J., Kane, I.A., Warchol, M.J., Porten, K.W. and McCaffrey, W.D.** (2017) Hybrid event beds dominated by transitional-flow facies: Character, distribution and significance in the maastrichtian springar formation, north-west vøring basin, Norwegian Sea. 747–776 pp.
- Southern, S.J., Patacci, M., Felletti, F. and McCaffrey, W.D.** (2015) Influence of flow containment and substrate entrainment upon sandy hybrid event beds containing a co-genetic mud-clast-rich division. *Sediment. Geol.*, **321**, 105–122.
- Soutter, E.L., Bell, D., Cumberpatch, Z.A., Ferguson, R.A., Sychala, Y.T., Kane, I.A. and Eggenhuisen, J.T.** (2021) The Influence of Confining Topography Orientation on Experimental Turbidity Currents and Geological Implications. *Front Earth Sci.* doi: 10.3389/feart.2020.540633
- Soutter, E.L., Kane, I.A., Fuhrmann, A., Cumberpatch, Z.A. and Huuse, M.** (2019) The stratigraphic evolution of onlap in siliciclastic deep-water systems: Autogenic modulation of allogenic signals. *J. Sediment. Res.*, **89**, 890–917.
- Soutter, E.L., Kane, I.A. and Huuse, M.** (2018) Giant submarine landslide triggered by Paleocene mantle plume activity in the North Atlantic. *Geology*, **46**, 511–514.
- Soutter, E.L., Kane, I.A., Martinez-Doñate, A., Boyce, A., Stacey, J. and Castellort, S.** (2022) The Eocene-Oligocene climate transition in the Alpine foreland basin: Paleoenvironmental change recorded in submarine fans.

- Palaeogeogr. Palaeoclimatol. Palaeoecol.*, **600**, 111064.
- Spalletti, L.A., Parent, H., Veiga, G.D. and Schwarz, E.** (2012) Amonites y bioestratigrafía del Grupo Cuyo en la Sierra de Reyes (cuenca Neuquina central, Argentina) y su significado secuencial. *Andean Geol.*, **39**, 464–481.
- Sprague, A., Garfield, T., Goulding, F., Beaubouef, R., Sullivan, M., Rossen, C., Champion, K., Sickafoose, D., Abreu, D., Schellpeper, M., Jensen, G., Jennette, D., Pirmez, C., Dixon, B., Ying, D., Ardill, J., Mohrig, D., Porter, M., Farrell, M. and Mellere, D.** (2005) Integrated slope channel depositional models: the key to successful prediction of reservoir presence and quality in offshore West Africa. *CIPM, cuarto E- ...*, **17**, 1–13.
- Spychala, Y., Hodgson, D. and Lee, D.** (2017a) Autogenic controls on hybrid bed distribution in submarine lobe complexes. *Mar. Pet. Geol.*, **88**, 1078–1093.
- Spychala, Y.T., Hodgson, D.M., Flint, S.S. and Mountney, N.P.** (2015) Constraining the sedimentology and stratigraphy of submarine intraslope lobe deposits using exhumed examples from the Karoo Basin, South Africa. *Sediment. Geol.*, **322**, 67–81.
- Spychala, Y.T., Hodgson, D.M., Prélat, A., Kane, I.A., Flint, S.S. and Mountney, N.P.** (2017b) Frontal and lateral submarine lobe fringes: Comparing sedimentary facies, architecture and flow processes. *J. Sediment. Res.*, **87**, 75–96.
- Spychala, Y.T., Hodgson, D.M., Stevenson, C. and Flint, S.S.** (2017c) Aggradational lobe fringes: The influence of subtle intrabasinal seabed topography on sediment gravity flow processes and lobe stacking patterns. *Sedimentology*, **64**, 582–608.
- Srivastava, S.P. and Roest, W.R.** (1991) Kinematics of the plate boundaries between Eurasia, Iberia, and Africa in the North Atlantic from the Late Cretaceous to the present. *Geology*, **19**, 613–616.
- Stevenson, C.J., Jackson, C.A.L., Hodgson, D.M., Hubbard, S.M. and Eggenhuisen, J.T.** (2015) Deep-water sediment bypass. *J. Sediment. Res.*, **85**, 1058–1081.
- Stevenson, C.J., Peakall, J., Hodgson, D.M., Bell, D. and Privat, A.** (2020) Tb or not tb: banding in turbidite sandstones. *J. Sediment. Res.*, **90**, 821–842.
- Steventon, M.J., Jackson, C.A.-L., Johnson, H.D., Hodgson, D.M., Kelly, S., Omma, J., Gopon, C., Stevenson, C. and Fitch, P.** (2021) Evolution of a sand-rich submarine channel-lobe system and impact of mass-transport and transitional flow deposits on reservoir heterogeneity: Magnus Field, northern North Sea. *Pet. Geosci.*, petgeo2020-095.
- Steventon, M.J., Jackson, C.A.L., Hodgson, D.M. and Johnson, H.D.** (2020) Lateral variability of shelf-edge and basin-floor deposits, Santos Basin, Offshore Brazil. *J. Sediment. Res.*, **90**, 1198–1221.
- Stow, D.A.** (1985) Brae oilfield turbidite system, North Sea. In: *Submarine Fans and Related Turbidite Systems* (Ed. A.H. Bouma, W.R. Normark, and N.E. Barnes), Springer, York, NY, 231–236.
- Stow, D.A.V. and Johansson, M.** (2000) Deep-water massive sands: Nature, origin and hydrocarbon implications. *Mar. Pet. Geol.*, **17**, 145–174.

- Strachan, L.J., Rarity, F., Gawthorpe, R.L., Wilson, P., Sharp, I. and Hodgetts, D.** (2013) Submarine slope processes in rift-margin basins, Miocene Suez Rift, Egypt. *Bull. Geol. Soc. Am.*, **125**, 109–127.
- Suárez, M. and de la Cruz, R.** (1997) Volcanismo pliniano del Lías durante los inicios de la cuenca de Neuquén, Cordillera del Viento, Neuquén, Argentina. Actas 7^o Congr. Geológico Chil. 266–270.
- Sugawara, E. and Nikaido, H.** (2014) Properties of AdeABC and AdeIJK efflux systems of *Acinetobacter baumannii* compared with those of the AcrAB-TolC system of *Escherichia coli*.
- Sumner, E.J., Amy, L.A. and Talling, P.J.** (2008) Deposit structure and processes of sand deposition from decelerating sediment suspensions. *J. Sediment. Res.*, **78**, 529–547.
- Sumner, E.J., Talling, P.J. and Amy, L.A.** (2009) Deposits of flows transitional between turbidity current and debris flow. *Geology*, **37**, 991–994.
- Sweet, M.L., Gaillot, G.T., Jouet, G., Rittenour, T.M., Toucanne, S., Marsset, T. and Blum, M.D.** (2020) Sediment routing from shelf to basin floor in the Quaternary Golo System of Eastern Corsica, France, western Mediterranean Sea. *GSA Bull.*, **132**, 1217–1234.
- Sylvester, Z., Cantelli, A. and Pirmez, C.** (2015) Stratigraphic evolution of intraslope minibasins: Insights from surface-based model. *Am. Assoc. Pet. Geol. Bull.*, **99**, 1099–1129.
- Sylvester, Z. and Lowe, D.R.** (2004) Textural trends in turbidites and slurry beds from the Oligocene flysch of the East Carpathians, Romania. *Sedimentology*, **51**, 945–972.
- Sylvester, Z., Pirmez, C. and Cantelli, A.** (2011) A model of submarine channel-levee evolution based on channel trajectories: Implications for stratigraphic architecture. *Mar. Pet. Geol.*, **28**, 716–727.
- Symons, W.O., Sumner, E.J., Paull, C.K., Cartigny, M.J.B., Xu, J.P., Maier, K.L., Lorenson, T.D. and Talling, P.J.** (2017) A new model for turbidity current behavior based on integration of flow monitoring and precision coring in a submarine canyon. *Geology*, **45**, 367–370.
- Talling, P.J.** (2013) Hybrid submarine flows comprising turbidity current and cohesive debris flow: Deposits, theoretical and experimental analyses, and generalized models. *Geosphere*, **9**, 460–488.
- Talling, P.J., Allin, J., Armitage, D.A., Arnott, R.W.C., Cartigny, M.J.B., Clare, M.A., Felletti, F., Covault, J.A., Girardclos, S., Hansen, E., Hill, P.R., Hiscott, R.N., Hogg, A.J., Clarke, J.H., Jobe, Z.R., Malgesini, G., Mozzato, A., Naruse, H., Parkinson, S., Peel, F.J., Piper, D.J.W., Pope, E.D., Postma, G., Rowley, P., Sguazzini, A., Stevenson, C.J., Sumner, E.J., Sylvester, Z., Watts, C. and Xu, J.** (2015) Key future directions for research on turbidity currents and their deposits. *J. Sediment. Res.*, **85**, 153–169.
- Talling, P.J., Amy, L.A. and Wynn, R.B.** (2007) New insight into the evolution of large-volume turbidity currents: Comparison of turbidite shape and previous

- modelling results. *Sedimentology*, **54**, 737–769.
- Talling, P.J., Amy, L.A., Wynn, R.B., Peakall, J. and Robinson, M.** (2004) Beds comprising debrite sandwiched within co-genetic turbidite: Origin and widespread occurrence in distal depositional environments. *Sedimentology*, **51**, 163–194.
- Talling, P.J., Masson, D.G., Sumner, E.J. and Malgesini, G.** (2012) Subaqueous sediment density flows: Depositional processes and deposit types. *Sedimentology*, **59**, 1937–2003.
- Talling, P.J., Peakall, J., Sparks, R.S.J., Cofaigh, C.Ó., Dowdeswell, J.A., Felix, M., Wynn, R.B., Baas, J.H., Hogg, A.J., Masson, D.G., Taylor, J. and Weaver, P.P.E.** (2002) Experimental constraints on shear mixing rates and processes: implications for the dilution of submarine debris flows. *Geol. Soc. London, Spec. Publ.*, **203**, 89–103.
- Tek, D.E., McArthur, A.D., Poyatos-Moré, M., Colombera, L., Allen, C., Patacci, M. and McCaffrey, W.D.** (2021a) Controls on the architectural evolution of deep-water channel overbank sediment wave fields: insights from the Hikurangi Channel, offshore New Zealand. *New Zeal. J. Geol. Geophys.*, **0**, 1–38.
- Tek, D.E., McArthur, A.D., Poyatos-Moré, M., Colombera, L., Patacci, M., Craven, B. and McCaffrey, W.D.** (2021b) Relating seafloor geomorphology to subsurface architecture: How mass-transport deposits and knickpoint-zones build the stratigraphy of the deep-water Hikurangi Channel. *Sedimentology*, **68**, 3141–3190.
- Tek, D.E., Poyatos-Moré, M., Patacci, M., McArthur, A.D., Colombera, L., Cullen, T.M. and McCaffrey, W.D.** (2020) Syndepositional tectonics and mass-transport deposits control channelized, bathymetrically complex deep-water systems (Aínsa depocenter, Spain). 729–762 pp.
- Terlaky, V. and Arnott, R.W.C.** (2014) Matrix-rich and associated matrix-poor sandstones: Avulsion splays in slope and basin-floor strata. *Sedimentology*, **61**, 1175–1197.
- Terlaky, V. and Arnott, R.W.C.** (2016) The control of terminal-splay sedimentation on depositional patterns and stratigraphic evolution in avulsion-dominated, unconfined, deep-marine basin-floor systems. *J. Sediment. Res.*, **86**, 786–799.
- Terlaky, V., Rocheleau, J. and Arnott, R.W.C.** (2016) Stratal composition and stratigraphic organization of stratal elements in an ancient deep-marine basin-floor succession, Neoproterozoic Windermere Supergroup, British Columbia, Canada. *Sedimentology*, **63**, 136–175.
- Thomson, K.D., Stockli, D.F., Clark, J.D., Puigdefàbregas, C. and Fildani, A.** (2017) Detrital zircon (U-Th)/(He-Pb) double-dating constraints on provenance and foreland basin evolution of the Aínsa Basin, south-central Pyrenees, Spain. *Tectonics*, **36**, 1352–1375.
- Tinterri, R.** (2011) Combined flow sedimentary structures and the genetic link between sigmoidal-and hummocky-cross stratification. *GeoActa*, **10**, 43–85.
- Tinterri, R., Muzzi Magalhaes, P., Tagliaferri, A. and Cunha, R.S.** (2016) Convolute laminations and load structures in turbidites as indicators of flow reflections and

- decelerations against bounding slopes. Examples from the Marnoso-arenacea Formation (northern Italy) and Annot Sandstones (south eastern France). *Sediment. Geol.*, **344**, 382–407.
- Tókéş, L. and Patacci, M.** (2018) Quantifying tabularity of turbidite beds and its relationship to the inferred degree of basin confinement. *Mar. Pet. Geol.*, **97**, 659–671.
- Trabucho-Alexandre, J., Dirkx, R., Veld, H., Klaver, G. and De Boer, P.L.** (2012) Toarcian black shales in the dutch central graben: Record of energetic, variable depositional conditions during an oceanic anoxic event. *J. Sediment. Res.*, **82**, 104–120.
- Tudor, E.P.** (2014) Facies variability in deep water channel to lobe transition zoneÇ Jurassic Los Molles Fm, Neuquen Basin Argentina.
- Twichell, D.C., Schwab, W.C. and Kenyon, N.H.** (1995) Geometry of sandy deposits at the distal edge of the Mississippi Fan, Gulf of Mexico. *Atlas Deep Water Environ.*, 282–286.
- Twiss, R.J. and Moores, E.M.** (1992) Structural Geology. W.H. Freeman and Company, New York.
- Valdez, V., Milana, J.P., Sobiesiak, M.S. and Kneller, B.** (2019) The Carboniferous MTD Complex at La Peña Canyon, Paganzo Basin (San Juan, Argentina). In: *Submarine Landslides: Subaqueous Mass Transport Deposits from Outcrops to Seismic Profiles*, 105–116.
- Van der Merwe, W.C., Hodgson, D.M., Brunt, R.L. and Flint, S.S.** (2014) Depositional architecture of sand-attached and sand-detached channel-lobe transition zones on an exhumed stepped slope mapped over a 2500 km² area. *Geosphere*, **10**, 1076–1093.
- Van Der Merwe, W.C., Hodgson, D.M. and Flint, S.S.** (2009) Widespread syn-sedimentary deformation on a muddy deep-water basin-floor: The vischkuil formation (Permian), Karoo Basin, South Africa. *Basin Res.*, **21**, 389–406.
- Van Der Merwe, W.C., Hodgson, D.M. and Flint, S.S.** (2011) Origin and terminal architecture of a submarine slide: A case study from the Permian Vischkuil Formation, Karoo Basin, South Africa. *Sedimentology*, **58**, 2012–2038.
- Van der Plas, L. and Tobi, A.C.** (1965) Reliability of point counting results; reply. *Am. J. Sci.* 263:722–724.
- Veiga, G.D., Schwarz, E. and Spalletti, L.A.** (2011) Análisis estratigráfico de la Formación Lotena (Calloviano superior- Oxfordiano inferior) en la Cuenca Neuquina Central, República Argentina. Integración de información de afloramientos y subsuelo. *Andean Geol.*, **38**, 171–197.
- Veiga, G.D., Schwarz, E., Spalletti, L.A. and Massaferró, J.L.** (2013) Anatomy And Sequence Architecture of the Early Post-Rift In the Neuquen Basin (Argentina): A Response To Physiography and Relative Sea-Level Changes. *J. Sediment. Res.*, **83**, 746–765.
- Vendettuoli, D., Clare, M.A., Hughes Clarke, J.E., Vellinga, A., Hizzet, J., Hage, S., Cartigny, M.J.B., Talling, P.J., Waltham, D., Hubbard, S.M., Stacey, C. and**

- Lintern, D.G.** (2019) Daily bathymetric surveys document how stratigraphy is built and its extreme incompleteness in submarine channels. *Earth Planet. Sci. Lett.*, **515**, 231–247.
- Vergani, G.D., Tankard, A.J., Belotti, H.J. and Welsink, H.J.** (1995) Tectonic Evolution and Paleogeography of the Neuquén Basin, Argentina. *Pet. basins South Am.*, **1904**, 383–402.
- Vicente, J.C.** (2005) Dynamic paleogeography of the Jurassic Andean Basin: Pattern of transgression and localisation of main straits through the magmatic arc. *Rev. la Asoc. Geol. Argentina*, **60**, 221–250.
- Watt, S.F.L., Talling, P.J., Vardy, M.E., Masson, D.G., Henstock, T.J., Hühnerbach, V., Minshull, T.A., Urlaub, M., Lebas, E., Le Friant, A., Berndt, C., Crutchley, G.J. and Karstens, J.** (2012) Widespread and progressive seafloor-sediment failure following volcanic debris avalanche emplacement: Landslide dynamics and timing offshore Montserrat, Lesser Antilles. *Mar. Geol.*, **323–325**, 69–94.
- Weaver, C.** (1931) Paleontology of the Jurassic and Cretaceous of West Central Argentina. Memoir University of Washington 1.
- Weaver, C.** (1942) A general summary of the Mesozoic of South and Central America. In: *Proceedings of the eighth American scientific congress held in Washington May 10-18*, 149–193.
- Weimer, P., Slatt, R.M. and Bouroullec, R.** (2007) Introduction to the petroleum geology of deepwater setting.
- Winker, C.D.** (1996) High-resolution seismic stratigraphy of a late Pleistocene submarine fan ponded by salt-withdrawal mini-basins on the Gulf of Mexico continental slope. *Proc. Annu. Offshore Technol. Conf.*, **1**, 619–622.
- Winterwerp, J.C. and Van Kesteren, W.G.** (2004) Introduction to the physics of cohesive sediment dynamics in the marine environment. *Elsevier*.
- Wynn, R.B., Kenyon, N.H., Masson, D.G., Stow, D.A.V. and Weaver, P.P.E.** (2002) Characterization and recognition of deep-water channel-lobe transition zones. *Am. Assoc. Pet. Geol. Bull.*, **86**, 1441–1462.
- Wynn, R.B., Talling, P.J., Masson, D.G., Le Bas, T.P., Cronin, B.T. and Stevenson, C.J.** (2012) The Influence of Subtle Gradient Changes on Deep-Water Gravity Flows: A Case Study From the Moroccan Turbidite System. *Appl. Princ. Seism. Geomorphol. to Cont. Base-of-Slope Syst. Case Stud. from Seafloor Near-Seafloor Analog.*, 371–383.
- Zachariah, A.J., Gawthorpe, R., Dreyer, T. and Corfield, S.** (2009a) Controls on early post-rift physiography and stratigraphy, lower to mid-Cretaceous, North Viking Graben, Norwegian North Sea. *Basin Res.*, **21**, 189–208.
- Zachariah, A.J., Gawthorpe, R.L. and Dreyer, T.** (2009b) Evolution and strike variability of early post-rift deep-marine depositional systems: Lower to Mid-Cretaceous, North Viking Graben, Norwegian North Sea. *Sediment. Geol.*, **220**, 60–76.
- Zhong, G. and Peng, X.** (2021) Transport and accumulation of plastic litter in

References

- submarine canyons—The role of gravity flows. *Geology*, **49**, 581–586.
- Zöllner, W. and Amos, A.J.** (1973) Descripción geológica de la hoja 32b, Chos Malal. Servicio Geológico Nacional. 97 pp.
- Zuffa, G.G.** (1985) Optical analyses of arenites: influence of methodology on compositional results. *Proven. arenites. Springer, Dordrecht.*, 165–189.

8. Appendix

Sample Bed	Sample	Quartz	Feldspar Group	Lithoclasts	Sheet Silicates	Accessory minerals	Organic particles	Matrix	Volcanic lithoclasts	Metamorphic lithoclasts	Sedimentary lithoclasts	Counted grains
S1	CH-1	27.6%	20.2%	29.5%	4.2%	0.0%	1.3%	17.3%	96.1%	2.8%	1.1%	400
S1	CH-2	26.9%	16.5%	33.1%	4.4%	0.0%	0.50%	18.6%	98.4%	0.0%	1.6%	400
S1	CH-3	28.1%	18.9%	34.7%	2.5%	0.0%	0.6%	15.2%	97.2%	1.1%	1.8%	400
S2	CH-4	22.1%	19.1%	25.1%	3.7%	0.0%	3.2%	26.9%	95.8%	0.0%	4.2%	400
S2	CH-5	22.7%	17.0%	21.9%	5.7%	0.8%	14.9%	17.0%	76.5%	0.0%	23.5%	400
S3	CH-A	28.8%	14.0%	43.8%	0.3%	0.3%	0.0%	12.7%	87.4%	3.1%	9.6%	400
S3	CH-B	27.5%	16.6%	33.9%	0.8%	0.0%	0.0%	21.2%	87.0%	13.0%	0.0%	400
S3	CH-C	24.2%	15.5%	33.3%	0.3%	0.3%	0.8%	25.6%	91.0%	6.0%	3.0%	400
S3	CH-D	27.1%	17.9%	26.1%	0.5%	0.5%	1.0%	26.9%	92.1%	5.5%	2.4%	400
S4	CH-E	29.1%	15.6%	36.6%	0.5%	0.5%	0.3%	17.4%	87.2%	10.9%	1.8%	400
S4	CH-F	27.1%	11.6%	44.3%	0.5%	0.0%	0.0%	16.5%	78.1%	19.2%	2.7%	400
S4	CH-6	38.2%	11.1%	46.2%	0.8%	0.0%	0.1%	3.5%	95.4%	4.1%	0.5%	400
S4	CH-7	36.8%	12.9%	40.8%	1.1%	0.0%	2.6%	5.8%	96.2%	2.5%	1.3%	400
S4	CH-8	48.3%	19.5%	22.8%	3.6%	0.8%	1.0%	3.9%	98.2%	1.4%	0.5%	400
S5	CH-9	13.6%	5.4%	32.3%	0.8%	1.0%	8.1%	38.8%	99.7%	0.0%	0.3%	400
S5	CH-10	17.3%	10.5%	18.1%	1.3%	0.3%	12.2%	40.3%	99.4%	0.0%	0.6%	400
S6	CH-11	30.2%	9.4%	30.0%	0.3%	0.0%	13.9%	16.2%	98.3%	1.7%	0.0%	400
S6	CH-12	28.8%	12.5%	26.3%	1.3%	0.3%	17.8%	13.0%	81.0%	1.9%	17.1%	400
S6	CH-13	33.1%	11.3%	33.1%	0.5%	0.0%	7.0%	14.9%	83.3%	0.0%	16.7%	400
S7A	CH-14	23.5%	15.8%	21.0%	5.6%	0.8%	7.7%	25.6%	86.4%	0.0%	13.6%	400
S7B	CH-15	22.7%	12.7%	21.1%	6.0%	0.5%	7.2%	29.9%	79.1%	1.5%	19.4%	400
S8	CH-G	29.2%	14.3%	28.7%	2.3%	0.5%	2.5%	22.5%	86.8%	3.5%	9.7%	400
S8	CH-H	24.4%	16.5%	36.9%	1.0%	0.3%	2.3%	18.6%	90.2%	0.8%	8.9%	400
S8	CH-i	33.8%	13.1%	28.7%	1.5%	0.0%	2.6%	20.3%	91.8%	1.1%	7.1%	400
S9	CH-16	36.5%	17.2%	30.7%	0.0%	0.3%	2.6%	12.7%	95.2%	2.9%	1.8%	400
S10	CH-17	38.6%	13.1%	29.7%	1.3%	0.5%	1.8%	14.9%	90.5%	2.7%	6.8%	400
S10	CH-18	27.7%	17.7%	16.5%	3.8%	0.8%	8.8%	24.7%	89.2%	0.0%	10.8%	400
S11	CH-19	19.0%	14.3%	23.8%	1.1%	0.3%	8.9%	32.4%	85.9%	0.0%	14.1%	400
S11	CH-20	22.3%	7.7%	25.1%	2.5%	1.1%	3.9%	37.4%	78.9%	0.0%	21.1%	400
S11	CH-21	32.5%	17.1%	12.5%	2.5%	0.5%	5.2%	29.6%	84.5%	0.0%	15.5%	400
S12	CH-22	30.6%	12.0%	33.8%	4.6%	0.5%	5.3%	13.1%	81.70%	0.00%	18.30%	400
S12	CH-23	24.2%	15.6%	33.6%	1.5%	0.8%	4.1%	20.2%	81%	0.00%	19%	400
S12	CH-24	28.7%	17.3%	27.4%	1.1%	0.3%	2.7%	22.6%	80.20%	0.00%	19.80%	400
S13	CH-25	30.6%	14.0%	36.3%	0.8%	0.0%	0.8%	17.4%	90.0%	5.7%	4.3%	400
S13	CH-26	34.7%	12.9%	16.7%	0.8%	0.5%	1.0%	33.4%	62.0%	0.0%	38.0%	400
S14	CH-27	31.7%	15.1%	43.1%	0.5%	0.0%	0.8%	8.8%	79.2%	17.2%	3.7%	400
S14	CH-28	33.7%	13.4%	38.4%	0.3%	0.3%	1.0%	12.8%	75.5%	14.9%	9.5%	400
S15	CH-29	28.7%	16.5%	32.5%	1.9%	0.3%	0.5%	19.6%	88.9%	6.3%	4.8%	400
S15	CH-30	24.1%	13.6%	35.3%	1.8%	0.8%	1.5%	22.8%	41.3%	8.7%	50.0%	400
S15	CH-31	24.6%	23.9%	18.6%	1.0%	0.3%	1.0%	30.6%	90.3%	5.4%	4.3%	400

Table 1 – Mineralogy table of detrital grains of the analysed samples: Lithoclast group is subdivided into volcanic (Lv), metamorphic (Lm), and sedimentary (Ls) lithoclasts.

Appendix

Sample	Sample Bed	Bed type	Modal size class	Mean (mm)	Median (mm)	Sorting (F & W)	Sorting (F & W)	Counted grains
CH-1	S1	F	Medium sand	0.3072mm	0.1477mm	1.27	poorly sorted	200
CH-2	S1	F	Medium sand	0.2910mm	0.0492mm	1.312	poorly sorted	200
CH-3	S1	F	Medium sand	0.2664mm	0.4361mm	0.831	moderately sorted	200
CH-4	S2	D	Very fine sand	0.1232mm	0.1449mm	0.817	moderately sorted	200
CH-5	S2	D	Very fine sand	0.1277mm	0.1737mm	0.771	moderately sorted	200
CH-A	S3	F	Coarse sand	0.8341mm	1.5535mm	1.489	poorly sorted	200
CH-B	S3	F	Coarse sand	0.6380mm	0.9349mm	1.326	poorly sorted	200
CH-C	S3	F	Coarse sand	0.6647mm	1.0157mm	1.036	poorly sorted	200
CH-D	S3	F	Medium sand	0.3152mm	0.5501mm	0.946	moderately sorted	200
CH-E	S4	B	Medium sand	0.7568mm	1.5690mm	1.564	poorly sorted	200
CH-F	S4	B	Very coarse sand	0.9931mm	0.2036mm	1.152	poorly sorted	200
CH-6	S4	B	Very coarse sand	0.9987mm	1.0557mm	1.142	poorly sorted	200
CH-7	S4	B	Medium sand	0.6497mm	0.5536mm	1.154	poorly sorted	200
CH-8	S4	B	Medium sand	0.4037mm	0.3805mm	0.829	moderately sorted	200
CH-9	S5	F	Fine sand	0.1696mm	0.1428mm	0.879	moderately sorted	200
CH-10	S5	F	Very fine sand	0.1020mm	0.0513mm	0.932	moderately sorted	200
CH-11	S6	B	Medium sand	0.3266mm	0.1514mm	0.966	moderately sorted	200
CH-12	S6	B	Fine sand	0.2074mm	0.0978mm	0.895	moderately sorted	200
CH-13	S6	B	Fine sand	0.1993mm	0.3100mm	0.962	moderately sorted	200
CH-14	S7A	D	Medium sand	0.2711mm	0.2768mm	0.974	moderately sorted	200
CH-15	S7B	D	Fine sand	0.1961mm	0.1762mm	0.859	moderately sorted	200
CH-G	S8	E	Medium sand	0.3315mm	0.3908mm	0.863	moderately sorted	200
CH-H	S8	E	Medium sand	0.3096mm	0.1906mm	0.861	moderately sorted	200
CH-I	S8	E	Fine sand	0.2130mm	0.1262mm	0.67	moderately well sorted	200
CH-16	S9	B	Coarse sand	0.4544mm	0.4377mm	1.167	poorly sorted	200
CH-17	S10	F	Medium sand	0.3860mm	0.7878mm	0.87	moderately sorted	200
CH-18	S10	F	Fine sand	0.2519mm	0.5500mm	0.893	moderately sorted	200
CH-19	S11	C	Fine sand	0.2179mm	0.1659mm	0.865	moderately sorted	200
CH-20	S11	C	Fine sand	0.2006mm	0.7142mm	1.033	poorly sorted	200
CH-21	S11	C	Very fine sand	0.1248mm	0.0978mm	0.857	moderately sorted	200
CH-22	S12	E	Medium sand	0.3235mm	0.2803mm	0.781	moderately sorted	200
CH-23	S12	E	Medium sand	0.2816mm	0.3158mm	0.864	moderately sorted	200
CH-24	S12	E	Fine sand	0.1804mm	0.2052mm	0.783	moderately sorted	200
CH-25	S13	A	Medium sand	0.3500mm	0.4914mm	0.887	moderately sorted	200
CH-26	S13	A	Fine sand	0.1458mm	0.0746mm	0.749	moderately sorted	200
CH-27	S14	B	Coarse sand	0.6170mm	0.5347mm	1.322	poorly sorted	200
CH-28	S14	B	Medium sand	0.4170mm	0.3589mm	0.962	moderately sorted	200
CH-29	S15	E	Medium sand	0.4374mm	0.3564mm	0.943	moderately sorted	200
CH-30	S15	E	Medium sand	0.3034mm	0.1072mm	0.899	moderately sorted	200
CH-31	S15	E	Medium sand	0.2877mm	0.1943mm	0.956	moderately sorted	200

Table 2 –Grain size table. The modal grain size, mean and median grain size (mm) and sorting (F & W) of each sample are shown.